

Proceedings of the 2004 Earthquake Engineering Symposium for Young Researchers



August 5-8, 2004 • Kiawah Island Golf Resort • Charleston, South Carolina

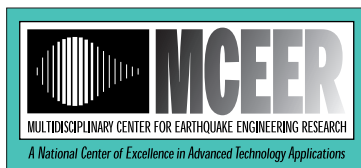
Sponsored by the National Science Foundation Earthquake Engineering Research Centers Program

Mid-America Earthquake Center

Multidisciplinary Center for Earthquake Engineering Research

Pacific Earthquake Engineering Research Center





The Multidisciplinary Center for Earthquake Engineering Research

The Multidisciplinary Center for Earthquake Engineering Research (MCEER) is a national center of excellence in advanced technology applications that is dedicated to the reduction of earthquake losses nationwide. Headquartered at the University at Buffalo, State University of New York, the Center was originally established by the National Science Foundation (NSF) in 1986, as the National Center for Earthquake Engineering Research (NCEER).

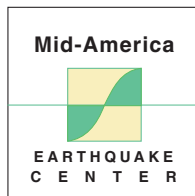
Comprising a consortium of researchers from numerous disciplines and institutions throughout the United States, the Center's mission is to reduce earthquake losses through research and the application of advanced technologies that improve engineering, pre-earthquake planning and post-earthquake recovery strategies. Toward this end, the Center coordinates a nationwide program of multidisciplinary team research, education and outreach activities.

Funded principally by NSF, the State of New York and the Federal Highway Administration (FHWA), the Center derives additional support from the Federal Emergency Management Agency (FEMA), other state governments, academic institutions, foreign governments and private industry.

Proceedings of the 2004 Earthquake Engineering Symposium for Young Researchers

Charleston, South Carolina
August 5-8, 2004

MAE



Mid-America Earthquake Center
University of Illinois at Urbana-Champaign
1241 Newmark Civil Engineering Lab
205 N. Matthews Ave. • Urbana, IL 61801
Phone: (217) 244-6302 • fax: (217) 333-3821
Website: <http://mae.ce.uiuc.edu>

MCEER



Multidisciplinary Center for Earthquake Engineering Research
University at Buffalo, State University of New York
Red Jacket Quadrangle • Buffalo, NY 14261
Phone: (716) 645-3391 • fax: (716) 645-3399
E-mail: mceer@mceermail.buffalo.edu
Website: <http://mceer.buffalo.edu>

PEER



Pacific Earthquake Engineering Research Center
University of California, Berkeley
1301 South 46th Street, RFS 451 • Richmond, California, 94804-4698
Phone: (510) 231-9554 • fax: (510) 231-9471
E-mail: peer_ctr@eerc.berkeley.edu
Website: <http://peer.berkeley.edu>

MCEER-05-SP02
April 2005

Sponsored by the National Science Foundation, Research Experience for Undergraduates Program

Compiled by: Patricia Kraemer, Linda Nelson, and Sandra Menke

Preface

The *2004 Annual Tri-Center Earthquake Engineering Symposium for Young Researchers*, held August 5-8, 2004 at Kiawah Island Resort in Charleston, South Carolina, and organized by MCEER, was a great success. Twenty young undergraduate researchers from MCEER, PEER, MAE and FSU gave presentations on individual research projects conducted during summer internships at the following host institutions: California Institute of Technology, Georgia Institute of Technology, Stanford University, Texas A&M University, University at Buffalo, University of California at Berkeley, Davis, Los Angeles and San Diego, University of Illinois at Urbana-Champaign, University of Memphis, University of Tokyo, University of Washington, and Washington University in St. Louis. The students' home universities were in California, Florida, Illinois, Indiana, Michigan, Missouri, New Mexico, New York, Ohio, South Carolina, Texas, Washington, D.C. and Washington State.



Students from the three centers toured the Cooper River Bridge with Project Manager Charles T. Dwyer. It will be the largest cable-stayed span bridge in North America when completed next summer.

In addition to the exchange of engineering research, the Symposium included a tour of the Cooper River Bridge in Charleston, where students visited the cable-stayed section after viewing a presentation about the bridge's design and construction. The field trip allowed students to witness the effects of earthquake research on engineering design in a seismic region.

There were also two guest speakers: MCEER Diversity Director Makola Abdullah, who discussed the resources available to undergraduate students interested in continuing their education and the importance of promoting diversity at the graduate studies level; and Joseph Herkert, of North Carolina State University, who explained the importance of engineering ethics.

The Symposium, part of the Research Experience for Undergraduates Program funded by NSF, was a wonderful experience, giving participants the opportunity to present their research in a formal setting and meet people that might become future colleagues.

*-Submitted by Karla Villarreal, Florida State University
Reprinted from the MCEER Bulletin, Volume 18, No. 2, Fall/Winter 2004*

Contents

Analysis of NATM Tunnel Responses due to Earthquake Loading in Various Soils <i>Zaneta G. Adme</i>	1
Development of a One-Story Model for Use on an Educational Shake Table <i>Lisa M. Anderson</i>	11
Ground Motion Distance Attenuation, Measurement & Tools <i>Timothy Brownawell</i>	31
Performance of Concentrically Braced Frames Under Cyclic Loading <i>Nathan Canney</i>	37
Seismic Isolation for Small Reinforced Concrete Structures: A Preliminary Investigation on Material Cost <i>Abiel Carrillo</i>	49
Simplifying Bridge Models for Fragility Analysis <i>Theodore Deligiannidis</i>	65
Performance of Existing Reinforced Concrete Columns under Bidirectional Shear and Axial Loading <i>Laura M. Flores</i>	93
Estimating Seismic Damage and Repair Costs <i>Raymond Foltz</i>	135
Building Loss Modeling and Benchmarking: EDP TO DV <i>Vivian D. Gonzales</i>	151
Advance Simulation Tools: Soil-Structure Interaction <i>Mary Grondin</i>	163
Bridge Abutment Soil Compaction Test <i>Ashford Kneitel</i>	175
Analysis of Rotational Column with Plastic Hinge <i>Michael Long and Corey Bergad</i>	183
Modeling Community Goal Dynamics: A System Dynamics Approach to Increasing the Goal of Safety without the Stimulus of Disaster <i>Meagan Mauter</i>	197

Contents (Cont'd)

3D Visualization Program for Earthquake Simulation <i>Christy Nishimoto</i>	215
HD-2A: Intra-Plate Source Modeling <i>Lindsey Oliver</i>	229
Lateral Loading of Cast-in-Drilled-Hole-Shaft <i>Manuel E. Ponce</i>	249
Identifying Configuration and Connection Details of Unreinforced Masonry Structures in Mid-America <i>Ty A. Stokes</i>	263
Effects of MR Damper Placement on Structure Vibration Parameters <i>Karla A. Villarreal</i>	279
Agenda	293
Participants	297

ANALYSIS OF NATM TUNNEL RESPONSES DUE TO EARTHQUAKE LOADING IN VARIOUS SOILS

Zaneta G. Adme

*Home Institution: Dept. of Civil and Env. Engineering FAMU-FSU College of Engineering
2525 Pottsdamer St., Tallahassee, FL 32310*

Host Institution: Tokyo University

Advisor: Makola M. Abdullah, Ph.D.

ABSTRACT

Tunnels play a large part in the redevelopment of urban areas. In almost all urbanized areas it is hard to avoid building in close proximity to previously constructed building. Many of these urban areas also lie in close proximity to water, in which weaker soils prevail. Some of these areas, also, are prone to frequent earthquakes. It is necessary, therefore, for these areas to implement standard tunneling techniques. The New Australian Tunneling Method (NATM), which addresses the concerns listed above, is becoming increasingly popular and has been adopted by some countries as the preferred method of tunneling. The NATM is a method that incorporates the surrounding rock or soil into a ring-like support for the structure. With the growing popularity of this method, it is necessary to determine which soils are best suited for this method of tunneling. In this project the soils of various cities will be analyzed to determine which of the soils perform better with the NATM using a two dimensional model of the tunnel that is being exposed to earthquake excitations.

KEYWORDS

New Australian Tunneling Method (NATM), earthquake, finite elements.

PROBLEM STUDIED

There are several reasons for utilizing tunnels. They can be used to connect land masses, to bypass impeding geologic formation, or stability issues, and to reduce environmental concerns. Most tunnels, however, are used to increase the flow of traffic. Fifty percent of the world's population live in urban areas and seventy percent of the population live in earthquake prone areas (Merritt, et al. 1985). Initially, tunnels were designed with no regard to seismic effects, but, recently, there has been enhanced awareness of seismic hazards for underground structures (Merritt, et al. 1985).

There are two broad categories of earthquake effects of tunnels: ground shaking and ground failure. When seismic waves propagate through the earth's crust, the resulting

ground motions are considered ground shaking. There are two basic categories of ground shaking. Body waves travel within the earth's inner layers. These waves can be either longitudinal P or transverse shear S waves. P waves move in a compressional motion similar to the motion of a slinky, while the S waves move in a shear motion perpendicular to the direction the wave is travelling. These waves can travel in any direction underground. Surface waves travel along the earth's surface in the same manner a ripple would travel through water. These waves can either be Rayleigh or Love waves. Love waves shake the surface side-to-side. Rayleigh waves move the surface of the earth around in a circle, forward and down then back and up. This is the same as the motion in an ocean wave (Merritt, et al. 1985). Any tunnel structure will be deformed as the ground is deformed by the traveling waves.

Ground failure can include different types of ground instability. These can include faulting, liquefaction, and tectonic uplift and subsidence. Faulting occurs when an increase in stress causes rocks to break. Liquefaction is a phenomenon in which the strength and stiffness of a soil is reduced by earthquake shaking or other rapid loading. Tectonic uplift and subsidence is the upward and downward movement of the ground due to plate movement. These phenomena have been responsible for tremendous amounts of damage in historical earthquakes around the world. Each of these hazards could possibly be detrimental to tunnel structures (Merritt, et al. 1985).

Many tunneling methods are in common use, and a suitable one is generally chosen according to geology, tunnel dimensions, and other factors (Kirzhner and Rosenhouse 2000). The New Australian is a method in which, after a section of tunneling is completed, shotcrete is applied to the surface of the tunnel and the surrounding rock or soil becomes integrated into the support structure (Yang, 2002). Extreme care is taken during excavation and immediate application of support media prevents unnecessary loosening of soil. These tunnels use rounded tunnel shapes to prevent stress concentrations in corners where most failure mechanisms start (Yamaji, 1998). These tunnels, also, utilize thin linings to minimize bending moment. Observation of tunnel behavior during construction is an important part of NATM. This optimizes working procedures and support requirements (Yang, 2002). Many countries have adopted this method as the primary method of construction.

OBJECTIVE

The objective of this project is to determine which soil types, when used in conjunction with a tunnel completed using the New Australian Tunneling Method, perform better when subjected to seismic excitation. For this purpose, soils from seven cities were selected and a finite element model of the tunnel created for each case. Comparisons based on the maximum displacement each soil experienced when subjected to an earthquake were then made.

RESEARCH APPROACH

The first step was to identify the physical problem. This included describing the physical structure, identifying the source of dynamic excitation, and determining the expected outcomes. The next step in the process was defining the inputs and then defining the model based on the inputs. The last step was to find the solution of the model and review the results of the project.

The world cities selected for this project were:

- Agadir, Morocco
- Avezzano, Italy
- Chimbote, Peru
- Los Angeles, California
- Mexico City, Mexico
- Tangshan, China
- Tokyo, Japan

There were four basic criteria used to select the cities used for this project. The first criterion was the earthquake history of the city. It was necessary to use cities that were susceptible to large magnitude earthquakes. The next criterion was the population of the city to evaluate the possibility of tunnel use, which is the third criterion. Tunnels are more likely to be used in cities that have a large population. The last criterion used was the variance in the soil types present in these areas. It was necessary to select cities with contrasting soils to obtain a broad range of results.

There are currently 15 different soil orders present in the world (Yamaji, 1998). Each city used in this experiment was classified by soil order. That soil order was then classified by the aggregate(s) associated with them as shown in Table 1.

Table 1. Soil order and soil types.

Location	Soil Order	Soil Type
Agadir, Morocco	Alfisols	Low Plasticity Clay
Avezzano, Italy	Ultisols	Low Plasticity Silt
Chimbote, Peru	Entisols	Gravel-Sand Mixture
Los Angeles, California	Mollisols	Organic
Mexico City, Mexico	Andisols	Medium Plasticity Silt
Tangshan, China	Inceptisols	Sandy Gravel
Tokyo, Japan	Oxisols	High Plasticity Clay

The specific properties of each soil are listed in Table 2. This properties listed are needed to in the calculations for each city.

Table 2. Soil Properties.

	Soil Type	Mass Density (kg/m³)	Elastic Modulus (Pa)	Poisson's Ratio	Internal Friction Angle (deg.)	Cohesion (Pa)
Gravel	Uniform	1600	4.00E+07	0.25	34	0
	Sandy w/ few fines	2100	4.00E+07	0.25	35	0
	Sandy w/ silt or clay	2100	4.00E+07	0.25	35	1000
	Mixture of gravel and sand	2000	1.50E+07	0.25	38	3000
Sand	Uniform, fine	1600	1.50E+07	0.25	32	0
	Uniform, coarse	1600	2.50E+07	0.25	34	0
	Uniform, well-graded	1800	2.00E+07	0.25	33	0
Silt	Low plasticity	1750	4.00E+06	0.25	28	2000
	Medium to high plasticity	1700	3.00E+06	0.25	25	3000
Clay	Low plasticity	1900	2.00E+06	0.28	24	6000
	Medium plasticity	1800	1.00E+06	0.25	20	8000
	High plasticity	1650	6.00E+05	0.25	17	10000
	Organic	1550	5.00E+05	0.25	20	7000
Rock	Granite	2700	7.40E+10	0.25	51	5.51E+07

The physical structure used for this simulation consisted of a tunnel surrounded by two ground layers, each 130 meters wide (Figure 1). The bottom layer was granite rock and was 106 meters in height. The properties for this layer remained constant during each trial. The uppermost layer was a 24 meter deep soil layer that changed according to the soil properties associated with each trial city. The tunnel was circular with a 22 meter diameter and was buried 67 meters below the ground surface.

Finite element method was used in this project. This method is used to model and solve complex two and three dimensional engineering problems. The Visual Finite Element Analysis (VisualFEA) program incorporates powerful finite element processing software with a user-friendly graphical interface that reduces the amount of time needed for programming.

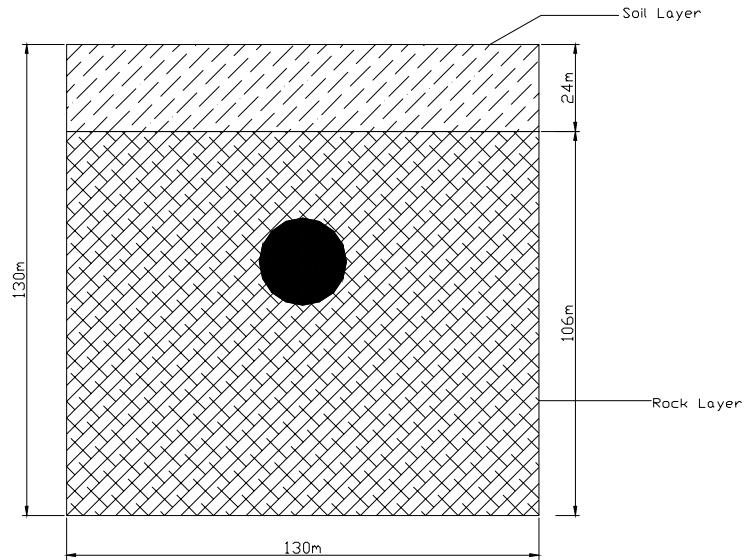


Figure 1. Physical Structure.

First a two dimensional plane strain model was used. This is used in modeling three dimensional structures that are uniform throughout their length, e.g. beams and cylinders. The data was taken from a point between the rock and soil interface directly above the highest point of the tunnel (Figure 2).

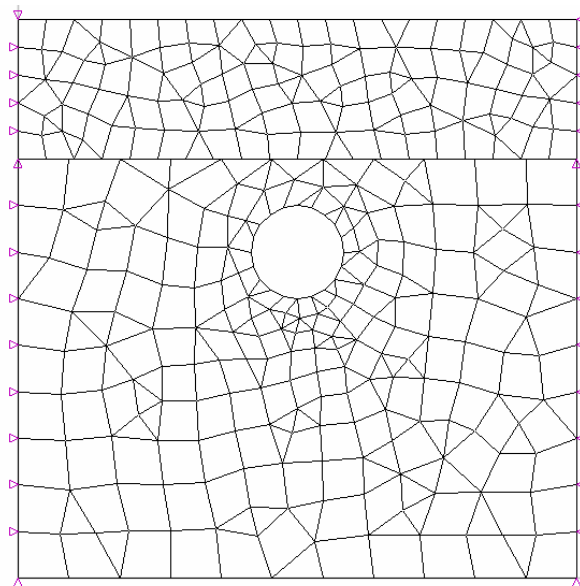


Figure 2. VisualFEA structure.

Fixed vertical ends were used to restrict the movement of the ends of the model. A damper was placed at the bottom boundary to keep it from moving uncontrollably. For

this model Rayleigh damping of 0.05 was used to model the natural damping characteristics of the rock and the soil.

The source of dynamic excitation used in this project was the acceleration record for the 1995 Kobe, Japan earthquake, as shown in Figure 3.

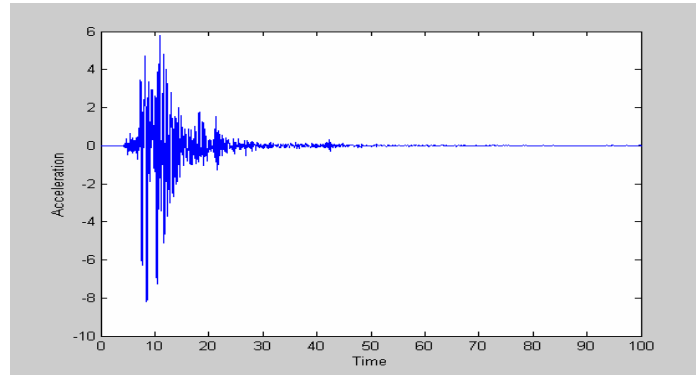


Figure 3. Acceleration record of the 1995 Kobe earthquake, Japan).

This earthquake data was used because this earthquake was the most devastating to civil infrastructure in recorded history. The acceleration input from the earthquake was applied to the bottom boundary.

OUTCOMES

Since there are thirteen different soil types, the recorded data from uniform gravel and medium to high plasticity silt are evaluated for comparison purpose.

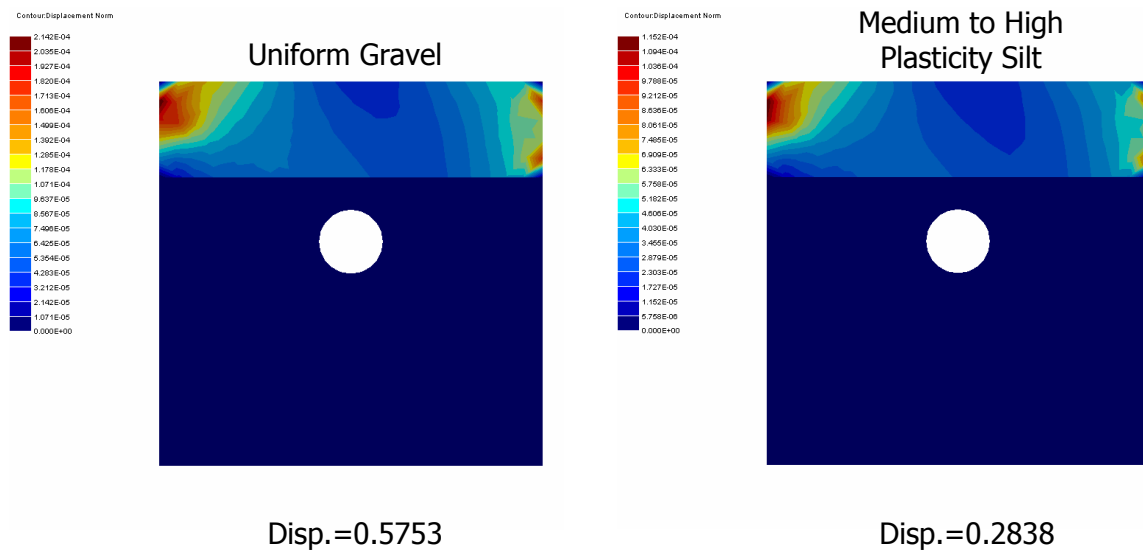


Figure 4. Graphical Results for Uniform Gravel and Medium to High Plasticity Silt

Although the bands of color seem similar in their placement, their difference is relayed in the scales of each soil. The scale for uniform gravel goes from 0-2.1406 cm and the scale for medium to high plasticity silt only goes form 0-1.1526 cm.

The displacement results for all soils tested are listed in Table 3. For this project, it was found that soils containing between ten and fifty percent fine particles performed better under excitation than soils with smaller amounts of fine particles(<10%). Soils with the greatest amounts of fines (>50%) performed unfavorably as compared to the other soils. Soils that had a relatively low modulus of elasticity had a greater maximum displacement than other soils in the study. The best performing soils were in the gravel category. These soils performed better overall than sand, silt, or clay. The sand category performed the worst overall, although uniform sand had one of the lowest maximum displacements in all categories.

Table 3. Displacement results.

	Soil Type	Maximum Displacement (cm)
Gravel	Uniform	0.5783
	Sandy w/ few fines	0.5708
	Sandy w/ silt or clay	0.02057
	Mixture of gravel and sand	0.05604
Sand	Uniform, fine	1.5550
	Uniform, coarse	0.03947
	Uniform, well-graded	1.1515
Silt	Low plasticity	0.2129
	Medium to high plasticity	0.28385
Clay	Low plasticity	0.4304
	Medium plasticity	0.85182
	High plasticity	1.4148
	Organic	1.7049

The results for each city are presented in Table 4. Tangshan, China recorded the smallest maximum displacement for the point of interest. The maximum displacement was only 0.02057 cm. The location that recorded the highest maximum displacement was Tokyo, Japan, 1.419 cm. Although Tokyo has the highest maximum displacement, these displacements would only produce minor cracks in the tunnel structure (Yang, 2002). Using the model representing a NATM tunnel, it is shown that tunnels constructed using this tunneling method produces relatively small displacements under earthquake loadings and could possibly considered as the primary method of construction in other projects.

Table 4. Displacement results for selected cities

Location	Soil Type	Maximum Displacement (cm)
Agadir, Morocco	Low Plasticity Clay	0.4304
Avezzano, Italy	Low Plasticity Silt	0.2129
Chimbote, Peru	Gravel-Sand Mixture	0.05604
Los Angeles, California	Organic	0.1704
Mexico City, Mexico	Medium Plasticity Silt	0.2839
Tangshan, China	Sandy Gravel w/ Silt	0.02057
Tokyo, Japan	High Plasticity Clay	1.419

POSSIBLE FUTURE WORK

To increase the accuracy of this project, a three dimensional model with varying ground layers can be used. A water table can be introduced to simulate the possibility of liquefaction. Also, a structure that does not include a tunnel could be used for comparison with each soil type.

ACKNOWLEDGEMENTS

I would like to thank MCEER, the REUJAT Program, the FAMU Undergraduate Program, and the National Science Foundation. I would also like to thank my host institution, the University of Tokyo, my host professor, Yozo Fujino, Ph.D., my home advisor, Makola M. Abdullah, Ph. D., and graduate advisors, Terri R. Norton, M.S.C.E. and Claudia M. D. Wilson, M.S.C.E.

References

- Kirzhner, F. and Rosenhouse, G., 2000. *Numerical analysis of tunnel dynamic response to earth motions*. Tunneling and Underground Space Technology, Volume 15, Issue 3, 249-258 .
- Merritt, J. L., Monsees, J. E., Hendron, A. J., 1985. *Seismic design of underground structures: Proc of the 1985 Rapid Excavation and Tunneling Conference, New York*. International Journal of Rock Mechanics and Mining Science & Geomechanics Abstracts, Volume 23, Issue 6, 255-282.
- Yang, M. W. W., 2002. *Principles of Tunnel Lining Design*. AGS/IMM Technical Meeting 2002 on “Underground Excavation in Urban Environments”.
- Yamaji, H. *Iwate-Ichinohe Tunnel on the Tohake New Trunk Line*. JSCE, Volume 30, Issue 10, 1435-1468 .
- Intuition Software, 1999. *VisualFEA-Visual Finite Element Analysis*. Chonbuk, South Korea: Intuition Software.

**DEVELOPMENT OF A ONE-STORY MODEL FOR USE ON AN
EDUCATIONAL SHAKE TABLE**

Lisa M. Anderson, State University of New York at Buffalo
REU Intern with the Multidisciplinary Center for Earthquake Engineering Research
REU Advisor: Dr. Michael C. Constantinou
Professor and Chairman, Department of Civil, Structural, and Environmental Engineering
State University of New York at Buffalo

Abstract

Instructional shake table demonstrations provide a basic depiction of structural dynamics and earthquake mechanics. Undergraduate students can benefit from these hands-on experiments. The properties and performance of an existing one-story model that has been tested on the instructional shake table have been determined and are presented in the following report. This data was then compared to a model retrofitted with fluid viscous dampers. The effect of a model seismic isolation system is also presented in this study. Based on this, conclusions can be made on the effectiveness of each seismic protective system. Through this experimentation, a valuable understanding of the qualitative properties of these models has been achieved.

1 - Introduction

The first instructional shake tables were developed through the University Consortium on Instructional Shake Tables (UCIST) in 1999. These small-scale shake tables have been implemented into classroom settings to depict earthquake solutions. As earthquake engineering becomes more prevalent, it is necessary to introduce basic concepts to students at the beginning of their educational paths.

Experimentation and hands on experience seems to be the best way to explain complex topics to young learners. The students are able to see a visual representation of resonance. The effects of damping devices on the period of oscillation can also be exposed.

In order to create a more “concrete” method of experimentation, a technical report must connect the visual occurrences with the underlying scientific principles. The focus of this paper is the technical presentation of the engineering properties of the model to be used in the demonstrations. The model is a One-story frame structure with flexible sides, fluid viscous dampers, and a sliding isolation system. Also included in this report will be an experiment with each variation of the structure using 4 different earthquake acceleration time histories.

These results will be used in shake table demonstrations to future civil engineers and other educational groups.

2 – Geometry of the Model

The model is constructed to a 1/16th length scale. When the time scale is taken to be 1/4th, the scale for acceleration is 1 (see *Proof for Scaling Factors* below).

Proof for Scaling Factors

$$S = \frac{1}{2} * a * t^2$$

$$\frac{1}{16} * S = \frac{1}{2} * a * (\frac{1}{4} * t)^2$$

$$S = \frac{1}{2} * a * t^2$$

(Eq 1)

Medium density fiberboard (MDF) is the material used for construction of this model. Because MDF is comprised of small wood particles glued together, a shear fracture is less likely to occur than in plywood or standard grain wood. Also, the bottom of each floor has been milled out to fit a 1/2" steel plate made of standard construction steel. This helps to reduce any chances of shear failure at the bonding points of the MDF. The sides of the model are 0.065" thick brass.

A sliding isolation system is used for the base of the model. The system is made to model an Earthquake Protection Systems, Inc. Friction Pendulum Bearing. This is shown below in Figure 1. The base is attached to the shake table using four screws.

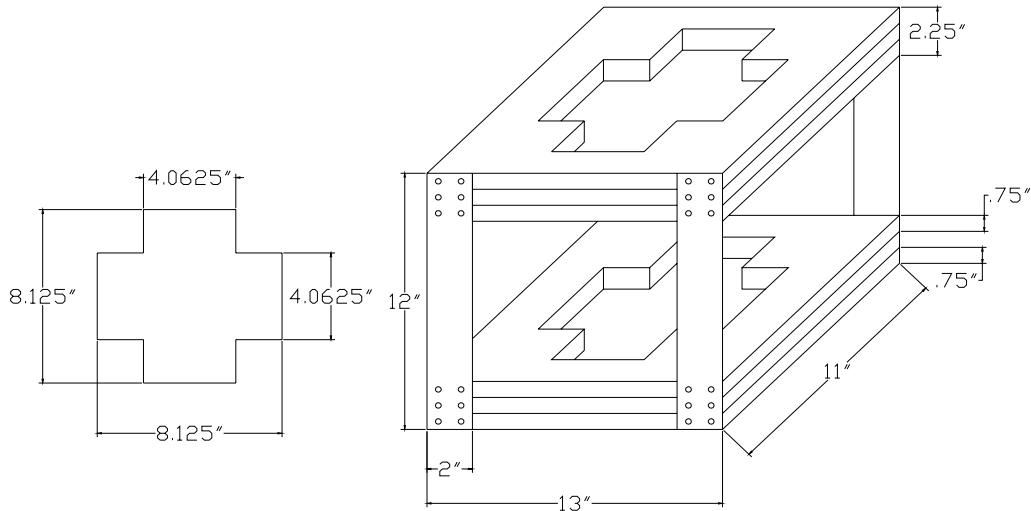


Figure 1

The system is isolated when the ball plunger supports are free to move on the aluminum cups. A large screw attaches the first floor to the base of the system to model non-isolated behavior.

The cups used to contain the bearings are simply aluminum cans filled with concrete. The cans are filled to reduce the softness of aluminum. Using a template method, the radius of curvature of the cups in the model is determined. Circles of different diameters are cut from a thin, rigid cardboard material. The templates are then fitted to the cups in the model. A light is pointed at one side of the cardboard. Trial and error is implemented for a perfect fit. See *Figure 2* below. The radius of curvature for these cups was determined to be 3.25”.

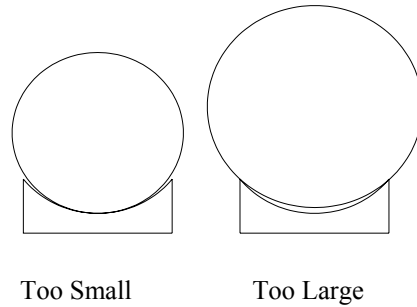


Figure 2

A schematic of the actual model is shown below in *Figure 3*.

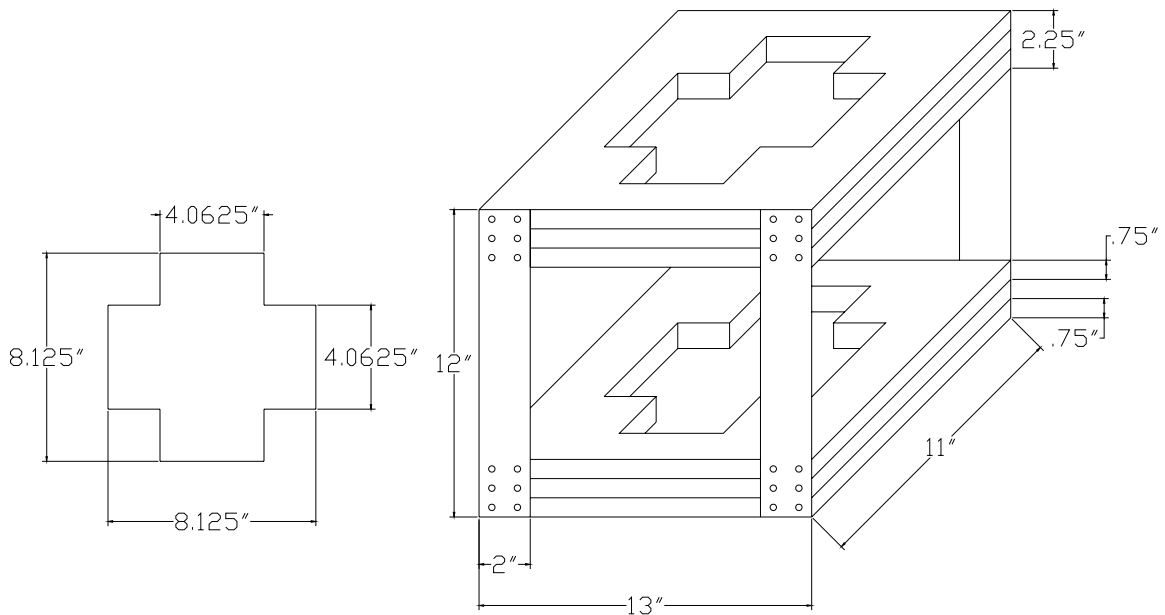


Figure 3

The brass sides are used to simulate the flexibility of the prototype structure. Note that they are screwed on to the structure securely, to ensure fixed end conditions. The cut outs on each floor are made for bricks, which can be added if more weight on either floor is desired. The structure, without the bricks, weighs 45.5 lbs.

The ball plungers, which support each corner of the structure, are shown in detail in *Figure 4*. Inside the plunger is a spring that pushes the ball against the lip. The spring will depress under a load that exceeds 50lb. In this case, the ball will roll freely; otherwise, the plungers will act as a slide bearing. The latter is the case for this model. However, the desired supporting system is a roller; to account for this dissimilarity, lubricating oil is applied to the cups. The actual ball plungers used on this model were produced by MSC. Both the body and the ball are constructed from stainless steel.

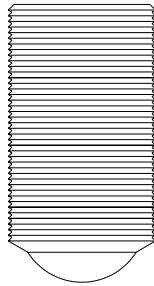


Figure 4

The damping devices to be added to the structure are relatively small. The dampers are intended for use in model car suspension systems. To modify them, the spring included with the damper is removed and the chamber is filled with oil. Because oil is only slightly compressible, orifices are drilled into the internal piston to lower the force required to initiate damping. Below is a detail of the model damper (*Figure 5*).

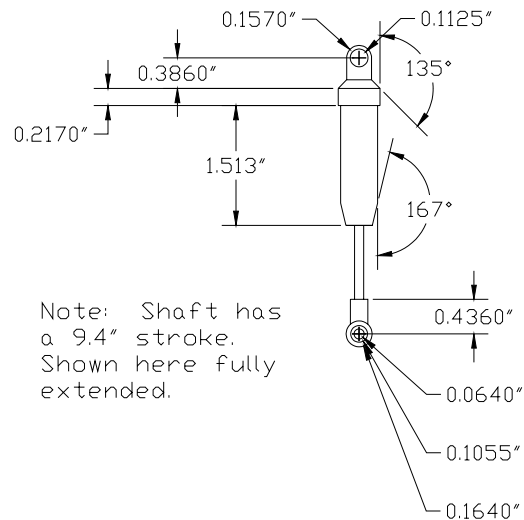


Figure 5

The dampers are modeled after Taylor Devices Inc. fluid viscous dampers used in large structures (see *Figure 8*).

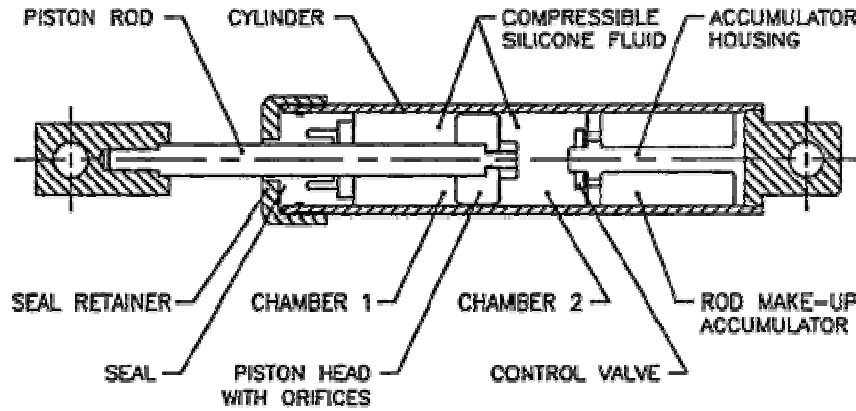


Figure 8

To mount the dampers, a chevron brace system like the one shown in *Figure 7* is used. This configuration is frequently used in practice when dampers are to be installed in braced frames.



Figure 7

The chevron used in the model is constructed from lightweight aluminum 6160. Aluminum is used because it will support the dampers while not adding significant weight to the structure.

Shown below in *Figure 8* is a detail of the mounting plates.

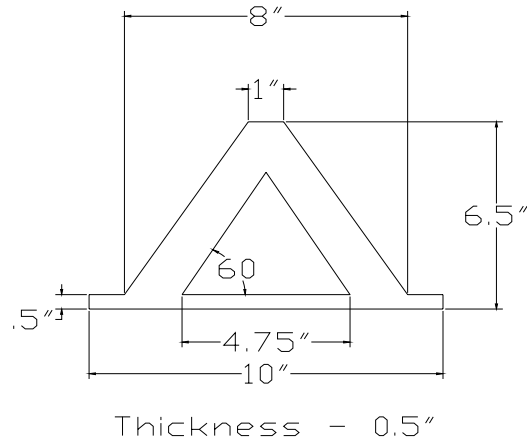


Figure 8

The braces are installed in each side of the model in the direction of excitation. Two screws fasten the chevron braces to the model floor. The two dampers will rest in a slot, secured by a pin, which is cut in the top part of the chevron. The other end of the damper has a ball bearing joint. This will be fastened to a pin connector added to the model. The latter slot is lowered approximately 1/2" so that the dampers are horizontal.

3 – Method of Experimentation

These demonstrations require the use of a UCSIT Shake Table, produced by Quanser Consulting Inc. The “Shaker II” comes complete with a shake table, power module, data acquisition system, and a pendant controller (see *Figure 9* below).

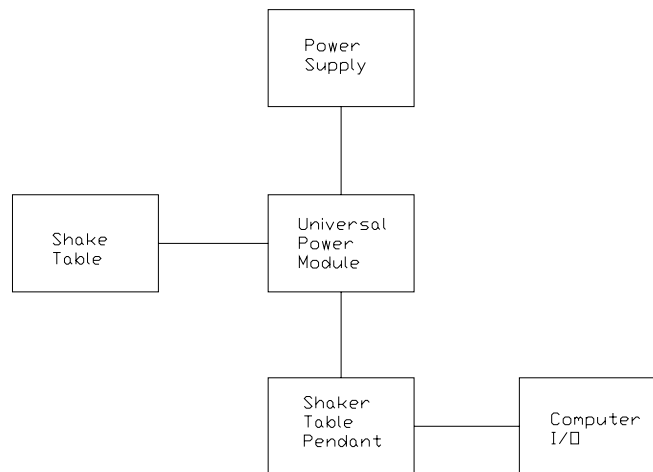


Figure 9

The shake table measures 18" x 18" and can carry up to 33 lbs at the maximum 2.5g acceleration. The software included with the set, WinCon, contains 4 actual time histories. The user can also program ground motions or even modify one of the 4 pre-programmed earthquakes using MatLab. The shake table accelerates in the x-direction based on these inputted commands. In order to attach models the user can tighten screws in the several pre-drilled holes on the shake table.

Accelerometers will also be used in this experiment. The range of each accelerometer is +/- 10g. Voltage is used as the means to measure the rate of change in distance; a conversion of 1 Volt to 1 magnitude of gravity is specified. Three accelerometers are affixed to the frame with hot glue, one on each level. Specifications for the three accelerometers and attached conditioners are shown below in *Table 1*.

Table 1

Accelerometer and Conditioner Specifications					
Accelerometer			Conditioner		
Position	Model Number	Range	Position	Model Number	Gain
Ground	Endevco MP39	(+/-) 10 g	Ground	72421	39.6
First	SN PE61	(+/-) 10 g	First	89765	48.4
Second	Endevco SN RM71	(+/-) 10 g	Second	72415	43.4

A Dell Optiplex GX270 with an Intel Pentium 4 processor drives the data acquisition system. The software used to set up the accelerometer to the data acquisition program is Lab View 7 Express. This is a programming system that appears in Graphical User Interface style. National Instruments DAQ Assistant is used as the connection between Lab View 7 Express and the three accelerometers. During experimentation, the data can be written to an excel file.

4 – Properties of the Model

The desired period of oscillation for the model is approximately 0.2 seconds. To determine the theoretical period we must find the stiffness and moment of inertia of the brass sides (see *Period Calculations* below).

Moment of Inertia

$$I = \frac{h^3 * b}{12}$$

$$I = \frac{(0.065")^3 * 2"}{12}$$

$$I = 4.58 \times 10^{-5} \text{ in}^4$$

(Eq 2)

Stiffness

$$k = \frac{48 * E * I}{L^3}$$

$$k = \frac{48 * (15,500 \text{ksi}) * (4.58 \times 10^{-5} \text{in}^4)}{(7.5 \text{in})^3}$$

$$k = 80.7 \text{lb/in}$$

(Eq 3)

Period

$$T = 2\pi \sqrt{\frac{W}{g * k}}$$

$$T = 2\pi \sqrt{\frac{22.75 \text{lb}}{386 * 80.7 \text{lb/in}}}$$

$$T = 0.17 \text{s}$$

(Eq 4)

Period Calculations

The calculated period of 0.17 seconds is close to the desired value of 0.2 seconds. The resulting cyclic frequency, the reciprocal of the period, is 5.9 Hz. The circular frequency corresponding to the period is 36.9 Hz.

To test this result, the model was attached to the shake table and was subjected to excitation at several different frequencies, or a “White Noise Test”. The model appeared to oscillate regularly at 5.0 Hz. This differs from our theoretical value by only 0.9 Hz.

It is also necessary to determine the damping qualities of the model. To find the damping coefficient we recorded the acceleration of the floor mass during free vibration, while the base was not isolated. The acceleration vs. time plot decays as expected (see Figure 10).

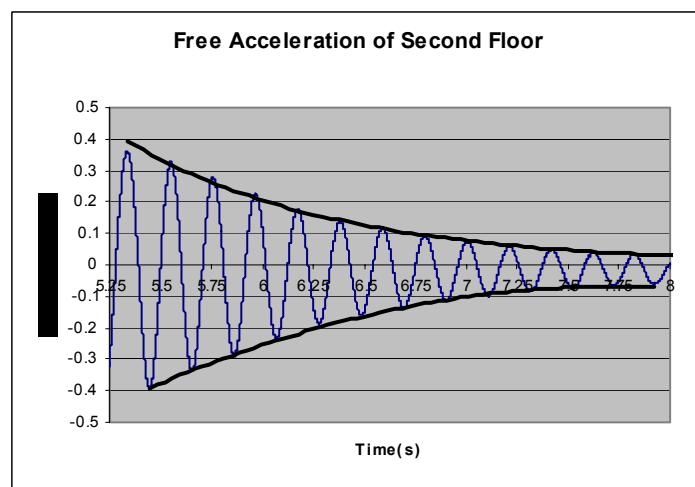


Figure 10

To find the damping ratio, we use the following process (see *Damping Calculations*).

$$\zeta = \frac{1}{2\pi * j} * \ln\left(\frac{a_i}{a_{i+j}}\right)$$

$$\zeta = \frac{1}{2\pi * 3} * \ln\left(\frac{0.079in/s^2}{0.045in/s^2}\right)$$

$$\zeta = .029 = 3\%$$

(Eq 5)

Where ζ is the damping ratio and j is the number of cycles.

Damping Calculations

The average damping ratio of the structure, without added dampers, is 3.1%. This is on the order of the damping ratio in actual structures, which is approximately 5%.

The acceleration vs. time plot for the damped structure is shown below in *Figure 11*.

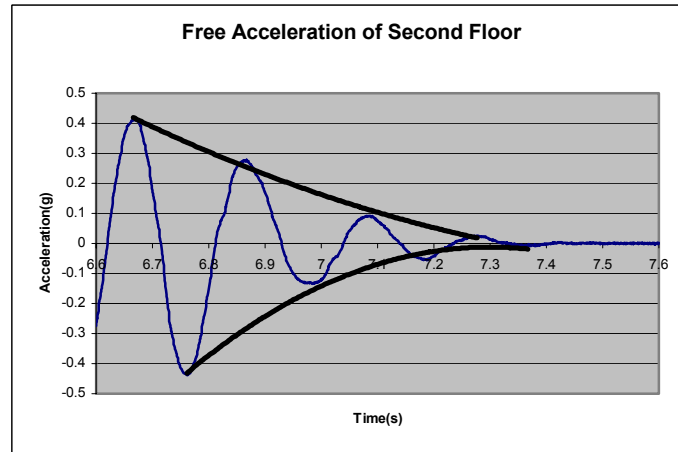


Figure 11

To find the damping ratio, we use the same process as the model without the dampers (see *Damping Calculations with Dampers*).

$$\zeta = \frac{1}{2\pi * j} * \ln\left(\frac{a_i}{a_{i+j}}\right)$$

$$\zeta = \frac{1}{2\pi * 1} * \ln\left(\frac{0.407in/s^2}{0.279in/s^2}\right)$$

$$\zeta = .060 = 6\%$$

(Eq 6)

Where ζ is the damping ratio and j is the number of cycles.

Damping Calculations with Dampers

The averaged damping ratio is found to be 14%. The addition of the dampers increases the damping ratio by more than 4 times.

5 – Earthquake Testing Results

The following four earthquakes will be modeled on the instructional shake table. The El Centro earthquake (magnitude – 7.1) occurred on May 18, 1940 in Imperial Valley, California. The Hachinohe earthquake (magnitude – 7.7) occurred on December 28, 1994 in Sanriku-Harjkaoki, Japan. The Kobe earthquake (magnitude – 6.9) occurred on January 17, 1995 in Kobe, Japan. The Northridge earthquake (magnitude – 6.7) occurred on the same day as the Kobe, one year earlier in Northridge, California.

Acceleration time history plots for the bare frame, isolated, and damped structures can be seen in the Appendix. Shown below, in *Table 2*, is a summary of the peak accelerations reached during earthquake testing. Units for the acceleration in the model are in percentage of gravity.

Table 2

	Bare Frame	Isolated	Damped
El Centro	0.76	0	0.01
Hachinohe	0.73	0.02	0
Kobe	1.21	0.01	0
Northridge	1.76	0.02	0.01

The largest accelerations always occur in the bare frame structure. Both damping devices lower the peak accelerations. However, the performance of each damping device is different for each earthquake. The El Centro earthquake is the only case where isolation performs better than dampers. This may be due to the variation in pulse of the El Centro earthquake. This is a topic for future research.

6 – Conclusions

Through this testing, it became evident that the prototype structure used is capable of qualitatively modeling actual structures. Also, the seismic protective system models reduced the seismic response as expected.

After experimental testing of the structure it was found that the stress transfer in the screws was warping the wood around the brass plates. After the connection is repaired, it is recommended that additional analysis be performed. Despite the expected result for the free acceleration and damping coefficients, the stress loss might have altered the data.

7 – Summary

Experimental presentations are an effective tool that can be used to convey a complex idea. In this case, earthquake acceleration patterns were imposed on a one-story model. Before the presentations are given, the properties of the model were checked and reported. Data was also reported from a damped version of the structure. By damping the structure, the students will learn the basic goal of accepting minimum damage to the structure.

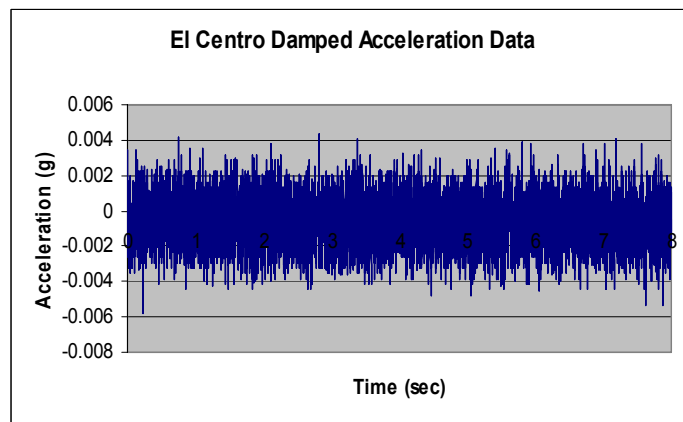
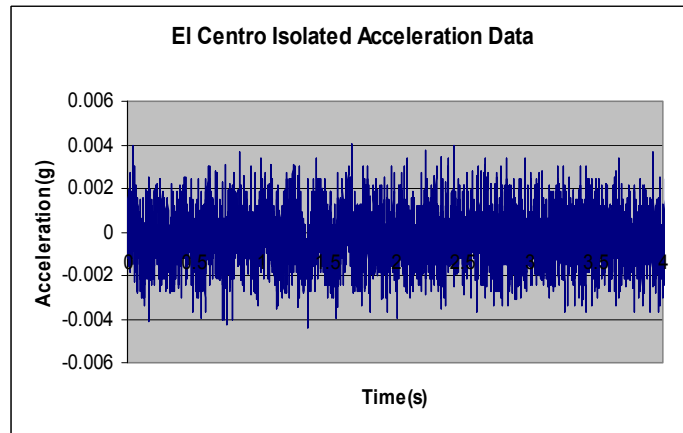
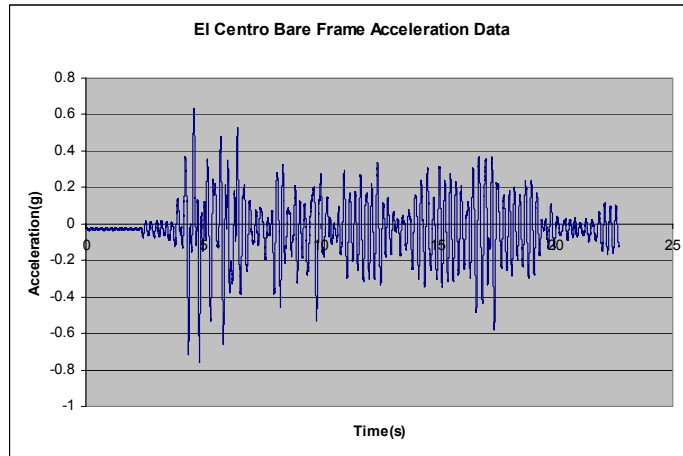
Acknowledgements

I would like to thank my advisor, Dr. Michael Constantinou. His knowledge of earthquake engineering and his professional experience has been invaluable tool towards the completion of this assignment. Graduate student, Daniel Fenz provided an excellent source of direction in the theory and presentation of my project. I would also like to thank Duane Kozlowski, Scott Weinreber, Mark Pitman, and Gary Majewski, of the Structural Engineering and Earthquake Simulation Laboratory, who aided in the development of the model and experimental devices.

In addition, thank you to MCEER and the National Science Foundation for allowing me the opportunity to perform research through the REU program.

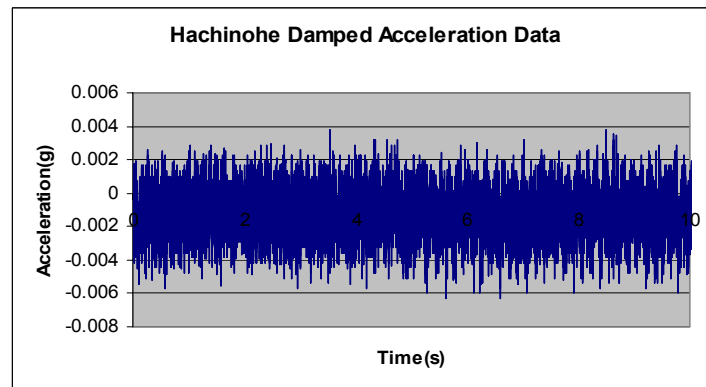
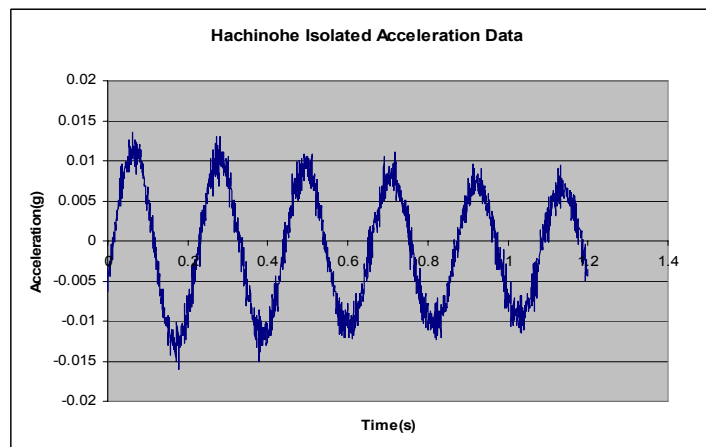
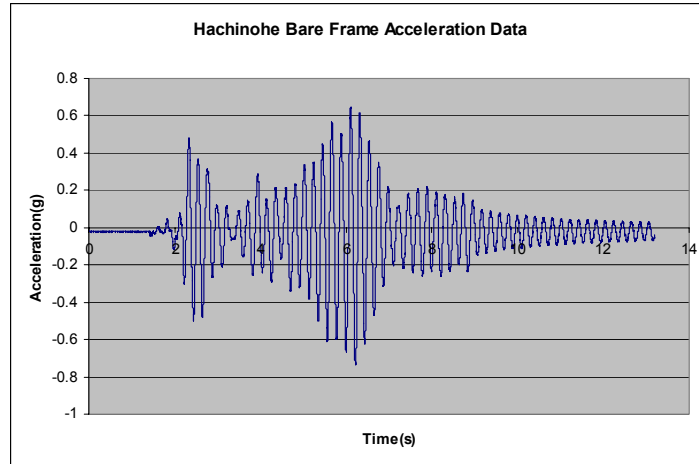
Appendix

El Centro



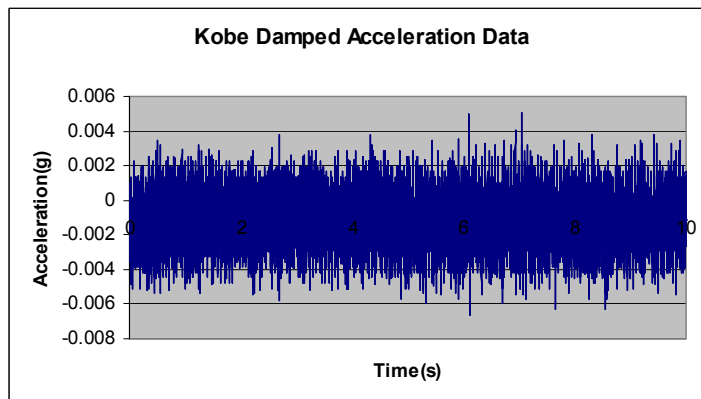
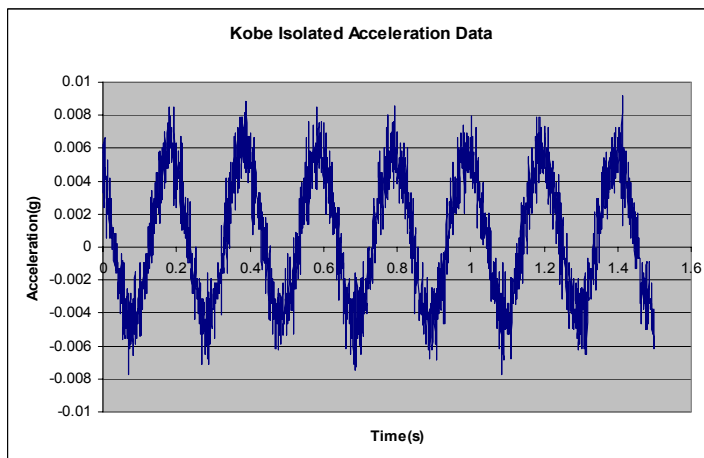
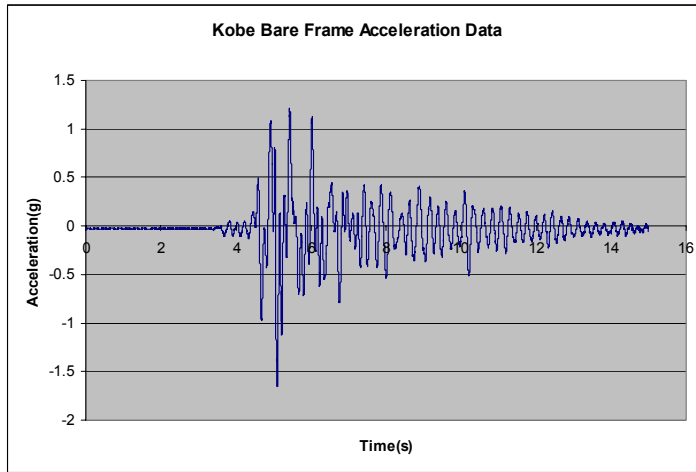
Appendix

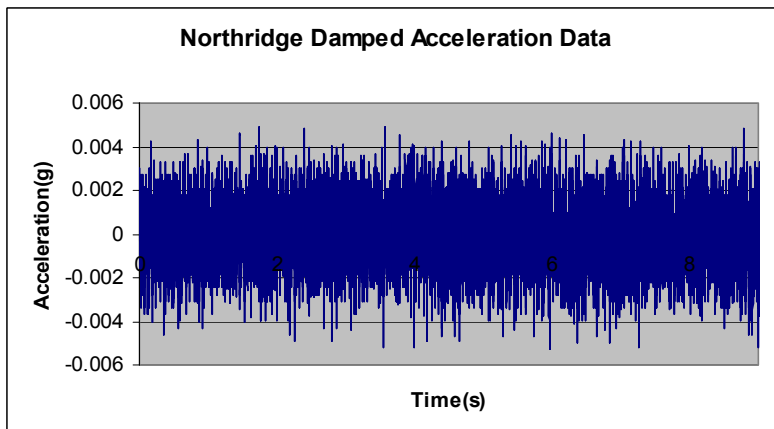
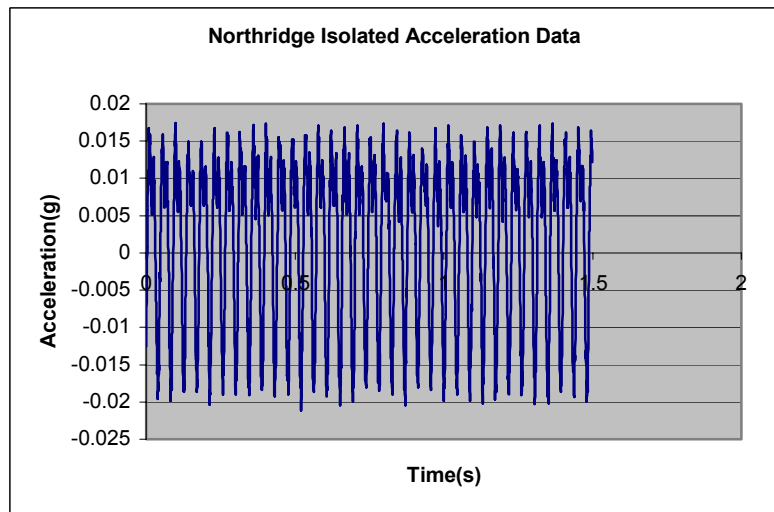
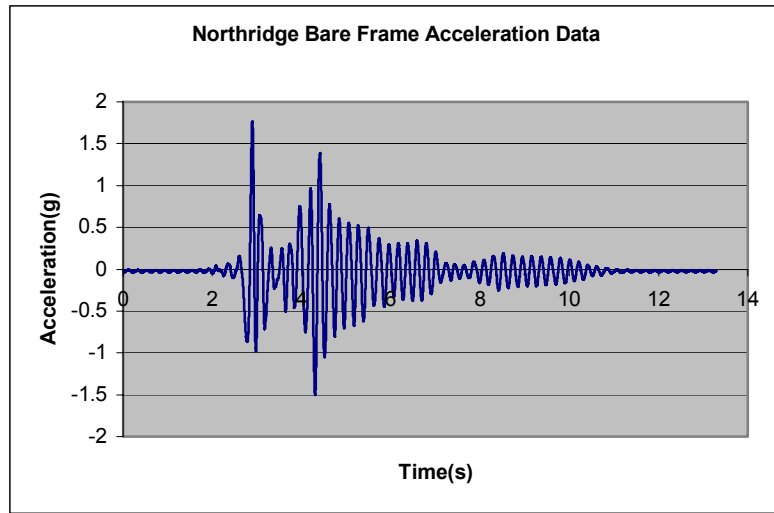
Hachinohe



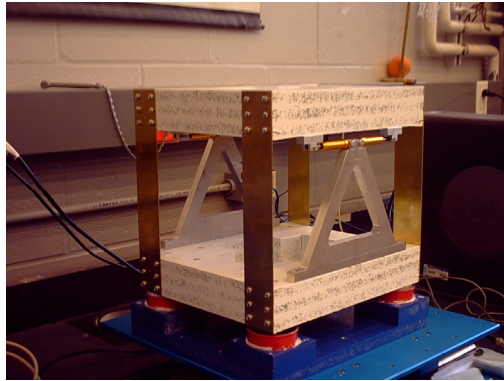
Appendix

Kobe

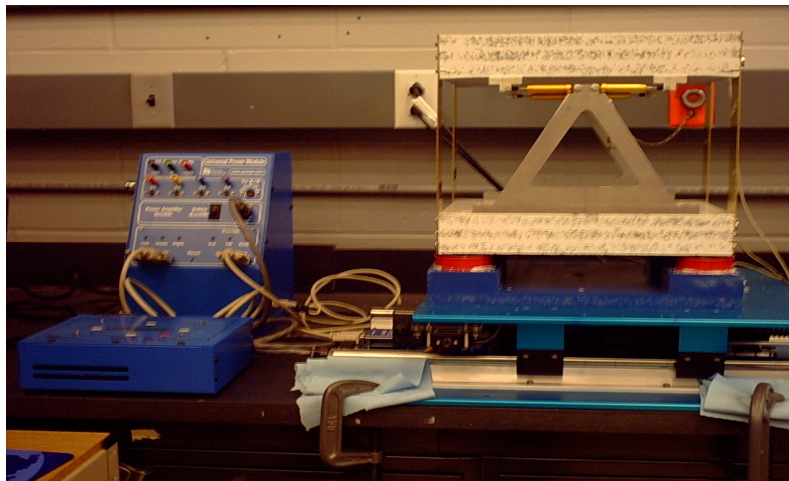




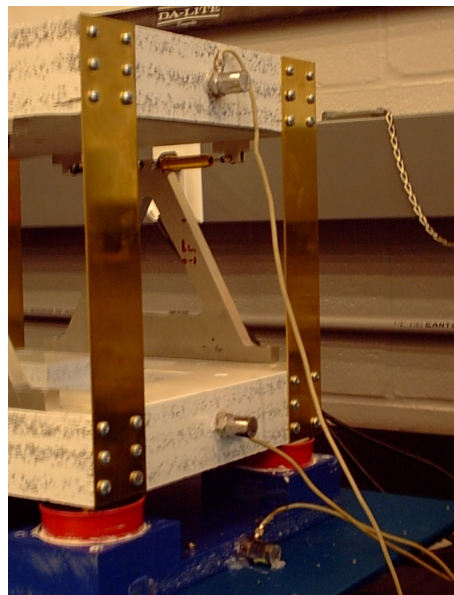
Photographs



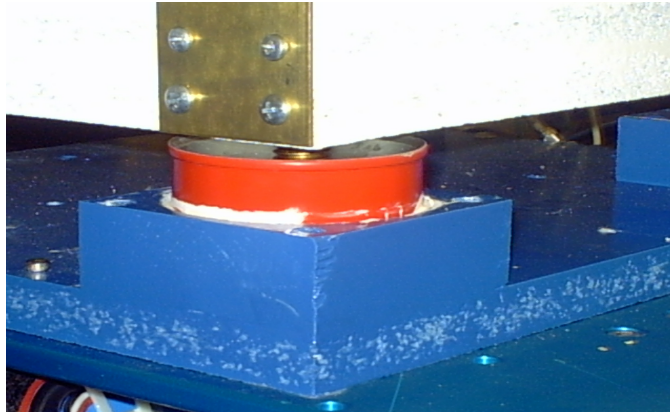
One-story Structure



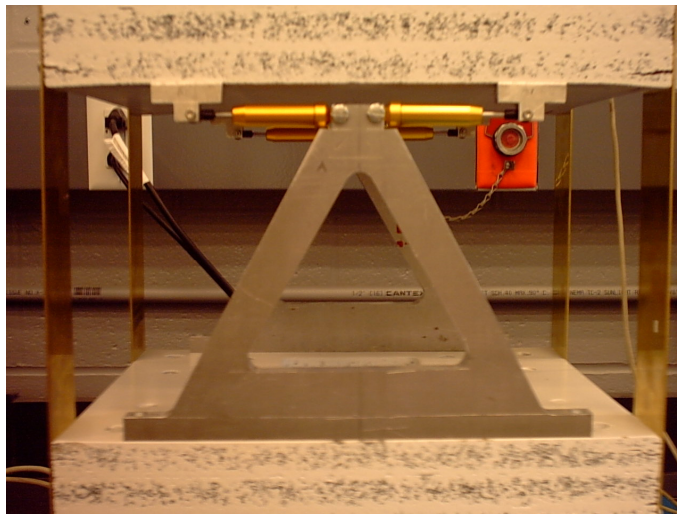
Shake Table



Instrumentation



Isolated Base System



Fluid Viscous Dampers

References

Chopra, A. K.; Dynamics of Structures: Theory and Applications to Earthquake Engineering: 2nd Edition. Prentice Hall: Upper Saddle River, NJ, 2001.

Constantinou, M.C.; Tsopelas, P., Kasalanati, A., Wolff, E.D., “Property Modification factors for Seismic Isolation Bearings,” *Technical Report MCEER-99-0012*, Buffalo, New York, USA, 1999.

<http://geot.civil.metro-u.ac.jp/archives/eq/94sanriku/>

<http://www.bris.ac.uk/news/2003/215>

<http://taylordevices.com>

<http://quanser.com>

<http://seismo.unr.edu/htdocs/students/CHAVEZ/scec95/scec95.html>

www.zephyrus.demon.com.uk/geography/resources/earth/kobe.html

GROUND MOTION DISTANCE ATTENUATION, MEASUREMENT & TOOLS

Timothy Brownawell
University of Illinois
University of Memphis
Prof. Charles Langston

Abstract

The overall goal of the "Seismic Path Modeling" project is to determine how the intensity of seismic waves in the central/eastern US decreases with distance from the source. How to do this is known; what remains is to actually do it. The idea is to compute the response spectra of the recorded motions at stations at various distances from the event, then compare these at the frequency of interest. This requires first correcting the data for instrument response. Existing tools are less than optimal, and certain steps can be rather tedious. My part of the project has been to write a graphical-interface tool (or rather, set of tools) to make these steps easier.

Introduction

Ground motion at any one location depends on both the source characteristics and the transmission characteristics of the ground between the source and the location under consideration. So in order to accurately predict future ground motions at various locations, it is helpful to know both of these parameters.

Objectives

This project focuses on determining the transmission characteristics of the ground in the central/eastern US. The specific part of the project discussed here was to build a software tool or set of tools to cover all steps to convert raw instrument data into usable response spectra. Part of this involves correcting the data for instrument response and initializing file headers. This part is not specific to this project, and the software is designed to allow it to be put into a separate, more generic tool, useful for anyone needing to correct raw data. The reason for these tools is to simplify or streamline certain aspects of the data processing needed for the overall project.

Work Done

A set of four tools was written in Matlab. Of the tools in the set, one exists primarily to provide an interface to track datasets and call the other tools on them. The other tools are: one to initialize the header fields of SAC files and provide instrument correction, one to convert between north-east-vertical components and radial-tangential-vertical components, and one to compute and display response spectra and amplitude/distance relationships. Only this last tool is specific to this project; the others would be useful for any project that needs SAC files which have been through initial processing.

All of the tools operate on sets of SAC files, intended to be the data collected from one event. Some of the tools can work with multiple sets of files at once. For instance, the response spectrum tool can display the response spectra of all files in a given set, and show the amplitude/distance plots for a specified frequency from the response spectra of all loaded datasets.

The header initialization and component conversion tools could have instead been implemented as SAC macros, but although this would likely have been simpler they would not have integrated nearly as well with the response spectrum tool, and would be essentially no different than current methods.

The tools work with sets of SAC files which are intended to be related in some way, such as being from the same event or being the same type of component.

Main interface

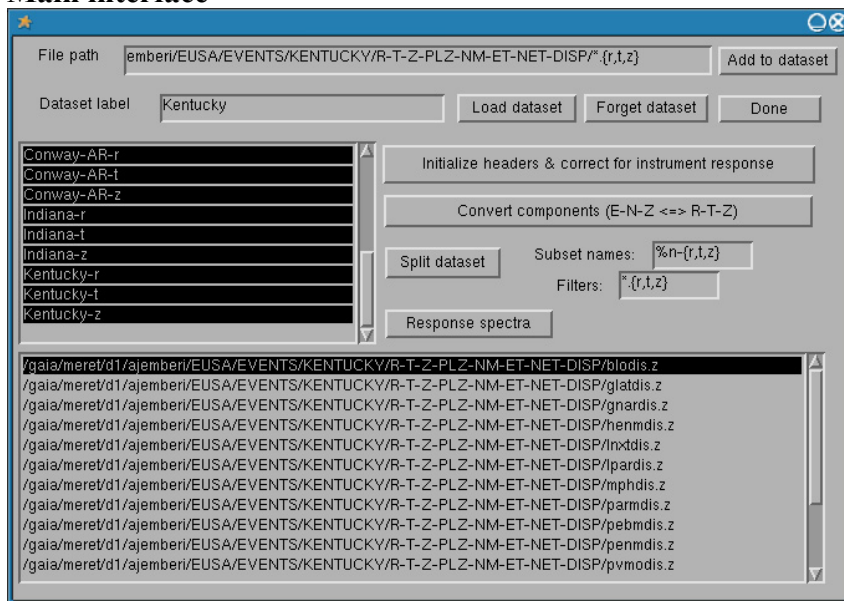


Figure 1

This tracks datasets, or groups of SAC files, and sends them to the other tools for processing. The results of this processing are placed into a new dataset, rather than replacing the original one. The tools do not edit files in place, but rather write new files to a user-specified location and return those filenames as the result dataset. It also provides a way to split a dataset into smaller datasets according to filename, useful for instance to separate the R, T, and Z components recorded for an event to analyze them separately with the response spectra tool. Datasets are an internal concept only, and have nothing to do with the actual location of data files.

Instrument correction and header initialization

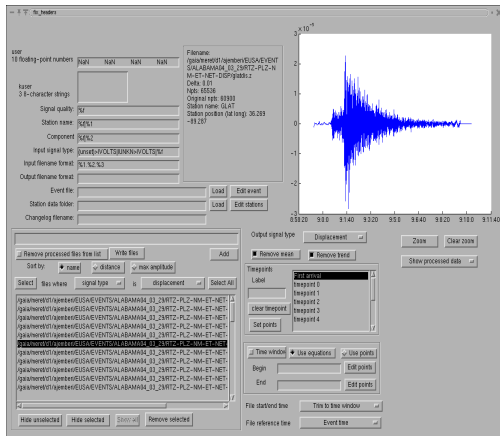


Figure 2

This tool uses a set of files with data about the recording stations, such as latitude, longitude, name, etc. and a dialog to enter data about the event to fill missing fields in the SAC headers. (Header fields are as described in the SAC program's built-in online documentation.) It also allows for changing the type of the variable in the SAC file to displacement, acceleration, or velocity, from whatever it previously was. If the original variable type is uncorrected, then it will correct it according to a supplied instrument response file. In addition to this header initialization and data correction, this tool also allows the time pick fields in the SAC headers of the data files to be chosen individually from a plot of the data and allows for time windowing and tapering of the files, again to times picked from a plot of the data.

The time pick and windowing functionality will likely be later moved into a separate tool, to allow additional processing (such as ENZ to RTZ component conversion) before windowing and setting time picks.

Component switching

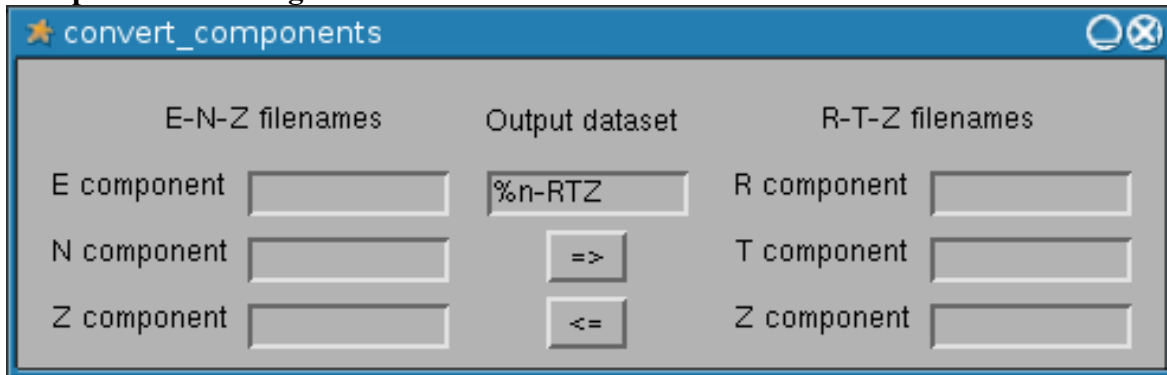


Figure 3

This tool groups the SAC files in the dataset by station, and then converts the files for each station between North, East, and Vertical components and Radial, Tangential, and Vertical components. It works by setting each result component to the sum of the parts of the input components in the direction of the result component, as calculated from the back azimuth (The angle at the station from north to the incoming signal.). This tool is not yet completed.

Response spectra

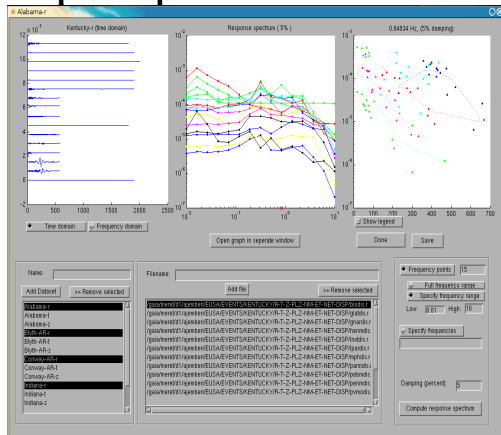


Figure 4

This tool will compute the response spectra of all files in all datasets it is given, and display the spectra from one dataset at a time.

A response spectrum is the relation between the maximum amplitude of oscillation of a single-degree-of-freedom oscillator and the natural frequency of oscillation, given a damping ratio and an input motion. (Kramer, 1996) The response spectra are computed by converting the recorded signal into the frequency domain using a Fast Fourier Transform (Kramer, 1996) (Langston) and multiplying by a single-degree-of-freedom filter

$$1/(1-\beta^2+2i*\beta*\zeta)-1$$

(Eq. 1)

(based on (Kramer, 1996)), then converting back to the time domain with an Inverse FFT.

When a specific frequency from the response spectrum is selected, it will display the amplitude vs. distance plot of each dataset for that frequency. Each file produces one point; files from the same dataset are the same color, and each dataset is given a best-fit line through the points. There should also be an indication of how well the points fit the line, but this is not yet implemented, other than visual inspection of the plot.

Conclusions

When completed, the general tools will provide an alternate way to perform initial processing of recorded motions. This will hopefully be easier and less time consuming than current methods. The data displayed by the screenshots of the tools was provided by Alemayehu Jemberie using other processing methods, and when the tools are completed will be used to verify that the tools work properly by comparison to what the tools produce from the same input files.

The response spectra tool should do the same for tasks more specific to this project's overall goal of measuring ground motion distance attenuation.

Although the response spectra tool allows the response to be plotted against distance, it make no consideration for direction or location; i.e., it assumes that the ground characteristics are spatially uniform.

References

Kramer, S. *Geotechnical Earthquake Engineering* Upper Saddle River, New Jersey, USA, 1996

Langston, C. *Misc. Class Notes*

**PERFORMANCE OF CONCENTRICALLY BRACED FRAMES UNDER
CYCLIC LOADING**

**Nathan Canney
Seattle University
University of Washington
REU Faculty Advisors:
Dr. Charles Roeder
Dr. Dawn Lehman**

1.0 Abstract

Steel Concentrically Braced Frames (CBFs) are strong, stiff and ductile, and are therefore ideal for seismic framing systems. The quality of the seismic response of CBFs is determined by the performance of the brace. In order to achieve the best performance from a CBF, the brace must fail before any other component of the frame does. For this project we are examining CBFs with Gusset Plate connections. Under current design codes, these connections can become oversized to meet requirements, decreasing the yield length of the brace, causing the CBF to fail earlier than expected. This project will use Performance-Based methods to set better guidelines for code regulations pertaining to the design of CBF connections.

The goal of this project is to design a failure hierarchy based upon the performance of various CBFs. Each CBF will use different connection designs and will be tested to complete failure. To test completely through failure will allow the CBF to displace the greatest amount of energy possible, and this is achieved by the following order of failures: the brace to buckle, and then yield, the connection to yield and finally the brace to fracture. By testing completely through this hierarchy, the upper limits on connection design can be found to guarantee more economic and practical connection design.

2.0 Introduction

Steel Concentrically Braced Frames (CBFs) have been used for years in steel construction and therefore have been studied extensively for seismic performance. These studies have produced guidelines for brace and connection design to give a desired capacity under seismic events. These guidelines, however are generally too conservative and actually produce CBFs that are ineffective in seismic events. This project aims to better define the performance of these CBFs, thereby allowing more specified guidelines for design.

2.1 Concentrically Braced Frames

CBFs are strong, stiff and ductile, making them ideal for seismic framing systems. The inelastic behavior of the brace provides most of the ductility, but in order to fully utilize the frame, the connections and framing members must also be taken into account. Therefore, it is important to consider not only the performance of the brace when designing, but also the ability for the connections and the framing members to withstand the strength and deformation demands transferred from the brace during cyclic loading. Through these considerations, a maximum amount of energy can be dispersed before the system fails.

Cyclic testing of conventional braced frames shows that these braces buckle in compression and yield in tension. Plastic hinges occur after the brace has buckled and the stiffness and resistance of the frame decreases, illustrated in Fig. 1. In Zone 0-A, the frame retains its elasticity, but the brace buckles at A, causing a plastic hinge to form in

Zone A-B. Load reversal in Zones B-C, C-D and D-E cause the brace to become unstable, decreasing the effectiveness of the frame. This unstable behavior is evident in the unsymmetrical response seen in Fig. 1a. For this reason, Special Concentrically Braced Frames (SCBFs), with braces in opposing pairs, are used given the stable inelastic performance seen in Fig. 1c.

In its entirety, this project will test both SCBFs and Buckling Restrain Braces, but while we were working with the project, we focused on the SCBFs.

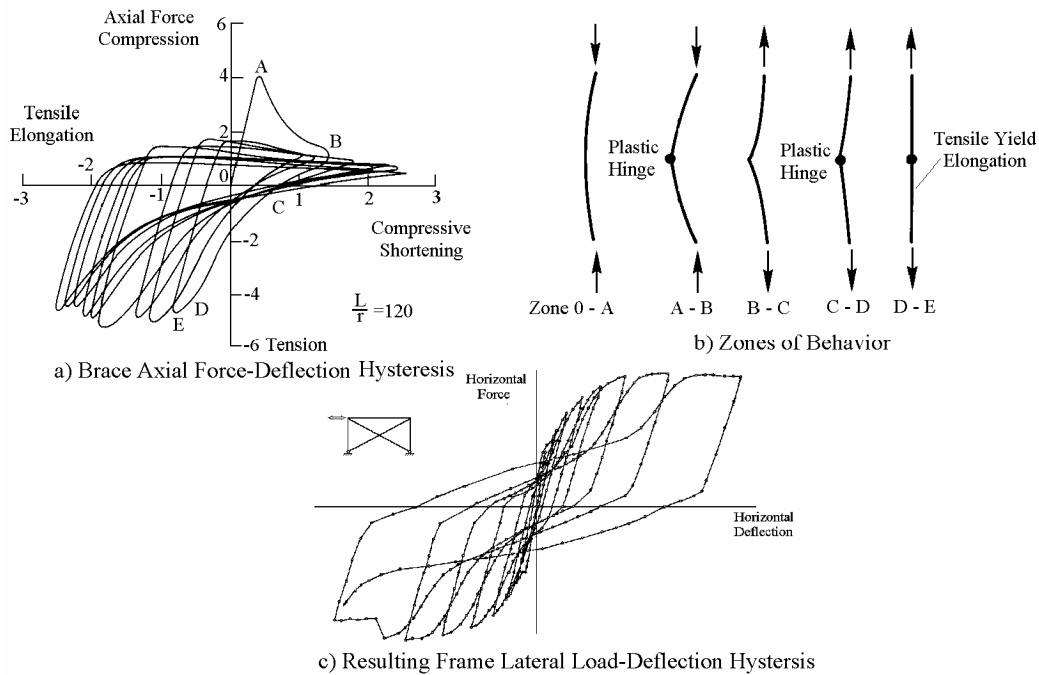


Figure 1: Behavior of Special Concentrically Braced Frames

2.2 Gusset Plates

The purpose of this project is to use Performance-Based Testing to set guidelines for future design codes, most notably, connection design codes. The current AISC codes give the following requirements for connection design:

(AISC 1997 13.3a) The required strength of bracing connections (including beam-to-column connections if part of the bracing system) shall be the lesser of the following

- a. *The normal axial tensile strength of the bracing member determined by $R_y F_y A_g$.*
- b. *The maximum bracing force, indicated by analysis, that can be transferred to the brace by the system."*

These codes require that the connection is “stronger” than the brace, therefore the brace will fail before the connection, but this is only a lower limit. The interpretation of this has led to the understanding that all elements of the connection, including bolts, welds, and gusset plates meet the following provision:

$$R_y F_y A_g < \phi R_n \quad (1)$$

Here R_y is the ratio of expected yield strength to the minimum yield strength for the brace, F_y is the minimum yield stress of the brace, A_g is the gross area of the brace, ϕ is the resistance factor and R_n is the connection resistance. The resistance factor decreases the connection resistance, so for factored loads that are lower than the expected yield strength of the brace, the connection is easily over designed (Roeder and Lehman, 2002). This leads to overly large connections that are not only uneconomical and a hindrance, but also decrease the performance of the brace. Overly large connections, like those in Fig. 2, decrease the effective length of the brace, causing ductility to decrease. In other words, the distance that deflects and rotates in the brace, required to dissipate energy, is shorter so more stress acts on the brace.



Figure 2: Oversized Gusset Plate Connections Used in SCBF

Other research has provided two other provisions that heavily dictate connection design. When plastic hinges form in the gusset plate from out-of-plane rotation of the brace, the plate needs to be able to rotate freely. To ensure this freedom, “the end of the bracing member should be terminated a distance of at least $2t$ away from the re-entrant corner of the gusset plate” (Astaneh-Asi, 1998). Here t is the thickness of the gusset plate. This requirement often causes large gusset plates.

The second provision vital to connection design is the Whitmore’s method. Whitmore found that the area most affected in a gusset plate is along a 30-degree line from the connection between the brace member and the gusset plate. This allows for the use of tapered gusset plates.

2.3 Performance-Based Methods for Connection Design

From the AISC code only one level of hierarchy is implied, simply that the brace fails before the connection does. The goal of the Performance-Based approach to this project is to create a more detailed hierarchy of failures. From previous work it a collection of permissible yield mechanisms and failure modes for a system have been identified. The permissible yield mechanisms are brace buckling and yielding, local yielding of the gusset plate, bolthole elongation, and the permissible failure modes include fracture or tearing of the brace. Unacceptable failure modes are buckling of the gusset plate or fracture of connection components such as bolt or welds. (Roeder and Lehman, 2002)

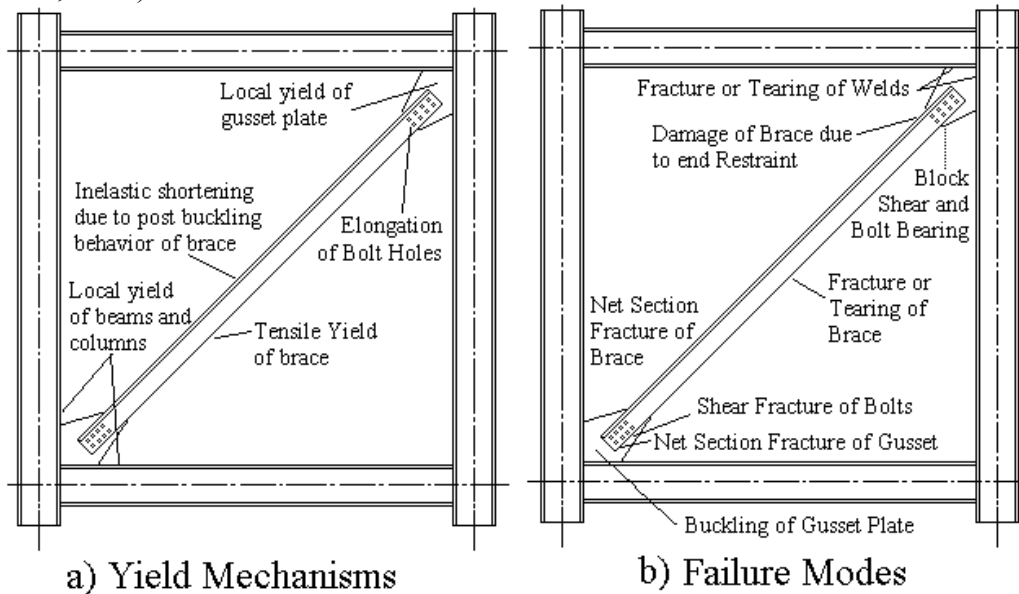


Figure 3: Yield Mechanisms and Failure Modes for SCBF Components

Performance-Based Methods match the performance of a structure and the damage that is expected with varying levels of seismic activity. Fig. 5 shows these possible relationships. The three performance levels are Immediate Occupancy (IO), Life Safety (LS) and Collapse Prevention (CP). As is expected structural damage increases with seismic levels and the permissible damage is more restricted with CP than IO.

From these restrictions on each Performance Level, the resulting hierarchy can be used as a template for the desired performance of the SCBFs.

$$\text{Brace Buckling} < \text{Brace Yielding} < \text{Connection Yielding} < \text{Brace Tearing} \quad (2)$$

This series of events in the brace gives the maximum energy dissipation for the system while avoiding undesired failure modes.


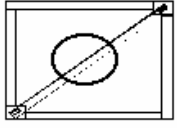

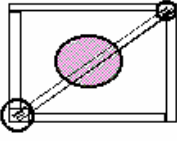
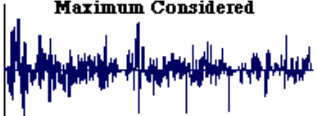
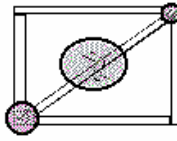
Seismic Hazard Level	Performance Level	Structural Damage
<p style="text-align: center;">Seldom</p> 	<p style="text-align: center;">Immediate Occupancy</p> <ul style="list-style-type: none"> ▪ Brace Buckling* ▪ Incipient Brace Yielding <p style="text-align: center;">* SCBF only</p>	
<p style="text-align: center;">Rare</p> 	<p style="text-align: center;">Life Safety</p> <ul style="list-style-type: none"> ▪ Brace Yielding ▪ Incipient Yielding of Gusset Plate ▪ Incipient Elongation of Bolt Holes 	
<p style="text-align: center;">Maximum Considered</p> 	<p style="text-align: center;">Collapse Prevention</p> <ul style="list-style-type: none"> ▪ Full of Brace ▪ Yielding of Gusset Plate ▪ Elongation of Bolt Holes ▪ Incipient Brace Fracture 	

Figure 5: Possible Performance Objectives for SCBFs

The overall objective for this project is to test multiple specimens to observe under what conditions each of these yield mechanisms and failure modes occur, the ideal would be a specimen that follows the hierarchy in Eq. 2. These results will be useful in modifying the design process to provide more economic and reliable CBFs.

3.0 Lab Setup and Process

This project is the graduate work of Shawn Johnson and Adam Christopolus at the University of Washington. Both Shawn and Adam have been working on this project since September 2003. I joined the project as the construction phase was beginning; therefore the entire design and preparation aspects of this project had already been completed. My role was to work with Shawn, Adam and other lab assistants to build the set up for the testing and build the first specimens.

3.1 Channel Sections

The setup for the experiment was designed to have a system where the braces were interchangeable in the setup. This required a system that was uniform to accommodate each frame, but flexible enough to allow each frame to be easily moved in and out. Shawn and Adam designed the setup such that each frame lies horizontally, approximately one foot above the ground. The bottom beam of each frame attaches to the strong wall through a set of channels and steel plate, seen in Fig. 6.

This channel section is attached to the strong wall by seven 1-inch diameter rods and five 2-inch rods. All of these rods were pre-stressed to the strong wall at up to 350 kips. This required the use of a pneumatic pump and jack. Fig. 7 shows these rods tying the channel section to the strong wall.

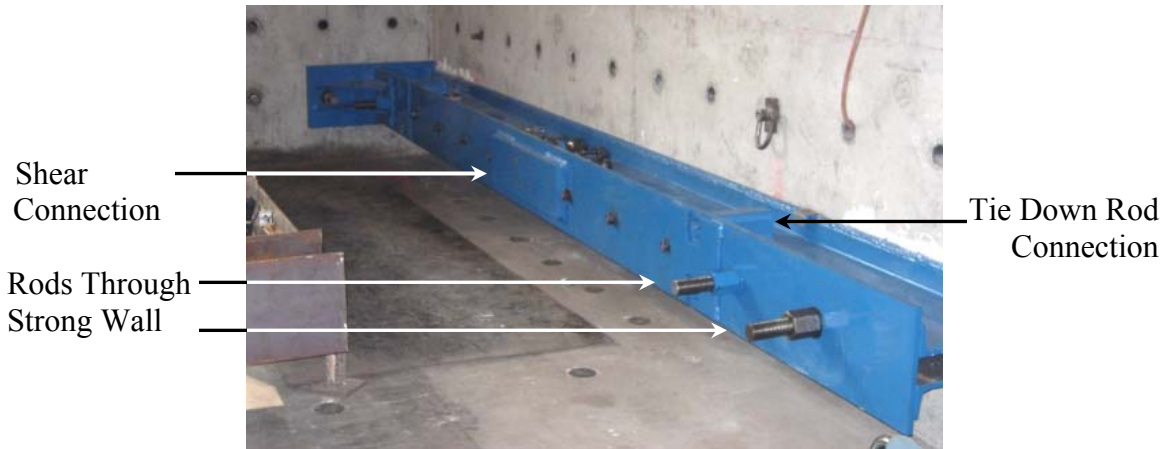


Figure 6: Channel Section Tensioned to Strong Wall

This setup creates a base which each frame can be connected to which will stay stationary for each test. Each frame is connected to the channel section by ten bolts at the shear connection, seen in Fig. 6 and four tie rods that are pre-stressed to simulate a gravity load on the frame. Rounded nuts set in the tie rod connection on the channel section allow the rods to rotate as the actuator pushes and pulls the frame.

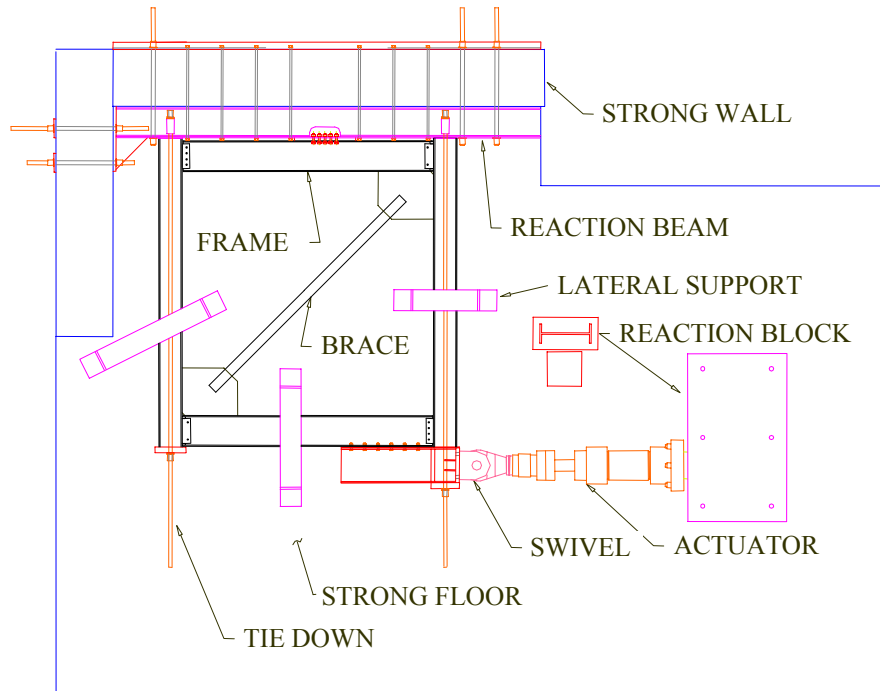


Figure 7: Plan View of Lab Setup

3.2 Lateral Support System

We made a lateral support system to prevent any out-of-plane rotation of the frame, and to keep the entire frame from lifting during testing. The frame is sandwiched between two W-section steel beams that are attached to the strong floor with threaded

rods. Greased nylon tubing is placed on the flanges of the frame to prevent any friction between the lateral supports and the frame.

3.3 Braced Frame Specimen

For this project the plan is to test 10 SCBFs and 10 Buckling Restrained Braces (BRBs). For my part of the project we built two of the SCBF frames, Fig. 8. Each frame is full sized (12x12 foot centerline to centerline) with varying gusset plate connections. The first frame that we built had the largest gusset plate and will be used as a base for all other experiments. Every gusset plate is $\frac{1}{2}$ inch steel and the braces for the SCBFs are 5 x 5 x $\frac{3}{8}$ inch square steel tubes. Welds are used to connect the brace to the gusset plate and the gusset plate to the frame. The frame is connected by bolts on the corners without the gusset plate; in the corners with the gusset plates the column and beam are welded together.

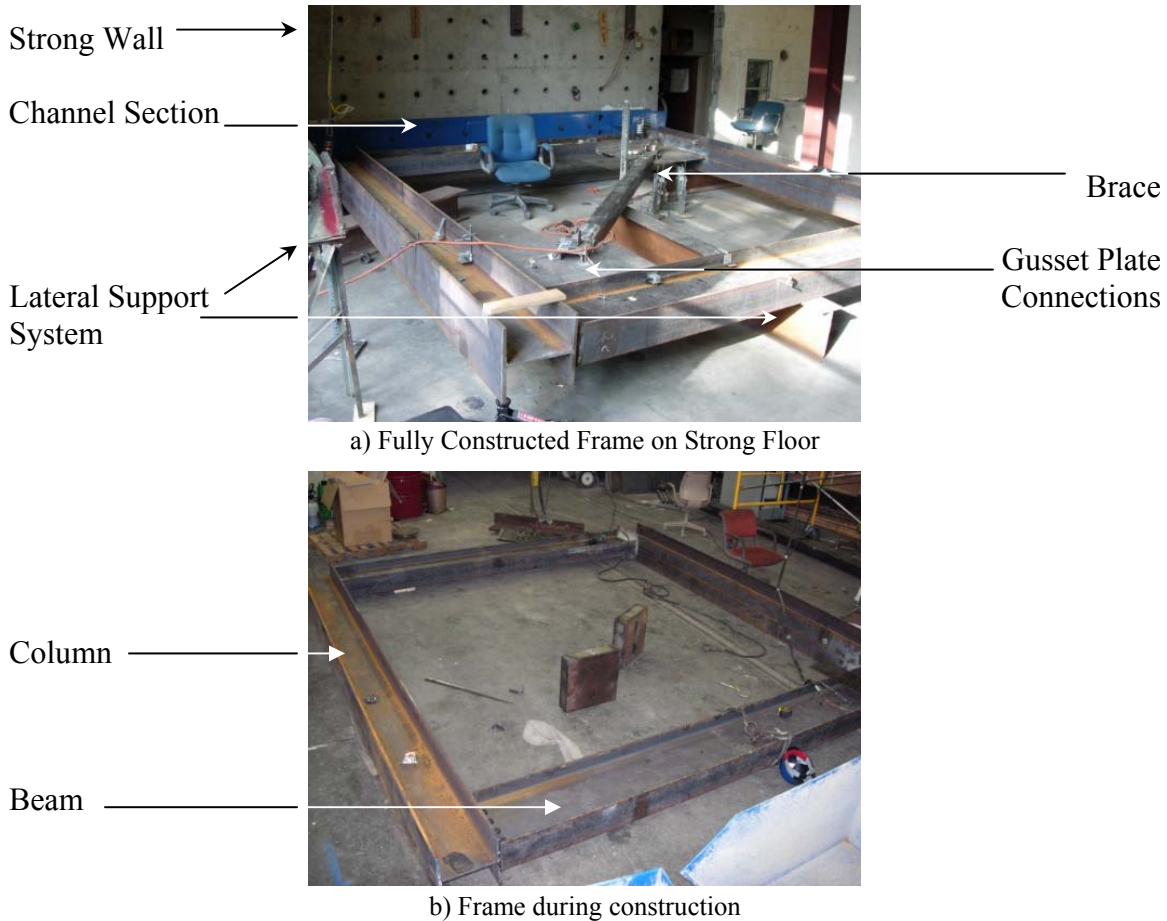


Figure 8: First two constructed SCBFs

3.4 Load Transfer System

Each frame is connected to the actuator by a load beam, Fig. 9a. This beam is bolted to the frame and also has the tie rods through it. The load beam is designed to

transfer the load from the actuator into the frame without any slipping in the connection. Potentiometers will monitor whether this is successful or not.

A swivel, manufactured in the lab, connects the actuator to the load beam. The actuator, seen in Fig 9b will produce over 350 kips into each frame through the load beam during testing, simulating a seismic event. A 6-½ ton concrete reaction block was made to resist the force of the actuator, effectively creating a temporary strong wall. The reaction block is held onto the strong floor by six 2-inch diameter rods. This configuration is shown in Fig. 7.

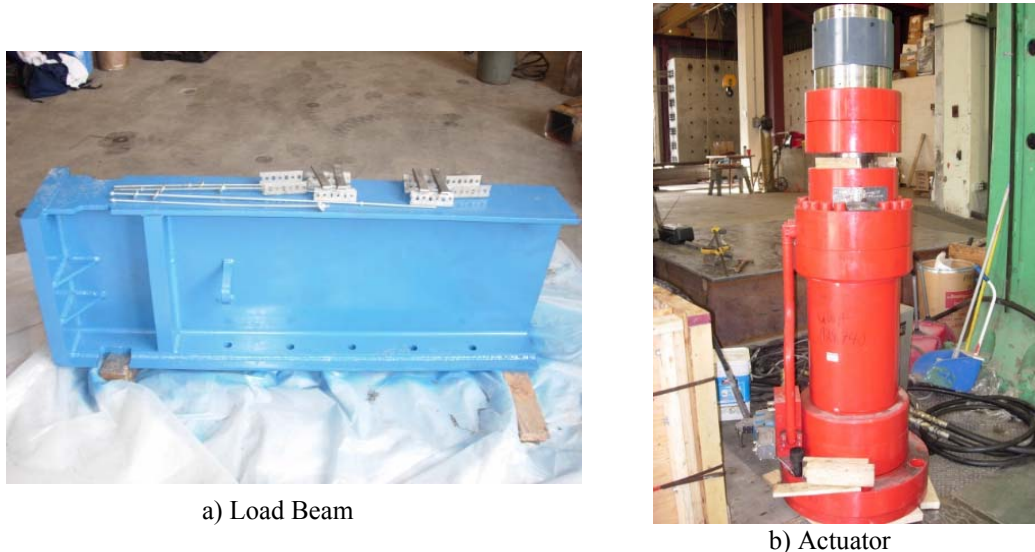


Figure 9: Load Transfer System

3.5 Instrumentation

A major component of the test preparations was setting up instrumentation for the system. Over 50 potentiometers were calibrated and organized to measure any displacements that could occur in each frame, the channel sections, load beam and reaction block. The placement of most of the potentiometers is shown in Fig. 10, but this changed as we began to set up the system in the lab; more instruments were added and some of the positions changed.

Most of the potentiometers were placed on and around each gusset plate to measure out-of-plane movement, any elongation or contraction of the brace or brace-gusset plate system. Other potentiometers measure any rotation of the brace at the gusset plate connection. Each connection between the gusset plate and the column or beam was instrumented as well as the pin connection between the beam and columns. Some were set up to monitor any movement in the channel section with respect to the strong wall or with respect to the frame. The reaction block was instrumented to make sure there was no slipping on the strong floor and no movement with respect to the actuator

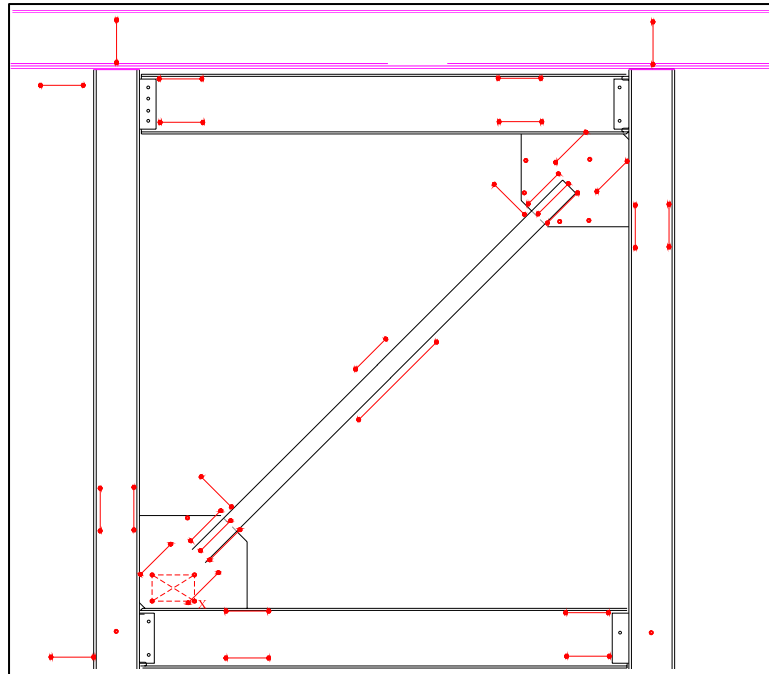


Figure 10: Instrumentation Layout

. The instrumentation of each brace also includes 16 strain gages on the brace, gusset plate and frame. All these potentiometers and strain gages were wired into the computer module and then programmed into LabView and calibrated.

3.6 Testing

Unfortunately by the time my internship ended, we were still in the construction phase, so there are no test results to report here.

4.0 Conclusion

Even though I did not see testing, the exposure to the research process was educational. I learned how to make the transition from designs to a physical product. This required precision, but also flexibility to adjust to fabrication errors and make many small alterations. Another source of required adjustment was learning to collaborate with multiple parties, from steel companies, to delivery trucks to other workers in the lab. Much of our time was spent coordinating with others to make the project run smoothly.

As far as the project itself is concerned, hopefully these test results will produce a more accurate and reliable way to design Concentrically Braced Frames and Buckling Restrained Braces.

5.0 Acknowledgements

I would like to thank PEER for giving me this opportunity; Dr. Eberhard, Dr. Roeder and Dr. Lehman at the University of Washington; Shawn Johnson and Adam Christopolus and Nick Kuffel for guiding me through this internship.

6.0 References

Astaneh-Asi, A., 1998. "Steel Tips: Seismic Behavior and Design of Gusset Plates," Abolhassan Astaneh-Asi, Alamo, CA, 1998.

Roeder, C.W., and Lehman, D.E., 2002. "Performance-Based Seismic Design of Concentrically Braced Frames," Award CMS-0301792, Proposal to the National Science Foundation, Washington, DC.

SEISMIC ISOLATION FOR SMALL REINFORCED CONCRETE STRUCTURES: A PRELIMINARY INVESTIGATION ON MATERIAL COST

By Abiel Carrillo, New Mexico State University, at State University of New York at Buffalo, advised and supervised by Dr. George C. Lee

Abstract

The objective of this investigation is to show the effectiveness of a rubber bearing isolation design for a low-rise reinforced concrete structure in Algeria, Africa. The results of this investigation focus on a specific example. The method followed was to design two possible frames, A and B; this was done according to applicable codes for an office building. Frame A is a moment resisting frame, and the latter is an isolated frame. The total material required for both was then compared. The building has a two story, 8100 square-foot square plan, with four rows of four columns. A high damping rubber bearing was chosen as the isolating device. The procedure to design the isolation systems was basically the following (adhering to UBC-97 standards): 1) Determine and establish parameter-dependent factors, 2) select a type of bearing and estimate target values such as stiffness, damping ratio and bearing displacement, 3) relate required dimensions of the unit with target values from previous step, and 4) produce isolator detail. The design of frame B called for 16 rubber bearing units. The resulting weight ratios between frames A and B showed a total steel ratio of 3.3 and a total concrete ratio of 1.8.

Objectives

The objective of this investigation is to show the effectiveness of a specific rubber bearing isolation design. The building is a symmetrical, low-rise reinforced concrete structure in the region of Algeria, Africa. Algeria was chosen because in May, 2003, the country was struck by its worst earthquake in 23 years. More than 2,000 people were killed and over 9,000 injured. Many homes were destroyed in the initial quake and thousands more were damaged and made uninhabitable. This investigation explores a system that could protect similar structures, preventing disasters like this in the future. As mentioned before, it focuses on a specific example; but it paves the way for the consideration of base isolation by demonstrating how cost effective it can be.

Research approach

Two possible frames were designed, A and B. Frame A is a moment resisting frame and Frame B is a lighter frame with an isolated base. Frame A was subjected to an equivalent lateral static earthquake load, (explained later), and then designed according to the appropriate code. An isolation system was designed for Frame B, as a result it was designed to only carry gravity

loads. The total required material for each major structural element was then compared for both structures. Ratios were found for the girders, columns and foundations.

Reinforced concrete was designed according to the American Concrete Institute's (1999) regulations, non-seismic design loads and base isolation designs conform to Uniform Building Code (1997) requirements, and seismic load determination was developed from Algerian seismic codes. Member forces were modeled and analyzed using RISA-2D (2004). It is important to note this software's sign convention: Positive moment refers to tension above and compression below the neutral axis of a member subject to bending. Moment envelopes and diagrams are presented with this convention.

As shown below, Figure 1, the plan considered was an 8100 ft² two story plan.

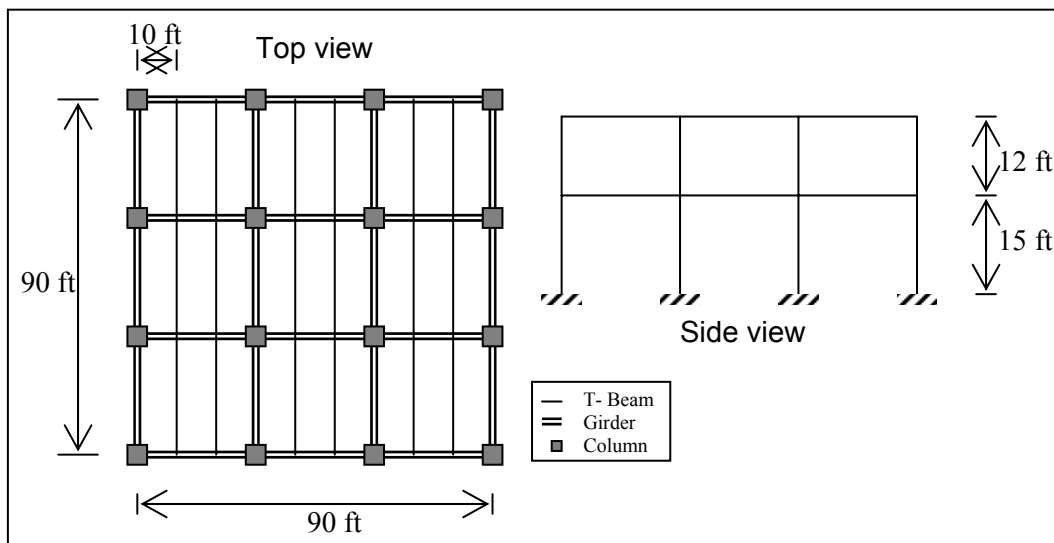


Figure 1. Structural plan

Parameters and assumptions

The parameters established for this project were selected to be representative of a typical situation in the region. The soil profile is a uniform stiff material that can support an allowable stress, $q_{all} = 4,000$ psi. The soil's unit weight, $\gamma_{soil} = 100$ lb/ft³. The site is in a Zone III region, (from Algerian Seismic Codes, which agrees with UBC-97). All concrete was decided to have a compressive strength, $f'_c = 3,000$ psi. Steel used for all reinforcement has a strength, $f_y = 60,000$ psi. The design methods used in this investigation are considered standard practice for reinforced concrete design; and although some resulting designs are conservative, the same degree of conservatism was used for parallel designs (girders, columns, etc of Frame A and Frame B).

A floor system was designed, not to be considered for comparison, but rather to obtain more accurate dead weight values. This is because the floor system, a slab and T-beam section as described later, are assumed to only carry gravity loads; so they are the same sections in both

frames. These gravity loads were defined as a live load of 50 psf for the first floor, and 20 psf for the roof. Dead loads were found to be 12 psf for both stories.

Algerian seismic codes allow the use of a static lateral force design method if three requirements are met: 1) Total structure height is less than 30 meters, 2) no soil liquefaction or resonance behaviors are predicted and 3) the structure is classified as regular (no more than a height difference of 25% per story, no eccentricity, symmetrical and consistent damping throughout plan). As shown in Figure 1, all three requirements are satisfied for this method.

Although a stiffer floor diaphragm needs to be designed for Frame B, this preliminary investigation only compares the cost of structural elements common to both frames. Consequently, it is omitted from this report.

Outcomes

The outcomes for Frame A and Frame B are discussed below. Detailed calculations are described in the Appendices for the design of the base isolation unit. Shear analyses are only highlighted in Appendix A-1 since minimum code requirements were sufficient for most structural elements. Thus it is assumed that including shear reinforcement in the analyses does not change the overall ratio of materials.

Frame A details

The procedure for determining a static lateral force resulted in the following loads:

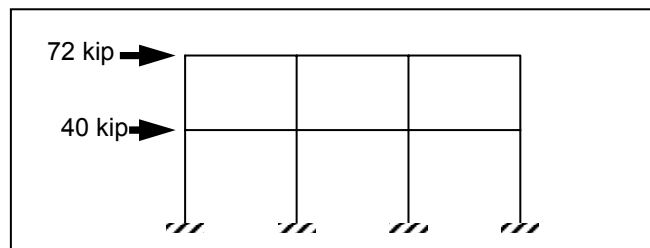


Figure 2. Earthquake loads

Identical slabs were used for the roof and first floor. They are simply supported, 6" thick, and reinforced with #3 bars spaced at 6½" on center. Temperature steel is also called for, so #3 bars at 12" are used. The beams used are considered to behave as T-beams:

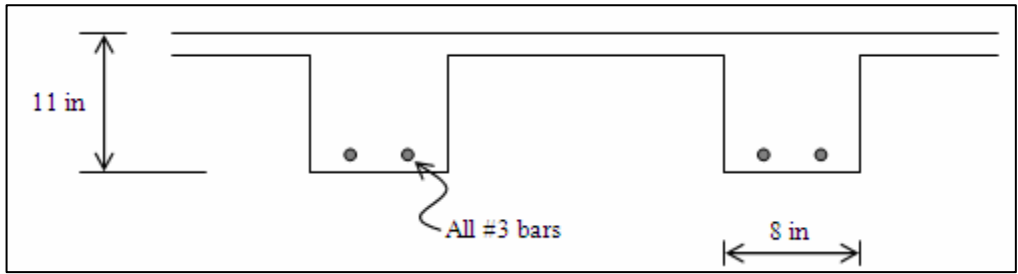


Figure 3. Floor system detail

Analyzing the system it is shown that the factored moment required, $M_u = 28 \text{ k- ft}$, which is sufficiently carried by the design.

A computer generated moment envelope for the factored loads of the worst case girder (first floor, interior) is as follows:

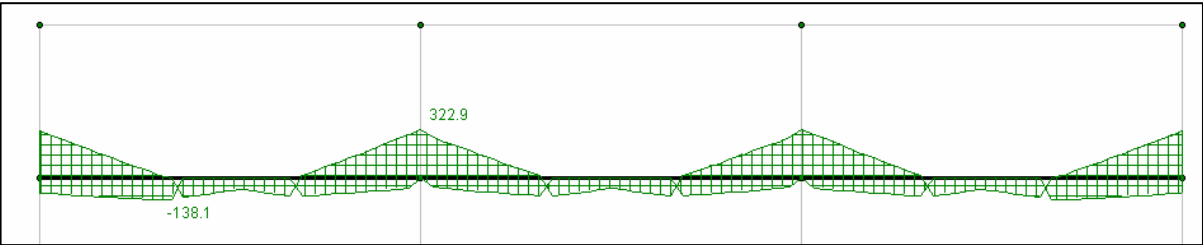


Figure 4. Moment diagram for interior girder, frame A.

The girder also has a worst axial load, $P_u = 86 \text{ kip}$. With a max $M_u = 323 \text{ k-ft}$, the beam-column was designed: A 16” by 27” cross section with three No. 10 bars on the bottom to carry the moment. To carry the axial load, the bars are continuous, and three No. 10 bars are placed on top to make the member symmetrical as required for a column.

The column’s moment envelope from RISA resulted in the following:

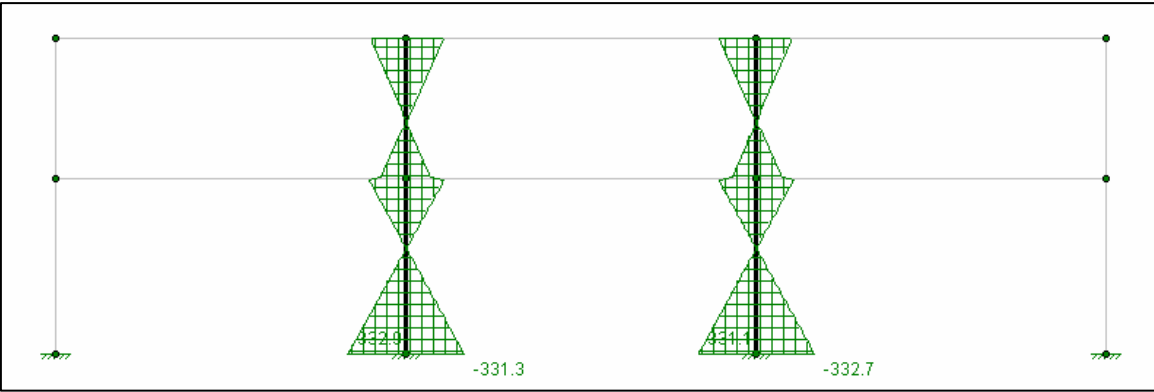


Figure 5. Moment envelope for interior columns, frame A.

Also, an axial requirement of 102 kips was reported. To accommodate this load, and the 333 k-ft of moment at the base, a 22" by 22" design was produced. Reinforcement was decided upon by following ACI interaction diagrams; so eight #10 bars in a square arrangement are necessary.

The footing for this frame has to withstand a $P_u=144$ kips and a $M_u=333$ k-ft. An 18" thick, 10' by 10' foundation was designed, and eight #11 bars are placed for reinforcement (4 per dimension).

Frame B

An isolated base is used for frame B. This allows the design to consider the earthquake loads negligible.

The purpose of base isolation is to increase the structure's period, T , from $T_A = 0.2$ sec (frame A) to target effective periods of $T_D = 2.5$ sec and $T_m = 2.7$ sec. Firstly, an isolator that complies with UBC-97 standards needed to be selected. The three basic requirements specify that the system has to 1) Be stable 2) Provide increasing strength with increasing displacement and 3) Not degrade under cyclic loading. A high damping rubber bearing was selected as the isolating device. It is one of the most commonly used devices, so numerous studies have quantified its properties and behaviors. A soft rubber with a modulus of rigidity, $G = 58$ psi is assumed. Only one bearing design that accommodates the worst load (from an interior column) is used for all 16 locations to save on the cost of using multiple molds. Figure 6 depicts the selected isolator and its final design dimensions.

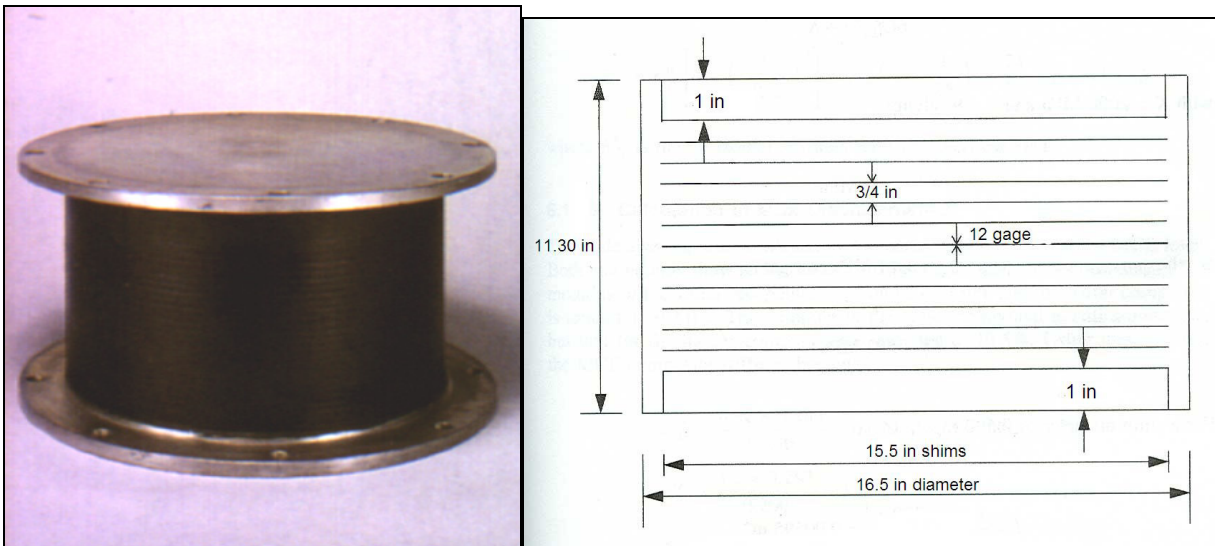


Figure 6. High damping rubber isolator and dimensions

As expected, the girder's moment diagram shows a much smaller worst-case value compared to frame A. Also, a negligible axial load results, and minimum axial load Code requirements are satisfied by the concrete cross section alone.

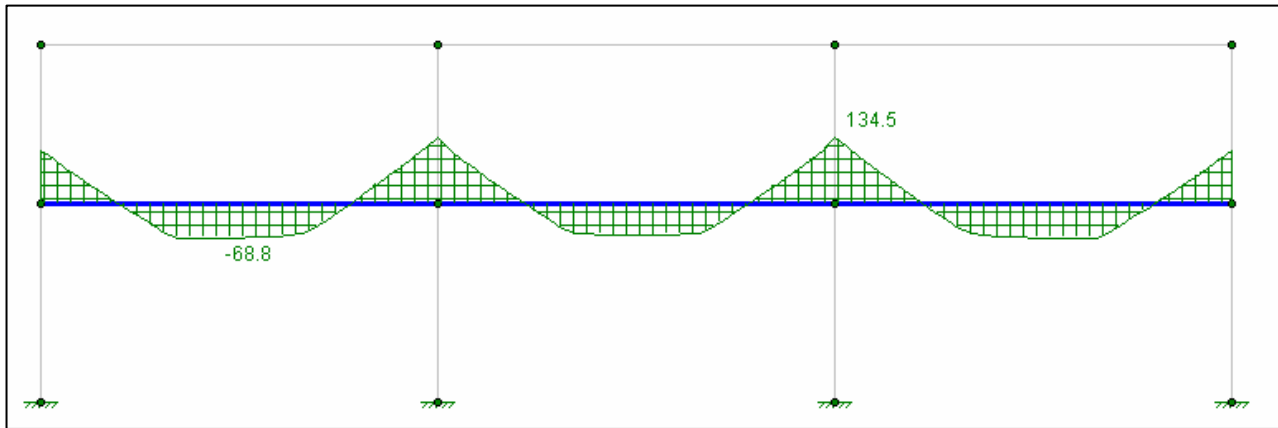


Figure 7. Girder moment diagram, frame B.

Figure 7 represents the moment diagram for an interior girder on the first floor, (worst case). The designed girder is a 12" by 21" face with reinforcement detailed below. The same member is used for all girders.

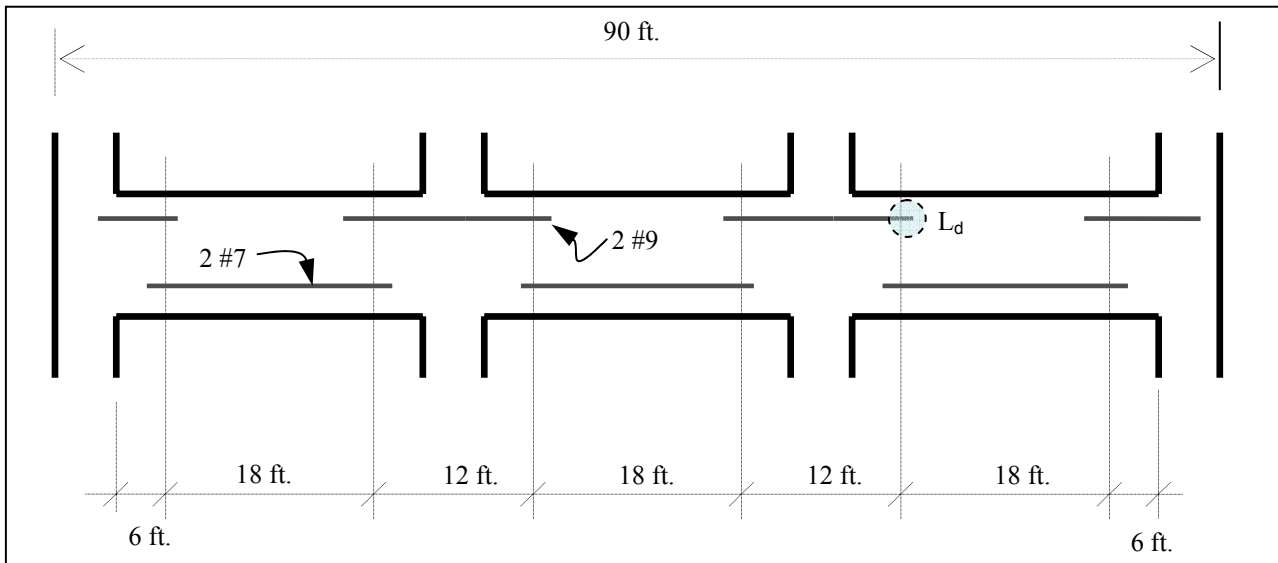


Figure 8. Girder reinforcement detail, frame B.

Development lengths, L_d , as shown in Figure 8, were not determined because it is assumed they do not contribute a significant change in the total amount of steel for the structure. They are depicted because they would have to be considered in a more finalized design, (as required by ACI).

The columns are assumed to only take axial load, and minimal moment capacity requirements are provided as recommended by ACI. For an interior column on the first floor, the $P_u = 88$ kips. An 18" by 18" column provides a much larger capacity than required, but it is a conservative design that will not be prone to buckling. For this column, only minimal reinforcement is required. Four #9 bars are placed at each corner with a minimum amount of concrete cover, the least amount of steel the Code suggests.

The foundations in this frame are only subjected to a gravity load, $P_u = 125$ kips. Using an 18" thick base, design calculations result in a 6' by 6' footing with 4 #11 bars each way.

When isolating a frame, the base-level diaphragm needs to be reinforced, to restrict independent movement of the columns. Minimal code provisions are required for this, so they are not considered in the comparison of materials.

Comparing frame A and frame B

As mentioned before, the research approach to compare costs is to get weight ratios of several elements, and also that of the entire structure. The table below presents results for the design weights, by elements, for each frame.

Table 1. Material take-off by element				
	Fixed-Base Moment Resisting Frame (frame A)		Isolated Base Frame (frame B)	
Structural Element	Concrete Weight, kips	Steel Weight, kips	Concrete Weight, kips	Steel Weight, kips
Beams	295.4	2.3	295.4	2.3
Girders	636.6	37.1	375.7	7.5
Columns	212.1	18.6	144	5.9
Foundations	357.9	6.8	128.4	4.1
Total	1502	64.8	943.5	19.7

From Table 1, the following ratios were computed:

Table 2. A / B weight ratios of main structural elements		
	Concrete ratio	Steel ratio
Girders	1.7	4.9
Columns	1.5	3.2
Foundations	2.3	1.8
Entire Structure	1.6	3.3

Conclusions

As expected, base isolation turns out to be the best design, economically speaking; this is due to the fact that the cost of the isolators will not surpass the need for 3.3 times more steel in the reinforced frame. The rubber bearings utilized are very common, so several manufacturers can offer competitive prices. Also, the same isolator is used in 16 footings, thus requiring just one cast or mold.

The results obtained are fairly typical, yet not all-inclusive. Design outcomes for other parameters can vary significantly. Factors that influence structural design are: importance of the building, architectural requirements, soil profile, height of the structure (more so than plan dimensions in some cases), regional issues (cost of labor, availability of specific materials, etc.), and many others.

Another interesting find, was that base isolation can be used to protect non-structural elements and equipment. In figure 8, a frame affected by a seismic loading is still standing, but the curtain walls are destroyed. If the frame had been isolated as a whole, the walls would have been subjected to a less destructive vibration, and probably still be standing in good shape.



Figure 8. An RC structure affected by 2003 Earthquake in Algeria

Base isolation can also be used to protect mechanical equipment or large fragile objects, as in a museum. For example, if it turns out that retrofitting a museum building is not cost-effective; objects that it houses can be fitted with smaller scale isolation systems to be protected in case of a seismic event.

References

Paz, Mario. *International Handbook of Earthquake Engineering : Codes, Programs and Examples*. October, 1994; Chapman and Hall. London, England.

McCormack, Jack. *Design of Reinforced Concrete*. 2001; John Wiley & sons, Inc. New York, New York.

Kelly, James M.; Naeim, Farzad. *Design of Seismic Isolated Structures: From Theory to Practice*. 1999; John Wiley & sons, Inc. New York, New York.

Appendices

Appendix A-1. Shear reinforcement sample calculation.

For girder in Frame B:

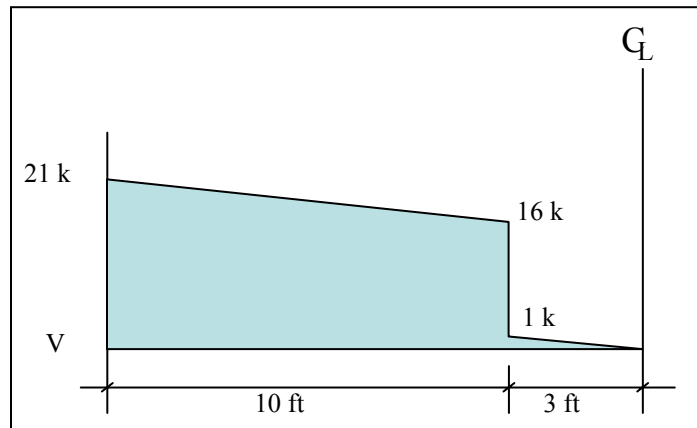


Figure A-1. Shear diagram for Frame B girder (worst case)

Width, $b_w = 12''$

Depth, $d = 18''$

$$\phi V_c = 2\sqrt{f'c}b_wd \longrightarrow \text{(ACI 11.3.1.1)}$$

$$\phi V_c = (.85)2\sqrt{3000}(12)(18) = 20.1 \text{ kip}$$

$$V_u(@18'') = -\frac{5}{120}(18) + 21 = 20.3 \text{ kip}$$

$$V_u > \frac{1}{2}\phi V_c \quad , \quad \therefore \text{Reinforcement is required} \longrightarrow \text{(ACI 11.5.5.1)}$$

Use maximum spacing for #3 stirrups:

$$s = \text{smaller of } \left[\begin{array}{l} \frac{A_v f_y}{50 b_w} = \frac{2(0.11)(60000)}{50(12)} = 22'' \text{ (ACI -11.5.5.3)} \\ \text{or } d/2 = 9'' (V_s = 0) \text{ (ACI -11.5.4.1)} \end{array} \right] , \quad s_{\max} = 9''$$

So all stirrups would be placed at 18'' from support spaced at 9'' for 10'-6''

Appendix A-2. Base isolation device design

From the 1997 Uniform Building Code,

$Z = 0.3$ → (Sec. 1653)

$S = S_D$ → (Table 16-J)

Assumed seismic source type => Type A → (Table 16-U)

Active fault is ~ 10 km from site, so

$N_a = 1.0$ → (Table 16-5)

$N_v = 1.2$ → (Table 16-T)

$$ZN_v = (0.3)(1.2) = 0.36$$

Interpolating for M_m in Table A-16-D,

$$M_m = 1.35$$

$C_v = C_{vD} = 0.54$ → (Table 16-R)

$C_A = 0.36$ → (Table 16-Q)

$$\text{For } M_m ZN_v = (1.35)(0.36) = 0.49 > 0.40$$

$C_{VM} = 1.6M_m ZN_v = 0.778$ → (Table A-16-G)

For $M_M ZN_a = 1.1(0.405) = 0.446$ → (Table A-16-F)

For an ordinary moment resisting frame, $R_I = 2.0$ (Table A-16-E)

A laminated rubber bearing with soft rubber is assumed to have 15% damping.

$B_D = B_M = 1.35$ → (Table A-16-C)

For preliminary design, the isolation system should provide effective isolated periods of :

$$T_D = 2.5 \text{ sec}$$

$$T_M = 2.7 \text{ sec}$$

From Eq. 4.7 and Eq. 4.8 (Naeim, Kelly),

$$T_D = 2\pi \sqrt{\frac{W}{K_{D \min} g}} \quad \text{and} \quad T_M = 2\pi \sqrt{\frac{W}{K_{M \min} g}}$$

where,

W = weight of building
g = gravity

An approximated weight of $W = 352$ kips is assumed from beam, girder, columns and slab information.

Solving equations 4.7, 4.8 for K gives

$$K_{D \min} = 5754.2 \text{ lb/in} \quad \text{and} \quad K_{M \min} = 4933.3 \text{ lb/in}$$

Estimation of design displacement, D_D :

$$D_{D,M} = \frac{g C_{VD,M} T_{D,M}}{4\pi^2 B_{D,M}} \quad (\text{Eq. 4.2, 4.3, Naeim})$$

Substituting values,

$$D_D = 9.79 \text{ in} \quad \text{and} \quad D_M = 15.23 \text{ in}$$

The Code requires design for a 5% accidental eccentricity, e :

$$e = (.05)(90)12 + 3.28(2) = 93.36 \text{ in}$$

$$D_{T_{D,M}} = D_{D,M} \left(1 + y \frac{12e}{b^2 + d^2} \right) \longrightarrow (\text{UBC 58-5, 58-6})$$

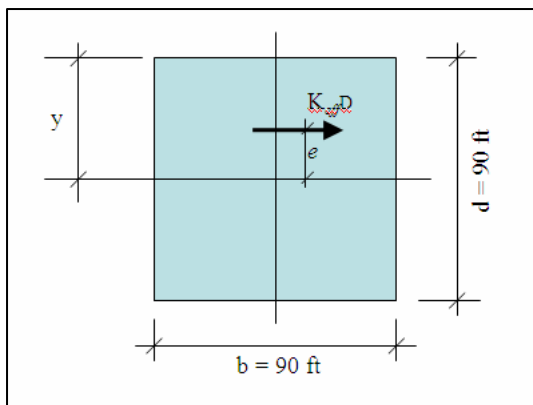


Figure A-2. Accidental eccentricity

$$y = (90)(12)(0.5) = 540 \text{ in}$$

$$b^2 + d^2 = [(90)(12)]^2 (2) = 2332800 \text{ in}^2$$

$$12e = 12 (93.36) = 1120.2 \text{ in}$$

$$D_{TD} = 12.33 \text{ and } D_{TM} = 19.18 \text{ in}$$

Check total displacements against minimum values:

$$D'_{D,M} = \frac{D_{D,M}}{\sqrt{1 + \left(\frac{T}{T_{D,M}}\right)^2}} \longrightarrow \text{(UBC 59-1,59-2)}$$

With $T = 0.2 \text{ sec}$ (From Frame A design)

$$(\mathbf{D}'_D = 9.42 \text{ in}) < (\mathbf{D}_{TD} = 12.33 \text{ in})$$

$$(\mathbf{D}'_M = 14.70 \text{ in}) < (\mathbf{D}_{TM} = 19.18 \text{ in})$$

Soft rubber bearing design:

Design load is worst axial load, $P = 88 \text{ kips}$; this load will be used to design a single bearing for all footings to save on mold costs.

Rubber properties are $G = 58 \text{ psi}$, $\beta = 0.08$, Max shear strain, $\gamma = 1.5$

Horizontal stiffness

$$K_H = P \left(\frac{2\pi}{T_D} \right)^2 \quad \text{(metric)}$$

$P = 88 \text{ kip} = 39.82 \text{ metric tons}$

$K_H = 0.252 \text{ MN/m} = 1.44 \text{ k/in}$

$\gamma = D / t_r$, where t_r = thickness of rubber

$$\mathbf{t_r = 8.2 \text{ in}}$$

$K_H = GA / t_r$ and solving for A with K_H and G gives a required area, $\mathbf{A = 203.6 \text{ in}^2}$

A trial bearing diameter is used, $\phi = 16^{1/2}$ ", $\mathbf{A = 213.8 \text{ in}^2}$

Bearing pressure, $p = P/A = 412 \text{ psi}$

Actual horizontal stiffness, $K_{H_{act}} = 1.51 \text{ k/in}$

Composite stiffness, $K_{H_{com}} = (16 \text{ units})(1.51 \text{ k/in}) = 24.16 \text{ k/in}$

Horizontal period, T_H :

$$K_{H_{com}} = (24.16 \text{ k/in})(1/5.72) = 4.22 \text{ MN/m}$$

$$W = (352 \text{ k})(1/2.206) = 159.6 \text{ metric tons}$$

Actual squared frequency , $w_H^2 = (4.22 \times 10^6 \text{ N/m})(1/159550)$, so $w_H = 5.15 \text{ rad/sec}$

$$T_H = \frac{2\pi}{w_H} \quad \therefore \quad T_H = 1.22 \text{ sec}$$

Composite damping remains 8% since $\beta_{com} = \frac{w_D}{2\pi K_H D^2} = \frac{K_H \beta}{K_{H_{com}}} = 0.08$

From UBC-97 Table A-16-C for $\beta = 8\%$,

$$1.0 + 3/5(1.2-1.0) = B_D = 1.12$$

$$D_D = \frac{g}{4\pi^2} \cdot \frac{C_{VD} T}{B_D} \quad \longrightarrow \quad (\text{UBC 58-1})$$

$$D_D = 5.73 \text{ in}$$

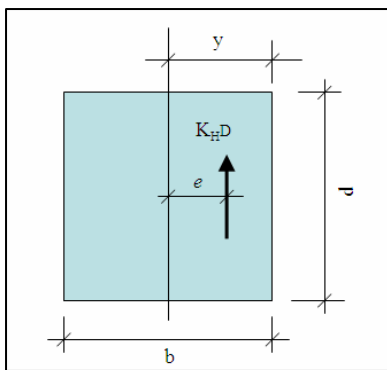
From earlier calculations, $D_T = 12.33$, but it seems too large, so the real torsional stiffness, K_θ

$$K_\theta = \sum_{i=1}^n K_{H_i} (x_i^2 + y_i^2)$$

where x and y are distances from isolator to plan centroid.

$$K_\theta = 72480 \text{ k-ft} = 869760 \text{ k-in}$$

The applied torque comes from:



$$M = (K_H D)e$$

So additional displacement is

$$\theta y = (K_\theta D e / K_\theta) y = 4.64 \text{ in}$$

Total displacement , $D_T = 10.37 \text{ in}$

Figure A-3. Composite torque

$$\gamma_{\max} = D / t_r = 1.3 < (1.5 \text{ assumed})$$

Check minimum torsion allowance:

$$D_{TD\min} = 1.1 D \longrightarrow \text{(UBC 1658.3.5)}$$

$$1.1(5.73) = (6.3 \text{ in}) < (D_T = 10.37 \text{ in})$$

Use $D_T = 10.37 \text{ in}$

Bearing Dimensions

Set vertical frequency $f_v = 10 \text{ Hz}$, then from $6S^2 \approx \frac{f_v^2}{f_H^2}$ and solving for S ,

$$S = \frac{1}{\sqrt{6}} \cdot \frac{10}{\left(\frac{1}{T_H}\right)} = 4.98$$

For the vertical frequency, it is necessary to have a small strain shear modulus, $\gamma \approx 20\%$. The compound will then have the following properties:

$$G_{0.2} = 101.5 \text{ psi and } K = 290 \text{ ksi} \quad (\text{from common lab tests, pg. 99, Naeim})$$

$$\text{Then } E_c = \frac{6GS^2K}{6GS^2 + K}$$

where,

$$G = 101.5 \text{ psi} = 0.7 \text{ MPa}$$

$$K = 290 \text{ ksi} = 2000 \text{ MPa}$$

$$S^2 = 4.98^2 = 24.8$$

So,

$$E_c = 14355.6 \text{ psi} \quad \text{and} \quad K_{vcom} = 5,988,736 \text{ lb/in}$$

$$w_v^2 = 1049 \times 10^6 \text{ N/m} (1 / 159.55 \times 10^3 \text{ kg}) = 6574.74 \text{ sec}^{-2}$$

$$w_v = 81.08 \text{ rad/sec}$$

$$f_v = 12.91 \text{ Hz} \quad (\text{close enough to assumed } 10 \text{ Hz})$$

So $S \approx 5.5$ is adequate

$S = \frac{\Phi}{4t}$, where t is the thickness of each layer. Solving for t , gives $t = 0.75$ in

The total thickness of rubber, $t_r = 8.2$ in, and $nt = t_r$, where n is the number of layers.

\therefore Use 11 layers with a thickness of $t = \frac{3}{4}$ in ($nt = \text{total rubber thickness} = 8 \frac{1}{4}$ in)

Final details are shown in Figure 6.

SIMPLIFYING BRIDGE MODELS FOR FRAGILITY ANALYSIS

Theodore Deligiannidis
University of South Carolina

2004 REU Student
Mid-America Earthquake Center
Georgia Institute of Technology
Reginald DesRoches

ABSTRACT

A large portion of the Central and Southeastern United States is defined as a potential hazard for seismic activity. Project DS-7b analyzes bridges typical to this region and ultimately produces fragility curves for these bridges. A fragility curve is a probabilistic way of assessing the vulnerability that a bridge, or any structure, has to a seismic event. Programs such as OpenSEES are used to build bridge models, and their fragility curves are then generated using programs such as MATLAB. Unfortunately, when these models become very complex, their analysis consumes a large amount of time.

This report presents a simplified model as a somewhat viable alternative to a complex model for fragility analysis, subject to two different suites of ground motions. This analysis is found to produce significantly less program run-times while resulting in component responses comparable to those of the complex model. Finally, the fragility curves for both the simple and complex models, taking many uncertainties into account, are plotted and compared.

PART I: INTRODUCTION

Acting as a connecting tool for the cherished roads across bodies of water and valleys, highway bridges are some of the most important components of the United States' infrastructure. Millions of resources and people travel across them each day. Therefore, maintaining a vast, healthy system of bridges across the country is a critical part of the economy and of human life. Consequently, when natural disasters occur and harm these bridges, the economy and life are somewhat disrupted. Such was the case, for example, in Northridge, California, and Kobe, Japan, during the mid-1990s. The powerful earthquakes that struck these areas provided a desire for awareness of an earthquake's consequences in preparation for such an unpredictable disaster.

This is the goal of Project DS-7b, Damage-Functionality Relationships for Bridges, of the Mid-America Earthquake (MAE) Center. More generally, it is the goal of the Damage Synthesis (DS) thrust to which it belongs and the goal of consequence-based engineering (CBE). In the eleven states which comprise the mid-America region, there are over 163,000 bridges, one-third of which are either single-span (SS) steel bridges or multi-span simply supported (MSSS) concrete bridges. Understanding the fragility behavior of individual bridges and then combining it with the damage-functionality relations of the bridges, the project produces fragility and functionality curves, which can then be used to determine transportation network performance. It has the potential for resulting in better decision-making and determination of appropriate intervention to minimize social and economic consequences across this network.

Fragility analysis of a bridge is what makes this project possible. Fragility is presented as a conditional probability which states the probability of meeting or exceeding some limit state, such as collapse, given some ground motion intensity. This is expressed with a fragility curve, which plots the conditional probability versus, for example, peak ground acceleration (PGA). Numerous uncertainties are involved and then quantified through the steps of this task.

The first step in the process is establishing an appropriate bridge model of interest in the study. The second step is generating a set of earthquake acceleration time histories, which cover various levels of ground shaking intensity. After quantifying numerous uncertainties in the bridge and local site conditions to establish a set of earthquake-site-bridge samples, a nonlinear time history of each of these samples is performed to simulate a set of bridge response data. Next, the probabilistic characteristics of both structural demand and structural capacity must be set up. Demand as a function of ground motion (e.g. PGA) is found by performing a regression analysis of the simulated response data. Capacity depends on defined bridge damage states (e.g. complete damage). Then, the conditional probability that demand exceeds capacity is calculated for various levels of ground shaking. Finally, the fragility curves are plotted based on the selected ground shaking parameter.

Every step in this analytical process heavily depends on the first task, the generation of the bridge model. The main software used for analysis in Project DS-7b is known as the Open System for Earthquake Engineering Simulation (OpenSEES). This program is a framework for developing applications to simulate the performance of structural and geotechnical systems subjected to earthquakes. OpenSEES has the capability to develop a variety of bridge models, from the most complex to the distinctly simplified.

In a trustworthy analysis, a bridge must be modeled in this program as it is built for daily use on a highway, with every component, material, and geometrical parameter taken into consideration. For example, if a bridge spans 500 feet, then OpenSEES must understand that a 500-foot model is being developed. Such a model is detailed and consistent, but it becomes very complex. Unfortunately, when it is subjected to a simulated earthquake, its analysis is also complex, and processing time becomes a factor. Furthermore, when the model is run through an entire suite of ground motions (60, for example), run times are significantly extended, further complicating the time issue.

Fortunately, a potential solution exists to alleviate this problem. OpenSEES understands the simplification of a model very well and can analyze it just as effectively. This proposed model would also take less time to generate. More importantly, it would be analyzed at a more rapid rate simply due to a lack of excessive bridge parameters. However, there is no precedence for the legitimacy of a simplified model, and whether or not its behavior will equate to the behavior of the more complex model in terms of fragility is the idea that will be tested.



Figure 1.1: There are over 163,000 bridges in the mid-America region. This is an example of a multi-span simply supported (MSSS) steel girder bridge, the model of study in this report.

PART II: THE COMPLEX MODEL

Before the simplification of a complex model is discussed in detail, the complex model itself must be understood. The following list outlines all of the components of OpenSEES complex model generation:

1. Setting the number of dimensions and degrees of freedom
2. Establishing all bridge nodes
3. Fixing the nodes that need to be constrained
4. Assigning masses to appropriate nodes
5. Generating materials, sections, and elements for columns
6. Generating elements for deck
7. Generating material and elements for fixed bearings
8. Generating material and elements for expansion bearings
9. Generating material and elements for impact elements
10. Generating material and elements for abutments
11. Generating rigid-link elements
12. Generating material and elements for foundations

Several of these sections of input will later be crucial to the development of the simplified model. For now, all are necessary for the analysis of the complex model. Figure 2.1 shows this model with its important components labeled.

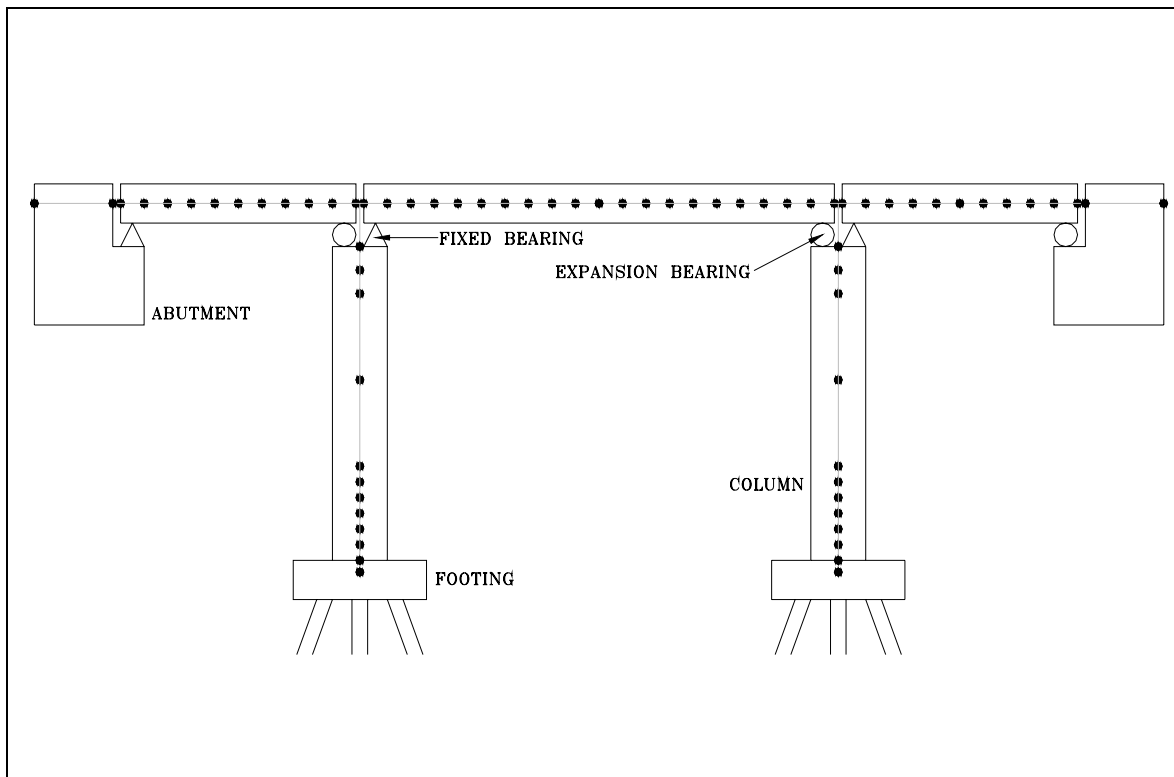


Figure 2.1: A two-dimensional view of the MSSS steel bridge being modeled. All nodes programmed in the model are shown. Note—figure not drawn to scale.

As seen, there are two abutments, three spans (the middle span longer than the end two spans), three fixed bearings, three expansion bearings, and two column-foundation systems. This model has 71 total nodes. Figure 2.1 is not drawn to scale, but the general location of all the nodes with respect to the real bridge is accurate. Unless constrained, each of these nodes has three degrees of freedom. The constrained nodes include all foundation and abutment nodes and the nodes at both ends of each span. The mass of the deck is distributed equally among its nodes while the mass of the columns and foundations are grouped at a few of their nodes.

Once nodes have been established, appropriately constrained, and assigned masses, the bridge must be generated. This generation must evolve one component at a time. The material, elements, and sections (each where needed) for these components are what use an extensive number of lines and commands for model building.

Perhaps the most complex component generation is the most significant: the column. Its complexity is attributed to the presence of concrete and steel, which each have mandatory input parameters, such as strength and modulus of elasticity. Furthermore, there are two layers of concrete, core and cover concrete. These, combined with the layer of reinforcing steel, necessitate three concrete sections. Finally, since a true representation of the bridge would give it four rows of columns, the connecting elements for the nodes must be input for all four rows. The OpenSEES code for the column generation is by far the longest out of all the components.

The deck element generation is the next longest. Though all nodes can be simply connected by elements which call for an area, modulus of elasticity, and moment of inertia, 40 elements are needed to connect the 43 nodes of three spans. For both the fixed and expansion bearings, non-linear materials, each with their designated parameters, are used, and zero-length elements are input to complete the generation of the bearings. Zero-length elements are mandatory and therefore popular in this model. They are mandatory because many nodes are established at the same point, points that occur at important locations in the model. This is true for the bearings as well as the impact elements, abutments, and foundations.

The impact elements are not pictured in Figure 2.1. They are merely, elements used for connecting the gaps on the deck, the gaps among the spans and between the left and right spans and their respective abutment. The exact type of material used for the impact elements is used for the abutments. The foundations are unique because they are the only component to use a purely elastic material. The only other elements present in the complex model that have not yet been discussed are the rigid-link elements. These elements are needed where each column meets its respective footing and the bridge deck.

This has been a general description of how the original complex model is built in OpenSEES. This model contains a high number of nodes, materials, sections, and elements. In the next section, significant reduction of the model's code will be discussed.

PART III: SIMPLIFYING THE MODEL

The portion of the complex OpenSEES file dedicated to building the model uses 309 lines of code, not counting commented out lines or lines left empty as separators. Once this model is understood, however, it may be modified to drastically reduce the amount of code, a modification which is certain to relieve the model time wise on more than one occasion during the running of analyses.

The proposal of simplifying involves reducing the complete model to five major degrees of freedom and producing a non-linear spring system, which can be developed to replace the column-foundation system. Figure 3.1 displays the system that is trying to be achieved. The first important parameter is the bridge's mass. All of the bridge's mass would be concentrated at five nodes, the mentioned degrees of freedom. The columns and foundations would essentially be eliminated and replaced by the indicated springs. These springs would have invaluable parameters that would ultimately determine the overall behavior of this model.

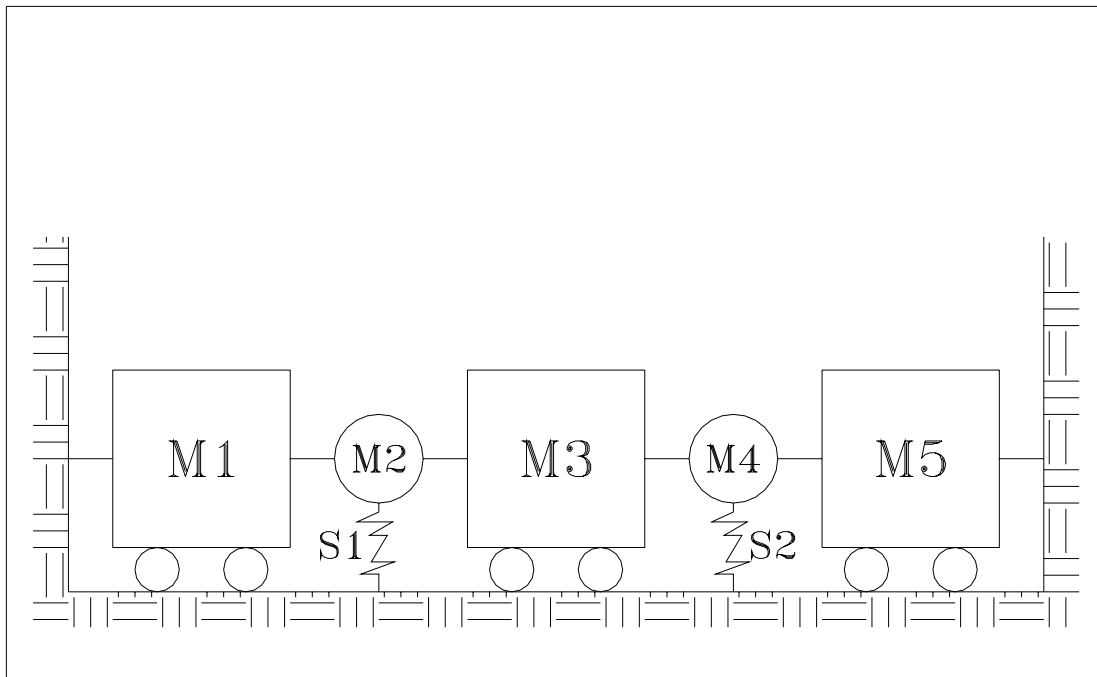


Figure 3.1: A theoretical sketch of the proposed system. Note—figure not drawn to scale

Because nodal masses are to be concentrated, the assigning of several nodes is not necessary. For the deck, the original idea was to leave one node for each of the spans and all end nodes. The end nodes were to be left for bearing connections. For the columns, nodes at the top and bottom were to remain. Using this method, only seven coordinates and therefore six theoretical “inches” of space were to be needed. The left abutment was to be placed at (0,0) and the right abutment at (6,0) with points (1,0) through (5,0) each containing one of the five degrees of freedom (three “spans” and two “columns”).

OpenSEES, however, was not willing to accommodate this arrangement. After some trial and error, it was found that OpenSEES would not agree with the prescribed material connections for the degrees of freedom of the model. Zero-length elements were going to be necessary throughout the simplified model, so all 17 original nodes were placed at the point (0,0). Later, it would be discovered that the end nodes for each span were also not needed. Thus, in the true simplified model, the one used for all intents and purposes, only 11 nodes exist, and they can be seen in Figure 3.2.

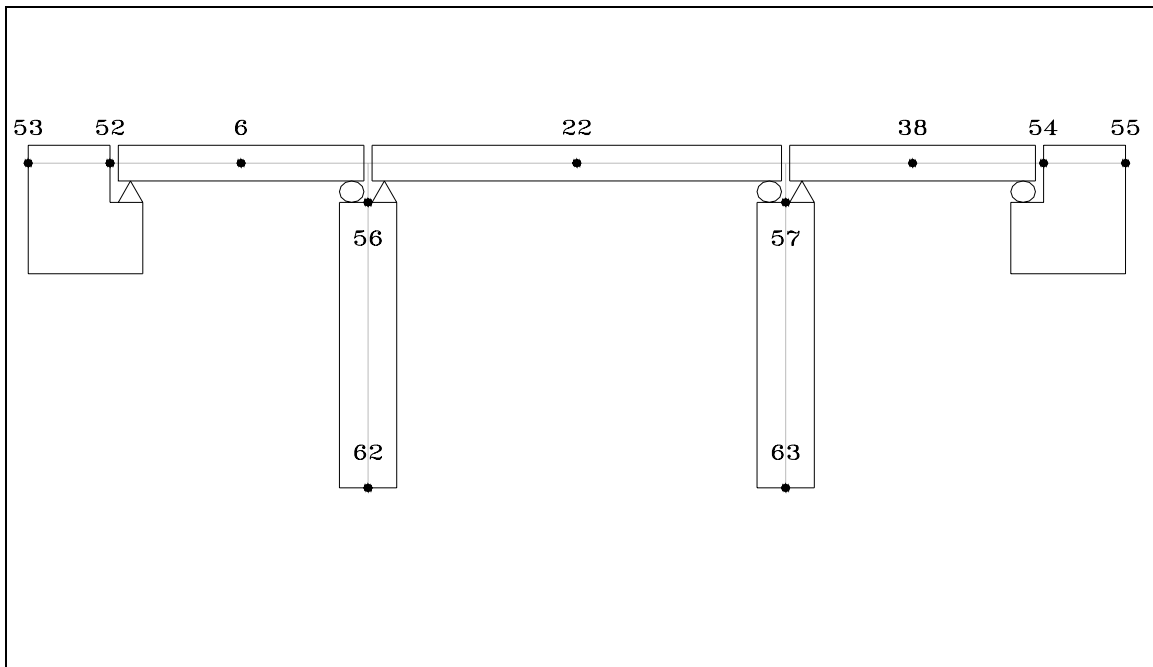


Figure 3.2: The simplified model. The 11 nodes are superimposed on the actual structure. Although the node track appears to have a geometry, all nodes are located at the same point and are connected by zero-length elements in OpenSEES. Note—figure not drawn to scale.

Figure 3.2 is based exclusively on Figure 2.1 with over 80% of the nodes having been removed. This elimination leads to a sharp decline in nodal constraints and thus the total number of degrees of freedom. Only nodes 53, 55, 62, and 63 are constrained. In the simplified model, the only nodes with mass are nodes 6, 22, 38 (each taking on the mass of its respective span), 56, and 57 (each taking on the representative mass for its column). These are the five working masses of the simplified model, but two additional masses are assigned to troubleshoot a former problem. A negligible mass is given to nodes 52 and 54. The mass given to these two abutment nodes is needed for the program's proper functioning. At the same time, this insignificant value does not influence numerical results and should not be deemed a hindrance.

To suit the simplified model, the remaining sections of code are modified, replaced, or removed, or untouched. The latter is true for only one section of code, the abutments; no changes were made to their material or elements. Modified sections are those involving fixed bearings, expansion bearings, and impact elements. Since these sections are impacted by only node reduction, the code for their material remains unchanged. However, this is not true for the elements.

In the complex model, the designated fixed-bearing area is connected with the left-most node of each span with a zero-length element. In this model, the key adjustment of connecting the fixed-bearing area with the “representative” node of each span, so node 52 is tied to node 6, node 56 to 22, and node 57 to node 38. For the expansion bearings, nodes 6, 22, and 38 must once again act as representatives for their spans. They are connected with their corresponding expansion bearing areas, nodes 56, 57, and 54, respectively. Fortunately for the impact elements, the three representative nodes can serve in multiple gaps. This time, they represent the left and the right nodes in their span. The abutment gaps are linked by the node 52-6 and 38-54 connections, and the internal gaps are designated by the node 6-22 and 22-38 connections.

The only completely removed section from the list given at the beginning of Part II is the section for deck element generation. The three remaining sections that have been unmentioned for simplified model generation were technically removed, but these three sections (generating material, elements, and sections for columns; generating material and elements for foundations; and generating rigid-link elements) are truly “replaced” by the newly proposed non-linear spring system. Throughout the gravity and transient analyses, the reliable MATLAB program is selected for plot comparison.

First, a new OpenSEES program must be created for attention to just the column’s replacement and its parameters. Recorded in this program are the force and displacement histories based on the set earthquake. The resulting force-displacement graph is plotted on top of the same type of graph for node 56 in the complex model, which, while tracking the displacement of the left column’s top node, essentially provides the displacement record for that column. MATLAB reads in these output files from OpenSEES. It produces the important force-displacement plots and has no problem producing them on top of each other. If, somehow, these plots could match up, meaning that the force-displacement records of the column and simulated column would be equivalent, a major step would be taken toward removing the column from the simplified model.

Because the breakthrough is developing the appropriate material for this simulated column, one certain type of material would prove to be critical: the hysteretic material. The following diagram shows the behavior of such a material:

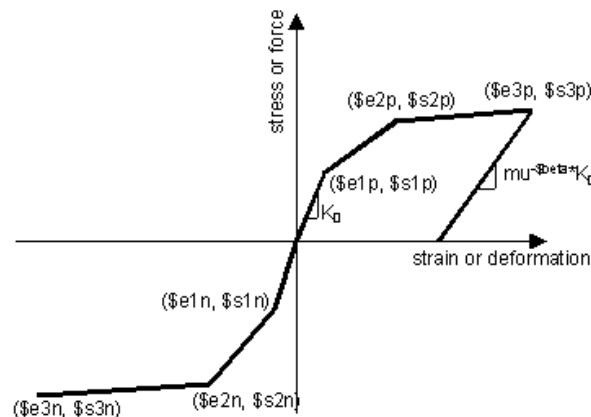


Figure 3.3: An elementary hysteresis. This pinpoints important force-deformation areas.

Figure 3.3 is known as a hysteresis. The force and deformation at first yield (which are significant because they key the rest of the arguments), second point in the envelope, and third point in the envelope, as well as the initial stiffness, can easily be seen.

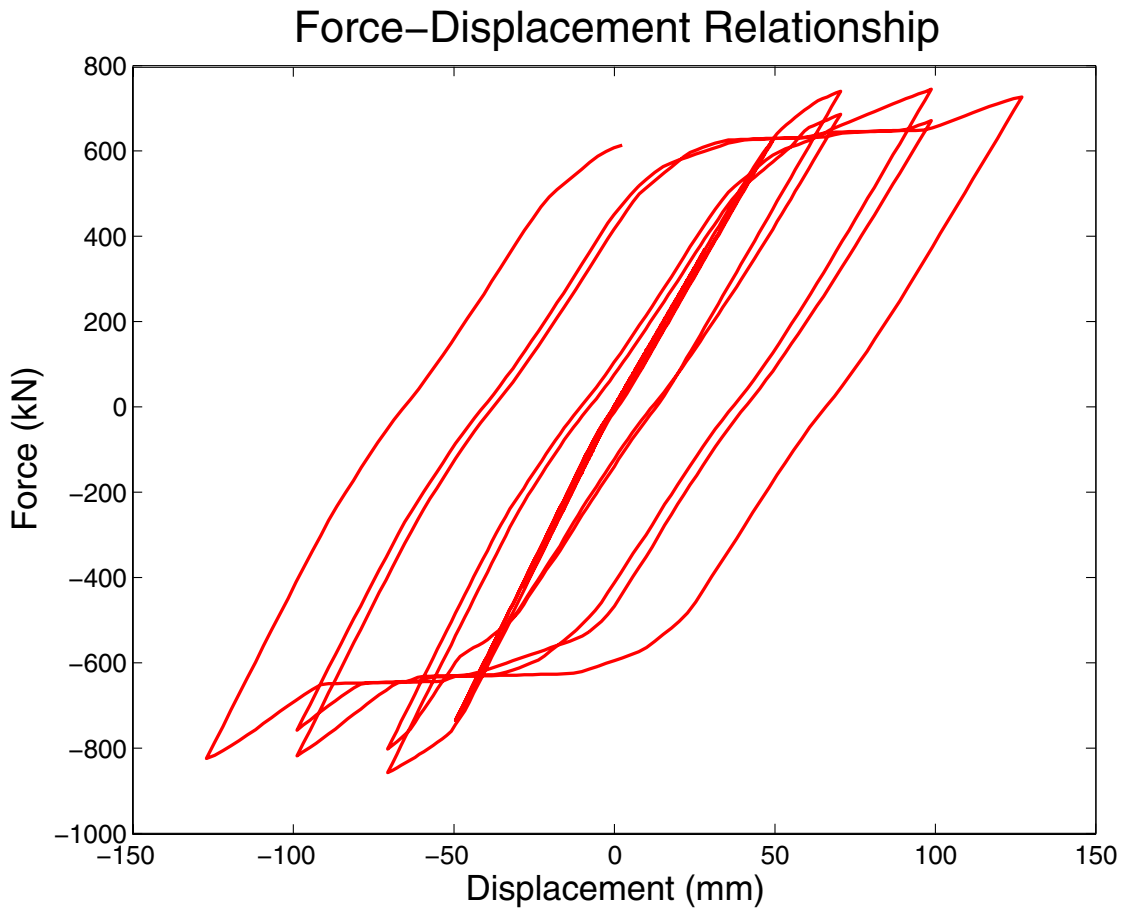


Figure 3.4: The newly developed hysteretic material—a much more complex hysteresis than the previous figure. The parameters obtained from this graph help develop the column’s replacement.

Figure 3.4 shows where these values are specifically pinpointed for the analytical model. Complete accuracy is not required. To avoid further complexities, the plot is assumed to be symmetric so that the force-deformation values for the negative portion of the envelope are simply the negatives of the positive values. Pinching factors for deformation and force and damage factors due to ductility and energy also play a role in column simulation. By default, these are zero. After all of the force and deformation values for the envelope are obtained, MATLAB is prompted to plot the resulting material’s diagram with the force-deformation diagram of the analytical model:

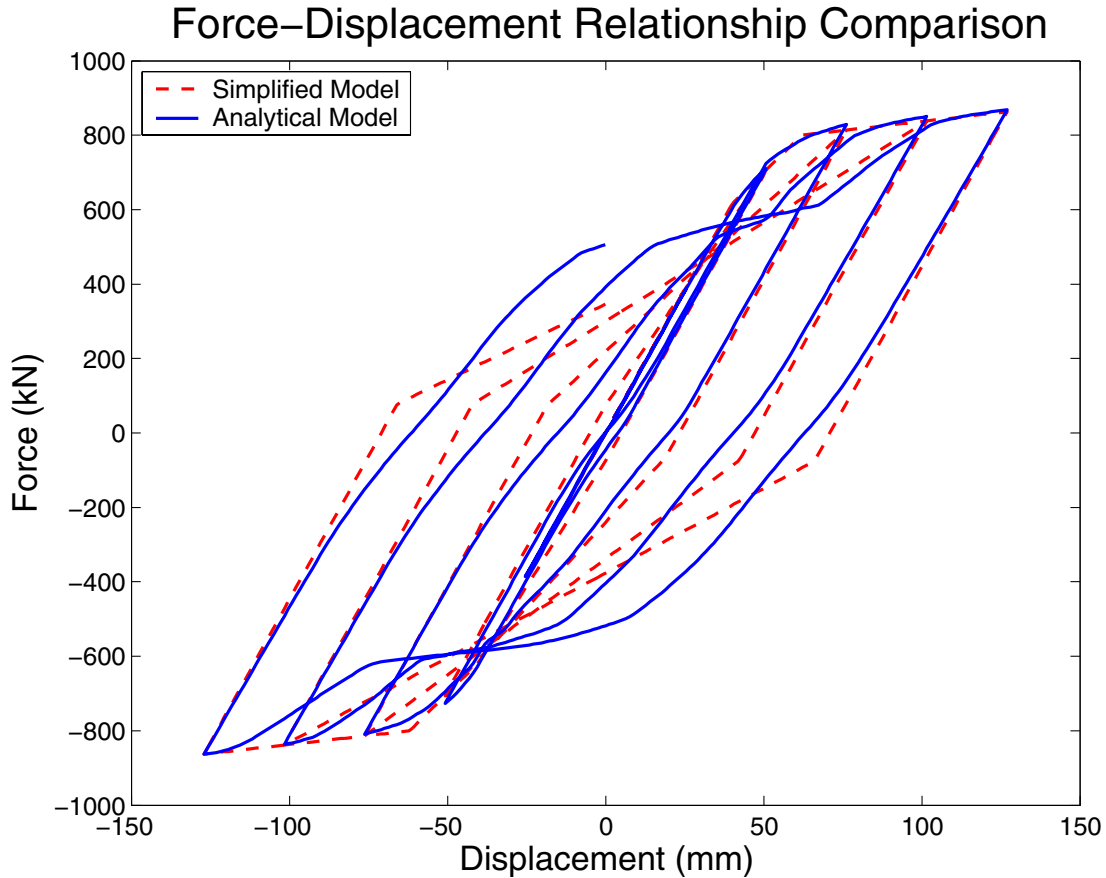


Figure 3.5: A comparison of force-displacement relationships. The behavior of the simplified model is seen to be very similar to the behavior of the analytical model.

It is easy to see how the plots are very similar to one another. Of course, this success did not occur immediately. Once the MATLAB M-file is set up to quickly run and produce this plot, a fair amount of trial-and-error, mainly involving damage and pinching factors, is involved to achieve the desired plot. This is how a deformation damage factor of -0.1 was determined to be best for this material. The same M-file which performs a plot comparison also calculates energy for both models. Once the analytical model's energy is close enough to the simplified model's energy, the parameters for the hysteretic material have been finalized. For this plot comparison, the simplified model's energy is 103% of the analytical model's energy. This is very pleasing. At this point, the OpenSEES file specializing in the column is no longer needed; its work is complete. The appropriate load-displacement parameters are in place, and the generation of the simplified model is finished. The next section explains the comparison of and the preliminary analysis involved with the complex and simplified models.

PART IV: BASIC MODEL COMPARISON

Thus far, most of the discussed OpenSEES programming has dealt with only the generation aspect of modeling. A series of preliminary analysis algorithms exists, but these algorithms will not be discussed in detail. The first step of preliminary analysis involves the running of one ground motion (not to be confused with an entire suite) and the comparison of bridge periods of both models. The period of a bridge, a very important parameter, is the time a bridge uses to complete one cycle of motion for a given mode shape. A mode shape is a characteristic form of a bridge during a ground motion and varies with the frequency of this motion. Table 4.1 displays the bridge periods of both models. Also, the first monitoring of run-times followed the prediction. The complex model used over 9 minutes (9:41) to complete this basic analysis, while the simplified model used only 18.5 seconds. This is an astonishing 96.8% decrease in run-time.

Table 4.1: The periods for the first five mode shapes of both models.

Mode Number	Complex	Simplified
1	0.274 s	0.289 s
2	0.177 s	0.149 s
3	0.148 s	0.083 s
4	0.084 s	0.032 s
5	0.074 s	0.030 s

In spite of a fundamental (first) period which differs by only 0.015 seconds, this comparison is not nearly as convincing as it needs to be. Therefore, more stages of preliminary analysis are needed. These stages, utilizing MATLAB, involve comparisons of time histories of the bridge decks and comparisons of component responses of the bridges. The deck time histories are found in Figures 4.1—4.3. All component responses are in Figure 4.4.

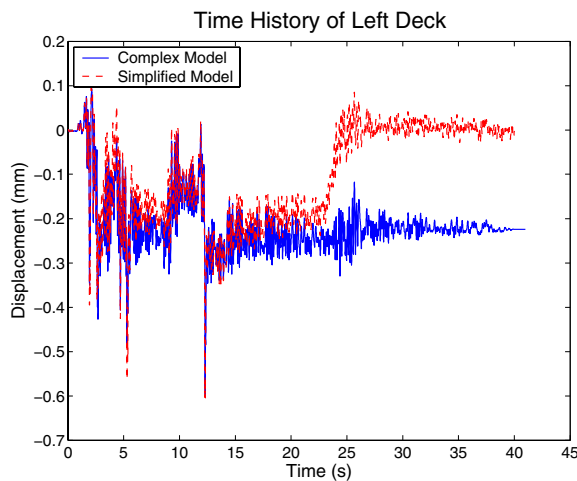


Figure 4.1: Time history of left span—complex model vs. simplified model

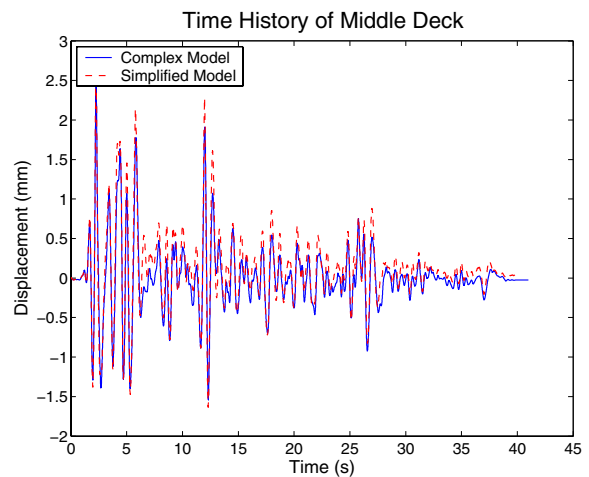


Figure 4.2: Time history of middle span—complex model vs. simplified model

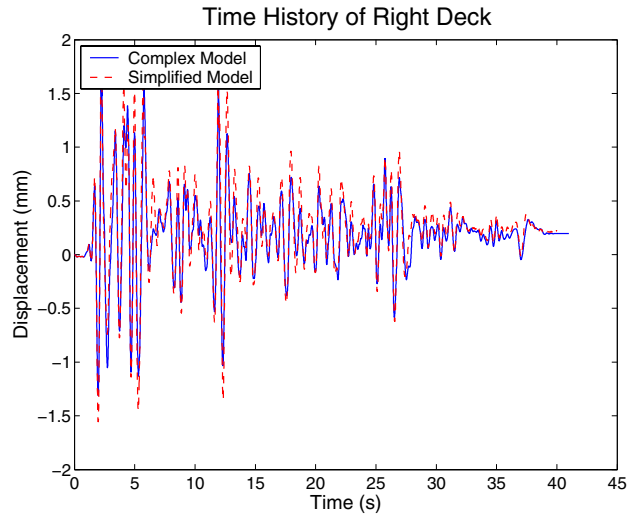
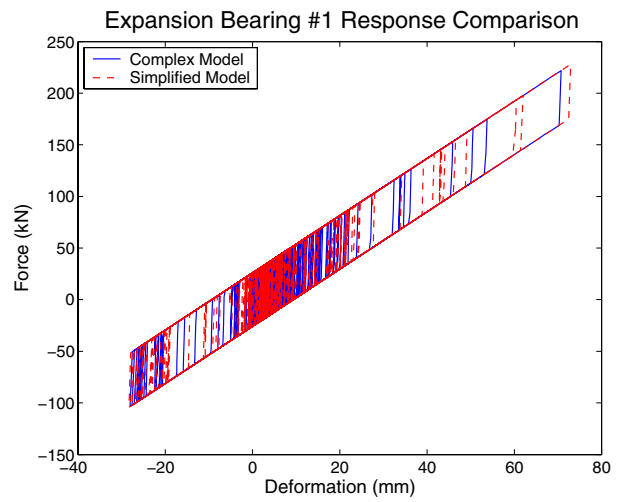
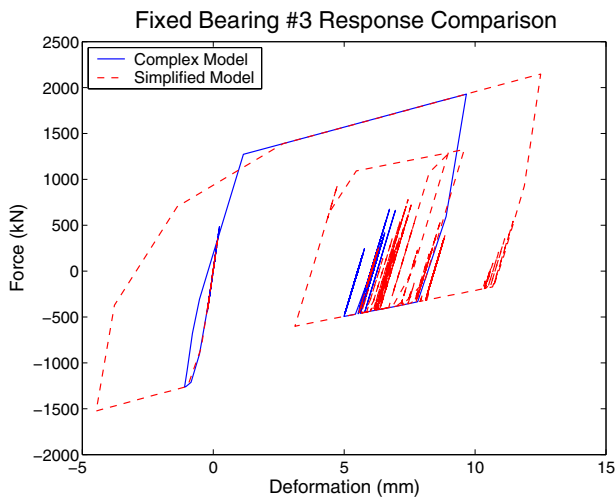
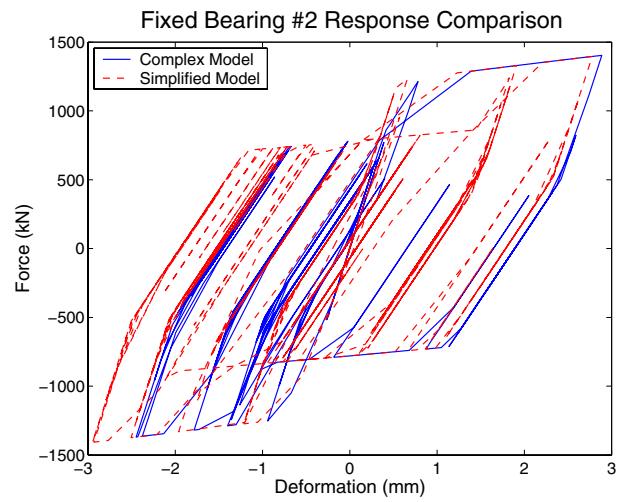
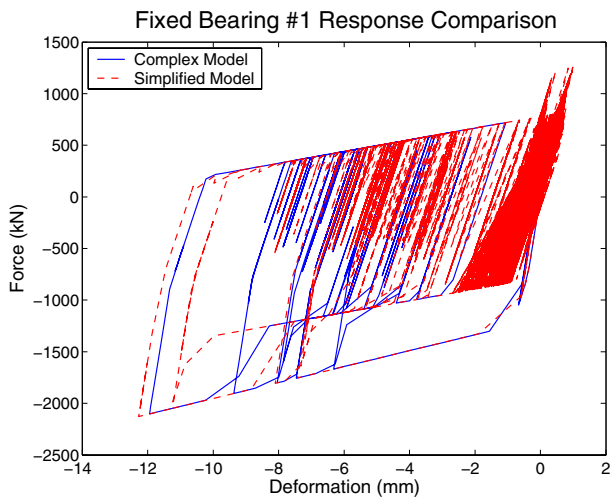


Figure 4.3: Time history of right span—complex model vs. simplified model



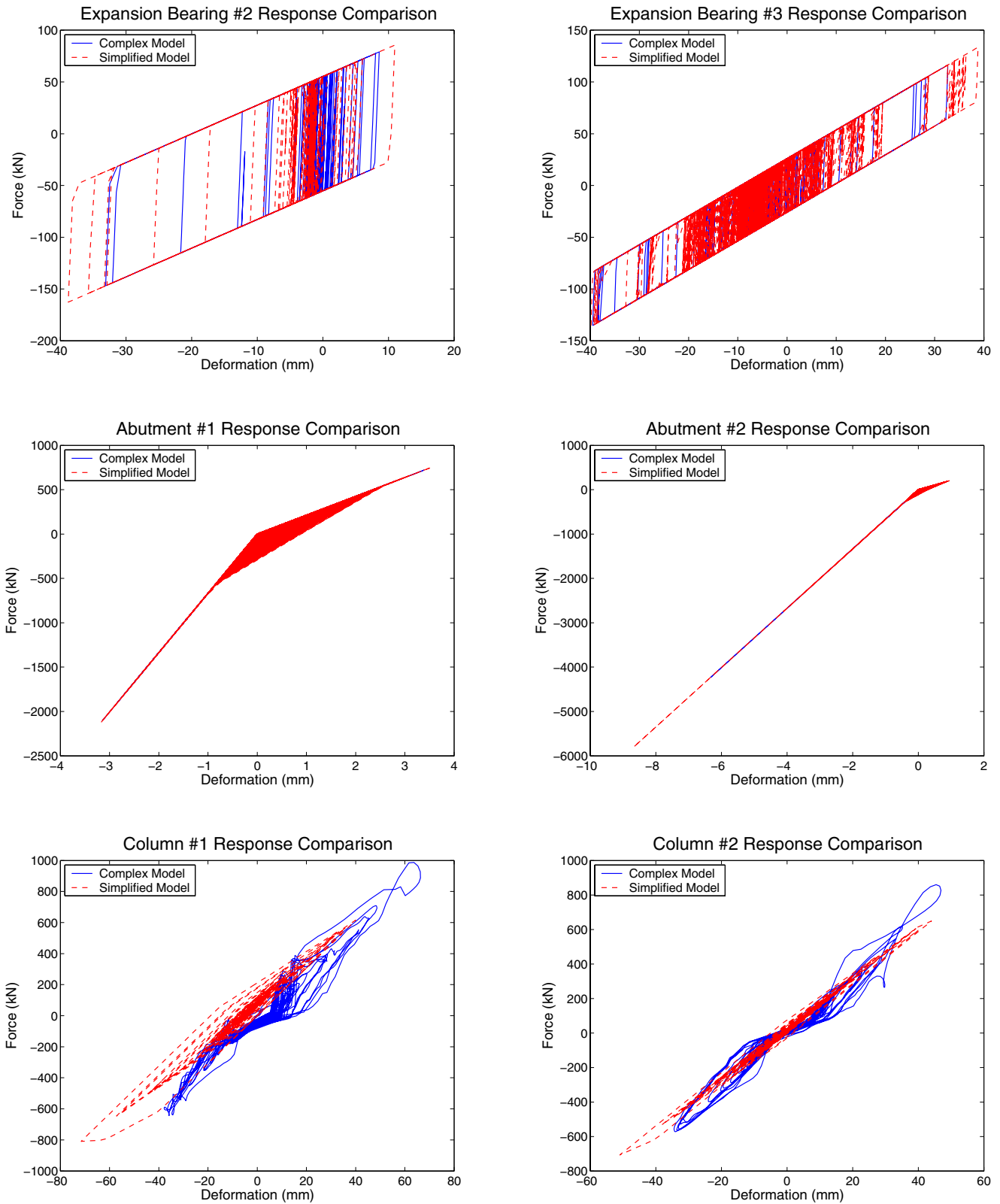


Figure 4.4: Comparison of all component responses—complex model vs. simplified model

Though some of the images may appear to serve no justice to the true behavior of one or both of the models, a closer inspection of these plots in MATLAB proves otherwise. Also, the most important behavior is that of the columns and the fixed bearings, so closer inspection of expansion bearings and abutments is only trivial.

Once more, the analysis proves to be unconvincing. Nowhere else to turn within the two compared models combined with the freedom to explore OpenSEES led to new ideas. These ideas soon became implemented in modifications for the simple and complex models. One idea was linearizing all components in both models. Another idea was removing the impact elements from both models. Still another idea was taking the replacement for the column-foundation system and simply inserting it into the original complex model. These ideas led to five new models, which, when added to the two models already in place, set up meaningful alternative model comparison:

1. Original complex model vs. original simplified model
2. Original complex model (impact elements removed) vs. original simplified model (impact elements removed)
3. Fully linearized complex model vs. fully linearized simplified model
4. Original complex model vs. replaced-column complex model

The goal was to run the same exact analysis, already performed on case 1, on cases 2, 3, and 4. A “winner” would be selected from these four cases. The two models from this “winner” would be used for fragility analysis and comparison. The factors that would determine the models of choice were closest proximity of periods, deck displacements, column responses, fixed bearing responses, and last but certainly not least, program run-times. The models were generated. The analyses for all four cases were performed, and the results are shown in Table 4.2.

Table 4.2: A summary of results of analysis and comparison for cases 1—4

Bridge Model Comparison								
	Simple vs. Complex		No Impact Elements		Fully Linearized		Column Replacement	
% Error (MD)								
Lt Deck	4.3		6.4		23.1		21.7	
Mid Deck	5.8		17.4		21.1		10.9	
Rt Deck	10.9		22.6		23.2		15.4	
FB1	9.5		9.9		30.5		21.8	
FB2	11.4		30.9		12.7		43.9	
FB3	57.4		12.8		23.3		61.4	
C1	57.6		17.4		22.2		12.7	
C2	24.0		22.4		23.5		17.4	
	Simple	Complex	Simple	Complex	Simple	Complex	Simple	Complex
Run Time (s)	18.5	581.4	16.9	564.5	8.3	34.7	24.1	571.2
Period (s)								
Mode 1	0.289	0.274	0.289	0.274	0.296	0.293	0.291	0.274
Mode 2	0.149	0.177	0.149	0.177	0.154	0.177	0.177	0.177
Mode 3	0.083	0.148	0.083	0.148	0.083	0.151	0.150	0.148
Mode 4	0.032	0.084	0.032	0.084	0.035	0.084	0.084	0.084
Mode 5	0.03	0.074	0.03	0.074	0.031	0.074	0.074	0.074

For every component, run time, or period, the “winner” is indicated. Ideally, one of the four cases would win all 10 categories. The first eight categories show the percent error of the simplified models for the maximum displacements (MD) of the eight listed components. Deck displacements and two of the fixed bearings favor the original model comparison while column displacements favor the column replacement comparison. The astonishingly low run times for the fully linearized models win that category, and with the exception of the fundamental period, column replacement wins period comparison. Considering this data, the most fitting models can be selected for fragility analysis.

Due to their lack of realism, the first two sets of models that can be eliminated are no impact elements and fully linearized. In no way could a bridge not have any impact elements, and saying that every component of the bridge had fully elastic behavior (which, incidentally, is what led to the fastest run times) stretches the original goal of this project too much. Though column replacement showed favorable comparisons, especially for periods, the original simplified vs. complex comparison had a better fundamental period comparison, more solid deck displacement data, a significantly better fixed bearing record, and a much simpler model generation. Thus, the comparison of the original models is selected from this analysis.

Although the time and effort spent on this portion of the project did not produce any permanent stronghold, they provided a great deal of reassured confidence in the original simplified model. This confidence would be necessary for fragility curve comparison. These curves are a result of behavior of the models after being subjected to certain ground motions and the next section will briefly discuss these ground motions.

PART V: THE GROUND MOTIONS

This project requires comparison of fragility curves that are generated using two different sets of synthetic ground motions. One set is known as the set of Wen and Wu ground motions and the other is the set of Hwang ground motions. Later, the impact that each of these sets had on the complex model, the simplified model, and the comparison of the two will be discussed in detail. At the present time, a few facts will be given on the suites themselves.

The Wen and Wu ground motions are developed for three sites of special interest: Memphis, Tennessee; Carbondale, Illinois; and St. Louis, Missouri. A large number of future events and ground motions are generated from which uniform hazard response spectra (UHRS) are obtained for each city for exceedance probabilities of 10%, 5%, and 2% in 50 years. Sixty Wen and Wu ground motions are used in this analysis, and they are broken down as follows: Each of the three cities of interest has 20 ground motions. These are broken down into two suites of ten—one for a 10% probability in 50 years and the other for a 2% probability in 50 years. These ground motions are for earthquakes which have magnitudes between 5.25 and 8.0; earthquakes with a magnitude less than 5 are not of interest in this study. For the 30 ground motions corresponding to the 10% probability, 21 of them are for a magnitude 5.25 to a magnitude 6.5 earthquake. For the 30 corresponding to the 2% probability, 26 are for the upper limit, 7.75 to 8.0. As the magnitude of an earthquake decreases, the chances of it occurring quickly become less.

To provide a more detailed description of Wen's and Wu's work, the ground motions for Memphis will be examined. For the suite of ten ground motions assigned to the 10% probability, magnitudes range between 5.3 and 8.0, with seven ranging between 6.0 and 6.8. Focal depths are as small as 2.1 km and as large as 25.6 km with half of them being less than 6.2 km. Epicentral distances are scattered everywhere between 29.6 km and 171 km. Peak ground acceleration (PGA), which will later become one of the parameters for fragility, ranges from 0.02 g to 2.0 g for this suite of ground motions. Finally, two plots are shown in Figure 5.2. The thick dashed line in both plots represents the mean response spectrum of this ground motion suite. In the top plot, the spectral acceleration (S_a) of all of the suite's ground motions is plotted. In the bottom plot, the thin solid line represents the median S_a , and the green hatched area covers most other ground motions, ranging from the 16th to the 84th percentile. It should be noted that these are ground motions for a representative soil profile, not for bedrock, which has its own response spectra records, and that a tremendous amount of uncertainty exists for soil and seismic parameters in Mid-America.

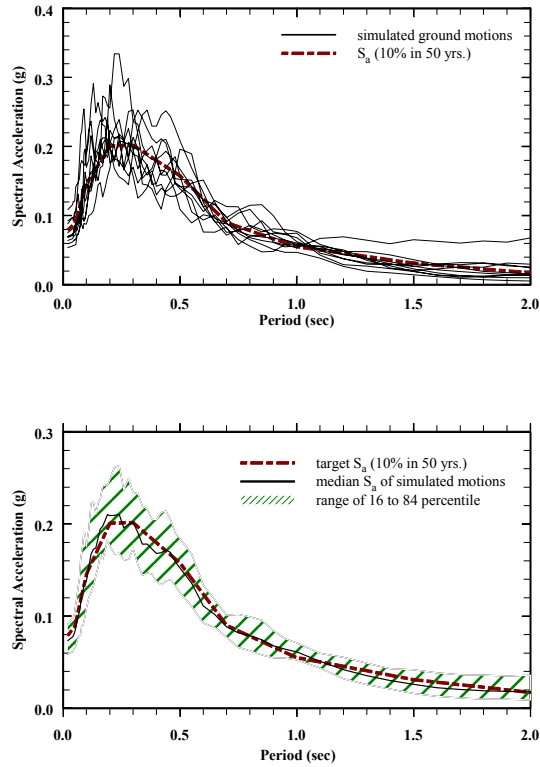


Figure 5.2: S_a and simulated ground motions for the 10% probability ground motion suite. This is for a representative soil profile; Memphis, Tennessee.

The second set of ground motions utilized in this report is the set of Hwang ground motions. This synthetic suite has 100 ground motion records, consumed by uncertainty just as the Wen and Wu records are. These ground motions are for earthquakes with magnitudes that span 6.0 to 8.0. Their epicentral distances only vary from 40 to 60 km. The PGA for these records ranges from 0.07 g to 0.51 g. Figure 5.3 shows a mean response spectrum very similar to that of Figure 5.2.

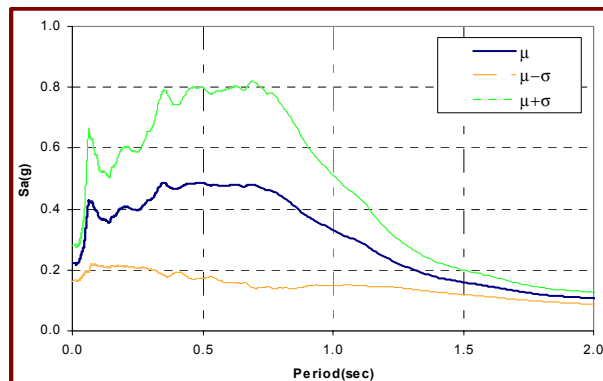


Figure 5.3: Mean response spectrum + or - one standard deviation for the Hwang ground motions.

This concludes the introduction to both the Wen and Wu and the Hwang ground motions. The next section discusses the fragility analysis that results when they are applied to the previously established bridge models.

PART VI: FRAGILITY ANALYSIS

Four major obstacles stand in the way of the two models being converted to their corresponding fragility curves. These obstacles take the form of two OpenSEES files and two MATLAB M-files, which are outlined as follows:

1. Create an M-file which can read in any number of steel and concrete strength values (f_y and f'_c) and print out the corresponding load-displacement values in the envelope.
2. Modify the simplified model to read in these values before running several ground motions as opposed to running a preliminary analysis with the original envelope values.
3. Set up an OpenSEES file which sources the model in Step 2 and runs the ground motions.
4. Set up an M-file which uses the response data and plots the fragility curves.

Step 1 is the key to this process. Because complete knowledge of f_y or f'_c of every product is never certain, a major source of uncertainty enters the picture. Therefore, randomizing these values in the analysis is both helpful and mandatory. The resulting set of load-displacement values computed by the M-file, now used for the replaced column's material, also incorporate uncertainty as each set corresponds to a different ground motion.

Earlier, a fragility curve was described as a display of the conditional probability that structural demand (structural response) caused by various levels of ground shaking exceeds structural capacity defined by a damage state. These two parameters must be set up. Median structural capacity corresponds to either curvature or displacement ductility ratios. Since every analysis is based on load-displacement in this project as opposed to moment-curvature, the displacement ductility ratios must be used in the MATLAB file. Each ratio, along with its corresponding limit state, is listed in Table 6.1.

Table 6.1: Curvature and displacement ductility ratios for all damage states

Limit State	Curvature Ductility	Displacement Ductility
Slight	1.0	1.0
Moderate	1.2	1.12
Extensive	1.76	1.39
Complete	4.76	2.41

Structural demand as a function of PGA is found by performing a regression analysis of the previously simulated response data for all components. Figure 6.1 is an example of this type of plot, where, once again, many uncertainties become quantified. It is the regression analysis for one column subject to the Wen and Wu ground motions.

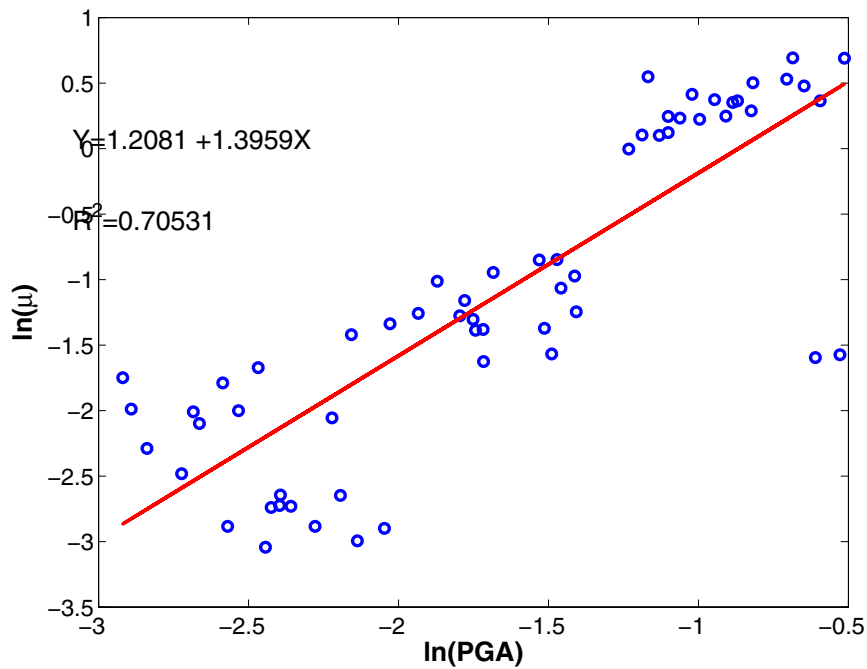


Figure 6.1: Regression plot for column—Wen and Wu analysis

There are 60 data points, corresponding with the 60 ground motions. The fact that R^2 equals only about 0.7 is not a concern; it simply means that there is more variation in the randomizing.

The main tool, however, for understanding the fragility curve's probability statement $P[DS | PGA=g]$, or more simply, $P[D>C]$, is the following lognormal function:

$$p_f = \Phi \left[\frac{\ln(S_d / S_c)}{\sqrt{\beta_d^2 + \beta_c^2}} \right] \quad (1)$$

Here, ϕ indicates the normalizing of the function, S_d and S_c are the median values for structural demand and capacity, respectively, and β_d and β_c are the logarithmic standard deviations. Figures 6.2 and 6.3 display the curves for the two suites of ground motions used in this project.

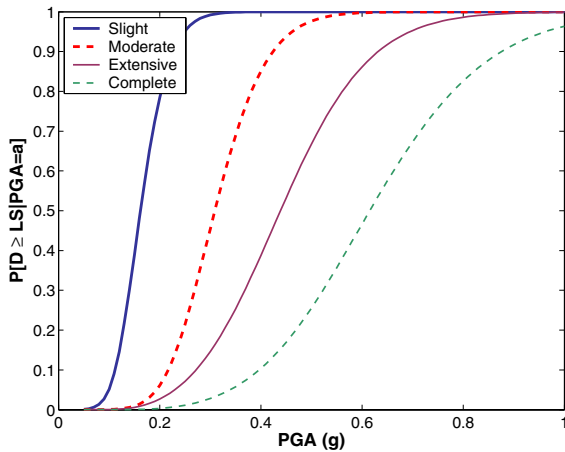


Figure 6.2: Fragility curve for simplified model; subject to the Wen and Wu ground motions

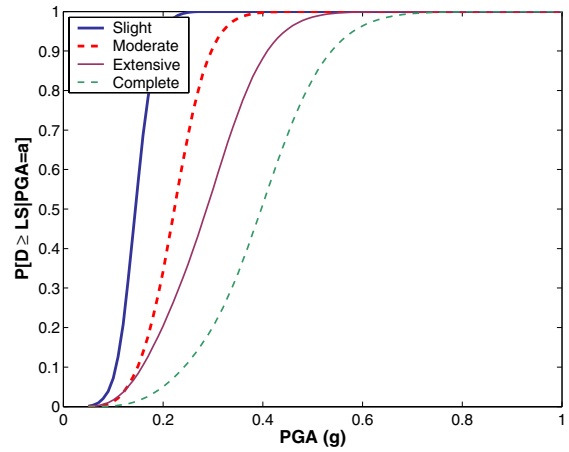


Figure 6.3: Fragility curve for simplified model; subject to Hwang ground motions

Now that these fragility curves have been developed for the simplified model, the ultimate goal of the project, comparing fragility curves of the complex and simplified models with respect to the same suite of ground motions, can be achieved. These curves can be regenerated (in Excel, for example) and then placed on top of one another so that they can be easily compared. This comparison is shown in Figures 6.4 and 6.5

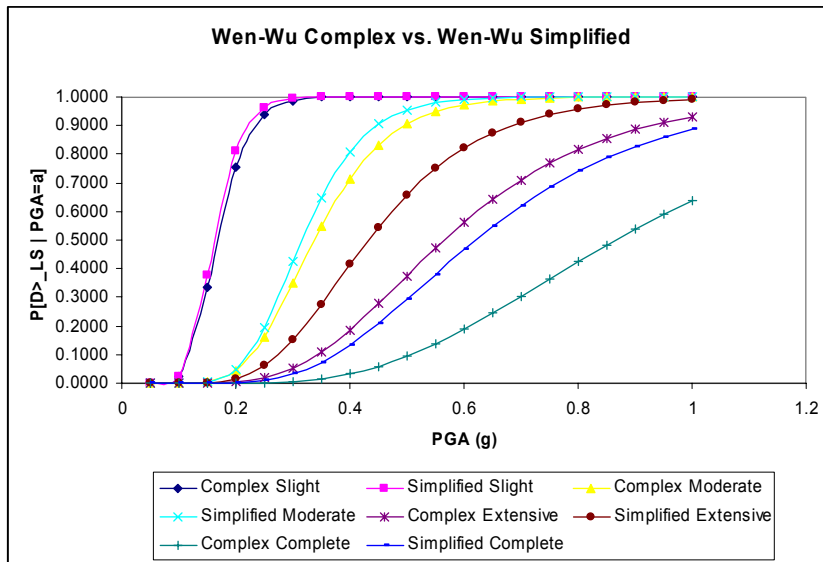


Figure 6.4: Fragility curve comparison for models; subject to Wen and Wu ground motions

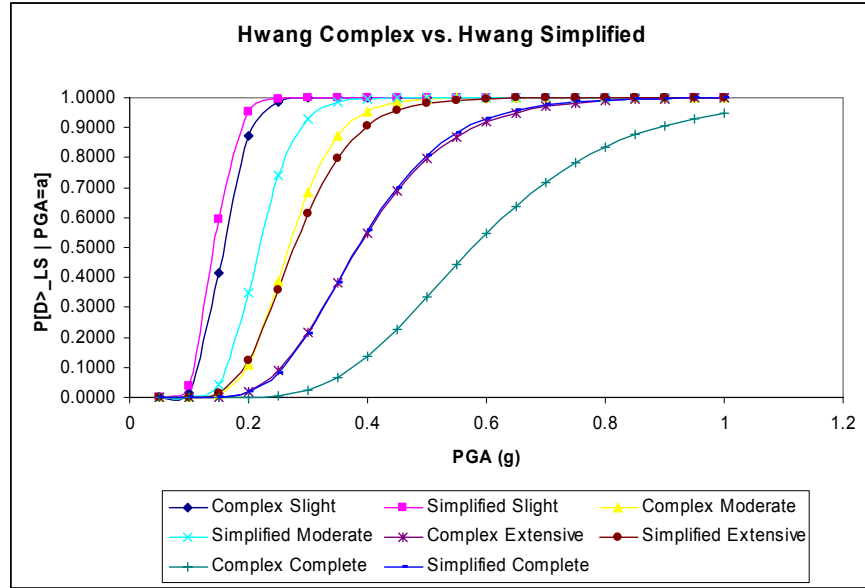


Figure 6.5: Fragility curve comparison for models; subject to Hwang ground motions

The eye can easily make a first-glance judgment about how much variation there is in the curves. Since numbers are kindest to pure analysis, Table 6.2 provides the source for the generation of all four fragility curves.

Table 6.2: Important values for fragility curve generation. The median and dispersion are most significant.

	Complex				Complex		
	Median(g)	Dispersion	R^2		Median(g)	Dispersion	R^2
<i>Slight</i>	0.1674874	0.2595331	0.9918756	<i>Slight</i>	0.1571418	0.2114985	0.9855885
<i>Moderate</i>	0.3376441	0.3010439	0.9796419	<i>Moderate</i>	0.2674683	0.2373571	0.9703885
<i>Extensive</i>	0.5657378	0.3858200	0.9787766	<i>Extensive</i>	0.3845806	0.3184731	0.9537206
<i>Complete</i>	0.866482	0.4158951	0.9813502	<i>Complete</i>	0.5775242	0.3356190	0.9568950
	Simplified				Simplified		
	Median(g)	Dispersion	R^2		Median(g)	Dispersion	R^2
<i>Slight</i>	0.1615871	0.2427967	0.9900914	<i>Slight</i>	0.1428268	0.2004375	0.9840188
<i>Moderate</i>	0.3155859	0.2716675	0.9757518	<i>Moderate</i>	0.2174059	0.2180478	0.9716474
<i>Extensive</i>	0.4326073	0.3561636	0.9752815	<i>Extensive</i>	0.2765585	0.2812663	0.9486910
<i>Complete</i>	0.6212084	0.3934488	0.9806103	<i>Complete</i>	0.3835366	0.3060247	0.9454935

It can be seen that, unfortunately, median g values between the complex and simplified models vary in the slight damage state, and they only continue to digress with more severe damage states. To quantify this digression, a mean of the probabilities produced in Excel for 0.05-PGA increments ($0.05 < PGA < 1$) is calculated. This is done for every damage state. Then, a percent error of simplified to complex is calculated for all damage states. The results of this brief analysis are shown in Table 6.3.

Table 6.3: Numerical comparison for fragility curves—both suites of ground motions

PROBABILITY AVERAGES (0.05<PGA<1; 0.05-s increments)						
Wen-Wu Complex vs. Wen-Wu Simplified						
PROBABILITY AVERAGES (0.05<PGA<1; 0.05-s increments)						
		<i>Slight</i>			<i>Moderate</i>	
	Complex	Simplified	% Error	Complex	Simplified	% Error
	0.8518	0.8586	0.8	0.6717	0.6976	3.7
		<i>Extensive</i>			<i>Complete</i>	
	Complex	Simplified	% Error	Complex	Simplified	% Error
	0.4279	0.5651	24.3	0.2053	0.3769	45.5
Hwang Complex vs. Hwang Simplified						
		<i>Slight</i>			<i>Moderate</i>	
	Complex	Simplified	% Error	Complex	Simplified	% Error
	0.8643	0.8793	1.7	0.7499	0.8024	6.5
		<i>Extensive</i>			<i>Complete</i>	
	Complex	Simplified	% Error	Complex	Simplified	% Error
	0.6205	0.7373	15.8	0.4210	0.6231	32.4

The one astonishing fact about this analysis that has not yet been presented is the disparity between run times. In Section IV, a preliminary analysis was performed to analyze periods and component responses. For this analysis, run times were recorded as 9 minutes, 41.4 seconds for the complex model and 18.5 seconds for the simplified model. As these two models have now been subjected to entire suites of ground motions, the extreme nature of program run times has been magnified. For the simplified model, the time used for OpenSEES to run the corresponding ground motions and for MATLAB to complete the regression analysis and the fragility curve plots is near 45 minutes. When the complex model is subjected to the same process, a robust eight hours are consumed. This is true for both the Wen and Wu and the Hwang ground motions.

For now, the fragility analysis is complete, and the final segment of the report summarizes what the results mean to the scope of DS-7b and to society.

PART VII: CONCLUSIONS

The subsequent list highlights the project's developments from the introductory stages to the most recent analysis. The numeral at the end of each line indicates the location of the line's contents in the report.

1. Understanding the scope of DS-7b and the potential benefits of the project's prescribed goals (I)
2. Understanding the complex model's generation (II)
3. Simplifying the complex model to include five degrees of freedom and a non-linear spring to replace the column-foundation system in place (III)
4. Comparing the complex and simplified models: inspecting deck displacements, component responses, periods, and run-times (IV)
5. Investigating other types of models to see if they showed more similarities than the two original models showed (IV)
6. Developing fragility curves for the chosen simplified model (VI)
7. Comparing the fragility behavior of the complex and simplified models and analyzing this comparison (VI)

This list only covers what has been discussed thus far. To complete the list and the project, the final item would be drawing conclusions based on the fragility analysis comparison, offering any possible future recommendations.

The results of this project did not fully meet the predictions, which stated that a simplified bridge model could be developed to reduce model generation time and analysis run time while still showing behavior very similar to a complex bridge model's behavior. Since the number of command lines for model generation was reduced from 309 to 61, the first prediction proved to be correct. Because the length of the preliminary analysis dropped from over nine minutes to under thirty seconds and the eight-hour fragility analysis period decreased to less than one hour, the second prediction was true. The Wen and Wu analysis and Hwang analysis resulted in percent errors of 45.5% and 32.4%, respectively, for the fragility curve of the most severe damage state, the state of stakeholders' largest interest. Unfortunately, since this behavior does not qualify as "very similar," the third prediction becomes somewhat inaccurate.

How inaccurate that prediction becomes, however, is completely up to the stakeholder. Graphically, the fragility behavior of the two models appears to be fairly similar in the slight and moderate damage states, especially for the Wen and Wu ground motions. Analytically, the percent errors for both ground motions are within 4% for slight damage and within 7% for moderate damage. Either way, model simplification has done its job for these two damage states, and it has failed to produce similar behavior in the extensive and complete damage states. For illustration of this disparity, the bridge will be subjected to two potential earthquakes. They will correspond to an identical PGA. The first will result from the Wen and Wu ground motions, and the second will be produced from the Hwang ground motions.

Earthquake #1, according to Wen and Wu, has a PGA of 0.5 g. This concerns the residents of the 11 mid-America states. The level of concern can be quantified by the fragility curve. Immediately, it can be seen this MSSS bridge will undoubtedly suffer slight damage, and there is very little doubt that it will suffer moderate damage. Realistically speaking, however, no lives will be lost because of a slightly or moderately damaged bridge, and repair costs won't become a factor until this bridge suffers extensive damage. The stakeholder can once again breathe a sigh of relief because there is only a 38% that this earthquake of 0.5-PGA will cause extensive damage. Or is he much more concerned because there is a 65% chance that the earthquake will cause extensive damage? The difference in the fragility curves has caused a problem. Finally, the residents think of the worst-case scenario, bridge collapse. One curve tells them that there is only a 10% chance of this occurrence while the other is 30% confident the bridge will suffer this complete damage. Each time, the lower probability was a product of the simplified model. All of a sudden, everyone is skeptical about this newly-developed model.

Earthquake #2, according to Hwang, also has a PGA of 0.5 g, and the potential for it equally concerns the residents of the 11 mid-America states. Once again, the fragility curve becomes a significant tool. This time, the stakeholder should be prepared for moderate damage at best because all curves show at or very near 100% chance for both the slight and moderate damage states. Furthermore, with the simplified and complex models showing 97% and 79%, respectively, for extensive damage, he has several areas of concern. But concern is apparently the highest for the average person traveling across this bridge because he knows there is an 80% chance that there will be some form of collapse involved. Or should he relax because the complex model believes this 80% chance is only 34%?

The one inescapable, recurring theme from this realistic example is that the simplified model is much more conservative, especially in the extensive and complete damage states. The reason for this inconsistency is the abundance of nonlinearity in the complex model. Since the complete damage state is the level that mostly likely leads to loss of life, to which no repair cost can truly be equated, the OpenSEES simplified bridge model is not an effective tool. The risk of inaccurate predictions is too high in spite of the many areas of quantified uncertainties in the project. Yes, the simplified model saved an unprecedented eight hours of analysis time, but if a monetary value cannot be placed on human life, then neither can an increment of time.

The major source of optimism for model simplification, however, is that the remaining set of generated models not exactly like the original simplified model, which proved to be a disappointment for the purpose of fragility analysis, still exists. The focus of this set, which includes fully linearized (complex and simple) and impact-element-removed (complex and simple) models, is still the model which featured no changes except the hysteretic material being inserted for the column. This model would have to go through the same preparation for fragility analysis that the original simplified model endured. The hope would be that waiting eight hours for fragility analysis would not enter the picture. The chance for this model to accomplish the project's goals of saving time and being accurate while fulfilling the MAE Center's goals of saving lives and money would be worth taking.

ACKNOWLEDGEMENTS

The work described in this report was conducted as part of the MAE Center's project DS-7b, led by Professor Reginald DesRoches and graduate students Bryant Nielson and Jamie Padgett at the Georgia Institute of Technology. A special acknowledgement goes to Mr. Nielson for attention to the specific details demanded by this report. Any statements, results, or conclusions do not necessarily reflect the views of Georgia Tech, the MAE Center, or the National Science Foundation of the United States.

REFERENCES

- Choi, E. (2002). *Seismic Analysis and Retrofit of Mid-America Bridges*. Thesis, Georgia Institute of Technology, Atlanta, GA.
- Choi, E., DesRoches, R., and Nielson, B. (2004). "Seismic Fragility of Typical Bridges in Moderate Seismic Zones," *Engineering Structures*, 25(2), 187-199.
- Hwang, H., Liu, J. B., and Chiu, Y. (2000). *Seismic Fragility Analysis of Highway Bridges*. Technical Report MAEC RR-4 Project, Mid-America Earthquake Center, Memphis, TN.
- Mazzoni, S., McKenna, F., Scott, M., Fenves, G., Jeremic, B. *Open System for Earthquake Engineering Simulation*. <http://peer.berkeley.edu/~silvia/OpenSees/manual/html/>.
- Pacific Earthquake Engineering Research Center. *Open System for Earthquake Engineering Simulation*. <http://opensees.berkeley.edu/>.
- Wen, Y. K., and Wu, C. L. (2001). "Uniform Hazard Ground Motions for Mid-America Cities," *Earthquake Spectra*, 17(2), 359-384.

**PERFORMANCE OF EXISTING REINFORCED CONCRETE COLUMNS UNDER
BIDIRECTIONAL SHEAR AND AXIAL LOADING**

Laura M. Flores

University of California, San Diego

REU Institution: University of California, Berkeley

REU Advisor: Professor Jack P. Moehle

ABSTRACT

Many existing reinforced concrete structures were designed before the introduction of modern seismic code and are thus vulnerable to collapse in the event of an earthquake. It is often more economically feasible to retrofit these structural components than to completely replace them. In order to strengthen these susceptible reinforced concrete structures against seismic loading, it is important to understand the progression of damage and mechanisms causing collapse in such structures under both gravity and seismic loads. Large-scale shake table testing and verification studies are currently being conducted at UC Berkeley-PEER to aid in the development of an *OpenSees* analytical model which will simulate and predict the hysteretic response of existing reinforced concrete structures in future verification studies.

The purpose of this study was to produce column hysteretic data used to calibrate the *OpenSees* analytical model. Empirical capacity models were used to predict the hysteretic response of shear-critical reinforced concrete columns under gravity and seismic loading; in particular, shear failure and axial load collapse of these columns were closely examined. Based on pre-seismic ACI code, a column cross sectional analysis was completed to determine the undamaged capacity of the column. A one-third scale model of the column was fabricated and an experimental setup allowing bi-directional loading (for simulation of seismic and gravity loads) was designed and constructed. Column specimens were then subjected to quasi-static testing and the measured column hysteretic response was compared to that predicted by empirical capacity models which form the basis of the *OpenSees* analytical model. .

1 Introduction

1.1 BACKGROUND

Existing reinforced concrete structures designed before the introduction of modern seismic code in the early 1970's are vulnerable to damage and collapse during an earthquake. Prior to the FEMA124 establishment of performance-based earthquake design specifications, reinforced concrete structures utilized in bridges and buildings were designed in accordance with AASHTO code which only required that reinforced concrete structures sustain a single hazard or maximum loading event. Often, these requirements resulted in the design of reinforced concrete columns with minimal transverse reinforcement (i.e. column confinement), highly spaced stirrups and/or low longitudinal reinforcement ratios. Thus, such structures inevitably experience significant column buckling, undergo excessive shear drift and degradation of shear and axial load capacity which pose a substantial danger to building occupants or bridge pedestrians supported by such columns.

Thus, it is vital that reinforced concrete structures, especially life-safety structures not designed in accordance to modern performance-based earthquake code, be retrofitted to sustain seismic loading. It is often more economically feasible to retrofit vulnerable existing reinforced concrete structures than to completely replace them. However, to properly strengthen these vulnerable reinforced concrete structures against complex seismic loading patterns, it is imperative to first understand the progression of damage and mechanisms causing collapse in reinforced concrete columns and frames.

1.2 PREVIOUS RESEARCH

Experimental research and post-earthquake investigations conducted in the past have produced numerous findings about the behavior of reinforced concrete columns under gravity and seismic load. Elwood and Moehle (2003) give a brief overview of experimental results based on various shear and axial loading tests performed on reinforced concrete columns and/or frames which form the foundation of this research. From the results, it was suggested that a loss of axial load capacity in a reinforced concrete column does not always immediately occur after a loss of shear capacity (Elwood and Moehle, 2003; Sezen, 2002). Also, it was observed that the lateral displacement or drift of a reinforced concrete column at axial failure is dependent upon and directly proportional to the spacing of transverse reinforcement and the axial stress developed within the column.

Elwood and Moehle state that from many pseudo-static tests that examined axial capacity in shear-damaged columns (Yoshimura and Yamanaka, 2000; Nakamura and Yoshimura, 2002; Tasai, 1999; Tasai, 2000; Kato and Ohnishi, 2002; Kabeyasawa et al., 2002), axial failure occurred when the columns lost all shear capacity. Further, it was noted that the lateral drift experienced by the column at axial failure was dependent upon and inversely proportional to the amount of axial load exerted on the column. From the research findings of Tasai (2000), Elwood

and Moehle note that the total lateral drift experienced by a column was dependent upon and inversely proportional to the column's residual axial capacity. Lastly, from the tests conducted by Minowa, et al. (1995), Elwood and Moehle stated that reinforced concrete columns with closer transverse reinforcement spacing sustained gravity loads at larger lateral displacements after shear failure than those columns having wider stirrup spacing.

1.3 OBJECTIVES AND SCOPE

Since the process by which shear failure degrades the residual axial capacity of a column is not well understood in columns designed prior to the introduction of modern seismic code, it is my objective to conduct such research. Test results that have been obtained for reinforced concrete columns suggest certain relationships between structural parameters; such relationships have been used to develop predictive hysteretic response and drift models and subsequently, analytical models by which to use in future verification studies of large scale structural testing. First, however, the ability of the *OpenSees* analytical model to accurately predict the interaction between the shear and axial capacity of the column must first be established; a verification study to predict the hysteretic response of a shear-critical reinforced concrete column under lateral and gravity load will be the focus of this study.

This study is limited to reinforced concrete columns that can be characterized by a shear-failure mode. Further, all hysteretic response and drift analysis is carried out assuming that the reinforced concrete column specimen behaves as a two-dimensional column under a cyclic, unidirectional lateral loading and constant gravity load; it is also assumed that throughout the experimental test program, the column base behaves elastically.

1.4 ORGANIZATION

This report is organized in the following manner: presentation of predictive capacity models; fabrication of column test specimens and experimental setup; experimental test program; presentation of test results; validation study between test results and analytical model predictions.

2 Linear-Elastic Response of RC Column

2.1 CAPACITY MODELS

A shear-critical reinforced concrete column is a column that fails in shear prior to yielding in flexure; thus, a shear-critical column will tend to exhibit a brittle mode of failure rather than the preferred ductile model of failure. Since such a column can fail suddenly when the shear load demand on the column exceeds its shear capacity, the design of a shear-critical reinforced concrete column is governed by the shear loading that must be sustained by the column.

In order to assess the maximum shear loading that will be applied to the column, one must take into account the moment at the base-column joint induced by the lateral loading when designing the column. Further, since reinforced concrete columns primarily act as supports to other structures, it is critical that such columns be designed to sustain gravity loads, in addition to seismic-induced lateral loading.

2.1.1 Axial Load

The axial load capacity of a reinforced concrete column depends on the axial load capacity of the longitudinal reinforcement, as well as the axial capacity carried by the concrete. According to MacGregor (1998) and ACI Code, the following equation is used to assess the maximum axial load capacity, P_N of a reinforced concrete column:

$$P_N = 0.85f_c'(A_G - A_{SL}) + f_{YL}A_{SL} \quad (2.1)$$

where the first term, $0.85f_c'(A_G - A_{SL})$ represents the axial capacity carried by the concrete and the second term, $f_{YL}A_{SL}$ represents the axial capacity carried by the longitudinal reinforcement. f_c' is the specified 28-day compressive strength of concrete (ksi), f_{YL} is the yield strength of the longitudinal reinforcement (ksi), A_G is the gross area of the column cross section and A_{SL} is the area of the longitudinal reinforcement. The maximum axial load capacity in a column is achieved when no flexural moment is induced in a column.

2.1.2 Flexure

The moment or flexural capacity of a reinforced concrete column depends on the cross section of the column. Given the cross section of the shear-critical column considered in this project, the maximum moment capacity of the column can be assessed by summing the internal forces from the longitudinal reinforcement and concrete about the centroid of the column.

The following equation is derived from Figure 2.1 and is used to evaluate the maximum moment capacity of a reinforced concrete column, M_n :

$$M_n = T_{S3}[(h/2) - d_{S3}] - C_c[(h/2) - (a/2)] + T_{S1}[d_{S1} - (h/2)] \quad (2.2)$$

where T_{Si} is the internal tensile force provided by the longitudinal reinforcement i , C_c is the internal compressive force of the concrete, h is cross section depth, a is depth of stress block, and d_{Si} is the distance from extreme compression fiber to reinforcement layer i . The maximum moment capacity of a column can only be reached if there are no axial loads applied to the column.

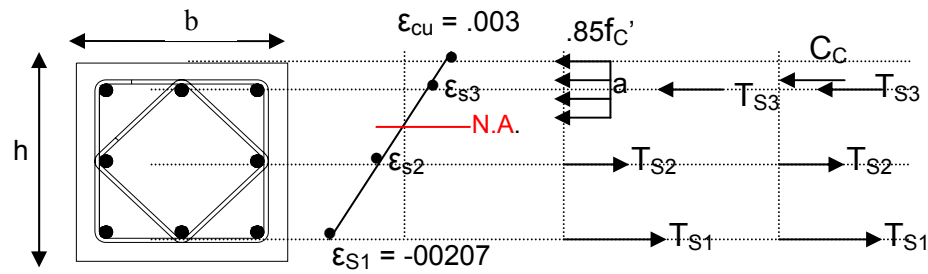


Figure 2.1: Cross section analysis used to compute the moment capacity of a reinforced concrete column.

2.1.3 Shear

The total shear capacity of a reinforced concrete column depends on the shear capacity of the concrete, V_C and the shear capacity carried by the transverse reinforcement, V_{ST} . According to MacGregor (1998) and ACI Code, the following equation is used to assess the maximum shear capacity, V_N of a reinforced concrete column subjected to combined shear, moment and axial compression loading:

$$V_N = V_C + V_{ST} = 2[1 + (P/[2000A_G])] \sqrt{f'_c} b_w d + (A_{ST} f_{YT} d) / s \quad (2.3)$$

where P is the applied axial load, b_w is the width of the column cross section, s is the transverse reinforcement spacing, d is the distance from extreme compression fiber to farthest tensile reinforcement, A_{ST} is the area of the transverse reinforcement, f_{YT} is the yield strength of the transverse reinforcement.

2.2 INTERACTION DIAGRAM

The load capacity of a reinforced concrete column subjected to both flexural and axial loading can be assessed from an interaction diagram; such a diagram shows the relationship between the axial load capacity and moment capacity of a reinforced concrete column prior to yielding of the longitudinal reinforcement. If the moment and axial load capacity of a reinforced concrete column is evaluated for different tensile yield strains, an interaction diagram can be plotted. Figure 2.1 shows an interaction diagram for the column cross sections considered in this project.

2.3 YIELD DISPLACEMENT

The lateral displacement under which the longitudinal reinforcement in the column first yields can be evaluated as a sum of three deformation components. The three deformation components that contribute to the overall yield displacement of the column are displacement due to flexure, bar (bond) slip and shear.

$$\Delta_{Y \text{ calc}} = \Delta_{FL} + \Delta_{SL} + \Delta_{SH} \quad (2.4)$$

2.3.1 Flexure Deformation

For a column that is fixed against rotation at both ends, flexural deformation results when a moment load is induced in the column and a lateral displacement occurs at the ends since there are no end restraints against horizontal displacement. Figure 2.2 exhibits this concept.

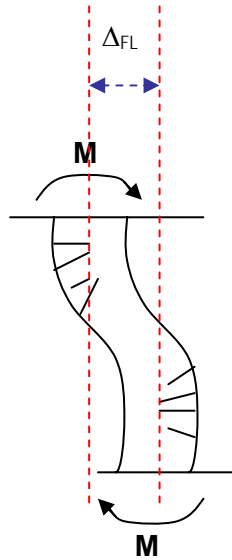


Figure 2.2: Flexural deformation in a column.

The following empirical equation, presented in Elwood and Moehle (2003), is used to estimate the lateral displacement due to flexure before yielding of the longitudinal reinforcement occurs:

$$\Delta_{FL} = L^2 \Phi_Y / 6 \quad (2.5)$$

where L is the column length and Φ_Y is the column curvature at yielding of the longitudinal reinforcement.

2.3.2 Bar (Bond) Slip

For a reinforced concrete column subjected to lateral load, slip of the longitudinal reinforcement within the anchor block of the column can occur; an elongation of the longitudinal reinforcement at the column-base joint results which then produces an additional lateral displacement in addition to the those caused by flexure. Figure 2.3 exhibits this concept.

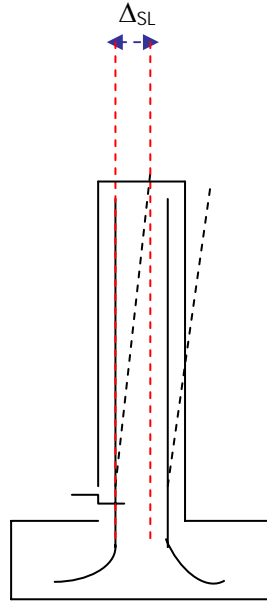


Figure 2.3: Bar (bond) slip in a column.

The following equation, derived in Elwood and Moehle (2003), is used to estimate the lateral displacement due to bar or bond slip before yielding of the longitudinal reinforcement occurs:

$$\Delta_{SL} = Ld_B f_{YL} \Phi_Y / 8u \quad (2.6)$$

where d_B is the diameter of the longitudinal reinforcement and $u = 6\sqrt{f_c}$ (psi unit) is the bond stress between the longitudinal reinforcement and the column footing.

2.3.3 Shear

For a column that is fixed against rotation at both ends, shear deformation results when lateral loading produces shear stresses at the column ends resulting in displacement. This concept is exhibited in Figure 2.4.

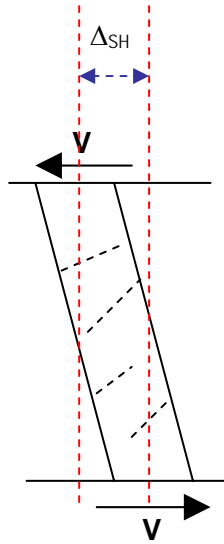


Figure 2.4: Shear deformation in a column.

The following empirical equation, presented in Elwood and Moehle (2003), is used to estimate the lateral displacement due to shear before yielding of the longitudinal reinforcement occurs:

$$\Delta_{SH} = 2M_Y / GA_V \quad (2.7)$$

where M_Y is the column moment at yielding of the longitudinal reinforcement, G is the shear modulus assuming the column is homogeneous in material, $A_V = 5/6 A_G$ is the shear area of the column cross section.

3 Inelastic Response of RC Column

3.1 INTRODUCTION

After the longitudinal reinforcement in a shear-critical reinforced concrete column yields, the column continues to undergo further lateral drift (i.e. plastic deformation) until the shear demand on the column exceeds its shear capacity. When the column's shear capacity is exceeded, shear failure and a loss of axial load capacity occurs.

3.2 MOMENT CURVATURE RESPONSE

While an interaction diagram is useful to assess the interaction between a reinforced concrete column's axial and moment capacity prior to yielding of the longitudinal reinforcement, another model is required to evaluate the degradation of shear capacity and subsequent loss of axial load capacity in a column, after yielding of the longitudinal reinforcement and at increasing lateral drifts. A moment curvature analysis relates the moment and curvature of a reinforced concrete

column at drifts beyond yield and thus, is used to evaluate the plastic response of a reinforced concrete column under shear and axial loading.

Since the shear-critical reinforced concrete column specimens tested in this project are to be loaded beyond shear failure, a moment curvature analysis will be more useful in this project for the analysis of the column's drift response to shear and axial loading. The analytical finite element program *OpenSees* is initially used to conduct a cross section analysis of the column specimens considered and a moment curvature response is then developed for the columns; utilizing Equations 2.4 to 2.7, the displacement at which yielding of the longitudinal reinforcement, shear failure and axial load failure occurs is then computed.

4 Shear Drift Capacity Model

4.1 INTRODUCTION

Conventional force-based drift capacity models (i.e. shear strength model) used to model the plastic behavior of shear-loaded columns are usually not appropriate when used to evaluate the drift of columns at shear failure since the force demand on a column remains constant after yielding while the displacement experienced by the column does not. As stipulated by Elwood and Moehle (2003), a displacement-based model is more useful when computing drift at shear failure. Thus, Elwood and Moehle (2003) develop an empirical shear drift capacity model that represents the shear strength degradation of a shear-critical reinforced concrete column and is also valid to access lateral displacement or drift beyond shear failure.

4.2 EXPERIMENTAL DATABASE

The empirical shear drift capacity model proposed by Elwood and Moehle (2003) is based on data from 40 prior (unidirectional loaded) tests conducted on shear-critical reinforced concrete columns and thus, the model is only valid to assess column drift behavior beyond yielding for those shear-critical columns with properties within those specified in the database. The shear-critical column specimens considered in this project were checked against the properties of those tested columns in the database and are found to be similar. Thus, utilizing the empirical drift capacity model to assess drift at shear failure of my specimens is valid.

4.3 DISPLACEMENT-BASED EMPIRICAL DRIFT CAPACITY MODEL

The empirical drift capacity model developed by Elwood and Moehle (2003) for reinforced concrete columns differs from earlier models since it is based, not on the performance of columns designed in accordance to modern seismic code, but rather, on older columns which fail in shear prior to the occurrence of flexural yielding (due to limited transverse reinforcement). Since this research focuses on the interaction between shear and axial capacity loss in shear-critical columns, the drift capacity model was utilized into this study.

4.3.1 Drift Ratio at Shear Failure

To quantify the lateral deformation occurring in a shear-critical reinforced concrete column subjected to shear and axial loading, a drift ratio is employed to illustrate column deformation in relation to the column's length. The following empirical equation developed by Elwood and Moehle (2003) is used to estimate the drift ratio at shear failure, (Δ_{SH} / L) of a shear-critical reinforced concrete column subjected to axial loading:

$$(\Delta_{SH} / L) = (3/100) + 4\rho'' - (1/500)(v/\sqrt{f'_C}) - [P/(40A_G f'_C)] \geq (1/100) \quad (4.1)$$

where $\rho'' = (A_{ST} / bs)$ is the transverse reinforcement ratio, b is the column cross section width, s is the stirrup or transverse reinforcement spacing, $v = (V_Y / bd)$ is the maximum shear stress and d is the depth to the farthest tensile reinforcement.

5 Axial Capacity Model

5.1 INTRODUCTION

Though a reinforced concrete structure may lose much of its shear strength after the occurrence of shear failure, it is important that an engineer be able to determine the column's ability to sustain gravity loads in the event of shear failure. Since total structural collapse in a reinforced concrete column is defined by axial load failure, an axial capacity model that is able to quantify the residual axial load capacity that a column possesses is required in order to establish whether the column is able to sustain gravity loads after shear failure.

5.2 CLASSICAL SHEAR-FRICTION MODEL

Based on the tests conducted by Lynn (2001) and Sezen (2002) on shear-critical reinforced concrete columns up to the point of axial failure, Elwood and Moehle (2003) develop an axial capacity model that allows one to assess the residual axial load capacity of a shear-critical reinforced concrete column after shear failure; this axial capacity model was developed with the assumption that load distribution across a column's shear failure plane occurs through the mechanism of shear friction forces.

5.2.1 Shear Failure Plane

After the occurrence of shear failure in a column, an inclined shear failure crack results as can be seen from the plane inclined at an angle, θ in Figure 5.1 that developed in a column tested by Elwood and Moehle (2003).

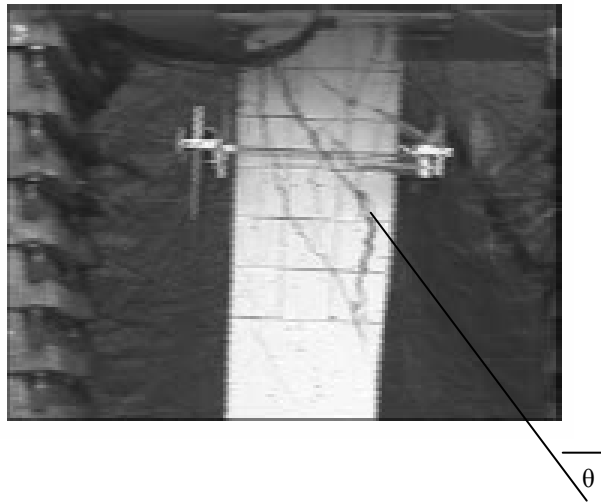


Figure 5.1: Shear failure plane in a reinforced concrete column after shear failure.

According to Elwood and Moehle (2003), once shear failure occurs in a shear-critical reinforced concrete column, gravity loads supported by the shear-damaged column must be transferred across the shear failure plane that develops if total structural collapse is to be prevented. This transfer of gravity load across the shear failure plane occurs via *shear friction forces* which arise from the internal forces of the longitudinal and transverse reinforcement.

5.2.2 Residual Axial Load Capacity

When shear failure occurs in a reinforced concrete column, gravity loads are supported by shear friction forces developed within the column and thus, the column continues to possess some axial capacity after shear failure. Figure 5.2 shows the vertical and horizontal internal forces of the longitudinal reinforcements and horizontal forces of the transverse reinforcement which produce the shear friction forces, as well as the applied shear, V and axial load, P on the column. The inclined shear failure surface is assumed to occur at a critical angle, θ which is representative of the inclined crack resulting from shear damage in the column.

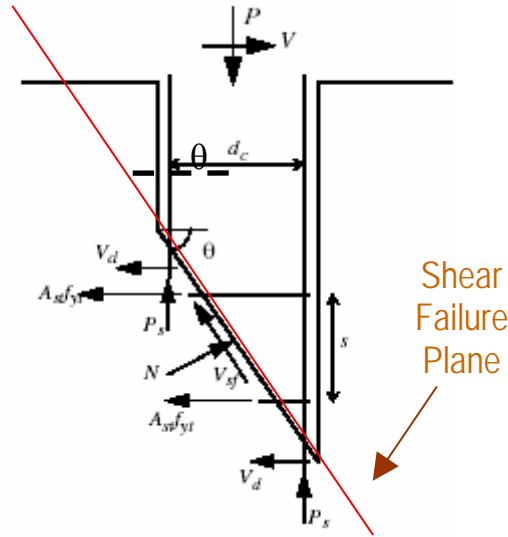


Figure 5.2: Free Body Diagram of column after shear failure.

From equilibrium of the internal and applied forces in Figure 5.2, Elwood and Moehle (2003) derived the axial load capacity of a shear-damaged column. The following equation represents the residual axial load capacity of a shear-critical, reinforced concrete column after shear failure:

$$P_R = \tan\theta[(A_{ST}F_{YT}d_C) / s][(\cos\theta - \mu_F \sin\theta) / (\sin\theta - \mu_F \cos\theta)] \quad (5.1)$$

where θ is the critical crack angle, d_C is the horizontal distance between the longitudinal reinforcement, μ_F is the effective coefficient of friction and s is the stirrup or transverse reinforcement spacing. In this report, the critical crack angle, θ is assumed to be 65° .

In the case where the effective friction coefficient and/or critical crack angle is not known prior to testing, the residual axial load capacity of a shear-critical, reinforced concrete column can reasonably be estimated as ten percent of the undamaged axial load capacity of the column, P_N as computed from Equation 2.1. This method of computing the residual axial capacity of the column specimens is used in this report to approximate the axial load that will be applied in the experimental test program discussed in Chapter 6.

When the axial load demand on the column exceeds the axial capacity provided by shear friction forces, axial load failure of the column results. Axial load failure signifies total collapse of the structure and is assumed to occur when the column has zero or negligible shear strength.

5.3 DRIFT RATIO AT AXIAL LOAD FAILURE

The maximum capacity drift model developed by Elwood and Moehle (2003) was based on the results achieved by Lynn and Sezen (2002) and is used to assess the lateral drift of a shear-critical reinforced concrete column at axial failure. The maximum capacity drift model depends only on the capacity of shear friction forces and not the longitudinal bar capacity of the column

since the shear friction capacity far exceeds that of the longitudinal reinforcement, at low lateral drifts. While the total capacity drift model, which incorporates drift capacity due to shear friction and longitudinal reinforcement, accurately predicts the drift at axial load failure that occurred in the specimens tested by Lynn and Sezen (2002), Elwood and Moehle recommend using the maximum capacity drift model to assess column drift at axial failure.

Based on the maximum capacity drift model, the following equation derived by Elwood and Moehle (2003) predicts the lateral drift taking place in a shear-critical reinforced concrete column at the onset of axial load failure:

$$(\Delta_{AX} / L) = [(4/100)(1+\tan^2\theta)] / [\tan\theta + P(s / [A_{ST}F_{YT}d_C\tan\theta])] \quad (5.2)$$

6 Design of Quasi-Static Test

6.1 INTRODUCTION

A quasi-static test was designed to observe the process of damage progression, shear degradation and axial load failure in a shear-critical reinforced concrete column subjected to dynamic shear and constant axial loading. This chapter provides an overview of the design, construction and testing of the reinforced concrete frame specimens.

6.2 RC COLUMN SPECIMEN

Two reinforced concrete column test specimens were designed by UC Berkeley graduate student, Yoon Bong Shin to exhibit the hysteretic behavior representative of existing, shear-critical reinforced concrete columns under simulated gravity and seismic load. The geometric design of the test specimens was chosen to be representative of a typical, existing shear-critical reinforced concrete column at one-third scale. This column design as well as the selection of reinforcement is shown in Figure 6.2.

6.2.1 Prototype and Design Requirements

Two test specimens were constructed and tested. Each column specimen was designed at one-third scale and representative of a typical shear-critical reinforced concrete column. A static axial/gravity load would be applied to each specimen, a load that is determined based on the residual axial capacity of the column specimen, P_R which was taken, as previously discussed in Section 5.2.2, to be ten percent of the undamaged axial load capacity, P_N of the reinforced concrete column. Based on the cross section of the reinforced concrete column specimens, the undamaged axial load capacity of the specimens was computed to be 240.97 kips; thus, the residual axial capacity of a shear damaged column specimen was estimated as ten percent of the total column capacity, or 24.1 kips. To ensure the occurrence of axial failure in both specimens during testing, a 30 kip static gravity load would be subjected onto the columns.

In addition to gravity load, a cyclic, unidirectional shear load of approximately 8 kips, calculated as the shear load capacity of the column [Equation 2.3] and used to simulate simple seismic

loading, is also to be applied. Gravity and shear loading, as they will be applied to each column specimen, is shown in Figure 6.1b.

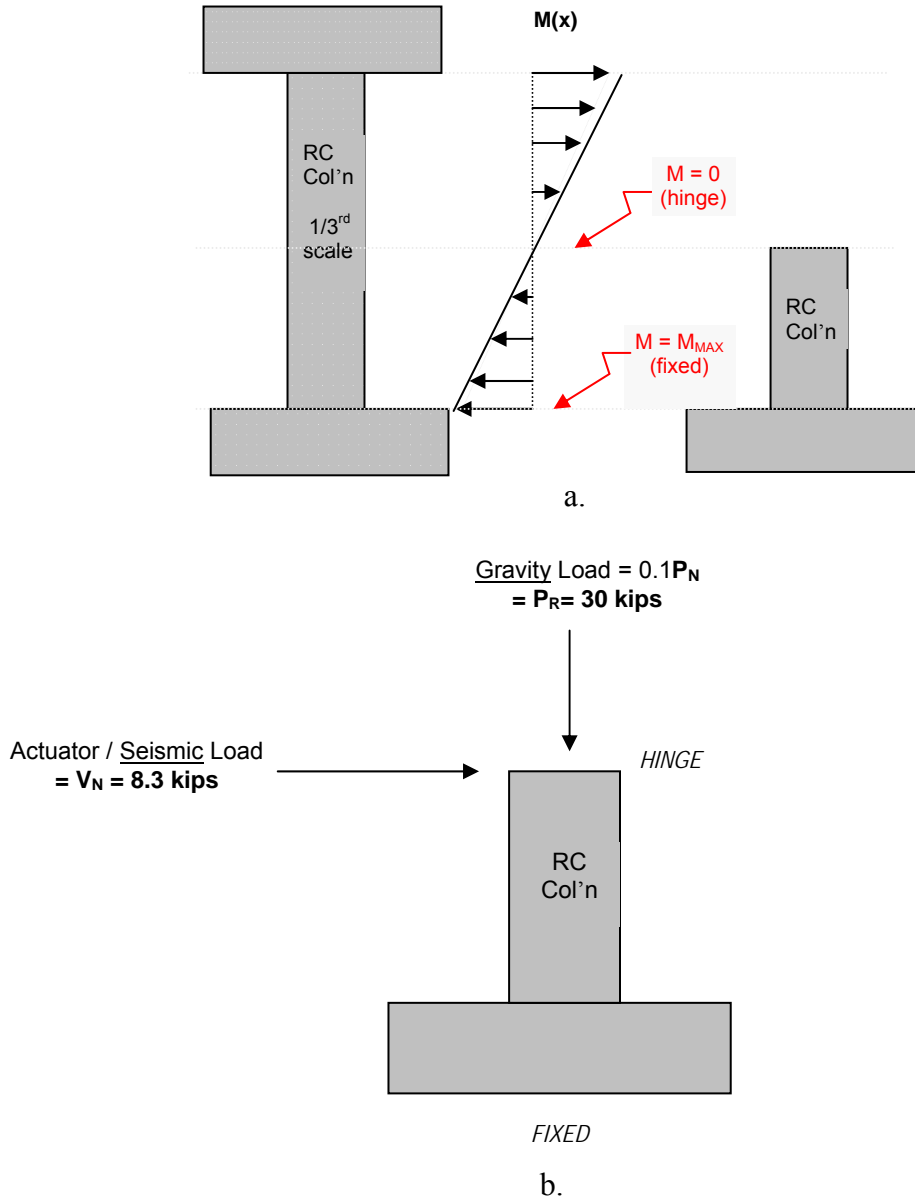


Figure 6.1: Simplified model of reinforced concrete test specimen.
a. Idealized cantilever model b. Applied loads on model

As shown in Figure 6.1a., to further simplify column analysis and fabrication in this project, the reinforced concrete column design would be idealized as a cantilever column fixed at one end and free on the opposite end; this simplification is valid for the representation of actual full column prototypes with no moment resistance at column center and maximum moment resistance at the fixed ends when it is subjected to end shear forces.

6.2.2 Geometry and Reinforcement

Each column specimen was designed and fabricated with a transverse reinforcement or tie spacing of 4 inches and a column height of 29 inches. Thus, the full-scale column prototype would have a 12 inch tie spacing for the entire column length of 87 inches making the column extremely vulnerable to shear failure, and subsequent axial load failure during the test program due to the minimal transverse reinforcement and wide tie spacing in the column.

The base of the column specimen, however, was not designed to be representative of existing reinforced concrete columns; rather, the column base was over-reinforced in design to ensure it would remain elastic throughout the testing of the specimens ensuring that shear damage and axial load failure would occur above the column-base joint.

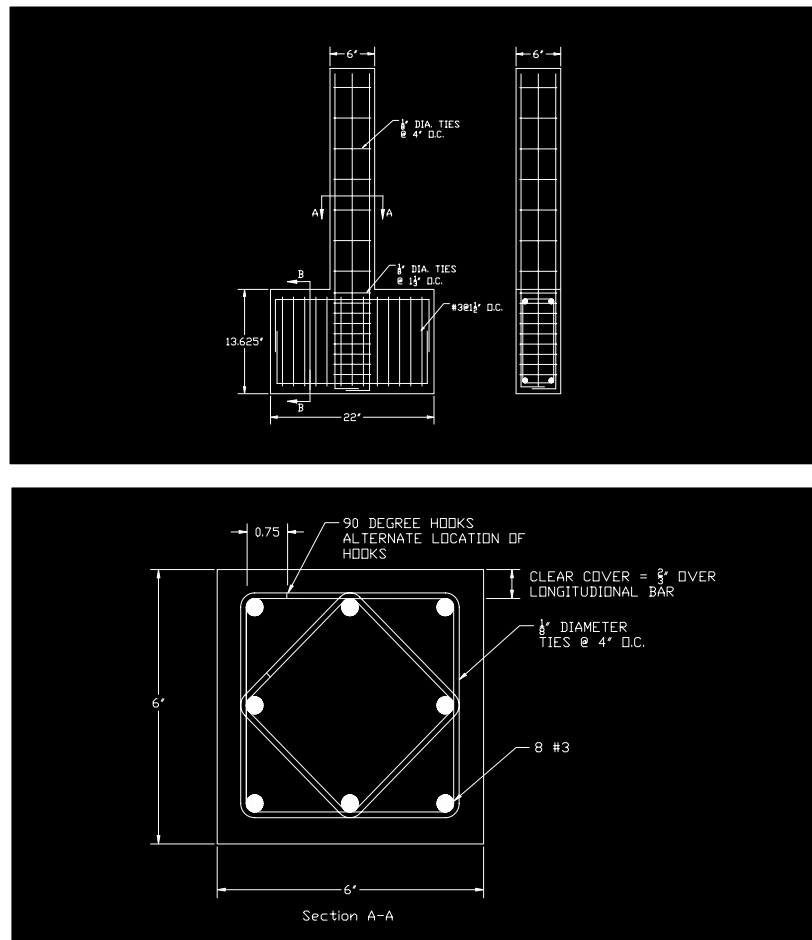


Figure 6.2: Reinforced concrete test specimen.

6.2.3 Fabrication

The test specimens were cast in a flat, horizontal position using forms fabricated previously. The column forms were constructed from marine-grade plywood and the specimens were cast at a site adjacent to the shake table lab. Steel reinforcement cages were then built using Grade 60 steel for all column reinforcement, #3 rebar for the longitudinal reinforcement, one-eighth inch diameter steel ties for the transverse reinforcement, #5 bent rebar [at 90 degree curvature] for the column base reinforcement and tie wires to hold the steel cage assembly together. Exact column reinforcement specifications are given in Figure 6.2 and the fabricated steel reinforcement cages used in the column specimens are shown in Figure 6.3.

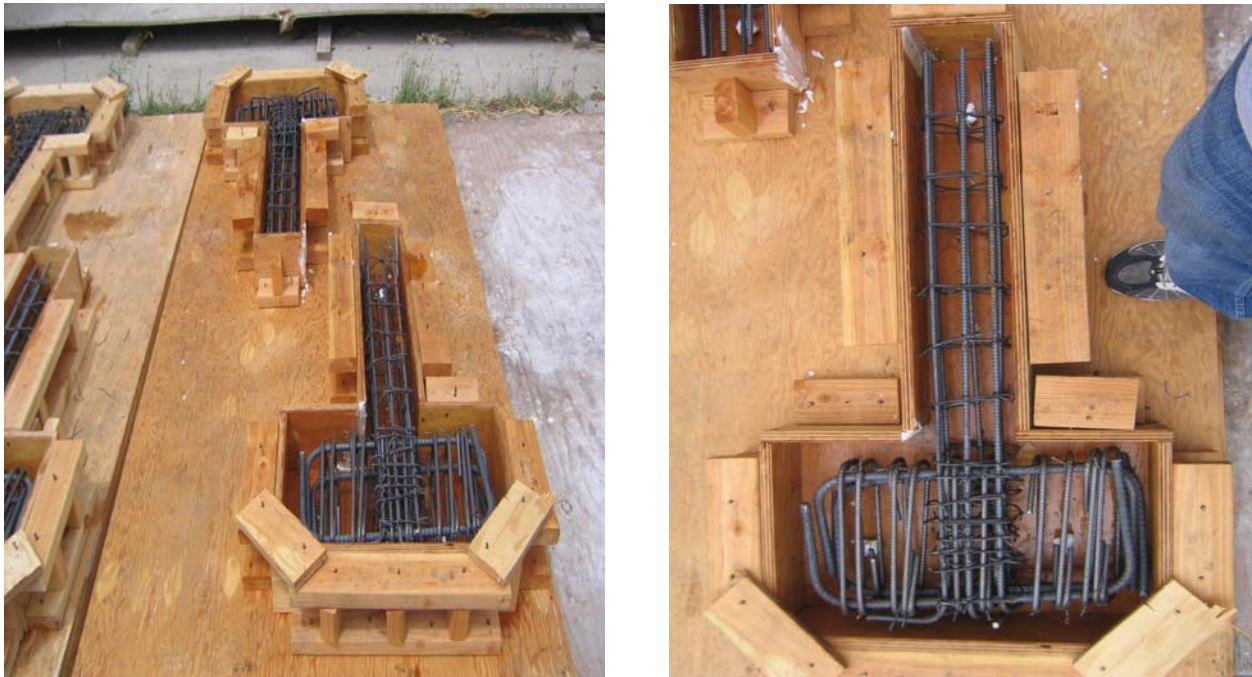


Figure 6.3: Forms and steel reinforcement cages of test specimens.

Normal-weight aggregate, high early strength concrete, with a 7-day early compressive strength of 3 ksi and an ultimate compressive strength of 6 ksi was used to cast the column specimens in one lift, as shown in Figure 6.4. Specimens were wet-cured for 22 days and then stored indoors until testing.



Figure 6.4: Casting of test specimens.

Concrete cylinders were also simultaneously fabricated, cured and stored alongside the concrete specimens for use in a crushing test. However, due to time constraints and budget considerations, the concrete cylinders were not tested for their compressive strength; thus, utilizing a concrete cure curve and based on the age at testing [specimen 1 age - 49 days, specimen 2 age - 51 days] as well as the concrete mix composition, it was estimated that the column specimens reached their ultimate compressive strength of 6 ksi by the testing date; thus, a concrete compressive strength value of 6 ksi was used in the analysis of this report.

Initially, a 3 ksi compressive concrete strength was desired in order to maintain consistency with full-scale tests conducted previously on shear-critical reinforced concrete columns; however, a column compressive strength of 6 ksi would be unavoidable at the time of testing; thus, a larger shear and axial loading was computed based on the higher compressive strength such that the specimen hysteretic response curves would be comparable to that of full-scale, shear-critical reinforced concrete columns subjected to similar loading.

6.3 EXPERIMENTAL SETUP

6.3.1 Design

An existing experimental setup, consisting of an actuator attached to a reaction wall and ideal for the testing of small-scale column structures was to be utilized in this study to provide a cyclic shear load on the column test specimens. However, there existed no means to subject the test specimens to a static axial load concurrently with the cyclic shear loading. Thus, after several revisions, an experimental setup was designed that would allow the test specimens to undergo bi-directional loading which simulate the gravity and unidirectional seismic loading experienced by

an actual column; Figure 6.5 shows the details of the experimental setup used in this project; the fabrication and functionality of the setup will be discussed in the following section.

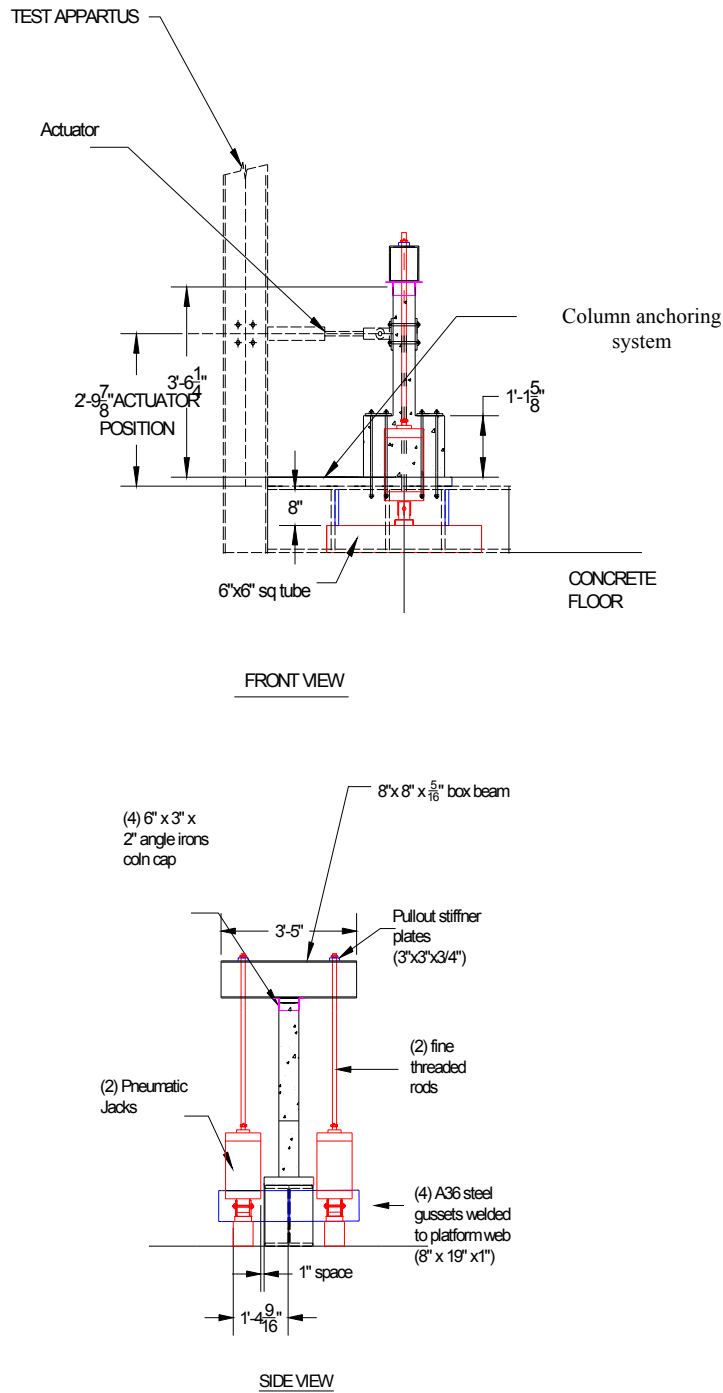
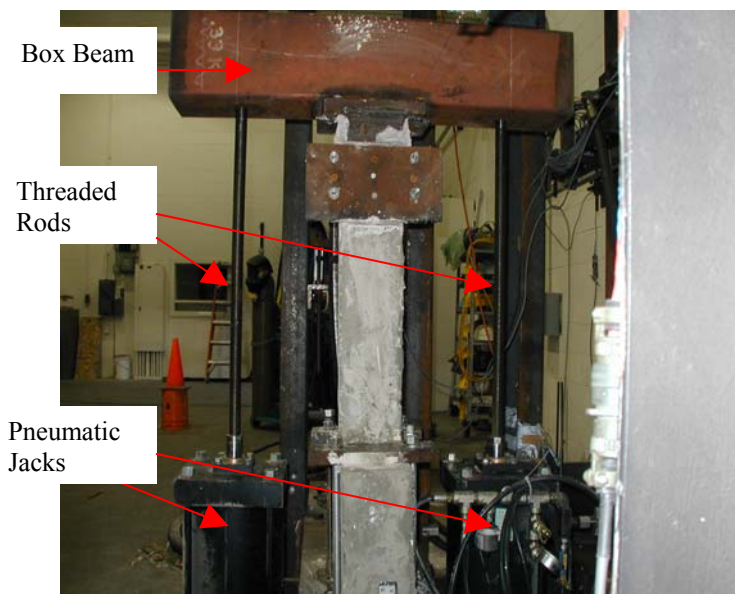


Figure 6.5: Experimental setup design for quasi-static tests on specimens.

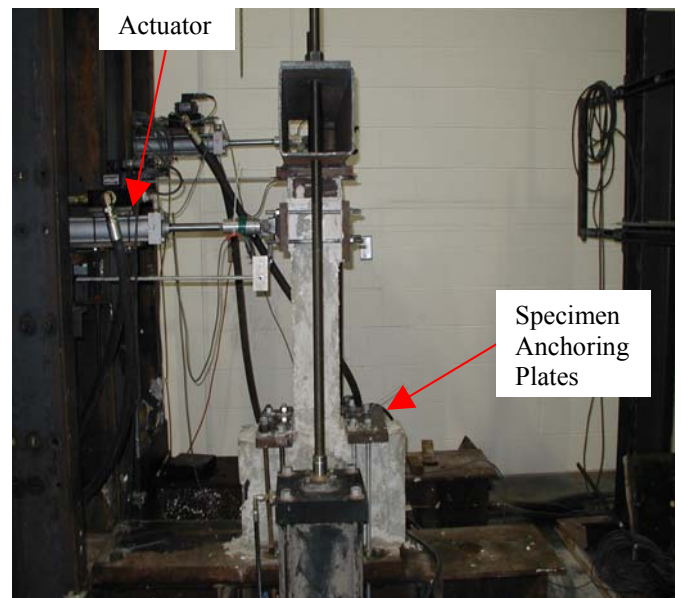
6.3.2 Fabrication

In order to secure the reinforced concrete test specimens to the existing actuator platform, the specimens were anchored to the platform such that no rotation or slip would occur between the column base and platform surface. To accomplish this, one-inch thick steel plates were placed onto the base of the columns and three-quarter inch threaded rods were used to anchor the column to the platform, as shown in Figures 6.5 and 6.6b. Ultracal 30 grout was used to ensure an even and level surface between the column and platform surface. The hydraulic actuator plates, used to provide a cyclic shear loading onto the column, were similarly grouted to the column specimens.

To minimize time needed to fabricate the experimental setup, two pneumatic jacks [shown in Figures 6.5 and 6.6a.] were utilized to provide a static gravity load of 30 kips to the specimens; the gravity/axial load supplied by the pneumatic jacks is representative of the inertial mass of the structure supported by each column specimen. The box beam [Figure 6.6a.], connected in tension to the pneumatic jacks, was supported by angle irons that capped the column and secured the beam on top of the column preventing slip between the column and beam; this connection also served to prevent out of plane motion of the column during testing. The pneumatic jacks were anchored to the ground by steel A36 gussets [Figure 6.6c.], dimensioned to withstand the buckling and shear loads developed within the gussets due to the upward force imposed by the pneumatic jacks, which were welded to the web of the wide-flange test platform. The pneumatic jacks were also positioned such that they would move in unison with the column and in the direction of the actuator motion (shear load).



a.



b.

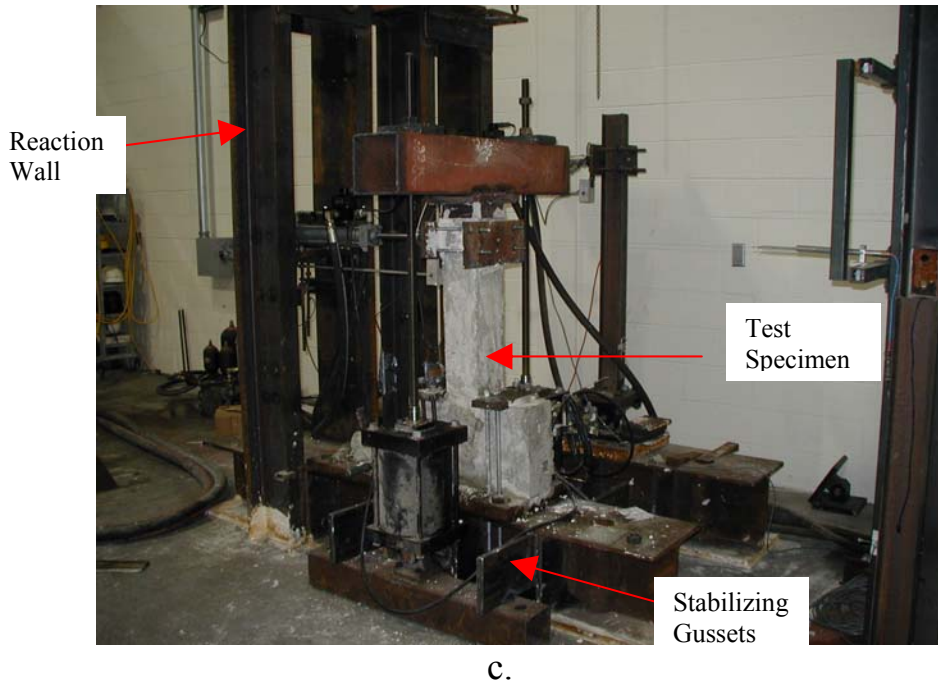


Figure 6.6: Fabrication of experimental setup for quasi-static tests on specimens.
 a. Side view of setup b. Front view of setup c. Overall experimental setup

Each pneumatic jack was calibrated to provide one-half of the total axial load that would be placed onto the column specimens on the gussets. Each column specimen was then moved to the earthquake simulator in the PEER lab at the Richmond Field Station before testing. Specimens were aligned with the intended shaking direction and bolted in place.

6.4 EXPERIMENTAL PROGRAM

Columns were fixed such that there was no moment between column ends while the column was subjected to a series of lateral displacements at increasing displacement amplitudes (i.e. $0.5\Delta_y$, Δ_y , $2\Delta_y$, etc.), where Δ_y is the column yield displacement, with three cycles at each displacement amplitude. The frequency of each cycle was 0.025 inch displacement per second up to yield displacement and 0.05 in. displacement per second for displacements after yield and up to the point of axial load failure. This frequency of shear loading was chosen because it would impose a cyclic motion of long enough duration (i.e. up to $4\Delta_y$ or 4 ductility) needed to reasonably observe damage progression in the columns up to axial failure, while also being of slow enough frequency to observe gradual shear degradation occurring with each specimen.

Since each column specimen was not tested as part of a larger reinforced concrete frame structure, no load redistribution after axial load failure in the column is possible. Thus, once axial load failure occurred in the test specimens, the quasi-static tests were terminated.

A calculated yield displacement, determined from Equation 2.4, was used to formulate the displacement steps used in the experimental program and compared to the perceived yield

displacement given by the hysteretic column response graph recorded by the Automated Test System (ATS), a test control and data acquisition system used to monitor and control the displacement of the hydraulic actuator; if the calculated yield displacement was found to differ from the perceived yield displacement, the experimental program was reassessed based on the perceived yield displacement.

Instrumentation used in the test program consisted of a displacement transducer connected to the length of the column and one connected to the base of the column. The transducer connected along the length of each column specimen was used to experimentally measure the horizontal displacement exhibited by the column throughout the test; the transducer attached to the column base, on the other hand, was used to measure any slip occurring between the column and platform.

The results of this experimental program for each test specimen are presented in Chapter 7 and analyzed in Chapter 8.

7 Quasi-Static Test Results

7.1 INTRODUCTION

This chapter presents the various damage states observed in each test specimen, as well as measured hysteretic response of the test specimens to dynamic shear and static gravity loading. The experimental results presented in this chapter are later compared in Chapter 8, to the results predicted by the capacity models introduced in Chapters 2, 4 and 5.

7.2 SHEAR-FAILURE TESTS

This section presents the actual displacement history and experimental program subjected onto test specimens 1 and 2, as modified during testing from the target displacement program introduced in Section 6.4. More importantly, this section introduces the force-deformation behavior or *hysteretic response* of both test specimens to bidirectional loading and compares these results with visual observations of damage progression made during the course of testing.

7.2.1 Specimen 1

Specimen 1 was subjected to the experimental test program shown in Table 7.1.

Table 7.1: Experimental test program conducted on specimen 1.

Yield Displacement, $\Delta_{Y \text{ calc}}$ (in) 0.213594 in				Axial Load, P 29.5 kips			
Ductility	+/- Displacement (in)	Total Stroke Length (in)	Cycle Period (sec)	Cycle Frequency (hz)	Test Velocity (in/sec)	# of Cycles	Observations during test
						0.5	Actuator start up
1.16 $\Delta_{Y \text{ calc}}$	0.247	0.494	39.52	0.0253	0.025	3	
2.3 $\Delta_{Y \text{ calc}}$	0.494	0.988	79.04	0.01265	0.025	3	Appears to yield at 0.3 in
2.8 $\Delta_{Y \text{ calc}}$	0.6	1.2	96	0.01042	0.025	3	
4.62 $\Delta_{Y \text{ calc}}$	0.987	1.974	78.96	0.01266	0.05	3	1 st half of 1 st cycle-shear failure, 1 st half of 2 nd cycle-axial failure

7.2.1.1. Progression of Observed Damage

Initially, at 1.16 yield displacement or 1.16 ductility, there was no visible elastic deformation. However, during the 3rd cycle at displacement step 1.16 yield, some initial, temporary cracking was detected after one complete cycle and observed to take place at the column-base joint of specimen 1 when the hydraulic actuator pushed, in tension, the specimen. No permanent cracks were observed in the test specimen at the end of the 3 cycles at 1.16 yield displacement.

At the beginning of the first cycle at 2.3 times yield displacement [2.3 ductility], yielding of the longitudinal reinforcement was determined to have occurred based on the hysteretic response of the test specimen as read from the ATS system, discussed in Section 6.4; yielding of the longitudinal reinforcement was defined from the ATS readings by the peak shear load sustained by the specimen as determined from by the hysteretic response curve. Two horizontal, permanent cracks were observed at the column-base joint at 2.3 ductility where the deep cracking resulting on one side of the column may be due to the position of the column anchoring plates and their restriction of lateral deflection at the base-column joint. Horizontal cracks were observed approximately 3 inches above the column base. Slight crushing of concrete then took place along the column-base joint with very little spalling of the concrete observed; the damage state of specimen 1 at first yielding of the longitudinal reinforcement is shown in Figure 7.1a.



a.



b.



c.

Figure 7.1: Progression of damage in specimen 1.

a. Damage state at yielding of longitudinal reinforcement. b. Shear failure. c. Axial load failure.

At 4.62 times yield displacement [4.62 ductility] and after the 1st half of the first cycle, a fine diagonal crack appeared indicating the formation of a shear failure plane in the test specimen, as evident in Figure 7.1b. The phenomenon of buckling of the longitudinal reinforcements is evident at this stage and can also be seen in Figure 7.1b. During the 2nd half of the first cycle at 4.62 ductility, extensive damage was initiated in the specimen with large blocks of concrete spalling off the column and opening of the crack along the shear failure plane observed. Due to the extensive buckling of the longitudinal reinforcements, further concrete spalling occurred due to severe crushing along the shear failure plane. During the 1st half of the second cycle at 4.62 ductility, total collapse (i.e. axial load failure) of the specimen resulted; the damage state at axial load failure for specimen 1 can be seen from Figures 7.1c. and 7.2.

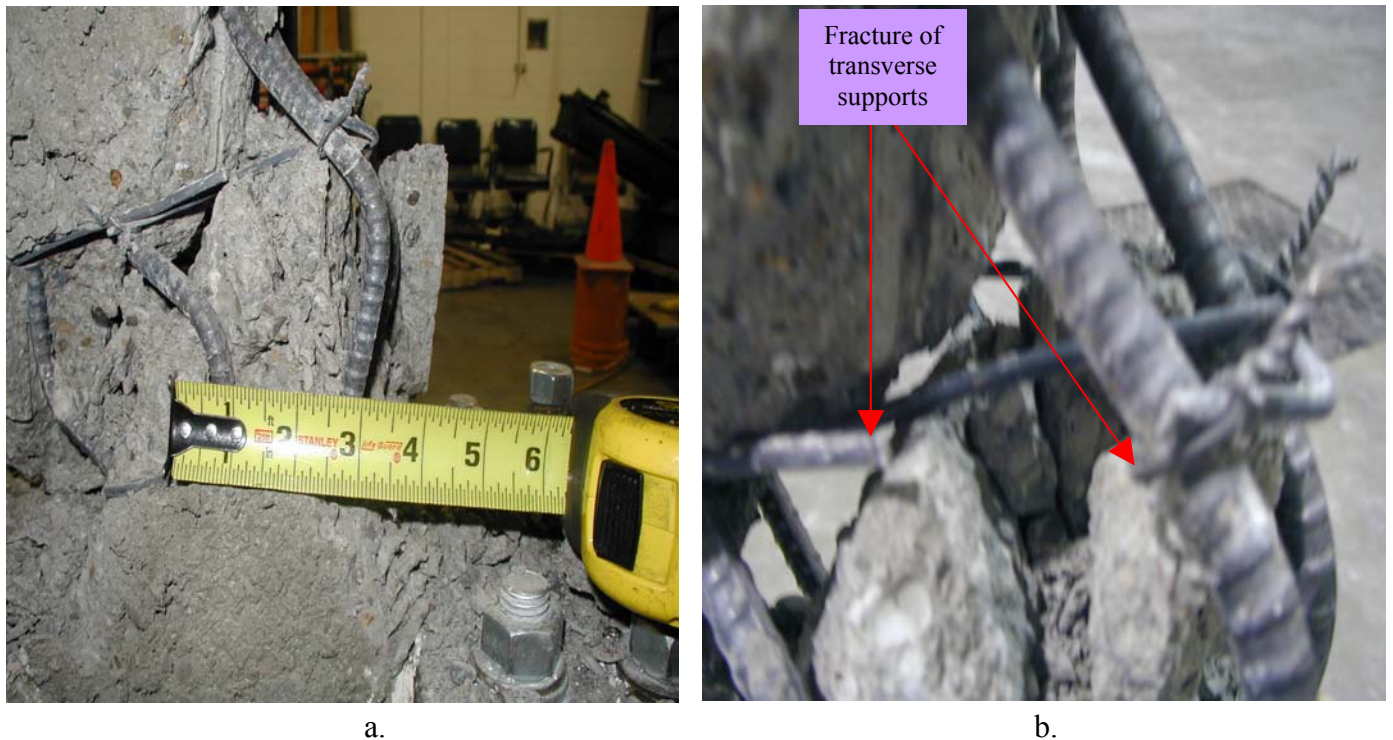


Figure 7.2: Specimen 1 damage at axial load failure.

- a. Buckling of longitudinal reinforcement. b. Fracture of transverse reinforcement.

The damage state of specimen 1 at axial load failure can be observed from Figure 7.2 by the fracture of the transverse reinforcement and resulting, maximum longitudinal reinforcement buckling of 3 in.

7.2.1.2 Measured Response

This section presents the hysteretic response of specimen 1 recorded during experimentation. The displacement history subjected onto specimen 1 is shown in Figure 7.3 and was based on the experimental program described in Section 6.4.

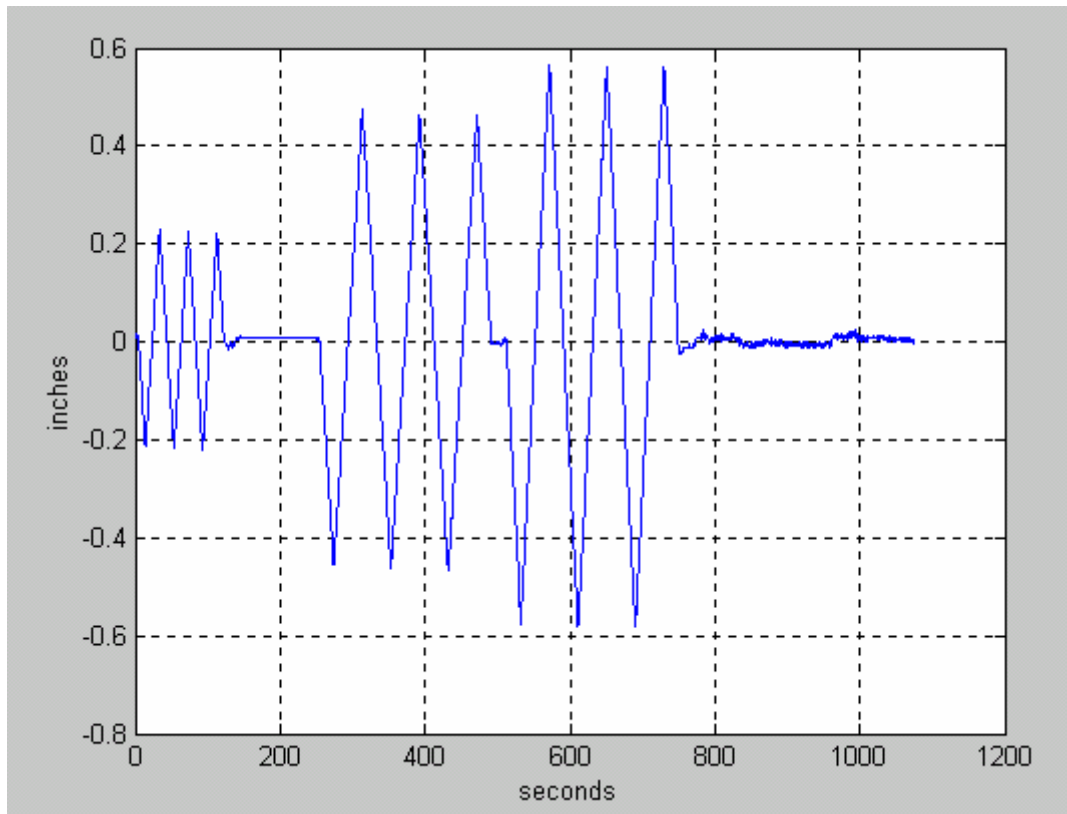


Figure 7.3: Modified target displacement history for specimen 1.

The force-deformation response of specimen 1 is shown in Figure 7.4.

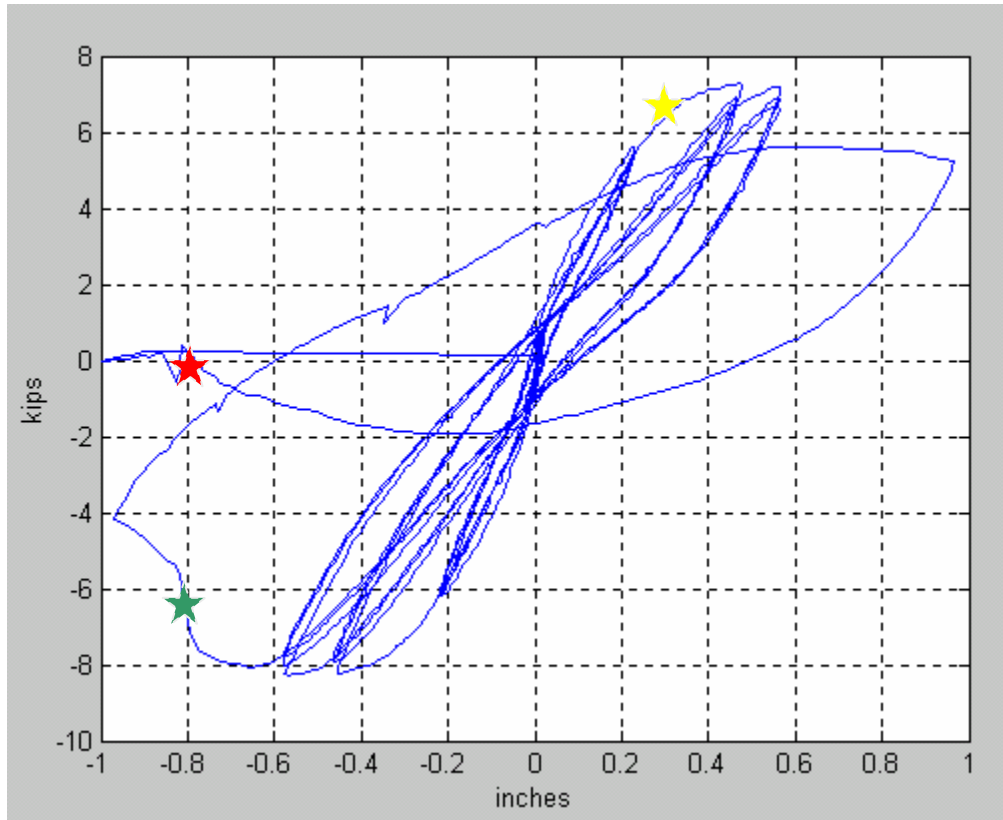


Figure 7.4: Experimental force-displacement response of specimen 1.

First yielding of the longitudinal reinforcement in specimen 1 is observed to occur at 0.3 inches lateral displacement and is indicated on Figure 7.4 by a yellow marker. The damage state for the specimen at yielding is shown in Figure 7.1a.

The occurrence of shear failure in specimen 1 is indicated by the green marker in Figure 7.4. Shear failure is defined, in this report, by a 20 percent drop in shear load carried by the specimen as observed on the hysteretic response curve. At the beginning of cyclic loading at a ductility of 4.62, the peak shear load sustained by the specimen prior to the initiation of shear failure is 8.2 kips; thus, a 20 percent drop in shear load (i.e. shear failure) occurs during the 1st half of the first cycle under a shear load of approximately 6.56 kips. This loss of shear load capacity corresponds with the pronounced crack developed within the specimen along a shear failure plane, shown in Figure 7.1b. After shear failure, specimen 1 undergoes further shear capacity degradation prior to axial load failure.

Since the onset of axial load failure in a shear-critical reinforced concrete column is defined by a complete loss of shear load capacity, axial load failure in specimen 1 is indicated in Figure 7.4 by the point on the hysteretic curve where zero shear load is sustained by the specimen. Axial load failure is indicated on Figure 7.4 by the red marker and occurs 1 cycle after shear failure. The occurrence of axial load failure in specimen 1 concurs with the damage progression observed in the specimen as shown in Figures 7.1c. and 7.2.

7.2. Specimen 2

Specimen 2 was subjected to the experimental test program shown in Table 7.2.

Table 7.2: Experimental test program conducted on specimen 2.

Yield Displacement, Δ_Y calc (in) 0.213594 in				Axial Load, P 29.5 kips			
Ductility	+/- Displacement (in)	Total Stroke Length (in)	Cycle Period (sec)	Cycle Frequency (hz)	Test Velocity (in/sec)	# of Cycles	Observations during test
						0.5	Actuator start up
0.75 Δ_Y calc	0.16	0.32	25.6	0.03906	0.025	3	
1.5 Δ_Y calc	0.32	0.64	51.2	0.01953	0.025	3	Appears to yield at 0.3 in
3 Δ_Y calc	0.64	1.28	102.4	0.00977	0.025	3	
4.5 Δ_Y calc	0.96	1.92	76.8	0.01302	0.05	3	1 st half of 1 st cycle-shear failure, 1 st half of 2 nd cycle-axial failure

7.2.2.1. Progression of Observed Damage

No noticeable yielding or cracking occurred with cycling at 0.75 ductility. In the 1st half of the 2nd cycle at 1.5 ductility, yielding of the longitudinal reinforcement was also determined to have occurred based on the hysteretic response of the test specimen as read from the ATS system, discussed in Section 6.4. Between the 3rd cycle at 1.5 ductility and 2nd cycle at 3 ductility, slight horizontal cracks became evident at the column-base joint; however, the horizontal cracks and concrete spalling occurring in specimen 2 at yielding were not as visibly noticeable as those occurring in specimen 1; thus, pictures of specimen 1 yielding were omitted from this report.

In the 1st half of the 1st cycle at 3 ductility, a fine diagonal crack appeared on the specimen indicating development of a shear failure plane in the specimen; further definition of the shear failure plane, as well as severe outward buckling of longitudinal reinforcement took place throughout displacement cycles at 3 ductility, indicating a failure of the transverse reinforcement at approximately 4 inches above the column base [Figure 7.5b.]. As a result, a large section of concrete began to spall off on one side of the specimen column, as can be seen from Figure 7.5a.

During the 2nd half of the first cycle at 4.5 ductility, extensive damage was initiated in the specimen with a large intact block of concrete buckling outward along one side of the column, some localized concrete spalling, and opening of the crack along the shear failure plane observed. During the 1st half of the second cycle at 4.5 ductility, axial load failure occurred in the specimen as observed by the complete loss of concrete cover above the column-base joint and crushing along the shear failure plane. The final damage state of specimen 2 at axial load failure is shown in Figure 7.6. The specimen slid along failure plane due to the gravity loads

remaining and thus, exposing the buckling of the longitudinal reinforcements and fracture of the transverse supports. Total collapse (i.e. axial load failure) of the specimen resulted; the damage state at axial load failure for specimen 2 is seen in Figure 7.6.



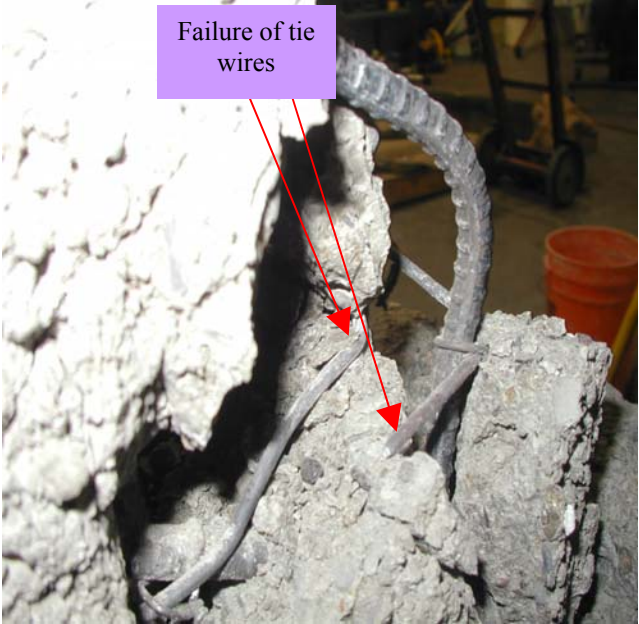
a.



b.

Figure 7.5: Progression of damage in specimen 2.
a. Shear failure. b. Axial load failure.

Similar to the case of specimen 1, the damage state of specimen 2 at axial load failure can be observed from Figure 7.6b. by the maximum longitudinal reinforcement buckling of 3 in. occurring approximately 5.5 inches above the column-base joint. However, unlike specimen 1, failure of the transverse reinforcements to contain the concrete core and longitudinal reinforcement did not occur due to fracture of the transverse supports; rather, failure in the tie wires used to bind the free ends of the transverse reinforcement were at fault [Figure 7.6a.].



a.



b.

Figure 7.6: Specimen 2 damage at axial load failure.

a. Fracture of transverse reinforcement. b. Buckling of longitudinal reinforcement.

7.2.2.2 Measured Response

This section presents the hysteretic response of specimen 2 recorded during experimentation. The displacement history subjected onto specimen 2 is shown in Figure 7.7 and was based on the experimental program described in Section 6.4.

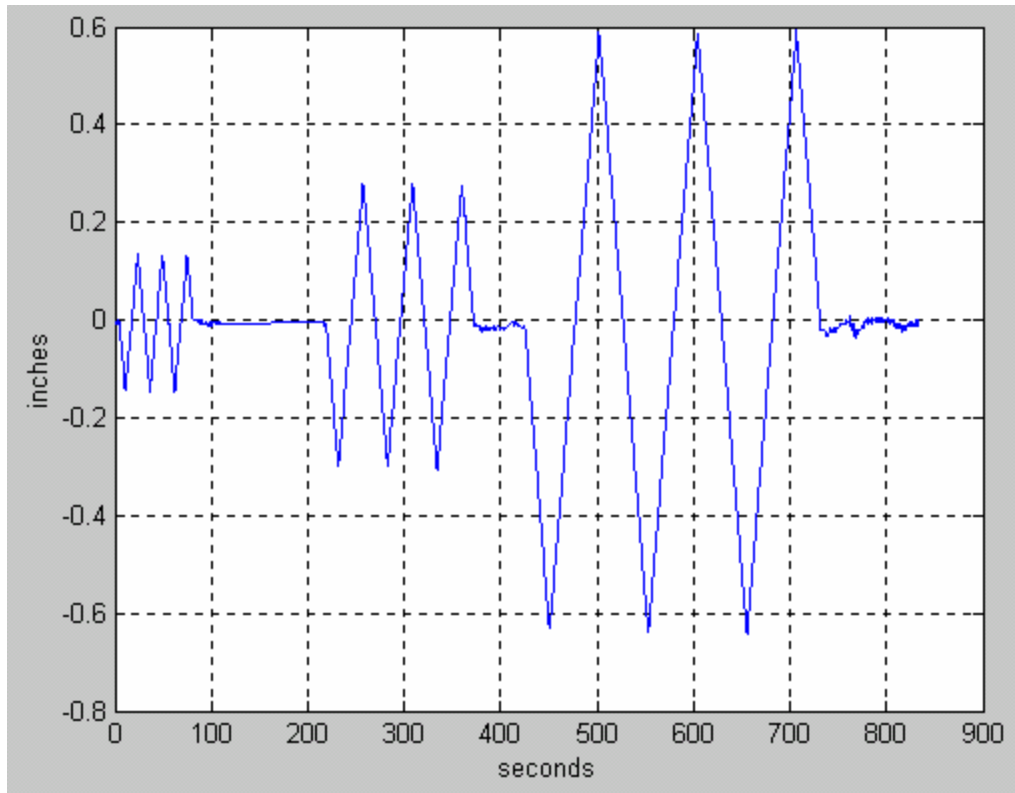


Figure 7.7: Modified target displacement history for specimen 2.

Figure 7.8 shows the shear hysteretic response of specimen 2.

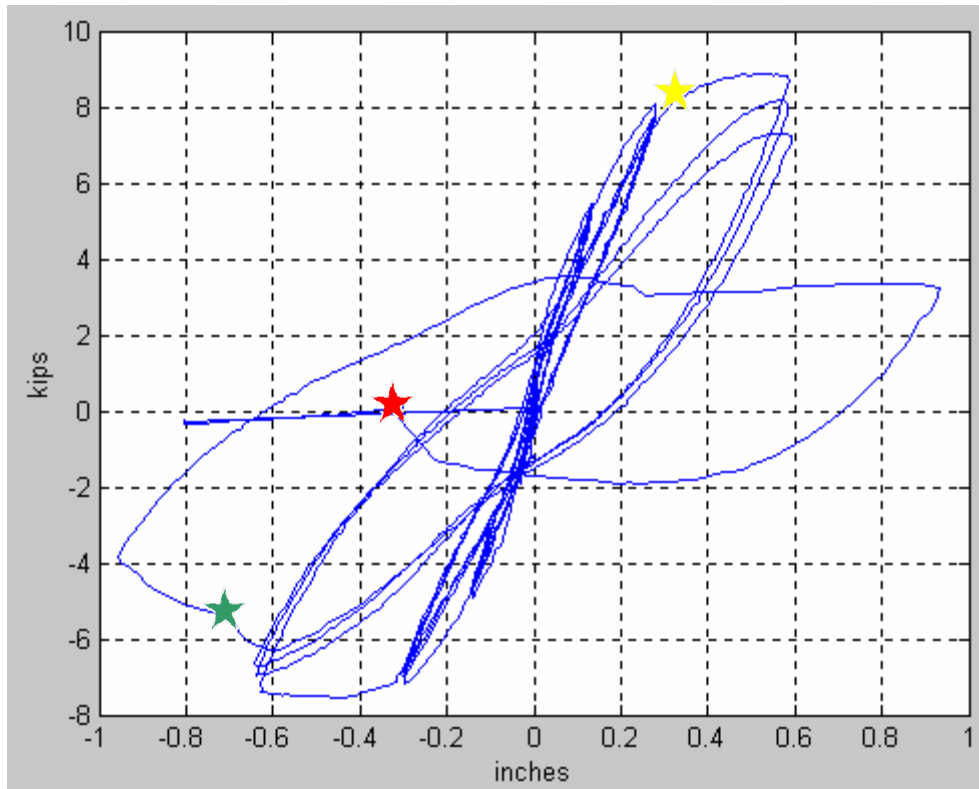


Figure 7.8: Experimental force-displacement response of specimen 2.

As for the hysteretic response for specimen 1, the damage states for specimen 2 are indicated by the colored markers in Figure 7.8: first yielding of the longitudinal reinforcement is represented by a yellow marker, shear failure by a green marker and axial load failure by a red marker.

For specimen 2, yielding was also observed to have occurred at approximately 0.3 inches lateral displacement

Prior to cyclic loading at a ductility of 4.5, the peak shear load sustained by the specimen is approximately 6.2 kips; thus, a 20 percent drop in shear load and initiation of shear failure in the specimen occurs during the 1st half of the first cycle under a shear load of approximately 5 kips. This drop in shear load coincides with the development of severe cracking along the shear failure plane and is accompanied by the continued crushing of concrete at the column-base joint, as evident in Figure 7.5a. After shear failure, it can be seen from the hysteretic response curve that specimen 2 undergoes a significant degradation of shear load capacity between the 1st half of the first cycle and the 1st half of the second cycle.

Since the onset of axial load failure is defined to have occurred when the specimen has zero shear-carrying capacity, axial load failure in specimen 2 was determined from Figure 7.8 to have occurred at a horizontal displacement of approximately 0.32 inches during the 1st half of the second cycle at 4.5 ductility, or one cycle after the occurrence of shear failure. The occurrence of axial failure in Figure 7.8 agrees with the observations of damage progression made during

this time and the total structural collapse along the shear failure plane took place which resulted; the damage states for the specimen at axial load failure are shown in Figures 7.5b. and 7.6.

8 Comparison of Test Data with Predictive Models

8.1 INTRODUCTION

This chapter will compare the test results presented Chapter 7 with those predicted by the empirical capacity models discussed earlier in Chapters 2, 4 and 5.

8.2 YIELD DISPLACEMENT AND MOMENT CURVATURE

To estimate the lateral displacement of the reinforced concrete column at first yield of the longitudinal reinforcement, Δ_Y using Equations 2.4 to 2.7, particular empirical parameters are required. Unknown parameters Φ_Y and M_Y are determined from the moment curvature response of the specimen shown in Figure 8.1 and represent, respectively, the curvature at first yield and the moment at first yield; the estimated yield point of the longitudinal reinforcement in the column is noted in Figure 8.1 by the yellow mark. The moment curvature of the column specimen was obtained from a cross sectional analysis of the column utilizing *OpenSees* and computed for an axial load of 30 kips.

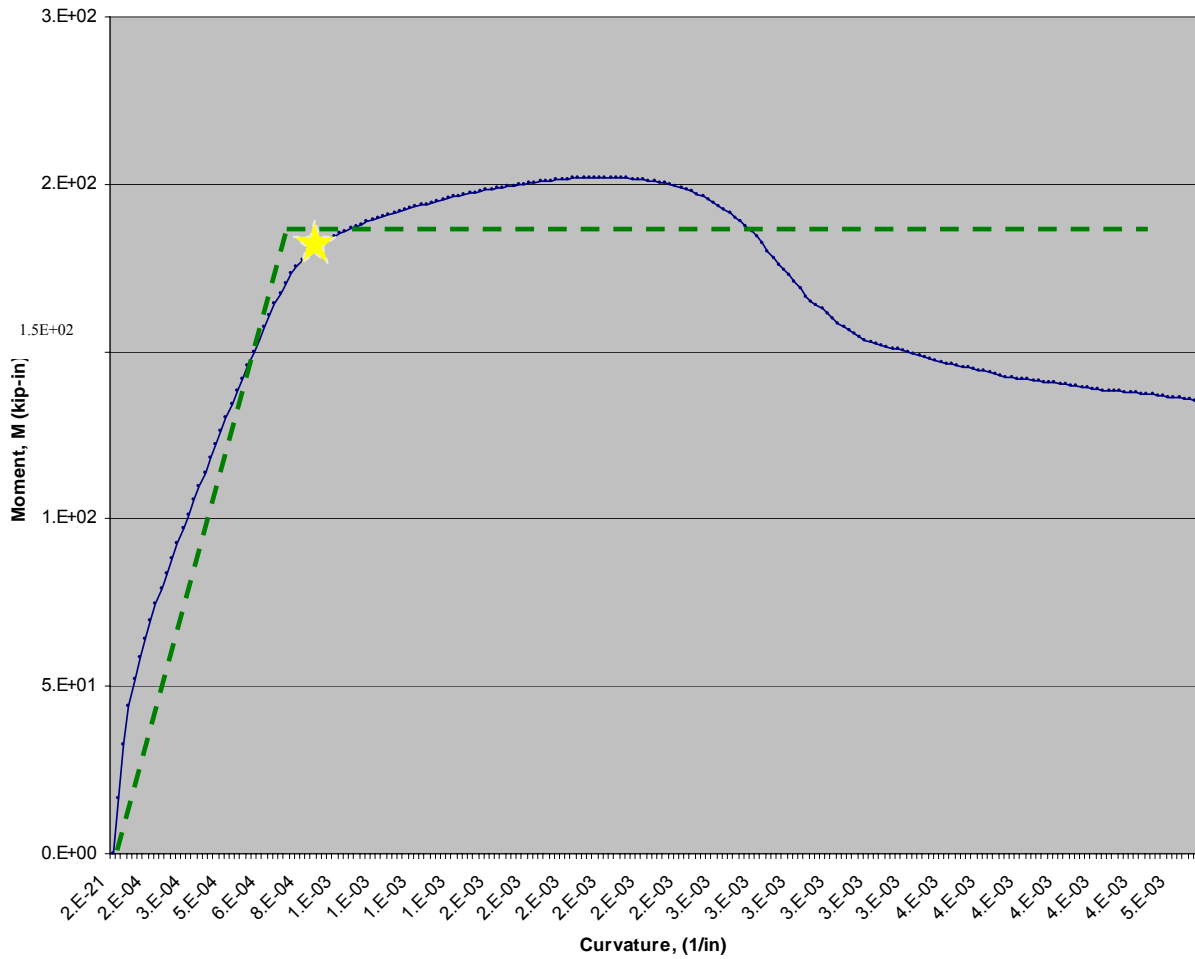


Figure 8.1: Moment curvature response of reinforced concrete column specimen based on section analysis.

Table 8.1 compares the lateral displacement of the column at first yield of the longitudinal reinforcement calculated from Equation 2.4 to the experimentally determined yield displacement assessed from the hysteretic response of each specimen.

Table 8.1: Calculated and experimentally determined yield displacement of the reinforced concrete column specimen.

Specimen	Δ_{FL} (in)	Δ_{SL} (in)	Δ_{SH} (in)	$\Delta_{Y \text{ calc}}$ (in)	$\Delta_{Y \text{ exp}}$ (in)	$\Delta_{Y \text{ calc}} / \Delta_{Y \text{ exp}}$
1	0.076211	0.137376	0.000008	0.213594	0.3	0.71198
2					0.33	0.647255

It should be noted that the yield displacement values given in Table 8.1 denote the total lateral displacement undergone by each column specimen at the onset of yielding of the longitudinal reinforcement. Further, displacements Δ_{FL} , Δ_{SL} and Δ_{SH} only represent the displacement *contribution* of deformation components flexure, bar (bond) slip and shear, respectively, to the

total yield displacement of each specimen as calculated using Equations 2.5-2.7; displacement Δ_{SH} does *not* reflect the total lateral displacement undergone by each column specimen at the onset of shear failure. Lateral displacement values at yielding, shear failure and axial load failure will be calculated, using the empirical drift capacity models discussed in Chapters 2, 4 and 5, and presented in the following section.

8.3 SHEAR DRIFT BACKBONE

The idealized backbone model, discussed in Elwood and Moehle (2003), can be used to approximate the shear load versus lateral displacement behavior of shear-critical RC columns with. The backbone model utilizes column drift ratios at yielding, shear and axial failure, as well as the yield moment derived from the column’s moment-curvature response, to generate a ‘shear failure surface’. This shear failure surface can then be used to assess the validity of the empirical (drift) capacity models to predict actual hysteretic response of shear-critical RC columns.

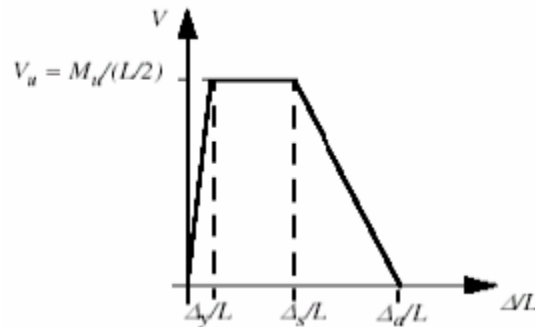


Figure 8.2: Idealized shear failure surface used to envelope the hysteretic response of RC test specimens.

Using a column length of 23.5 in. (distance between column-base joint and actuator loading position), the lateral displacement at yielding, shear and axial load failure are calculated using Equations 2.4, 4.1 and 5.2, respectively. Displacement values used to generate the shear-failure surface for both specimens are presented in Table 8.2; the resulting shear surface is superimposed onto the experimentally-derived hysteretic response curves of each specimen, as can be seen in the following sections.

Table 8.2: Calculated lateral displacement values at yielding, shear and axial load failure based upon empirical drift capacity models presented in Chapters 2, 4 and 5.

Δ_Y (in)	Δ_{SH} (in)	Δ_{AX} (in)
0.11609	0.616828	0.826801

8.3.1 Specimen 1

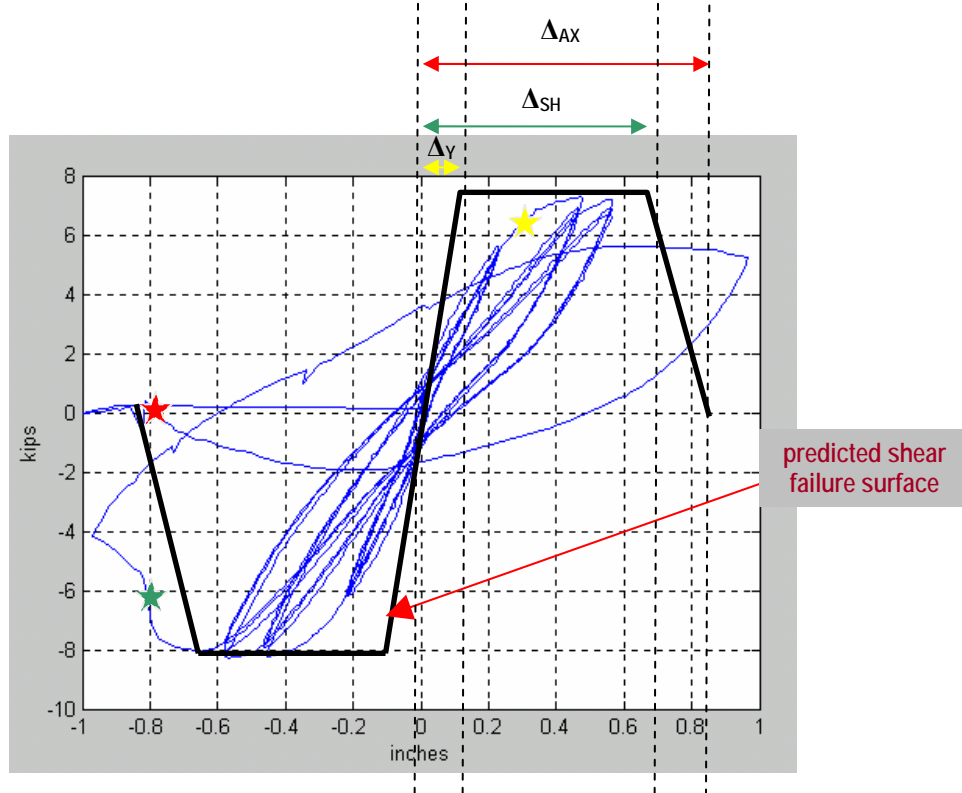


Figure 8.3: Experimental force-displacement [hysteretic] response of specimen 1 with idealized shear backbone.

From the calculated drift values presented in Table 8.2, an idealized shear failure surface, for a shear-critical RC column with cross section and material properties matching those of the test specimens, is superimposed onto the hysteretic response of specimen 1 [Figure 8.3]. As previously discussed in section 7.2, first yielding of the longitudinal reinforcement is indicated by the yellow marker, shear failure with a green marker and axial load failure with a red marker. The position of such markings on the hysteretic curves was determined from observations made during specimen testing and also, from the ATS real-time measurements as discussed in Section 6.4.

The largest variation between the shear failure surface prediction and actual hysteretic response of specimen 1 seems to occur at the first yield of the longitudinal reinforcements. First yield was observed during the test to occur at 0.3 in. while the shear surface projects first yielding at 0.11609 in. Thus, a significant error of 61.3% exists between the empirical model prediction of yield and that actually observed. Next, shear failure in specimen 1 was observed to have occurred approximately at 0.8 in. while a shear failure at 0.616828 in. was predicted; therefore, a smaller error of 22.9% exists in the ability of the empirical models to predict shear failure. Lastly, it was predicted that axial load failure would occur at a displacement of 0.826801 in. while an observed axial failure was recorded at approximately 0.8 in; prediction error in this case is small at 3.35%.

8.3.2 Specimen 2

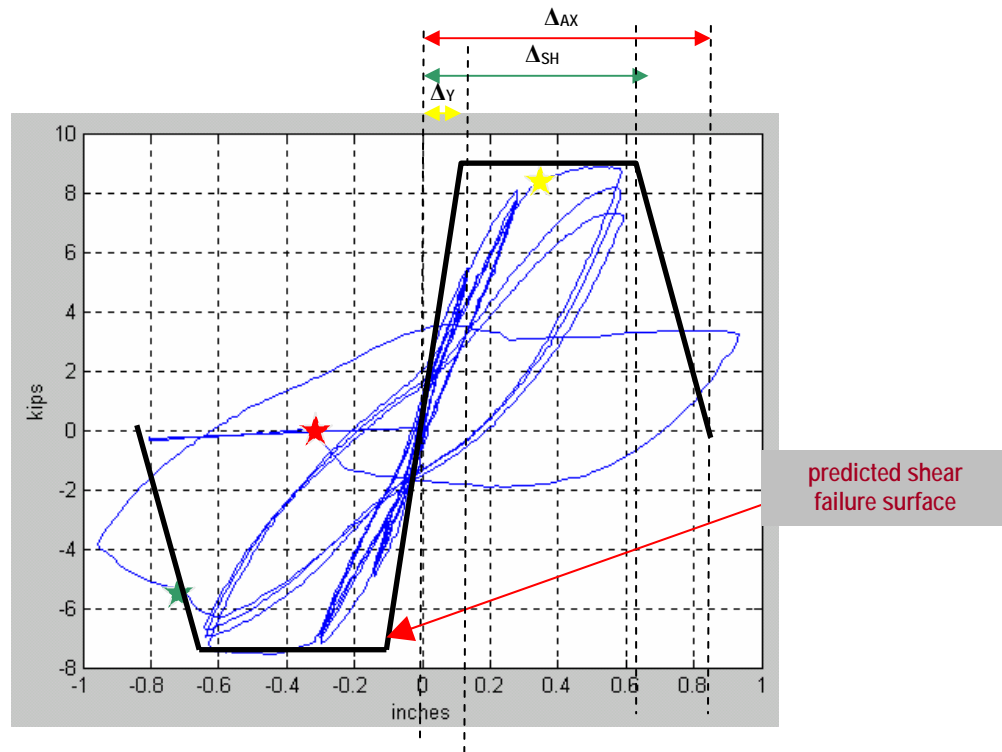


Figure 8.4: Experimental force-displacement [hysteretic] response of specimen 2 with idealized shear backbone.

Again, as for specimen 1, the largest variation between the shear failure surface prediction and actual hysteretic response of specimen 2 seems to occur at the first yield of the longitudinal reinforcements [Figure 8.4]. First yield was observed during the test to occur at approximately 0.33 in. while the shear surface projects first yielding at 0.11609 in; a significant error of 64.8% exists between the empirical model prediction of yield and that actually observed. The error in predicting shear failure in specimen 2 is smaller than that for specimen 1. Shear failure in specimen 2 was observed to have occurred approximately at 0.7 in. while a shear failure at 0.616828 in. was predicted; therefore, a smaller error of 11.9% exists in the ability of the empirical models to predict shear failure. On the other hand, an unacceptably large deviation between predicted and observed displacement at axial failure exists for specimen 2. It was predicted that axial load failure would occur at a displacement of 0.826801 in. while an observed axial failure was recorded at approximately 0.32 in; prediction error in this case is much larger than in the case of specimen 1.

9 Conclusion

9 Conclusion

Earthquake reconnaissance has shown that columns in reinforced concrete buildings constructed prior to the introduction of modern seismic ACI code in the early 1970s are particularly vulnerable to shear failure. The goal of this project was to develop validation data to test empirical capacity models which seek to predict the inelastic response and in particular, failure mechanisms of existing, shear-critical reinforced concrete columns to gravity and seismic loading. Quasi-static earthquake simulation tests on scaled shear-critical reinforced concrete columns were conducted and compared to the theoretical capacity models used to develop the PEER/UC Berkeley-developed *OpenSees* analytical program. As previously discussed, the RC structure deformation components and capacity models implemented in *OpenSees* had significant errors in predicting the hysteretic response of the shear-critical RC column test specimens under bi-directional loading. However, it is to be concluded that hysteretic data produced in this research cannot, by itself, either validate or invalidate the empirical capacity models used to develop *OpenSees* since the scaling methodology used to design and fabricate a scaled model of a shear-critical RC column from its prototype failed to produce hysteretic response data representative of the prototype column. Assumptions made in the scaling process oversimplified the design of the test specimens and thus, affected the integrity of the hysteretic data recorded. In other words, it is concluded that the validation data presented in this research does not accurately represent the actual inelastic behavior of full-size, shear-critical RC columns under unidirectional seismic loading.

Nevertheless, there is a need for further calibration of the *OpenSees* analytical model before such earthquake simulation models, at the expense of laboratory and field testing, are the sole influence factor in RC column seismic design and retrofit. Therefore, it is proposed that future research incorporating better scaling procedures be used to conduct cost-effective laboratory tests on scaled column models or large-scale column testing be undertaken for the purpose of producing validation data from which to calibrate developing analytical models. With appropriate calibration and further validation studies, a revised *OpenSees* program can be used to predict hysteretic response of existing shear-critical, RC beam-column frames under seismic & gravity loading. Further, based on individual RC column component validation tests, *OpenSees* would make it possible to predict the deformation response of existing, multistory RC building frames subjected to gravity load and various MDOF seismic loading patterns.

ACKNOWLEDGEMENTS

This research was conducted as part of the 2004 Pacific Earthquake Engineering Research Center (PEER) Research Experience for Undergraduates and funded in part by PEER through the Earthquake Engineering Research Centers Program of the National Science Foundation. I would like to give special thanks to my PEER advisor, Professor Jack P. Moehle for his patience and guidance in the direction of my project and working hard to secure the funding which made this research experience possible. I would like to thank UC Berkeley graduate students, Wassim Michael Ghannoum & Yoon Bong Shin for their assistance in every aspect of this project. Also, I would like to thank the PEER laboratory personnel for their advice, hard work and constructive feedback in the design & fabrication of my experimental setup, as well as their assistance in the experimental phase of my project.

REFERENCES

- [1] MacGregor, J. G. G. Reinforced Concrete: Mechanics and Design. Prentice Hall Professional Technical Reference, 1996.
- [2] Elwood, K.J. and Moehle, J.P. “*Shake Table Tests and Analytical Studies on the Gravity Load Collapse of Reinforced Concrete Frames*”, PEER Report Series, November 2003/01.
- [3] Lehman, D.E. and Moehle, J.P. “*Seismic Performance of Well-Confined Concrete Bridge Columns*”, PEER Report Series, December 1998/01.
- [4] Esmaeily-Gh., A. and Xiao, Y. “*Seismic Behavior of Bridge Columns Subjected to Various Loading Patterns*”, PEER Report Series, December 2002/15.

Appendix A

A.1 CONCRETE COMPOSITION MIX

3/8 in. size Aggregate (1% Moisture): 1120 Lb.

Sand (6.4% Moisture): 1820 Lb.

Cement: 725 Lb. (9 sacks)

Fly Ash: 125 Lb.

Water Reducing Admixture: 25 Oz.

Water: 10 Gals.

A.2 DATA REDUCTION – MATLAB CODE

Data Reduction for Specimen 1:

```
/** cycle 1 data for specimen 1 - actuator startup **/
data1 = load('04090201.txt');
/** cycle 2 data for specimen 1 - before yield **/
data2 = load('04090202.txt');
/** cycle 3 data for specimen 1 - after yield **/
data3 = load('04090203.txt');
/** cycle 4 data for specimen 1 - nothing **/
data4 = load('04090204.txt');
/** cycle 5 data for specimen 1 - shear failure, then axial load failure **/
data5 = load('04090205.txt');

/** gets time sequence from start to end of testing **/
t1 = data1(:,1);
t2 = data2(:,1) + max(t1);
t3 = data3(:,1) + max(t2);
t4 = data4(:,1) + max(t3);
t5 = data5(:,1) + max(t4);
time = [t1',t2',t3',t4',t5'];

/** gets actuator force recorded over entire test sequence **/
force = [data1(:,3)',data2(:,3)',data3(:,3)',data4(:,3)',data5(:,3)'];
/** gets column tip displacement recorded over entire test sequence **/
dispt = -[data1(:,4)',data2(:,4)',data3(:,4)',data4(:,4)',data5(:,4)'];

/** plots actuator (SHEAR) force vs. time - shear loading history **/
plot(time,force); grid; xlabel('seconds'); ylabel('kips');

/** plots column tip (lateral) displacement vs. time - applied displacement history **/
plot(time,dispt); grid; xlabel('seconds'); ylabel('inches');

/** plots actuator (SHEAR) force vs. column tip (lateral) displacement - shear hysteretic
response graph **/
plot(dispt,force); grid; xlabel('inches'); ylabel('kips');
```

Data Reduction for Specimen 2:

```
/** cycle 1 data for specimen 2 - actuator startup **/
data1 = load('04083101.txt');

/** cycle 2 data for specimen 2 - before yield **/
data2 = load('04083102.txt');

/** cycle 3 data for specimen 2 - after yield **/
data3 = load('04083103.txt');

/** cycle 4 data for specimen 2 - nothing **/
```

```

data4 = load('04083104.txt');

/** cycle 5 data for specimen 2 - shear failure, then axial load failure **/
data5 = load('04083105.txt');

/** gets time sequence from start to end of testing **/
t1 = data1(:,1);
t2 = data2(:,1) + max(t1);
t3 = data3(:,1) + max(t2);
t4 = data4(:,1) + max(t3);
t5 = data5(:,1) + max(t4);
time = [t1',t2',t3',t4',t5'];

/** gets actuator force recorded over entire test sequence **/
force = [data1(:,3)',data2(:,3)',data3(:,3)',data4(:,3)',data5(:,3)'];
/** gets column tip displacement recorded over entire test sequence **/
dispt = -[data1(:,4)',data2(:,4)',data3(:,4)',data4(:,4)',data5(:,4)'];

/** plots actuator (SHEAR) force vs. time - shear loading history **/
plot(time,force); grid; xlabel('seconds'); ylabel('kips');

/** plots column tip (lateral) displacement vs. time - applied displacement history **/
plot(time,dispt); grid; xlabel('seconds'); ylabel('inches');

/** plots actuator (SHEAR) force vs. column tip (lateral) displacement - shear hysteretic
response graph **/
plot(dispt,force); grid; xlabel('inches'); ylabel('kips');

```


ESTIMATING SEISMIC DAMAGE AND REPAIR COSTS

Raymond Foltz

The Citadel

Texas A&M

Advisor: Dr. Mary Beth Hueste

August 2004

Abstract

Since many structures in seismic regions are seismically vulnerable, building owners and decision makers must determine whether they will rehabilitate their structures. While this may seem to be a simple decision, in business it could possibly not be justified to retrofit, especially if the retrofitting costs are very large or the probability of a damaging earthquake is exceedingly low. Significant research exists pertaining to the cost to retrofit certain structures; however, less information is available to estimate the cost to repair an unretrofitted building following a damaging earthquake, an essential piece of information for the decision-making process. Because the level of earthquake damage is directly connected to the cost to repair the building, this report also investigates the relationship between interstory drift ratios and various levels of damage. A case-study is developed for a 1980s five-story reinforced concrete in Memphis, Tennessee, and the cost to repair the structure for specific scenario earthquakes is explored.

Introduction

The Mid-America Earthquake (MAE) Center project CM-4, entitled “Structure Retrofit Strategies,” is mainly concerned with different seismic intervention techniques, but the aspect of the project discussed in this paper focuses on damage estimation and the cost of repair. In many instances, this information will be an impetus to lead building owners to strongly consider an intervention technique, in which case the rest of the project’s findings will prove quite germane. The New Madrid Seismic Zone has not experienced a devastating earthquake in a long period. While the probability of such an event is lower than on the West Coast of the United States, the consequences of such an event would be severe. The notorious earthquakes during the winter of 1811-1812 were some of the largest in recorded history; however, there were less than four thousand denizens in the area. Now, Memphis, Tennessee and St. Louis, Missouri alone contain a population several hundred times that size. Also, many of the buildings which have been constructed since were built to an antiquated and inadequate code for earthquake demands, so seismic intervention is a very real concern. The MAE Center has been working on a new paradigm called Consequence-Based Engineering (CBE), which essentially focuses on regional seismic risk reduction and quantifies risks for policy and decision-makers. This research addresses one component of the CBE paradigm.

Currently, policy makers and building owners must decide whether or not they want to retrofit their structures. With adequate information to present the advantages and costs of each option, the decision would be quite obvious to the decision maker; however, a void exists in the information. While information concerning the cost of seismic rehabilitation or retrofitting of buildings has been documented in both FEMA 156 (Hart 1994) and FEMA 157 (Hart 1995), there is not an analogous amount of information pertaining to the cost to repair a damaged building. Such information would greatly benefit the decision makers within a community. If there were a low probability that an earthquake of a severe magnitude would occur, and if the cost to repair the building were not large, then perhaps it would be more cost effective to not retrofit. At the same time, if the cost to repair a building after a very mild earthquake were

substantial, then perhaps this information would be a very telling case in favor of retrofitting. Therefore, information quantifying expected earthquake damage and cost of repair is an integral part of the decision to retrofit a building. Further still, earthquake loss estimation is an essential part of preparing for a disaster and for good decision making at the local, regional, state, and national levels of government. If one can estimate the loss, then one could effectively prioritize retrofit or seismic intervention programs, if one decides that he or she wants to retrofit. Emergency response and contingency planning are also benefited by loss estimation because it could be predicted where extensive damage may take place. Clearly, damage estimation and the cost to repair these buildings is a very important part of CBE.

Damage Estimation

Traditionally, building codes emphasized life safety as their primary goal in design, but life safety criteria may not be sufficient to ensure the building maintains functionality after an earthquake. Therefore, the social and economic impacts caused by the loss of a building's function have led to a desire to better control damage. It has been generally accepted that interstory drift can be used to gauge expected damage. Thus, to limit and estimate damage, one must understand the relationship between interstory drift and the corresponding level of damage. Further, performance objectives are often described in several ways according to the level of damage. In performance-based design, it is then important to identify the drift associated with various damage levels of different structural elements and systems.

Performance-based design is a design philosophy where the design objectives are expressed in terms of defined performance limits when subjected to certain levels of seismic hazard. The first requirement is to define different performance levels. Figure 1 provides an example of performance levels in terms of a generic capacity curve for reinforced concrete structures. The structure is considered to suffer no damage up to concrete cracking. Between concrete cracking and the steel's first yield, crack sizes should still be less than two millimeters and the damage is considered repairable. Beyond steel yield, where cracks are wider than two millimeters, repairs can be impractical and costly, thus irreparable damage is noted. One must note that this is for ductile systems. Nonductile systems, however, may experience brittle failure at any point along the capacity curve (Ghobarah 2004).

Relating basic displacement or drift limits to damage is an oversimplification because the level of damage is also influenced by the structural system, the distribution of damage, the failure mode of the elements, the non-structural elements, and the specific characteristics of the earthquake. Likewise, the difference in each specific building requires different drift limits for each type of structural system. Ghobarah (2004) defined the different damage states as no damage, repairable, irreparable, and severe. He defined "no damage" as no structural damage observed; "repairable damage" as light damage, such as hairline cracks, and moderate damage, such as flexural and shear cracking in beams and columns; "irreparable damage" as yielding of steel reinforcement such that cracks are larger than two millimeters; and "extreme damage" as

partial collapse of lateral and gravity load carrying elements, as well as shear failure of columns and failure of infill walls.

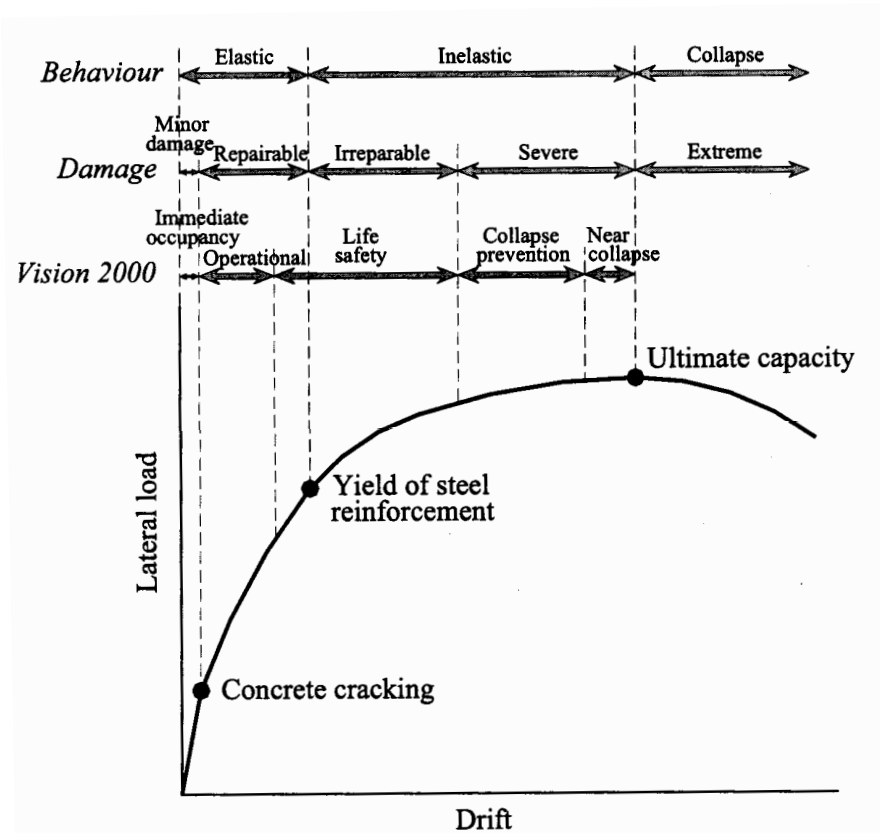


Figure 1. Typical structural performance and respective damage levels (Ghoborah 2004)

Three structural characteristics tend to dominate performance: stiffness, strength, and deformation capacity. Often it is difficult to determine which characteristic is dominating performance because they may impose conflicting demands on each other. Ductility describes a building's ability to deform. Since drift limits will vary significantly for ductile and nonductile systems, it is necessary to assign different drift thresholds for the associated damage states of each type of building system (Ghoborah 2004). For this purpose, Ghoborah (2004) defined five structural systems. Reinforced concrete moment resisting frames were divided into three categories: ductile, nonductile, and moment resisting frames with masonry infills. Structural walls were divided into two categories: flexural structural walls with an aspect ratio (height/length) greater than 1.5 and squat walls with an aspect ratio less than 1.5. Sometimes roof drift is related to damage, but that does not consider the distribution of the drift along the height of the structure or identify weaker elements, such as soft stories. Thus, Table 1 defines interstory drift thresholds for the defined structural systems and damage states. The drift limits are defined based on experimental data and theoretical analyses, but they could all be further refined with additional testing.

Table 1. Drift ratio (%) limits associated with various damage levels for reinforced concrete structures (Ghoborah 2004)

State of Damage	Ductile MRF	Nonductile MRF	MRF with Infills	Ductile Walls	Squat Walls
No Damage	< 0.2	< 0.1	< 0.1	< 0.2	< 0.1
Repairable Damage a)Light b)Moderate	0.4 < 1.0	0.2 < 0.5	0.2 < 0.4	0.4 < 0.8	0.2 < 0.4
Irreparable Damage (>yield point)	> 1.0	> 0.5	> 0.4	> 0.8	> 0.4
Severe Damage-Life safe-Partial Collapse	1.8	0.8	0.7	1.5	0.7
Collapse	> 3.0	> 1.0	> 0.8	> 2.5	> 0.8

While many have assigned drift values to different thresholds of damage, Mayes (1995) states that little data exists on the direct relationship between drift and structural damage because it is difficult to develop and it depends on the more complex relationships among drift, ductility, and stiffness. Mayes (1995) also assigns drift values to damage, and he believes that current code provisions are adequate for the 475-year design event or a 2% to 6% drift ratio. However, these limits are well beyond the non-structural damage threshold, which he believes to be between 0.5% and 2% drift.

FEMA 356 (ASCE 2000) also prescribes drift values that are considered typical values to illustrate the overall structural response related to various defined performance levels. However, they are not provided as drift limit requirements for the standard, and do not supersede the member-level analysis which assesses plastic rotation. Table 2 summarizes the structural performance levels and damage to vertical elements found in FEMA 356.

Table 2. FEMA 356 structural performance levels and damage for vertical elements in concrete frames (ASCE 2000)

	Collapse Prevention	Life Safety	Immediate Occupancy
Damage Description	Extensive cracking and hinge formation in ductile elements. Severe damage in short columns.	Extensive damage to beams. Spalling of cover and shear cracking <1/8" for ductile columns.	Minor hairline cracking. Limited yielding possible at a few locations.
Drift	4% transient or permanent	2% transient; 1% permanent	1% transient; negligible permanent

The FEMA 356 drift limits are guidelines for a global analysis of a structure, but a more extensive member analysis is recommended to check for the development of plastic hinges. The relationship between drift and damage certainly exists, but damage cannot be completely predicted using only drift because of the complex relationships of other building characteristics. Further, most established damage-drift relationships are created upon a limited amount of data, so more extensive and collaborative research would help refine these guidelines.

Estimation of Repair Costs

General

While being able to estimate the damage using different drift limits is very useful, the more telling data for decision-makers would be the cost to repair a building given a certain damage state following a seismic event. The objective is to provide the decision-makers with the proper information when deciding whether to mitigate or to allow the building to remain as built. There is a considerable amount of uncertainty in loss prediction and since rapid compilation of actual losses is feasible, a strong emphasis has not really been placed on loss estimation. However, it is important to predict losses. Often such information will prove to be a very telling case for retrofitting because of the possible negative economic impacts and the potential for injuries and casualties.

Before one can begin to estimate losses, it is necessary to understand the different variables and cost influence factors involved in estimation. The estimation procedure must first consider the area where the structure is located. The seismicity of the region and the earth's ability to attenuate the energy in the particular location is the primary information about the region required for loss estimation. However, the areal inspection should not be limited to seismicity. Also important is the potential for fires, tsunamis, landslides, and the release of hazardous materials in the event of an earthquake. These factors are considered induced damages because they are secondary consequences of a natural hazard other than damage resulting from the primary hazard that led to losses (Whitman et al., 1997). The next major aspect to consider is the building. The structural system is the main factor, but also important is the size of the building, the occupancy, and the age. The next step is to consider the different

types of potential damage. Direct costs are the costs to repair damage to the building as a result of the earthquake. The direct costs can be divided into structural damage, nonstructural damage, and content damage. Depending on building type, the value of the structure ranges from about 10% to 25% of the construction cost, while the non-structural components range from about 12% to 33%, and thus the larger proportion of the investment in the building is in the non-structural components (Mayes 1995). Because structural and nonstructural damage affect costs differently, they must be considered separately. In fact, nonstructural components need to be subdivided into drift sensitive elements, such as windows and infills, and acceleration sensitive elements, such as mechanical equipment and ceiling tiles. Indirect costs are the final cost consideration, and they consider lost income, temporary housing, unemployment costs, and economic impacts to the community. Since each building has unique nonstructural components and contents, an updated inventory is necessary to predict damage. For the purpose of this research, damage to contents, nonstructural damage, and indirect costs will not be considered.

Methodologies and Case Study

There have been several different methodologies developed to predict building-specific losses as a result of an earthquake. The most notable is the Federal Emergency Management Agency's (FEMA) methodology, which was developed through the National Institute of Building Sciences (NIBS). This methodology starts with an inventory on general building stock, essential and high potential loss facilities, utility systems, and transportation systems. The next step is to develop the ground motion of the scenario earthquake event, input ground motion with attenuation relationships, and overlay geologic information. Damages are then considered, starting with direct damage in terms of probabilities of occurrence for specific damage states, and then considering induced damage, which are secondary consequences of a natural hazard. Finally, the method will predict the direct losses, which include cost of repair, replacement of structures, casualties, loss-of-function losses, casualties, and short-term shelter needs (Whitman et al., 1997).

Porter et al. (2001) developed a building-specific loss estimation technique. Their method uses mean repair cost for each damage state by component category and then sums the individual results for the total cost. First, one must know the location, site, and design details. Next, an acceleration time history appropriate to the site is selected. A structural analysis is then performed to determine peak structural response, and the parameters are recorded. For each building assembly input parameter, fragility functions are referenced to determine the probability of damage or repair. A probability density function (PDF) for each unit cost and another PDF for the time of repair is assessed to determine individual cost contributions. The total costs are then added to arrive at a total cost of repair (Porter et al. 2001).

The Applied Technology Council's study, ATC-21 (ATC 1988), provides another method to predict loss as a percentage of the building replacement cost. First, one must identify the building type and the NEHRP map area corresponding to the effective peak acceleration likely to occur during the life of the building. These factors will give the Basic Structural Hazard score, which ranges from 1.0 to 8.5. The next considerations are Performance Modifiers, which range from -2.5 to +2.0, depending on whether they modify or detract from the overall seismic

performance of the building. The Structural Score is the sum of the Basic Structural Score and all of the Performance Modifiers. The Structural Score can then be graphed versus a defined Mean Damage Factor to express the damage incurred as a percent of replacement cost (McCormack 1997).

For this study, a method developed by Hwang et al. (1994) is used to estimate building losses in Memphis, Tennessee. To illustrate the method, a case study building is used. The case study building is a five-story reinforced concrete building designed for the mid-1980s building codes for Memphis, Tennessee (Bai 2004). The method used will begin with the selection of the scenario earthquakes. The earthquakes were selected from the seismic hazard curve, shown in Appendix 1 and established by Hwang et al. (1994), considering the probabilities of exceedance and return period. The scenario earthquakes selected had 0.1g, 0.2g, and 0.3g peak ground accelerations (PGA), and the estimated return periods are 325, 1,409, and 3,891 years, respectively. The next step is to gather attribute data about the buildings in question. The case study building is a 78,400 square foot concrete moment frame, which corresponds to building code seven. The complete table of building codes is shown in Appendix 2. Next, a structural score must be determined using the ATC-21 structural form score (ATC 1988). These scores are used to create a seismic vulnerability index (SVI), which rates the buildings as a 1, 2, or 3, where the magnitude of the number is indicative of the seismic risk. The case study building was considered to have a moderate seismic risk, and thus an SVI rating of 2.

In 1985, the Central United States Earthquake Preparedness Project (CUSEPP) developed fragility curves for Memphis (FEMA 1985). These curves were adopted for this research, although Hwang et al. (1994) considers the damage estimation to be slightly too conservative for reinforced concrete structures. Five damage states were defined for the study: (1) nonstructural damage, (2) slight structural damage, (3) moderate structural damage, (4) severe structural damage, and (5) collapse. Table 3 displays the central damage ratio and the range of damage ratio. The central damage ratio is the ratio of the average cost of repair to the cost for building replacement (Hwang et al. 1994).

Table 3. Damage ratios corresponding to various damage states (Hwang et al.1994)

Damage State	Damage Ratio (%)	Central Damage Ratio (%)
1.Nonstructural Damage	0.05-1.25	0.3
2. Slight Structural Damage	1.25-7.50	3.5
3. Moderate Structural Damage	7.5-20	10
4. Severe Structural Damage	20-90	65
5. Collapse	90-100	95

The fragility curve for the Memphis area that corresponds to the case study building is shown in Appendix 3. The appropriate curve is selected based on the basis of type of construction, number of stories, and seismic vulnerability index. The fragility curve can then be used to predict the probability damage state, PDS_{ij} , given the PGA equal to a_j and damage state i . PF_{ij} is the probability that damage will exceed the i -th damage state with PGA equal to a_j . The damage state can thus be determined from fragility curves using the following formulas:

$$PDS_{ij} = PF_{ij} - PF_{i+1j} \quad \text{when } i \text{ does not } = 5 \quad (\text{Equation 1})$$

$$PDS_{ij} = PF_{ij} \quad \text{when } i = 5$$

Table 4 shows the probability of each damage state for the case study building given the three scenario earthquakes, determined from the fragility curve provided in Appendix 3.

Table 4. Probability of each damage state given the defined scenario earthquake for the case study

	0.1g PGA	0.2g PGA	0.3g PGA
(1) Nonstructural Damage	47%	5%	0%
(2) Slight Structural Damage	47%	50%	18%
(3) Moderate Structural Damage	3%	45%	77%
(4) Severe Structural Damage	0%	0%	4%
(5) Collapse	0%	0%	0%

Now that the probability of each damage state for each scenario earthquake has been established, the direct cost of repairing the building may be calculated. The cost from repairing or replacing the contents and the indirect costs of the damage to the structure are not considered for this research. The central damage ratios from Table 1 can be used to compute the mean damage ratio (MDR_j) for an earthquake with PGA equal to a_j using the following equation:

$$MDR_j = \sum PDS_{ij} * CDR_i \quad (\text{Equation 2})$$

Once the mean damage ratios have been computed, the damage cost, DC_j , for an earthquake with PGA equal to a_j can be computed for the building. The following equation was used to calculate the damage costs, where RPV is the replacement cost of the building:

$$DC_j = MDR_j * RPV \quad (\text{Equation 3})$$

Table 5 summarizes the results of the aforementioned calculations for the case study building. The replacement cost was obtained using information from the Dodge Estimating Guide, and it was determined to be \$3,832,354 (National Building Cost Manual 2004). FEMA 228 (1992) recommends using estimating guides, such as Dodge, Means, or other national square foot cost estimating guides to obtain replacement values of buildings.

Table 5. Summary of case study mean damage ratios and estimated damage costs

Scenario Earthquake	Mean Damage Ratio	Damage Cost (dollars)
0.1g PGA	0.021	79,943
0.2g PGA	0.063	240,097
0.3g PGA	0.109	418,877

Conclusions

This study investigated the relationship between drift and damage during an earthquake, as well as the repair cost for buildings damaged in an earthquake. It was found that many variables affect the damage resulting from an earthquake, and it would often be an oversimplification to use only drift to predict the damage level. Drift estimates are beneficial to overall damage estimation, but are only one component of a more comprehensive loss analysis. Estimations of this nature are difficult to do on a building-specific basis because of the unique nature of each individual building. A complete and thorough inventory of the building would be necessary to get more accurate results, and even then the estimation would be subject to considerable uncertainty. Likewise, cost estimation to repair a building is subject to similar uncertainty. The estimations will typically show that the repair cost is a relatively low percentage of the replacement, but the estimations neglect casualties and other factors which a decision-maker should consider. Nonetheless, estimations are useful to quantify the predicted damage, and to afford decision-makers the opportunity to make a more educated choice when contemplating mitigation techniques and when establishing emergency response agendas. Much more research could be conducted in both of these arenas to further mitigate earthquake damage and to establish an extensive foundation of information.

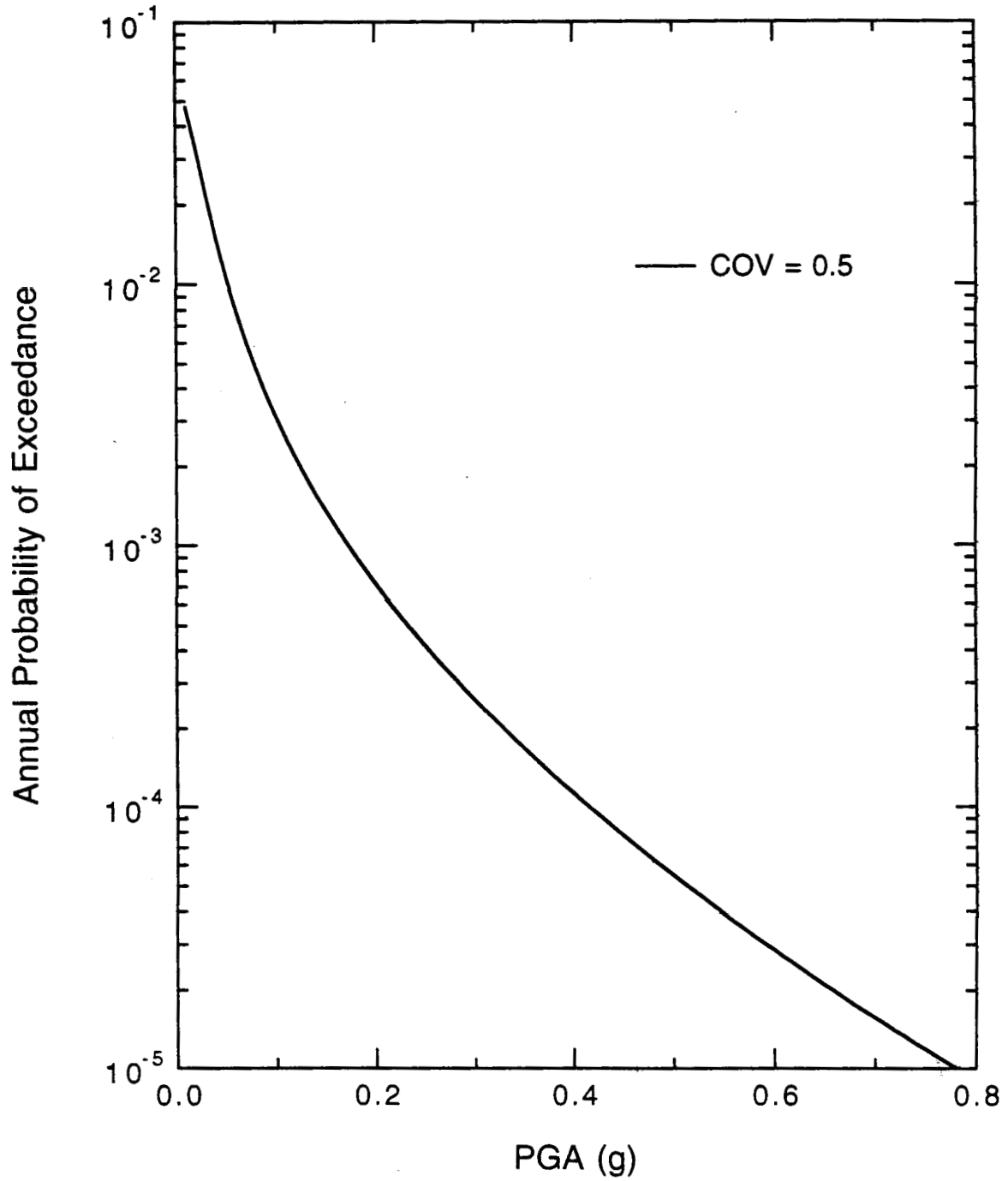
References

- ASCE (2000), *Prestandard and Commentary for the Seismic Rehabilitation of Buildings* (FEMA 356), prepared by American Society of Civil Engineers for the Federal Emergency Management Agency, Washington D.C.
- Applied Technology Council (1988), "Rapid Visual Screening of Buildings for Potential Seismic Hazards: A Handbook," ATC-21, Redwood City, California.
- Bai, Jong-Wha (2004). "Seismic Fragility and Retrofitting for a Reinforced Concrete Flat-Slab Structure," *MS Thesis*, Department of Civil Engineering, Texas A&M University, College Station, TX.
- Erduran, E. and Yakut, A. (2004), "Drift Based Damage Functions for Reinforced Concrete Columns," *Computers & Structures*, Vol. 82, pp. 121-130.
- FEMA (1985), "An Assessment of Damage and Casualties for Six Cities in the Central United States Resulting from Earthquakes in the New Madrid Seismic Zone," Report for Central United States Earthquake Preparedness Project, Federal Emergency Management Agency, Washington, D.C.
- FEMA (1992), *A Benefit-Cost Model for the Seismic Rehabilitation of Buildings* (FEMA 228), prepared by VSP Associates, Inc. for the Federal Emergency Management Agency, Washington D.C.
- Ghobarah, A. (2004), "On Drift Limits Associated with Different Damage Levels," *International Workshop on Performance-Based Seismic Design*, Department of Civil Engineering, McMaster University, June 28-July 1, 2004.
- Hart (1994). *Typical Costs for Seismic Rehabilitation of Existing Buildings, Volume I: Summary (FEMA 156)*, prepared by the Hart Consultant Group for the Federal Management Agency, Washington, D.C.
- Hart (1995). *Typical Costs for Seismic Rehabilitation of Existing Buildings, Volume II: Supporting Documentation (FEMA 157)*, prepared by the Hart Consultant Group for the Federal Management Agency, Washington, D.C.
- Hwang, H.M., Xu, M., and Huo, J.-R. (1994), *Estimation of Seismic Damage and Repair Cost of the University of Memphis Buildings*, Memphis, Tennessee.
- Kircher, C.A., Nassar, A.A., Kustu, O., and Holmes, W.T. (1997), "Development of Building Damage Functions for Earthquake Loss Estimation," *Earthquake Spectra*, Vol. 13, No. 4, November 1997, pp. 663-682.

- Kircher, C.A. and Whitman, R.V. (1997), "Estimation of Earthquake Losses to Buildings," *Earthquake Spectra*, Vol. 13, No. 4, November 1997, pp. 703-719.
- Mayes, R.L. (1995), "Interstory Drift Design and Damage Control Issues," *The Structural Design of Tall Buildings*, Vol. 4, pp. 15-25.
- Miranda, E. and Aslani, H. (2002), "Building-Specific Loss Estimation Methodology," *Report to PEER*, March 2002.
- McCormack, T.C. and Rad, F.N. (1997), "An Earthquake Loss Estimation Methodology for Buildings Based on ATC-13 and ATC-21," *Earthquake Spectra*, Vol. 13, No. 4, November 1997, pp. 605-621.
- National Building Cost Manual. (2004), "Craftsman Book Company – Construction Estimating Software – National Estimator," <<http://costbook.com>>, 3 August 2004.
- Porter, K.A., Kiremidjian, A.S., and LeGrue, J.S. (2001), "Assembly-Based Vulnerability of Buildings and Its Use in Performance Evaluation," *Earthquake Spectra*, Vol. 17, No. 2, May 2001, pp. 291-312.
- Porter, K.A., Beck, J.L., and Shaikhutdinov, R.V. (2002), "Sensitivity of Building Loss Estimates to Major Uncertain Variables," *Earthquake Spectra*, Vol. 18, No. 4, November 2002, pp. 719-741.
- Whitman, R.V., Anagnos, T., Kircher, C.A., Lagorio, H.J., Lawson, R.S., and Schneider, P. (1997), "Development of a National Earthquake Loss Estimation Methodology," *Earthquake Spectra*, Vol. 13, No. 4, November 1997, pp. 643-661.

Appendix 1

Seismic Hazard Curve for the Memphis Area (Hwang et al. 1994)



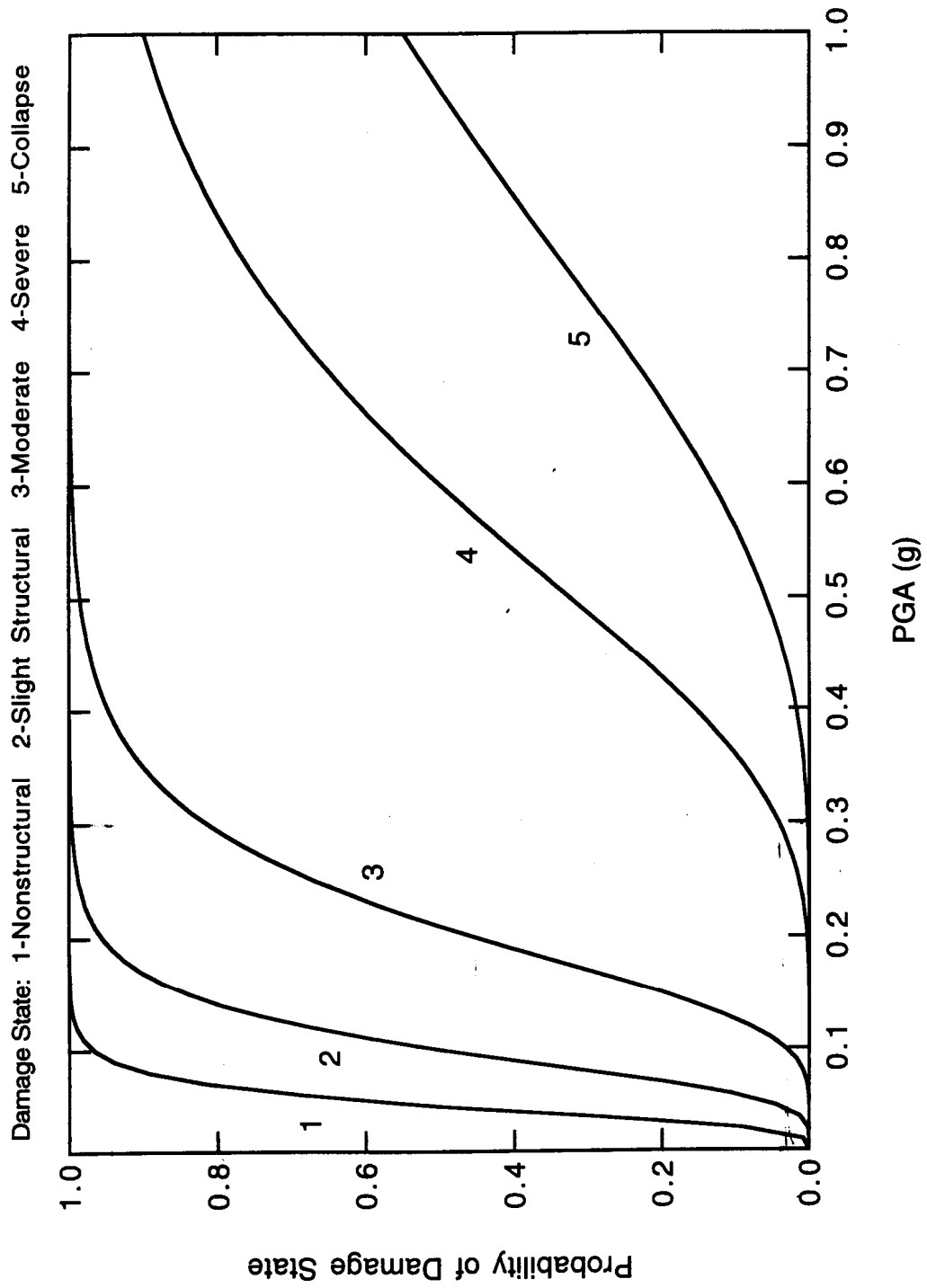
Appendix 2

Codes of Construction Type (Hwang et al. 1994)

Code	Description
1	Wood frame building
2	Wood frame with brick veneer
3	Load-bearing masonry walls and wood construction
4	Load-bearing masonry walls and steel construction
5	Steel construction and masonry walls
6	Lift-slab, reinforced concrete construction
7	Reinforced concrete construction
8	Quonsets and temporary steel buildings
9	Other construction
10	Load-bearing masonry walls and concrete construction
0	Unknown

Appendix 3

Fragility Curve for a Concrete Structure with Moderate Seismic Vulnerability in Memphis, TN
(1-5 stories) (Hwang et al. 1994)



BUILDING LOSS MODELING AND BENCHMARKING: EDP TO DV

Author Name: Vivian D. Gonzales
Home Institution: University of California, San Diego
REU Institution: California Institute of Technology
REU Advisor: Keith A. Porter, Judith Mitrani-Reiser

Abstract

The approach pursued by the Pacific Earthquake Engineering Research (PEER) Center to performance-based earthquake engineering is developed in four stages: hazard analysis, structural analysis, damage analysis and loss analysis. This paper summarizes the last two stages of the approach - damage and loss analysis conducted at the California Institute of Technology. In the damage analysis, engineering demand parameters (EDP) such as accelerations, ground failure and drifts are used with fragility functions of the many components (assemblies) that constitute a facility. Once the EDP's are used with the fragility functions one can determine the measures of damage (DM) of the components of a facility. In the loss analysis, the DM's obtained are used to evaluate the decision variables (DV) of a facility. The decision variables measure the seismic performance of the facility in terms of death, dollars, and downtime.

The main objectives of this project is to evaluate and benchmark the performance of new reinforced-concrete building, and to simplify and package the algorithms that describe the probability distribution of damage measures (DM) and decision variables (DV). The packaged algorithms will facilitate implementation by other users of OpenSees or other automated performance based earthquake engineering generation II (PBEE-2) evaluation code. Also, the packaged algorithms and data will facilitate the evaluation of the probabilistic relationship between EDP and DM, and DM and DV.

Introduction

There are various methodologies for developing performance-based earthquake engineering (PBEE). This particular methodology is through the Pacific Earthquake Engineering Research (PEER) Center.

PBEE is a framework by which many structures (existing or new) are analyzed for their seismic performance. PBEE focuses on the seismic performance of the structure through decision variables (DV). The decision variables measure the performance of a facility in terms of repair costs, fatalities, risk of collapse and post-earthquake operability (Porter, 2003).

PEER's PBEE approach has four stages: hazard analysis, structural analysis, damage analysis and loss analysis. Research conducted at Caltech, Stanford and UCLA are making this project possible. Each university focuses on a specific stage of the project. As shown below in Fig.1, is PEER's methodology. The UCLA team research on the hazard analysis, Stanford on the structural analysis and Caltech on the damage and loss analysis (circled in red). Thus, one of Caltech's goals is to Benchmark PEER's PBEE-2 methodology for calculating damage and loss for IBC-2003 compliant buildings. Calculating the damage and loss of buildings would be very beneficial for facility stakeholders since it would provide them with valuable information such as repair cost, fatalities and downtime (Porter, 2003).

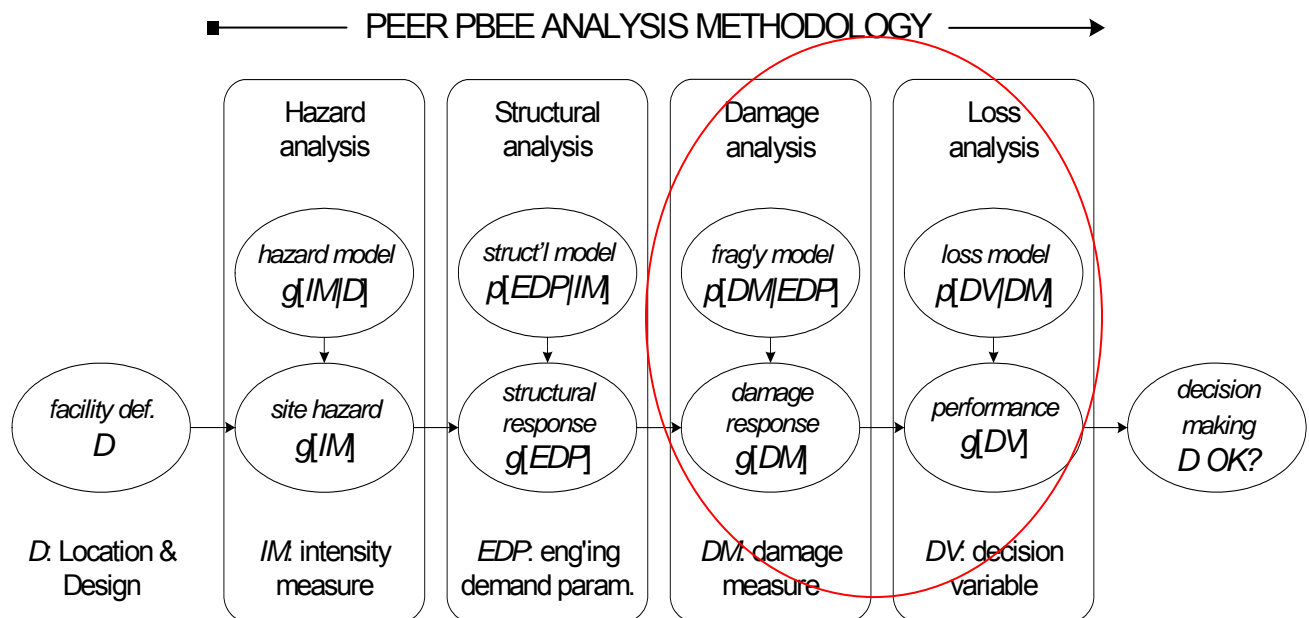


Fig. 1 (PEER Analysis Methodology, Mitrani 2004)

My contribution to the project

The algorithms of dollars, death and downtime were packaged by creating libraries of logarithmic medians and standard deviations for capacity and for repair costs of damageable assemblies. For example, I found the logarithmic median and standard deviations for the capacity of different assemblies using fragility curves illustrated below in Fig. 2. Fragility functions were obtained from different sources such as, lab experiments, analytical, earthquake data, and engineering judgment.

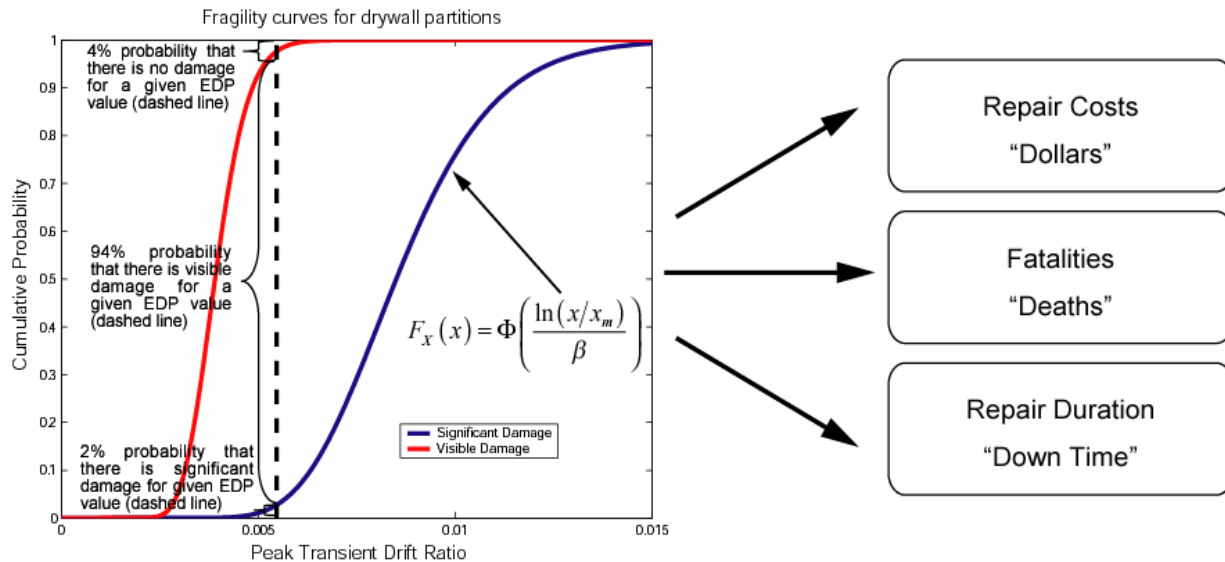


Fig. 2 (Fragility curves for drywall partitions, Mitrani 2004)

Once the algorithms are packaged they are used with a Matlab toolbox that will run a “Monte Carlo Simulation”—a method for propagating uncertainties. As shown above, in Fig. 2 after using the information from the fragility curves of assemblies (in this case, drywall partitions) and using it in a Matlab program, we get a probability of the assembly performance in terms of: dollars, death and downtime.

However, before running this analysis with Matlab and packaging all the algorithms, it is necessary to have an inventory of a specific structure to be tested. Thus, with the floor plans of an “imaginary building” at UC Merced, it was possible to learn about the different assemblies that make up a building. Reviewing the floor plans of that building was very informative.

With the help of the UC Merced library floor plans, I created an imaginary building. The design was made with Microsoft Office Visio 2003; however the structural design (columns, beams and dimensions) was provided by the team at Stanford as shown in Figs. 3, 4.

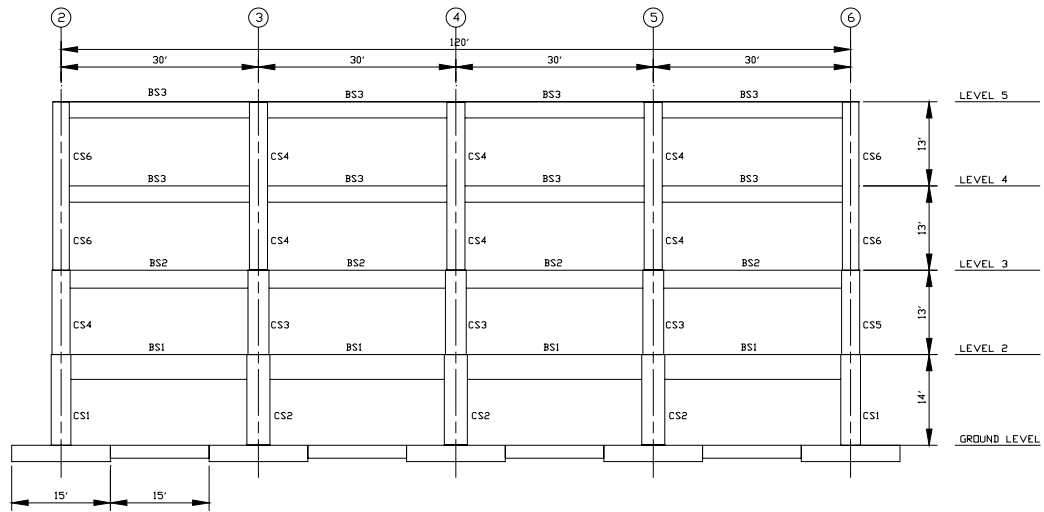


Fig. 3 (Mean Frame Elevation)

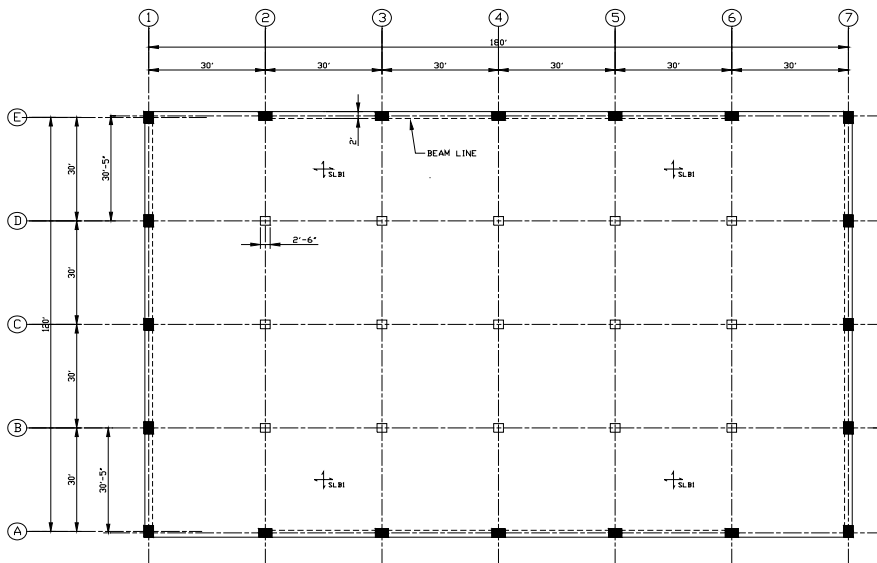


Fig. 4 (Plan View)

The “imaginary building” has 4 levels and the inside design for levels 1 and 2-4 are shown in Figs. 5, 6.

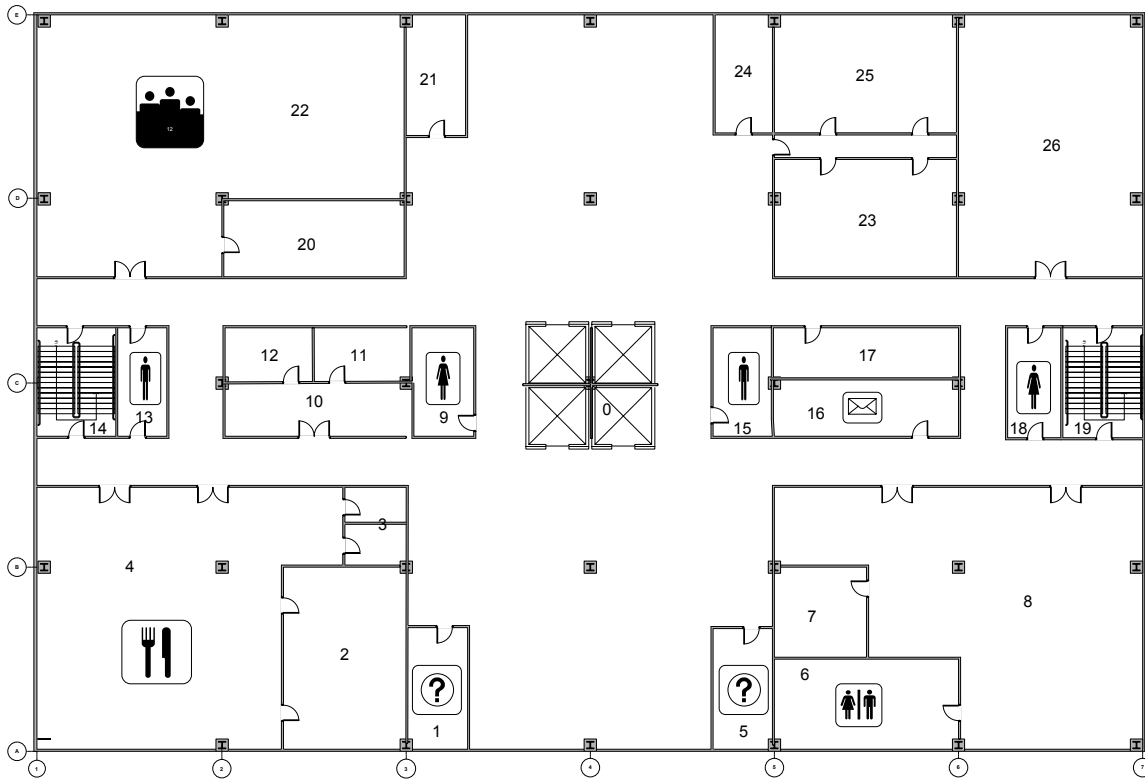
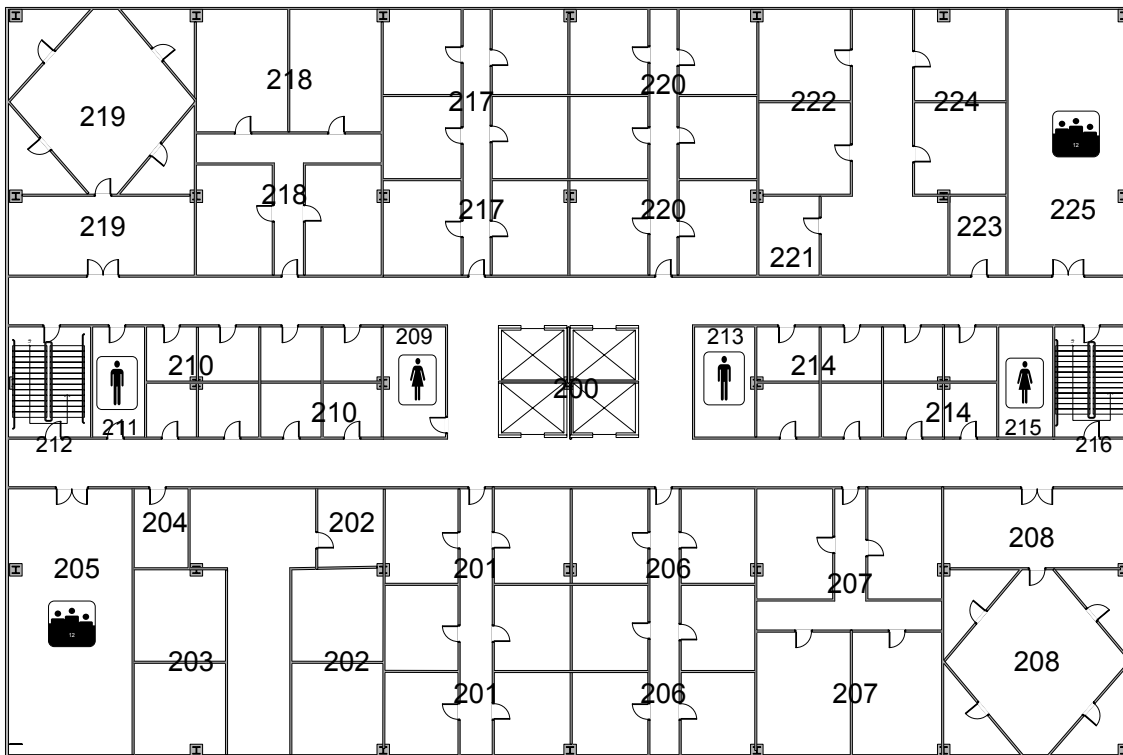


Fig. 5 (Level 1, author’s work)



(Level 2-4, author’s work)

Fig. 6

After creating the design of this ‘imaginary building,’ it was necessary to create an inventory of all the assemblies (of structural importance) that make up the building. Creating an inventory of all the assemblies is necessary in order to have a table that includes the logarithmic medians and standard deviations for capacity and for repair costs of all the damageable assemblies. Shown below in Fig. 7 is an example of the inventory of assemblies with the logarithmic medians and standard deviation for capacity and repair cost, depending on their limit state. The limit state ranges from 1-4, from least damage to complete collapse, respectively. This particular example was taken from a 66,000sf, seven-story hotel building located in Van Nuys, California. The ‘imaginary building’ that was created with Visio has not been tested yet; however, the example of the Van Nuys Hotel will suffice to explain the process of this project.

Taxonomy		Fragility			Loss		
Assembly description	Unit	Limit state; repair	EDP ⁽¹⁾	Capacity		Cost, \$	
				x_m	β	x_m	β
Stucco finish, 7/8", 3-5/8' metal stud, 16"OC	64 sf	1. Cracking; patch	PTD	0.012	0.5	125	0.2
Drywall fin., 5/8-in., 1 side, metal stud, screws	64 sf	1. Visible dmg; patch	PTD	0.0039	0.17	88	0.2
Drywall fin., 5/8-in., 1 side, metal stud, screws	64 sf	2. Signif. Dmg; replace	PTD	0.0085	0.23	253	0.2
Drywall ptrn., 5/8-in., 1 side, metal stud, screws	64 sf	1. Visible dmg; patch	PTD	0.0039	0.17	88	0.2
Drywall ptrn., 5/8-in., 1 side, metal stud, screws	64 sf	2. Signif. Dmg; replace	PTD	0.0085	0.23	525	0.2
Nonductile CIP RC beam or column	ea	1. Light, epoxy	PADI	0.08	1.36	8000	0.42
Nonductile CIP RC beam or column	ea	2. Moderate; jacket	PADI	0.31	0.89	20500	0.4
Nonductile CIP RC beam or column	ea	3,4. Severe or collapse; replace	PADI	0.71	0.8	34300	0.37
Window, AL frame, sliding, hvy sheet glass	ea	1. Cracking; replace	PTD	0.023	0.28	180	0.2
Paint on exterior stucco or concrete	sf	Paint	(2)	N/A		1.45	0.2
Paint on interior concrete, drywall, or plaster	sf	Paint	(2)	N/A		1.52	0.2

Fig. 7 (Matlab Toolbox Packaging, Mitrani 2004)

Outcomes

After having all the information necessary which includes, logarithmic median and standard deviations for the capacity of different assemblies using fragility curves one can run the analysis to see the building performance. Below in Fig. 8 are the results for one simulation of one ground motion and structural model pair for an earthquake scaled to $S_a = 0.5g$ of the same Van Nuys Hotel.

Building Performance							
Assembly Type	Total Num	DM 0	DM 1	DM 2	DM 3	DM 4	
3.5.180.1101.01	63	34	23	5	1	0	
3.5.190.1102.01	74	34	31	7	2	0	
4.7.110.6700.02	252	223	29	0	0	0	
6.1.500.0001.01	385	38	170	177	0	0	
6.1.500.0002.01	403	32	171	200	0	0	
6.1.510.1202.02	56	44	12	0	0	0	

Fig. 8 (Van Nuys Hotel Building Performance, Mitrani 2004)

Fig. 8 shows the performance of each specific assembly at different damage measurements. For example, above in Fig. 8 the first column describes the assembly by giving it a number, the second column gives the total number of assemblies that will be evaluated for performance, in the following columns 3-7, it gives the number of assemblies with DM (0-4) from least damage to complete collapse, respectively. The Damage measurements are explained in detail below in Fig. 9.

Qualitative term	Translation	Example
Negligible, few, little	0 - 1%	“Generally negligible [ceiling] damage:” less than 1% of ceiling area is damaged.
Some, minor	1 – 10%	“Some cracked [glazing] panes; none broken:” Between 1% and 10% of lites visibly cracked; no glass fallout.
Distributed	10 – 30%	“Distributed [partition] damage:” between 10% and 30% of partitions need patching, painting or repair, measured by lineal feet.
Many	30 – 60%	“Many fractures at [steel moment frame] connections:” between 30% and 60% of connections suffer rejectable damage.
Most	60 – 100%	“Most [HVAC equipment] units do not operate:” at least 60% of HVAC components inoperative.

Fig. 9

(Quantify Damage Measure, Porter et al. 2001)

After obtaining the building performance by running the simulation, we can obtain a probability histogram that shows the performance of the entire structure in terms of repair cost, fatalities and

downtime operability. Below in Fig. 10 is the total cost histogram, after running 200 simulations for the Van Nuys Hotel.

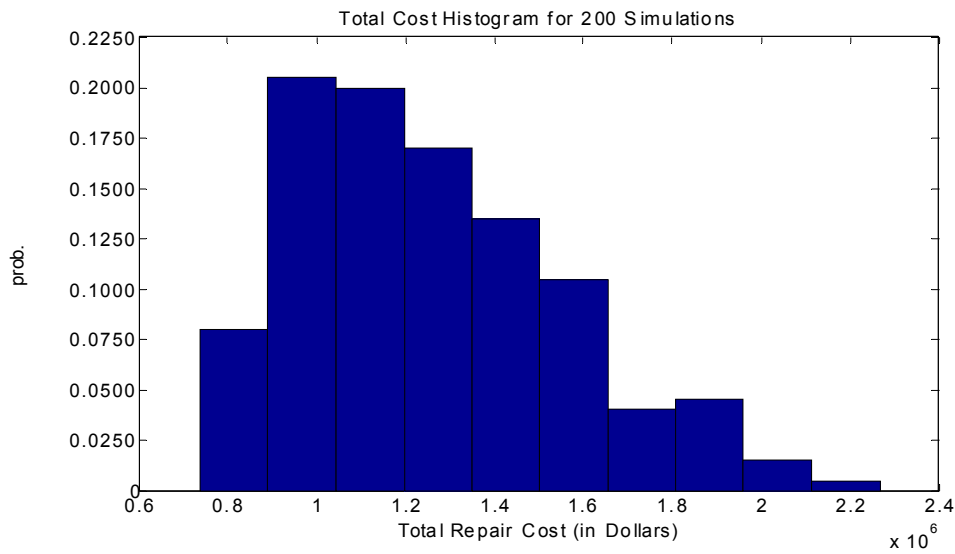


Fig. 10 (Van Nuys Hotel Cost Histogram, Mitrani 2004)

Conclusions, Future Work

This paper has summarized the two stages (damage and loss analysis) of a performance-based earthquake engineering methodology by the Pacific Earthquake Engineering Research (PEER) center; also, my contribution to the project during the summer of 2004 at the California Institute of Technology. The project objectives focus on informing stakeholders about the seismic performance of their structures in terms of cost, fatalities and downtime; furthermore, to hopefully implement the design code or provide different ways to meet the design code.

The probabilistic approach of this project contains many uncertainties and these uncertainties could be diminished by using different techniques and programs.

Currently the Matlab toolbox includes loss estimation based on Monte Carlo Simulation (MCS), but in the future it will be expanded to include First-moment second order (FOSM) and moment matching (MM) estimation (Mitrani, 2004). These techniques of propagating uncertainties are far more accurate and effective than the Monte Carlo Simulation.

Furthermore, the toolbox with capacity and cost parameter for different assemblies will be available from a complete database for the use people interested in this type of research.

Acknowledgments:

I want to thank PEER for giving me the opportunity to participate in the summer internship program. Many thanks to my advisor, Keith A. Porter for sharing his knowledge and mentorship with me and finally, I am very thankful to Judith Mitrani-Reiser for being such a great advisor and friend.

References:

Mitrani-Reiser, J. *Methodologies in Performance Based Earthquake Engineering and Proposed Extension to other Disasters- Group Meeting*. Pasadena, CA 2004

Porter, K.A., 2003, "An Overview of PEER's Performance-Based Earthquake Engineering Methodology," Proc. Ninth International Conference on Applications of Statistics and Probability in Civil Engineering (ICASP9) July 6-9, 2003, San Francisco, CA. Civil Engineering Risk and Reliability Association (CERRA). <http://keithp.caltech.edu/publications.htm>

Porter, K.A., J.L. Beck, and R.V. Shaikhutdinov, 2002b, *Investigation of Sensitivity of Building Loss Estimates to Major Uncertain Variables for the Van Nuys Testbed*, Report to Pacific Earthquake Engineering Research Center, Berkeley.

Porter, K.A., A.S. Kiremidjian, and J.S. LeGrue, 2001, "Assembly-based vulnerability of buildings and its use in performance evaluation," *Earthquake Spectra*, **17** (2), 291-312.

Advance Simulation Tools

Soil-Structure Interaction

Damage Synthesis Project DS-3
Mid-America Earthquake Center

Mary Grondin

REU Final Research Report

Home Institute: Michigan State University

Research Institute: University of Illinois at Urbana-Champaign

Research Advisors: Dr. Amr Elnashai & Dr. Jian Zhang

August 5, 2004

ABSTRACT

Traditionally, in earthquake engineering, it has been common to assume that soil-structure interaction (SSI) is beneficial during an earthquake. Because of this it has become common practice to avoid the complication of accounting for SSI by simply ignoring its effects. This avoidance is thought to lead to improved safety margins while simplifying the analysis. New trends in earthquake engineering include analyzing the displacement that a structure undergoes during an earthquake, and considering the structural as well as nonstructural damage that this causes. Even though soil-structure interaction induces dampening, it can also cause increased displacement in the overall structure. Due to this possibly detrimental effect, it is necessary to take soil-structure interaction into consideration during analysis. The problem is that this interaction is a very complex phenomenon, dealing with nonlinear and frequency-dependent behavior. Although methods for analyzing SSI in a linear environment have been developed, a method that includes the nonlinear behavior of the soil and foundation is not available. The objective of this project is to develop advanced response analysis methods that can estimate the response of different structures subject to earthquake induced ground motion, and include linear as well as nonlinear behaviors.

INTRODUCTION

Large structures such as buildings and bridges depend on their strong foundations to support their mass and their vertical load demands. Structures are more than what can be seen above the ground. Their foundations continue under the ground in different forms including shallow foundations, embankments and pile foundations. Pile foundations, the foundation type that this paper will be focusing on, are long underground columns used to support large vertical loads. When a structure is built on soft or unstable soil, the piles provide support by reaching down to more stable rock in the depths of the ground.

In Mid-America there has not always been a strong concern about the dangers of earthquakes. Most structures have been built simply to hold their own mass and predicted vertical loads. Consideration for environmental loads has typically been limited to the demands of wind, rain, and snow. Structures here have not necessarily been designed to withstand the lateral forces and displacements that can be caused by seismic ground motion. Although earthquakes in this area are infrequent, the damage they cause can be severe in some cases. Research in this area has revealed the hazard posed by the New Madrid seismic zone. This zone extends from the western edge of Memphis Tennessee to the southern tip of Illinois. It is here that one of the largest historical earthquakes in the continental United States took place, during the winter of 1811-1812. According to the U.S. Geological Survey, the hazard in this region is as high as some places in California, despite the present lower level of earthquake activity.

ADVANCED SIMULATION TOOLS SYMULATION

The Mid-America Earthquake Center, based at the University of Illinois at Urbana Champaign, has three thrust areas in which all of the research projects are categorized. The three areas, Consequence Minimization, Hazard Definition, and Damage Synthesis, are guided by the principles of consequence based engineering developed in the Framework Development project. The relationship of these thrust areas is illustrated in Fig1. The DS-3 project, titled Advanced Simulation Tools, is one of the projects under the Damage Synthesis thrust area. The objective of the project is to develop and maintain advanced response analysis methods that can be used in estimating peak structural response quantities. The intention being that the responses can be utilized to accurately and efficiently define vulnerability functions.

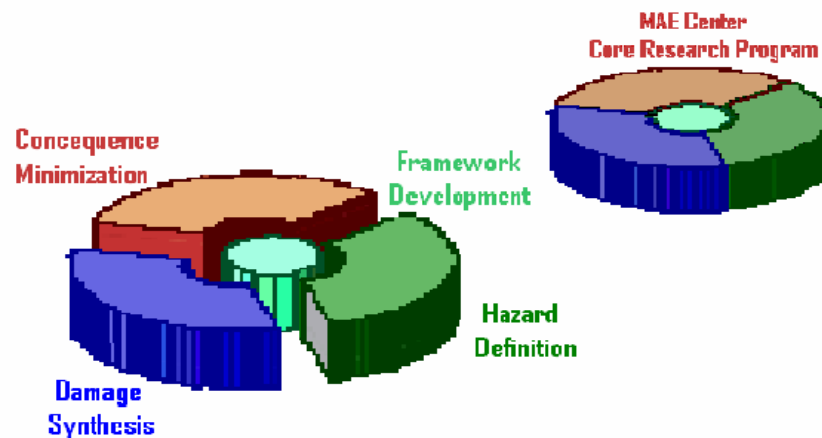


Figure 1: MAE Center Core Research Program

This paper reflects the REU (Research Experience for Undergraduates) work done during a ten week period from May to August, 2004. The work done during this period is a small specific portion of the entire DS-3 project, and will be the main focus of this paper. DS-3 is divided into three main sections, focusing on the projects more specific objectives. The first section of the project is referred to as Detailed Analysis Environment. The second section of the DS-3 project concentrates on Simplified Demand Estimation.

The third division, and focus of this paper, is the section that deals with Soil-Structure Interaction. This portion of the project focuses on assessing current analysis procedures as well as the development of simplified analysis procedures, accounting for the effects of SSI in different foundation types. It also investigates the effects of the interaction on the overall response of structures and implements them in the current analysis environment.

SOIL-STRUCTURE INTERACTION

There has been a significant amount of controversy over the perceived effects of soil-structure interaction on the overall performance of structures, especially on soft soils. Soil-structure interaction has been initially deemed beneficial during seismic motion, but trends in research are changing and this causes different notions of the phenomenon.

Conventionally, it has been common practice in Earthquake Engineering to study the force that ground motion imposes on a structure during an earthquake, when analyzing its seismic capacity. During this type of analysis soil-structure interaction consistently appears to be beneficial for seismic response. Large pile foundations, for example, dissipate energy into the soil. This phenomenon, known as dampening, reduces the force imposed on the structure above. Because of this, the complication of accounting for soil structure interaction is typically avoided, thus its effects ignored. This is done by inputting the ground motion of an earthquake directly at the base of the structure, instead of including its effects on the foundation first. The avoidance of SSI is thought to simply lead to improved safety margins while simplifying the analysis. This practice is even suggested in a number of seismic codes.

New research reveals flaws in this concept. More recent trends in Earthquake Engineering include analyzing the displacement that a structure undergoes during an earthquake, and considering the structural as well as nonstructural damage that this causes. Even though soil-structure interaction increases dampening, which is beneficial, it can also cause additional displacement to the overall structure. This demand in the structure can, in some cases, have detrimental effects. In tall, rigid structures on softer soil, the interaction can cause large increases in the natural period of the structure, leading to much larger relative displacements.

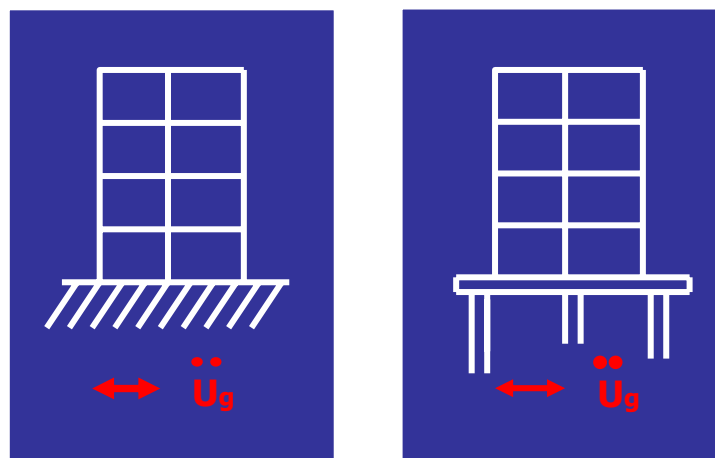


Figure 2: Soil-Structure Interaction

This is illustrated in Fig.2. The first image in Fig.2 shows ground motion being applied to the base of the above ground structure. The second image shows the pile foundation being taken into consideration during analysis.

OBJECTIVE

The problem arising is that soil structure interaction is traditionally seen as beneficial and ignored for simplification. SSI can in fact have dangerous effects during an earthquake depending on the type of soil and seismic input. Although this is not always the case, it is important to include SSI in analysis so that this potential problem can be foreseen. But soil-structure interaction is not something easily taken into consideration. Its nonlinear and frequency-dependent behavior is very complex, leading to the need for this project.

As stated above, the objective of the soil-structure interaction portion of the DS-3 project is to assess current analysis procedures for analyzing soil structure interaction as well as develop simplified procedures. It is important to provide a simple method for researchers to use so that they can accurately include the effects of soil structure interaction during analysis of a structure. Although some methods for analyzing the interaction in linear environments have been developed, there has been little development in the cases of nonlinearity in the soil and pile shaft. This behavior can produce very different results. This project focuses on creating a method that can be used in both linear and nonlinear conditions.

MODELING

Movement of soil can be studied through physical equipment such as laminar boxes, shake tables and centrifuges. The problem with these devices is that they can be very time and economically expensive to build and run. To avoid the financial expenses, as well as create a method that can be preformed in a timely fashion, this project uses finite element analysis software to model foundations and surrounding soil. ABAQUS is one program used in this project.



Figure 4: ABAQUS

If the entire pile can be analyzed during ground motion using software, and the behavior at the head of the pile found, then the behavior of the entire pile can be represented on a shake table with springs and dashpots at the base of the structure. This collaboration between physical and virtual modeling provides a way to test a structure more accurately on a shake table. The foundation is represented without the entire foundation and surrounding soil needing to be built onto the table.

The type of model that this paper focuses on is a single pile foundation. Pile groups and pile-soil-pile interaction are considered in this project, although not the focus of this paper. It is important that this effect is later inspected because the behavior of a pile group is much more complex than a single pile. For example, the stiffness of a pile group is not equal to the sum of the individual pile stiffness' because each pile has a lateral effect on each other.

In ABAQUS the pile shafts are modeled as well as subjected to finite element analysis. The piles, and the soil in which they are embedded, are modeled in ABAQUS using the Beam-on-Winkler foundation model. This modeling begins with the linear behavior of a single pile shaft embedded in soil. The object of the analysis is to receive a dynamic response from a system limited to a single degree of freedom.

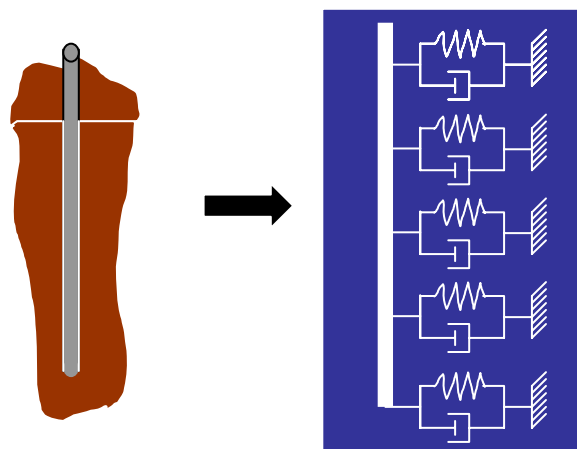


Figure 5: Beam-on-Winkler-Foundation Model for Single Pile

As shown in Fig.5, the Winkler foundation is a model that can be created in order to represent the stiffness and the dampening effects of the soil surrounding a pile shaft. The stiffness of the soil is represented with springs and the dampening effect of the soil is represented with dashpots. These are simple interactions existing in ABAQUS, which can be attached to each element of the pile, representing the soil that it is founded in. Different types of soil from hard clay to soft sand can be represented in this manner. The three dimensional beam is shown as a single line in the model, but all of its properties including cross section, density, and young's modulus are entered into ABAQUS and assigned to the pile. ABAQUS uses these properties during analysis. In this study, beam piles with consistent cross section were used. For specific dimensions and properties to create the pile models, Deepak Badoni's Paper titled *Nonlinear Response of Pile Foundations Under Inertial and Seismic Loading* was used as a reference.

The soil surrounding the pile was assumed to be of a homogeneous spectrum, therefore all the spring and dashpots held consistent values down the length of the beam. Layered soil can be modeled using this same method simply by adjusting these values at each element on the beam. The number of elements used to analyze the beam are subjective, but the more the beam is divided the more accurate the results will be.

ANALYSIS

Once the models of pile beams were created in ABAQUS they were subjected to different tests. There are three different tests used in this study to analyze the models. The first test is a Static Pushover test. This test applies a static, lateral load to the head of the pile, and the displacement resulting can be measured. The second test, a steady-state dynamic analysis, is similar to the first, using a dynamic load instead of a static load at the head of the pile. The third type, referred to as Dynamic Time-History Analysis, applies a dynamic displacement to the foot of the pile to simulate vertically propagating S-waves. The resulting displacement at the head of the pile is recorded over time.

The analysis started with a single pile subjected to the static pushover test. Different loads were applied to the head of the pile modeled in ABAQUS. In this model it is not necessary to specify if the pile is an end-bearing pile or a floating pile because only the upper portion of the shaft experiences significant displacement. This part of the pile is referred to as the active length. The actual length of the pile has little effect on the results as long as the model is longer than the active length of the shaft. By adjusting the load applied to the head of the pile, graphs similar to the one shown in Fig.6 could be made for each individual pile modeled. The linear portion of the graph is representative of the results of this test. This test is only accurate for linear behavior of the beam and soil. The curve in this figure is a representation of how nonlinear results would differ from the results given in this analysis.

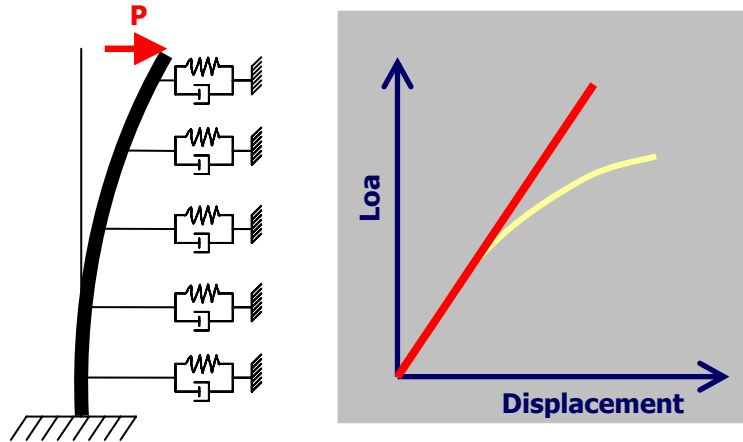


Figure 6: Static Pushover Analysis

The second test used was the steady state dynamic analysis. Instead of using an instantaneous load P , this test applies a dynamic load consisting of a sine function to the head of the beam. With the output from ABAQUS, a Matlab program is written to plot the displacement versus load at the head of the pile at every .01 seconds. An example of the resulting scatter plot output from Matlab is shown in Fig7. In these plots, the points form a shape in which the area enclosed represents the quantity of the energy dissipated into the soil due to dampening. The less dampening that takes place, the smaller or more slender the shape appears. Once again the length of the pile is insignificant to the results, as well as whether the pile is end-bearing or floating.

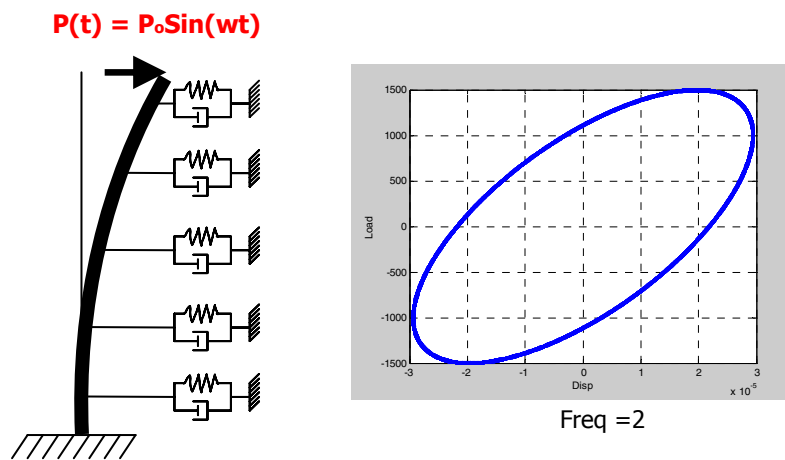


Figure 7: Steady-State Dynamic Analysis

This third type of analysis, Dynamic Time-History Analysis, consisted of subjecting the piles to harmonic motion from below. This was done by moving the boundary condition at the base of the pile in a sine function motion, representing the type of motion induced by an earthquake. The area of interest is the relative displacement resulting at the head of the pile. This is the added displacement that the structure as a whole would be subject to. This analysis differs from the head loading tests because this motion will cause excitation over the entire length of the pile. For these cases the length of the pile must be specified because it does have an effect on the results of the analysis. These models were also assumed to be end bearing where the displacement at the base of the pile is equal to the forced movement, without separation.

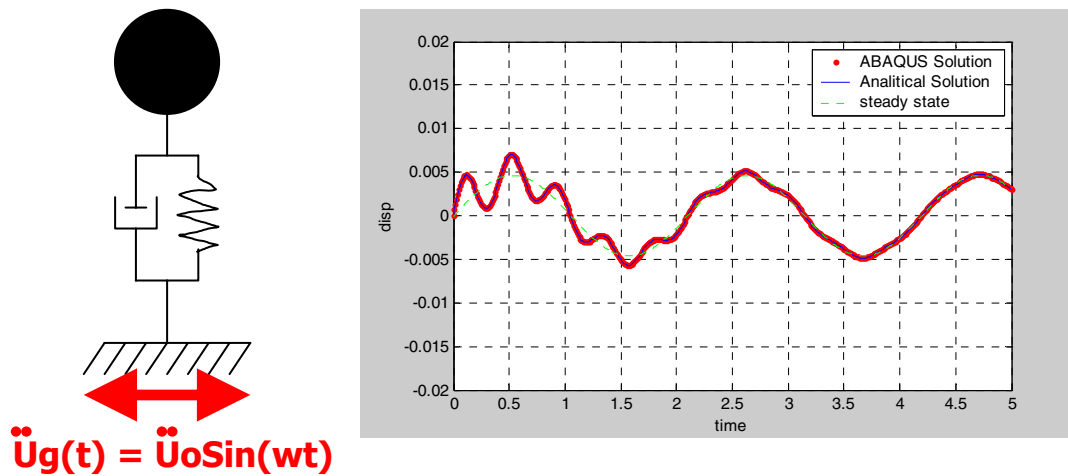


Figure 8: Time History Dynamic Analysis

Because this test is slightly more involved than the earlier examples, it was first tested with a simpler model. Before running the analysis on a full length pile, it was run on the simple system shown in Fig.8. This model consists of a lumped mass, one spring and one dashpot. The input motion was added to the base of the system. The reason for using a simple model was because the analytical solution for the system could easily be solved. When the analytical solution is shown to be the same as the ABAQUS solution then the model is verified to be accurate. The analytical solution comes from the formula of dynamics shown as Eq.1. The input ground motion is expressed as Eq.2 below. Using the initial conditions, the analytical solution for this simple system was found. These mathematics was guided by Chopra's textbook, *Dynamics of Structures*.

$$M\ddot{U} + C\dot{U} + KU = -M\ddot{U}_g \quad (\text{Eq.1})$$

$$\ddot{U}_g = \ddot{U}_o \sin(\omega t) \quad (\text{Eq.2})$$

Matlab was used to write a program that would plot this analytical solution along with the ABAQUS results. Fig.8 also shows an example of this graph. As the legend shows, the thick dots are the output given from the ABAQUS analysis. The solid line is the graph of the analytical solution, and the dashed line is the steady state analytical solution. The dashed line is plotted just to show that the solutions eventually calm to the steady state due to dampening. This graph shows that the analytical solution coincides with solution given from the simple ABAQUS model. Now that the ABAQUS procedure is verified, the analysis is done with the entire full size pile models.

FUTURE OF THE PROJECT

This is where the REU (Research Experience for Undergraduates) portion of the project ended, but the DS-3 project as a whole has an important future that will continue on. Not only are these models of single pile foundations important, but models of pile groups will be analyzed as well, because the motion of one pile can actually have an effect on the piles adjacent to it. This is a phenomenon referred to as pile-soil-pile interaction. In addition, other types of foundations are being analyzed as well, including embankments, and shallow foundations. The analysis will also extend to include three dimensional finite element analyses, where more degrees of freedom can be explored.

One important output of this project is to the Mid-America Earthquake Center's DS-4 project, titled Vulnerability Functions. The methods developed in DS-3 will give the researchers working on DS-4 a resource for estimating demand on a structural system, including its foundation, during an earthquake. And from this they are able to derive vulnerability functions. These procedures can also assist the DS-5, Response Simulation Across Regions with developing models of large populations of structure. The results of this project also reach across to the Consequence Minimization thrust area, where methods can be used in CM-4 with structural retrofit strategies.

ACKNOWLEDGMENTS

The opportunity to participate in the REU program was made available by the Mid-America Earthquake Center at Urbana Champaign. Funding was provided by the Nation

Science Foundation. The author thanks the principal investigator of the project, Professor Jian Zhang for all her guidance and teachings, as well as the center's director Professor Amr Elnashai for his excellent example and encouragement. Special thanks are also due to graduate student Jayram Ramachandran for his assistance.

REFERENCES

Badoni, D., "Nonlinear Response of Pile Foundations Under Internal and Seismic Loading," University of Notre Dame, Notre Dame, Indiana.

Chopra, A.K., *Dynamics of Structures: Theory and Application to Earthquake Engineering*, Prentice Hall, Englewood Cliffs, New Jersey, 1995.

Mylonakis, G. and G. Gazetas, "Seismic Soil-Structure Interaction: Beneficial or Detrimental?" *Journal of Earthquake Engineering*, Vol.4 No.3, 2000.

Bridge Abutment Soil Compaction Test

Ashford Kneitel
East Los Angeles College
University of California, San Diego
Scott Ashford

Abstract

A new bridge is about to be erected in San Diego's Camp Elliot army base. Azadeh Bozorgzadeh headed the design of the bridge. We tested the soil of the site location in order to determine the optimum level of water to add in order for the soil to have the best characteristics to support the bridge abutments. The preferred properties to be improved are strength, compressibility, volume stability, erodibility, and hydraulic conductivity.

Our modified soil compaction test required soil to be compacted into 5 layers in a 6" mold. Each layer was given 56 blows from a 10-lbf hammer dropped from 18" high, exerting a total effort of 56,000 ft-lbf/ft³. The test was repeated 5 times until a relationship between water content and dry unit weight of the soil was established. For bridges, it is best to use 95% or more of the optimum recorded water content.

During my PEER Summer Internship at UCSD, I worked on two projects. The first project consisted of setting up a laminar box on top of a shake table. I worked 8 hours a day on jobs such as repairing holes in the laminar box bladder, assembling the strain gauges on the aluminum pile, and cleaning the actuators. We completed the set up on time, and were able to do the testing of the pile in sand and water.

For the second project, I worked with doctoral candidate Azadeh Bozorgzadeh. Ms. Bozorgzadeh has designed a bridge that is being built in Camp Elliot army base in San Diego, California. The construction of a bridge abutment will be the first step. The conduction of a soil compaction test was necessary in order to determine the optimum level of water to add to the soil.

Our objective was to discover how to allow the soil to have the best characteristics in order to maximize support of the abutment. The properties of the soil that we were looking to optimize were its strength, compressibility, volume stability, erodibility, and hydraulic conductivity. Specifically, we were looking at an increase in shear strength, an increase in swell potential, an increase in density, a decrease in shrinkage, a decrease in permeability, and a decrease in compressibility. Optimized soil comes from a compaction process which will give a maximum weight of soil per volume.

Our approach consisted of a carefully performed soil compaction test. We decided to use the modified version of the standard test. We considered this test to be very reliable. The very same data collected from this test was to be used in the construction of an actual bridge. The modified soil compaction test has been proven to be the most effective method of discerning the optimum attributes.

The first step began with Camp Elliott sending us buckets of the real soil that the abutments would be built on. This was the soil we would be using for the test. The soil was first air-dried to remove the minute amount of moisture in the soil. It was then screened through a No. 4 sieve. Compaction tests were conducted on 5 soil samples. Five measurements of tap water were added to different soil samples. Thus, each soil sample had a different water content. The water was thoroughly mixed in a large bowl until it was evenly mixed in the soil. The soil was then placed into 5 layers in a 6" mold. After each layer was completed, the soil was given 56 blows from a 10-lbf hammer dropped from 18" high. This exerted a total effort of 56,000 ft-lbf/ft³. Soil samples were removed from the molds and broken up into smaller chunks. Chunks were weighed and recorded. They were then placed into a drying oven overnight. The next day, the dried soil was weighed again. The dry unit weight was recorded for each water level. The optimum average water content occurred at 10.21% which produced a dry unit weight of 19.74 Kn/m³. For bridge building, it is best to use 95% or more of the optimum recorded water content. This means that anywhere from 7.57 - 11.5% water content will yield optimum results.

I would have liked to stay in San Diego longer to continue work on the new bridge at Camp Elliot. There are lots of new ideas and concepts to be tested out. I am very grateful to have been given the opportunity to get so much hands on experience. I was able to see how hard it is to stage an experiment such as a laminar box test. The test itself runs around 20 seconds, yet it takes several months of hard, laborious work go into those 20 seconds.

Knowing that the data collected from a soil compaction test will be used in a major structure puts a lot more pressure on yourself. People's lives can be at stake if wrong data is being used for the bridge. We really had to be extra careful in the soil testing.

I gained so much information in this internship. I learned more in these 10 weeks than I have in years of previous schooling. Hands-on really is the best experience to learn about engineering from all angles (literally)! Graduate work is so important to the field of Structural Engineering. Earthquake engineering has so many unopened doors. It is a subject that has relatively little information compared to other engineering areas. I will be continuing my studies beyond undergraduate work.

Acknowledgments

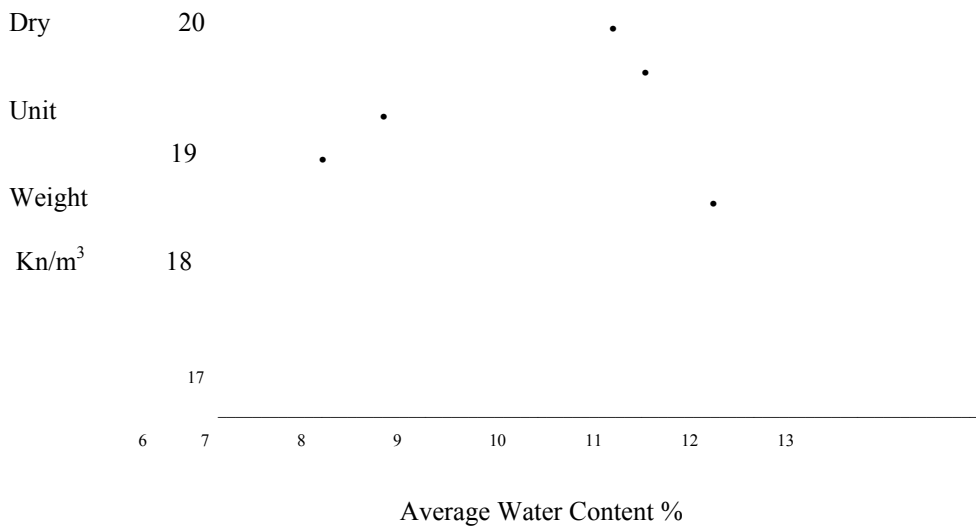
I wish to thank the following for all their help and generosity during my internship:

Scott Ashford
Linda Nelson
Azadeh Bozorgzadeh
Liang
PEER
REU
UCSD

Table 1. Compaction Test Results

<i>Run Number</i>	<i>Units</i>	<i>Test #1</i>	<i>Test #2</i>	<i>Test #3</i>	<i>Test #4</i>	<i>Test #5</i>
Wet Unit Weight	Kn/m ³	20.38	21.76	20.78	21.46	20.87
<i>Tare Number</i>		<i>Pt 1,1</i>	<i>Pt 2,2</i>	<i>Pt 3,3</i>	<i>Pt 4,4</i>	<i>Pt 5,5</i>
Water Content	%	6.56 8.57	9.76 10.65	12.08 12.43	11.34 10.31	8.67 8.59
Ave Water Content	%	7.57	10.21	12.26	10.83	8.63
Dry Unit Weight	Kn/m ³	18.95	19.74	18.51	19.36	19.21

Figure 1. Soil Compaction Dot Plot



Soil Compaction Hammers



Drying Oven



Soil Compaction Molds



References

Day, R.W., *Soil Testing Manual: Procedures, Classification Data, and Sampling Practices*, New York, NY, USA, 2000

Head, K.H., *Manual of Soil Laboratory Testing*, New York, NY, USA, 1996.

Smolczyk, U., *Geotechnical Engineering Handbook Vol 2: procedures*, Washington, D.C., USA, 2003

Analysis of Rotational Column with Plastic Hinge

Michael Long, Rice University; Corey Bergad, Bates College;
EERC Name: MCEER
Host Institution: SUNY at Buffalo
Faculty Advisor: Dr. Andrei Reinhorn

Abstract: A plastic hinge is a type of energy dampening device allowing plastic rotation of an otherwise rigid column connection. This device is composed of a weakened portion of the column prevented from rotating by relatively small steel members. These small bars are designed to yield and allow rotation before the capacity of the column is reached, thus acting as mechanical fuses protecting the column from fatigue. After a seismic event the fuse bars can be easily replaced, restoring the column to its original condition. To function properly the hinge must become plastic before the column above it yields, but limiting the deflection at the top of the column is also desirable for the stability of the overlying structure, necessitating a hinge with some degree of strength. The experimental setup of this study was constructed in the University at Buffalo's Structural Engineering and Earthquake Simulation Laboratory in 2004 and was comprised of a steel column subjected to lateral displacement at the top with a plastic hinge fixed at the base, simulating earthquake-induced ground motion on a bridge column. The purpose of this research was to develop an accurate model of the column-hinge system in the elastic range of the fuse bars, allowing consideration of the above design criteria for later testing. Plastic behavior of the fuse bars was not tested. Experimental data was generated using a quasi-static cyclic loading pattern. The behavior of the system was shown to be in agreement with the analytical model.

Introduction

Plastic hinges are an extension of the ductile design concept in building seismically resistant structures. Energy is dissipated through the plastic deformation of specific zones at the end of a member without collapsing the rest of the structure. In conventional reinforced concrete columns, this plastic hinge action can result in damage and permanent strain in the column, necessitating replacement of the entire member and possibly the entire structure. However, through the use of specially designed plastic hinge zones, damage due to large seismic displacements can be localized and repaired after an earthquake. This design philosophy was termed Control and Repairability Damage (CARD) by Cheng and Mander (1997).

In reinforced concrete columns, the detailed plastic hinge consists of a weakened portion of the column near the top and bottom where the longitudinal reinforcement is decreased, allowing yielding in this zone before the rest of the column is damaged. These specially weakened steel bars are termed fuse-bars since they are designed to yield and thus protect the rest of the column during repeated ground motion. Fuse-bars are attached so as to be easily replaced, restoring the column to its original condition. The practicality

and effectiveness of this method was demonstrated in the work of Cheng and Mander (1997).

The column used for this study was designed using a similar concept meant to simulate an earthquake-induced deflection on a bridge column. The experimental setup, shown in Figure 1, consisted of an S3x5.7 steel member subjected to lateral displacement at the top applied by a hydraulic actuator, while remaining fixed at its base to a specially designed plastic hinge. A pinned connection at both actuator mounts ensured that the actuator applied no axial force on the column. The plastic hinge, detailed in Figure 2, consisted of a pinned connection between the column and load cell at the base, which is in turn bolted to the reaction frame. The pin is surrounded by four small, vertical steel members preventing rotation and acting as fuse-bars. These bars were threaded into place and held by hand-tightened nuts, thus making them easily replaceable. The fuse-bars themselves are 5" sections of 1/2" threaded 100 ksi stainless steel. There is a 2" section in the middle of these bars where the threads have been removed and the diameter is 3/8".

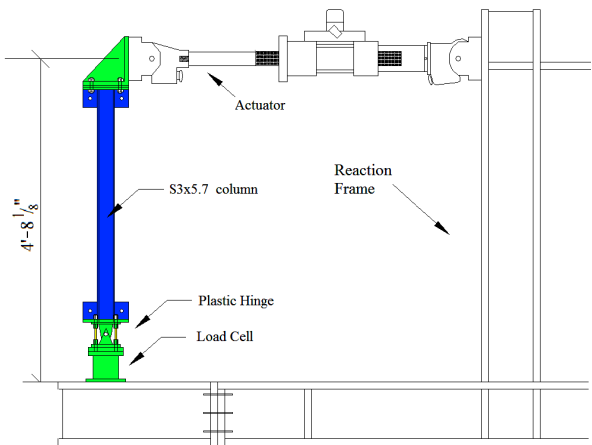


Figure 1: Overall Experimental setup

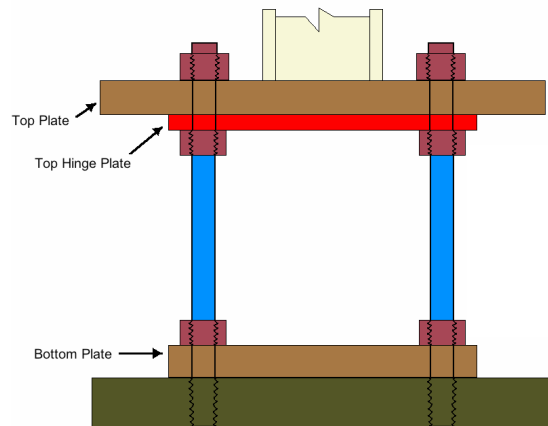


Figure 2: Detail of Hinge

The objective of this research was to analytically model the behavior of this specific rotational column, and then compare the model to experimental observations. The model could then be used by other researchers to appropriately design the strength of the plastic hinge and run a displacement-controlled test pattern on the column which would yield the hinge, but not damage the column. Therefore, both a stress and deflection analysis of the column-hinge setup was required. Only an elastic analysis of the hinge was made; the fuse-bars were not yielded during experimentation.

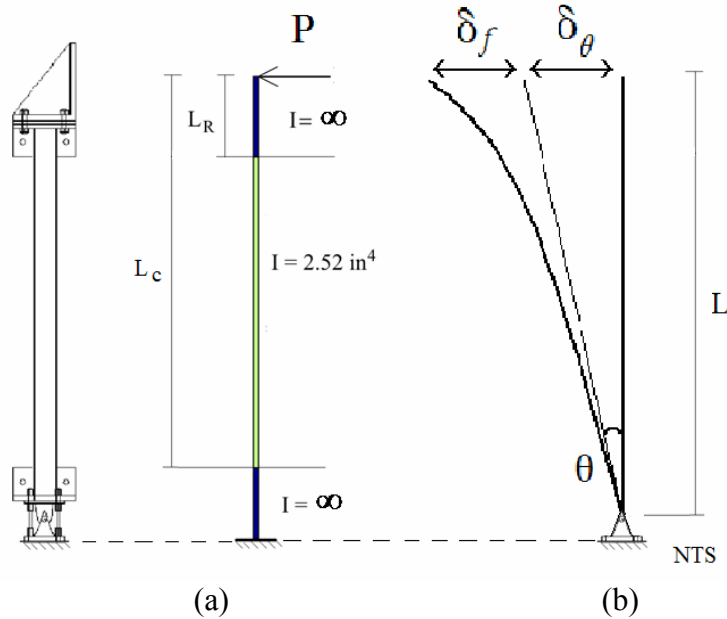


Figure 3: (a) Theoretical model of flexural stiffness and (b) Deflection due to rotation of hinge and flexure of S3x5.7 member

Analytical Model

A load P imposed by the actuator acting at a distance L from the pin results in deflection due to flexure of the S3x5.7 member, labeled δ_f , and rotation of the pinned connection at the base by some angle θ , labeled δ_θ . These deflections can be independently calculated and then combined using theoretical stiffness coefficients for rotation of the pin and flexure of the beam:

$$\delta_\theta = \theta \times L = \frac{PL^2}{K_\theta} \quad \text{Eq. (1)}$$

$$\delta_{flex} = \frac{P}{K_{flex}} \quad \text{Eq. (2)}$$

where PL = moment acting on the hinge; K_θ = angular stiffness of the hinge; and K_{flex} = flexural stiffness of the column.

The flexural stiffness of the column was determined using the assumption that all connecting plates and the widened portion of the steel member were rigid (i.e. $I = \infty$), as illustrated in Figure 3(a). Flexure would then only occur in the S3x5.7 member. Treating it as a cantilever with a rigid extension at the end allowed the derivation of a simple formula for flexural deflection:

$$\delta_{flex} = \frac{PL_c^3}{3EI_c} \left[1 - \left(\frac{L_R}{L_c} \right)^3 \right] \quad \text{Eq. (3)}$$

where L_c = free length of the S3x5.7 column plus the rigid extension on top; L_R = length of the rigid connecting portion at the top; E = Young's Modulus for steel; and I_c =

second moment of area for the X-X axis of an S3x5.7 member given by the ASCI manual.

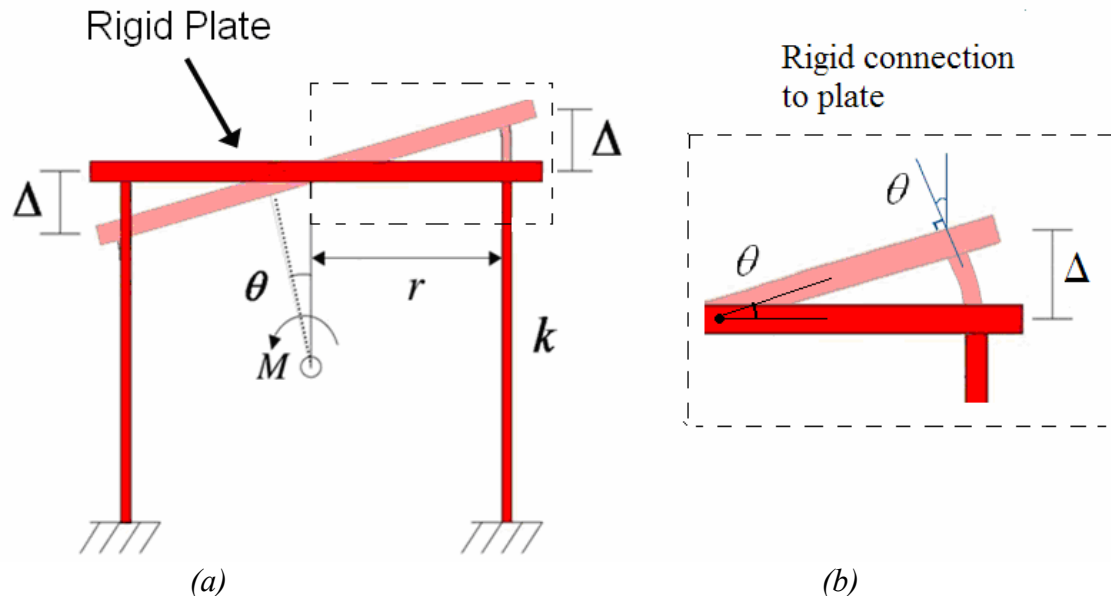


Figure 4: (a) Motion of the hinge is due to moment about pin in center. (b) Using small angle theory, rotation of the top plate can be modeled

The stiffness of the hinge is related to the moment acting about the pin in the center. This moment causes rotation of the hinge, resisted by the axial and bending forces within the fuse-bars. Assuming the top plate of the hinge is rigid, axial elongation will be symmetrical for tension and compression, and the end rotation of the fuses will equal the rotation of the pin, denoted by θ . Furthermore, by small angle approximation the axial elongation will be:

$$\Delta = \theta r \quad \text{Eq. (4)}$$

where r = lateral radius from the pin to the center of the fuse. Multiplying Eq (4) by the axial stiffness k of each fuse will then give the axial force in each fuse.

Although the tip rotation and deflection were symmetric for tension and compression, the deformable length of the fuse-bars was believed to differ for bending, axial tension, and axial compression. This discrepancy was corrected by the calculation of an effective length for axial force calculations that modeled the overall behavior of the four-fuse system.

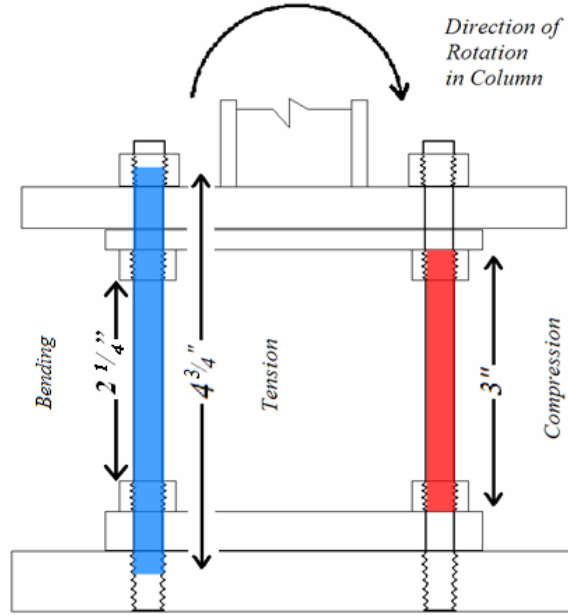


Figure 5: Effective lengths for bending and axial deformations

After solving for the average stiffness, the effective length for axial elongation l_e could be determined and a different value l used for bending calculations:

$$F_{axial} = \frac{EA}{l_e} \theta r \quad \text{Eq. (5)}$$

$$M_{bending} = \frac{EI}{l} \theta \quad \text{Eq. (6)}$$

where A = cross-sectional area of the fuse and I = second moment of area of the fuse. Any difference in magnitude between the axial force in the tension fuse and the compression fuse was balanced by a vertical force in the pin, not affecting the moment equilibrium about the pin.

A special consideration for the fuse-bar in compression was buckling failure. As shown in Figure 5, bending, and thus buckling, was confined to the portion exposed between the inside nuts; the surrounding material prevents flexural movement in other regions. The critical compression load P_{cr} at which the column will buckle is given by:

$$P_{cr} = \frac{\pi^2 EI}{L_E^2} \quad \text{Eq. (7)}$$

$$L_E = k_E L \quad \text{Eq. (8)}$$

where L_E = Euler length for buckling found by multiplying the physical length L by constant k_E . The Euler length used for buckling calculations depends on the boundary conditions of the member, as shown in Figure 6.

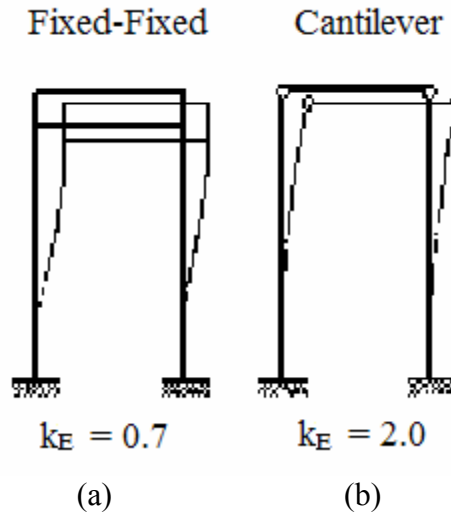


Figure 6: Euler length coefficients for buckling; the two extreme cases for this experiment are shown

The fuse bars weren't free to rotate at their ends, but neither were they completely fixed; a specific end rotation was imposed by the hinge plate. Therefore, the boundary conditions lay somewhere in between the fixed-fixed and cantilever case shown in Figure 6(a) and 6(b), respectively. For axial compression, the failure load is given by:

$$P_{cr} = \sigma_y A \tag{Eq. (9)}$$

where σ_y = the yielding strength of the steel. Even using the more conservative cantilever case for Eq (8) and a high compressive strength of $\sigma_y = 100$ ksi, the critical buckling load given by Eq (7) of 17.4 kips was well above the yielding load of 10 kips given by Eq (9).

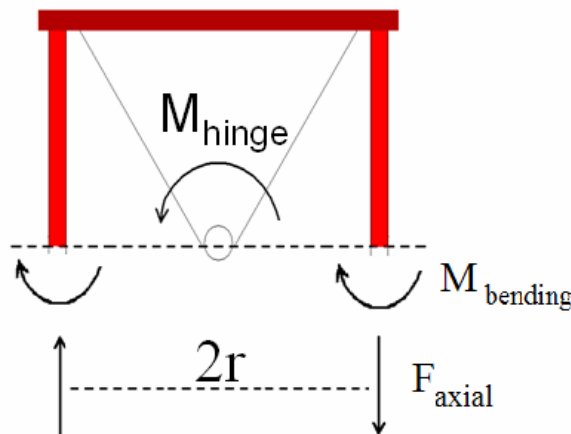


Figure 7: Free body diagram of hinge, illustrating moment equilibrium about pin

As shown in the free body diagram in Figure 7, the moment from an external load M_{hinge} is counteracted by the axial force couple $F_{axial} \times 2r$ and the local bending moment $M_{bending}$ within each fuse. The relationship between these is made clear by summing the moments about the pin for the entire hinge:

$$\Sigma M_{pin} = M_{hinge} - 4(F_{axial} \times r + M_{bending}) = 0 \quad \text{Eq. (10)}$$

The resultant angular stiffness for the hinge therefore has a bending and an axial component. Using Eq (5) and (6):

$$K_{\theta} = \frac{M_{hinge}}{\theta} = 4 \left(\frac{EA r^2}{l_e} + \frac{EI}{l} \right) \quad \text{Eq. (11)}$$

Together with the theoretical flexural stiffness given by Eq (3), the deflection of the whole system could now be predicted by adding Eq (1) and (2) for a given load from the actuator.

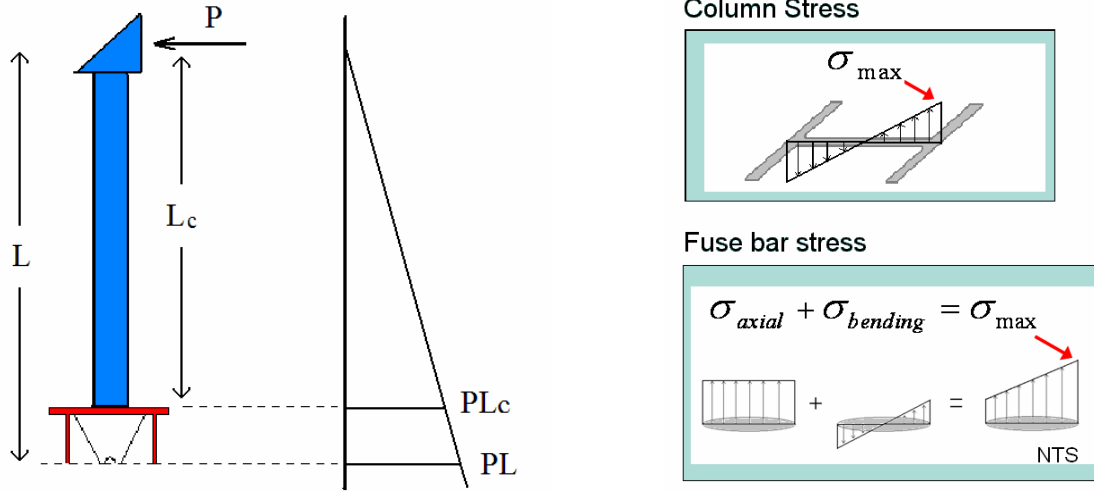


Figure 8: Determination and comparison of maximum stress in the flexural member and the fuse bars

Determining the maximum stress in the different components of the setup was the next step. As shown in Figure 8, the stress in each fuse-bar was a combination of axial and bending stress:

$$\sigma_{axial} = \frac{F_{axial}}{A} = \frac{Er}{l_e} \frac{PL}{K_{\theta}} \quad \text{Eq. (12)}$$

$$\sigma_{bending} = \frac{M_{bending}}{S} = \frac{EI}{lS} \frac{PL}{K_{\theta}} \quad \text{Eq. (13)}$$

where S is the section modulus of the circular fuse-bars. The maximum stress occurred at the extreme outside fiber of the fuses, where these two stress components act in the same direction. By plugging in Eq (11) for K_{θ} the stress can be expressed as:

$$\sigma_{fuse} = \sigma_{axial} + \sigma_{bending} = \frac{PL}{4\left(\frac{Ar^2}{l_e} + \frac{I}{l}\right)} \left(\frac{r}{l_e} + \frac{D}{2l}\right) \quad \text{Eq. (14)}$$

where D = diameter of the circular fuse-bars. This combination related stress to a load applied at the top of the column and controlled the moment capacity of the hinge. Similarly, the moment capacity of the S3x5.7 column at its own point of maximum stress could be related to the actuator load by:

$$\sigma_{column} = \frac{M}{S} = \frac{PL_c}{S_{xx}} \quad \text{Eq. (15)}$$

allowing comparison of stress in the column to stress in each fuse-bar using a common parameter P, the actuator load.

Given a material with a specific yielding strength, Eq (14) shows that the three parameters controlling the moment capacity of the hinge are the fuse-bar's cross-section, radius from the pin, and effective length. For the practical design of this specific setup, cross-sectional area and yielding strength are the only variables which could be altered to raise or lower the moment capacity of the hinge.

As noted previously, Eq (4) made use of small angle assumptions to relate axial elongation of the fuse to rotation of the pin in a simple linear fashion. For comparison, the same relationship for the general case can be expressed as:

$$\Delta = 2 \frac{r}{\cos \beta} \sin\left(\frac{\theta}{2}\right) \cos\left(\frac{\theta}{2} + \beta\right) \quad \text{Eq. (16)}$$

where the angle β is a function of hinge geometry. The error associated with this approximation was considered negligible at the displacements involved in the elastic range of the hinge. For illustration, Table 1 shows the error in the Δ calculation, as well as two derived quantities, the deflection and load imposed by the actuator at the top, at the predicted linear elastic limit of the system.

Table 1. Comparison of results at theoretical elastic limit of hinge			
	Small Angle Approx (Eq 4)	General Case (Eq 16)	% Error
Δ (in)	0.0102623	0.0102595	0.03%
δ_{top} (in)	0.76032	0.76063	0.04 %
P (lb)	1418.85	1418.48	0.03 %

The assumption was therefore justified for the range of motion considered in this particular experiment.

Experimental Protocol

During testing of the structure, the actuator followed a quasi-static cyclic deflection pattern. The pattern ran for 12 cycles of increasing amplitude, with a

maximum displacement of .185 inches from equilibrium. The test protocol ran approximately 125 seconds at speeds low enough to make dynamic forces negligible. Due to the limited moment capacity of the load cell at the bottom of the setup, the plastic limit of the hinge could not be reached and the fuse-bars remained elastic.

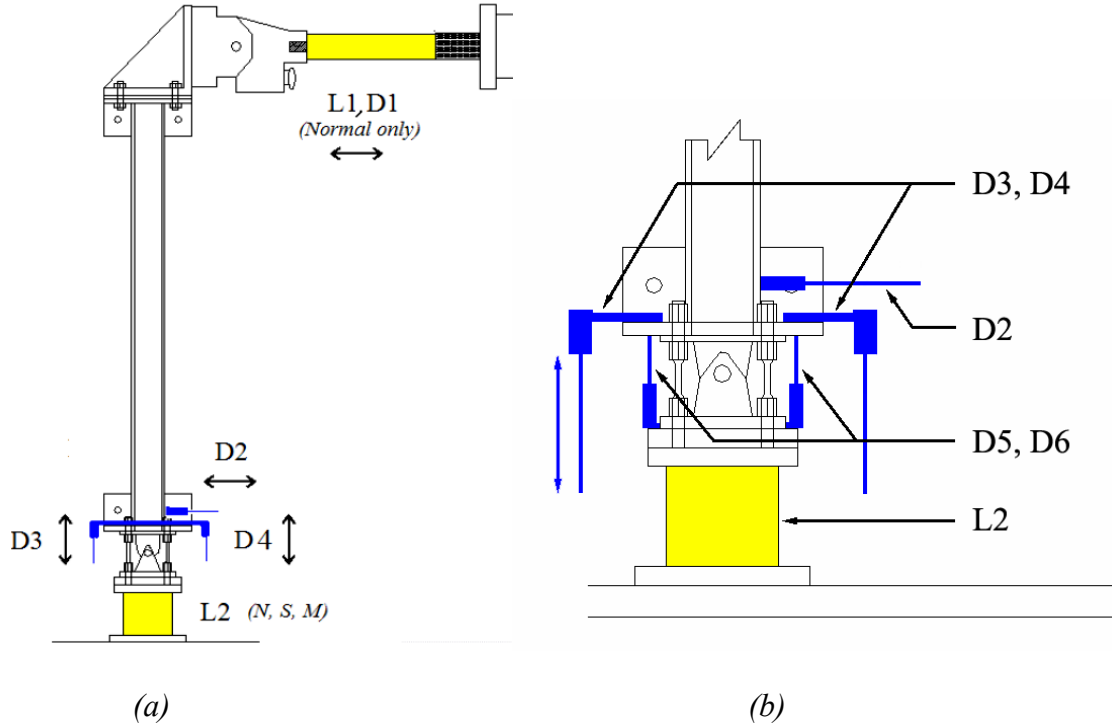


Figure 9: (a) Overall experimental setup and gauge placement; (b) Instrumentation

Initial Instrumentation

For all testing, the deflection (D1) and load (L1) imposed by the actuator was measured by gauges within the actuator arm itself. The overall stiffness of the system could be calculated using these two experimental values. The initial instrumentation for the hinge setup used two vertical displacement gauges (D3 and D4), one on either side of the hinge, as shown in Figure 9(a). This allowed the derivation of the rotation θ at the top of the hinge according to:

$$\theta = \arctan\left(\frac{D3 + D4}{x}\right) \quad \text{Eq. (17)}$$

where D3 and D4 = absolute displacement measurements (referenced to the reaction frame) and x = distance between these gauges. A third displacement gauge measuring lateral displacement (D2) was placed on top of the hinge. Using these two parameters, the resulting displacement at the top of the column due to movement of the hinge could be calculated by:

$$\delta_{\theta} = \theta \times L + D2 \quad \text{Eq. (18)}$$

This quantity could then be subtracted from the total displacement, allowing the flexural component of deflection, δ_{flex} , to be separately analyzed. Placed underneath the hinge

was another load cell measuring moment, shear and normal forces, but due to extraneous rotation in this load cell the data taken from it was distorted and not used in analysis.

Modified Instrumentation

Subsequent tests used additional gauges about the hinge to separate the movement of various components making up the base fixture. Two additional gauges, labeled D5/6 in Figure 9(b), measured the relative movement of the top and bottom plate of the plastic hinge, thereby completely isolating the hinge from any rotations originating elsewhere. The final test setup enlisted the use of the Krypton Coordinate Measurement System, a camera system capable of recording the three-dimensional motion of small LEDs fixed to the structure. Nine such LEDs were placed on the various connecting plates and load cell, allowing the movement of each individual component to be tracked separately.

Analysis of Initial Experiment

Initial results using data from the actuator (L1 and D1 on Figure 9) yielded an unexpectedly low overall stiffness when compared to analytical predictions. Looking at Figure 11, the rotational stiffness of the hinge was also much lower than predicted using the rotations given by gauges D3/4. The experimental flexural stiffness, however, came within 5% of the expected value, presented in Table 2. Evidently, the flexural model for the S3x5.7 member was adequate, but as shown in Figure 11 the top of the hinge was rotating about three times more than predicted, creating the large error seen in overall stiffness in Figure 10. Understanding the rotational behavior of the hinge required more data.

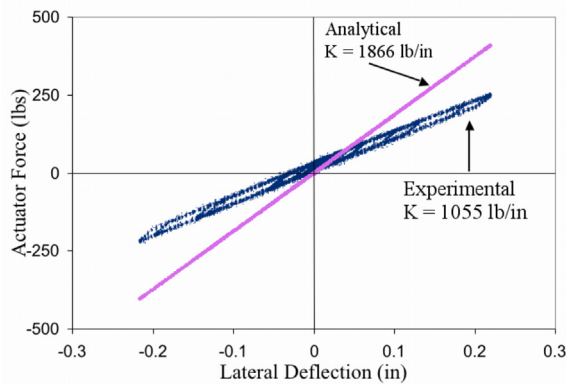


Figure 10: Total stiffness of entire setup

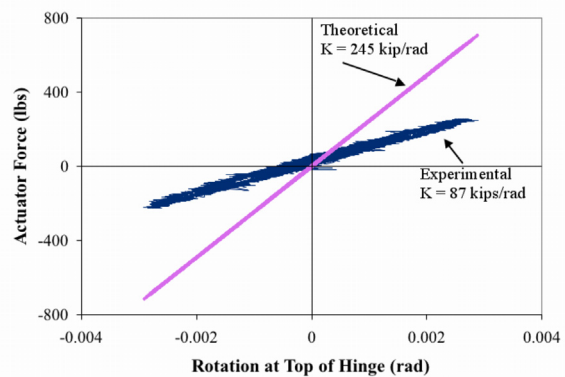


Figure 11: Rotational stiffness of base (includes hinge and load cell)

Analysis of Modified Experiment

Using the data taken from gauges D5/6, the rotation of the hinge was separated from the motion of the remainder of the base. The true rotational stiffness of the hinge found using these gauges came within 5% of the originally predicted value, as shown below in Table 2. A comparison of the rotations taken from gauges D3/4 (magenta) and D5/6 (blue) shows an obvious discrepancy in Figure 12. These results clearly indicate that some other component was contributing to the rotation of the base, skewing results for the hinge and overall stiffness. Further separation of the motion in various components of the base was required to identify the source of this extra rotation.

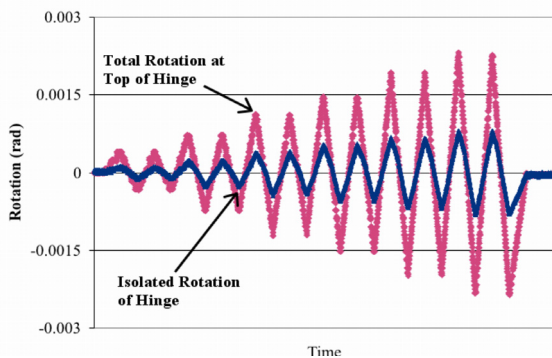


Figure 12: Rotational Comparison of Isolated Hinge and Top of Hinge

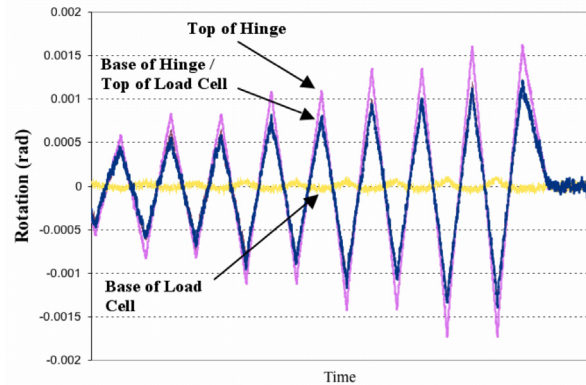


Figure 13: Rotational Comparison of Top and Bottom of Load Cell and Hinge

With the use of the Krypton Coordinate Measurement System, the motion of each connecting element was recorded and used to derive the rotation of each element in the base structure. A comparison of the increasing rotation as one moves up from the reaction frame to the top of the hinge is shown in Figure 13. The considerable change in amplitude between the base and top of the load cell indicates that flexure of part or all of this load cell was the source of extraneous rotation skewing the total rotation at the top of the hinge.

Table 2. Comparison of analytical and initial experimental results			
	Analytical Result	Experimental Result	% Error
Rotational Stiffness	245 (kips/rad)	233 (kips/rad)	4.9 %
Flexural Stiffness	2930 (lb/in)	2800 (lb/in)	4.4 %

Energy Dissipation

Despite the absence of yielding in the fuse-bars, hysteresis was present during the loading cycles of the actuator, as shown in Figure 14. It is apparent that some component in the setup was yielding or slipping in a regular fashion, causing a transient behavior as the actuator switched direction of motion. Due to the numerous interfaces bolted together, the location of this component could not be determined. Figure 15 presents the

net work done on the column due to this phenomena, equivalent to the area within the hysteresis loop. In order to accurately analyze the energy dissipated by plastic hinge action, this work would have to be subtracted from the total work done on the column. It is desirable to stop this additional energy absorption since the component in question may weaken and fail after repeated cycles. Only the fuse-bars were intended to wear out and be replaced.

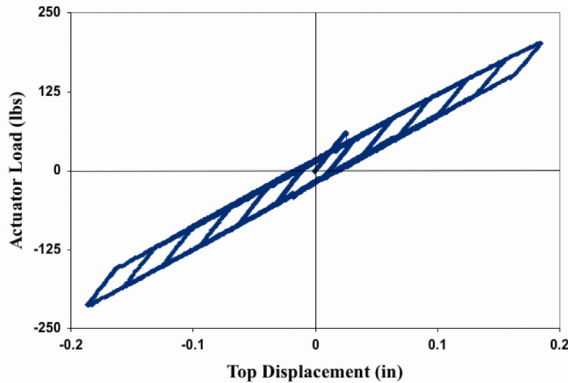


Figure 14: Total stiffness, shown with hysteresis

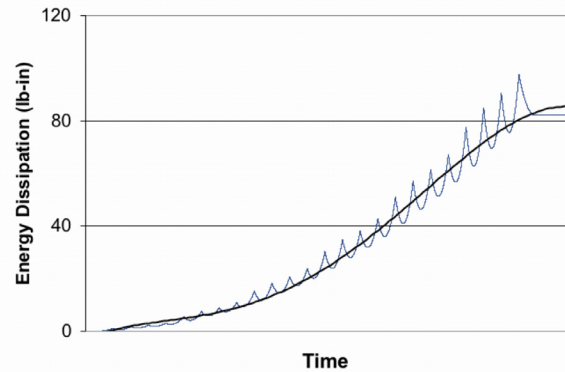


Figure 15: Work done due to hysteresis

Conclusions:

Through experimental and analytical processes, an accurate model was developed for this hinge-column system within the elastic range of the fuse bars. In order for this hinge to be effectively used as an energy-dampening device, several design considerations must be investigated:

1. The moment capacity of the hinge, determined by the position, axial and bending stiffness, and yielding strength of the fuse bars, must be lower than that of the column.
2. The effective length of the fuse-bars can vary depending on direction of motion. Careful consideration of the manner in which the fuse bars are attached to the hinge is imperative.
3. The amount of deflection required to yield the hinge depends on the total stiffness of the system. This can be calculated by a series summation of the rotational stiffness of the hinge and the flexural stiffness of the column. As shown in this study, extraneous motion in the setup can greatly alter the total stiffness and must be taken into account for accurate predictions of deflection-controlled behavior.

Future Research:

Based on the results and methods used in this study, further analytical and experimental investigations of the following topics are suggested in order to more fully understand the setup:

1. Compression and tension tests of the hinge separate from the remainder of the setup could directly determine the effective length of the fuse bars, allowing for further verification of the analytical model for the hinge.
2. The hysteresis shown in the graphs above requires further investigation to determine the location of the yielding or slipping component. This may be achieved by use of the Krypton system.
3. In order to complete the model of the hinge, investigation of the plastic behavior of fuse bars must be made.

References

Cheng TC, Mander JB (1997): Seismic design of bridge columns based on control and repairability of damage. *Technical Report NCEER-97-0013*, Multidisciplinary Center for Earthquake Engineering Research, Buffalo, NY.

MODELING COMMUNITY GOAL DYNAMICS: A SYSTEM DYNAMICS APPROACH TO INCREASING THE GOAL OF SAFETY WITHOUT THE STIMULUS OF DISASTER

Meagan Mauter, Rice University, Washington University in St. Louis, Dr. Phillip Gould

Abstract

Despite the 90% chance of a 6.0 earthquake by 2040, few communities in the Midwest have adequately addressed the risk that the New Madrid Fault poses for this region. Although structures constructed since 1990 have been required to meet codes that reflect this earthquake risk, older structures are not evaluated for their earthquake resistance and seismic retrofit is not mandatory on earthquake prone buildings. The goal of this project is to identify the avenues most effective in raising earthquake preparedness and in initiating mitigation projects. Interview questions were developed for the owners, architects, and engineers of three seismically rehabilitated buildings in the St. Louis area in order to identify primary stimulants behind sample retrofit projects. As a product of my investigation into Recent Seismic Retrofits in the St. Louis area, I was able to draw a number of conclusions about the motivations that owners had for undertaking retrofit projects, the engineering details, and the challenges faced by those initiating the retrofit. This data will be incorporated into a system dynamics model of community goal change. By modeling the competing goals of safety and economic development, this project will enable policy makers to access the most effective long-term solutions for raising earthquake awareness in their communities.

Background

The largest recorded earthquake in the contiguous United States struck in March of 1812. Measuring 8.3 on Richter scale, this seismic event was powerful enough to cause rivers to change direction, to create new lakes, and to drastically change the topography of the region. Most people are surprised to discover that the epicenter of this earthquake was not on the west coast, but rather in the small town of New Madrid, Missouri. As the most seismically active region east of the Rocky Mountains, the New Madrid Fault Zone (NMFZ) still has the potential to cause severe damage throughout the Midwest. Despite historical data on the 1812 earthquake, and the 90% probability of a 6.0 earthquake by 2040, populations in the Midwest have a very low perception of the risks that this fault poses to both population safety and the structural integrity of buildings. Although the 1812 earthquake caused little damage in the then sparsely populated region, the now dense Midwestern population and the low percentage of seismically resistant buildings puts this region at high risk for substantial disaster in the next earthquake (MAE, 2004).

Because building codes for seismic resistance were not established in most regions until 1990, many buildings remain particularly prone to seismic damage. The

high impact, low frequency nature of seismic events, however, makes it difficult for people to justify the expenditure of time and money to adequately protect themselves. Although the implementation of building codes was an important step towards earthquake preparedness, buildings constructed before this point are still not subject to inspection or mandatory retrofit.

Many decision makers fail to grasp the enormous costs associated with post disaster recovery. In addition to rebuilding and infrastructure replacement costs, a great deal of the region's economic productivity is lost in the clean-up process. As a result of the rising costs for disaster cleanup, the federal government has acknowledged the value of pre-disaster planning, mitigation, and preparedness as effective strategies for cutting costs and maintaining productivity.

The Mid-America Earthquake (MAE) center is a product of this push for mitigation as a strategy to preemptively reduce the cost of damage before an earthquake occurs. The MAE center uses Consequence-Based Engineering (CBE) as a formal framework for their research. CBE is a multidisciplinary approach towards seismic risk assessment that incorporates social and economic impact into engineering design. CBE has three primary thrusts including hazard definition, damage synthesis, and consequence minimization.

Hazard Definition seeks to determine a region's magnitude of seismic risk and to gain a physical understanding of an earthquake's source, its path and site effects, and the resulting ground failures. Damage Synthesis uses modeling to predict the damage produced by a seismic event. Consequence Minimization completes this comprehensive CBE approach by exploring mitigation strategies to reduce the consequences of earthquake disasters to acceptable levels defined by stakeholders. Thus, the CBE project aims to produce tools that allow stakeholders to determine their level of risk, evaluate their potential losses, and design socially and economically feasible levels of mitigation that reduce the consequences of an earthquake to acceptable levels.

One branch of consequence minimization is the use of system dynamics modeling to assist in defining the acceptable consequences of a seismic event. CM-2 is a joint effort between the School of Social Work and the Department of Civil Engineering at Washington University in St. Louis. These two departments work together to:

- 1) Identify feedback loops that impact community safety over time,
- 2) Demonstrate cost consequences of alternative policies that enhance safety,
- 3) Model the relationship between the conflicting goals of safety and economic development,
- 4) Identify those policies most effective for increasing earthquake mitigation,
- 5) Produce a system dynamic model for small communities in the Midwest with populations of 10-100K, and
- 6) Compare consequences of policies that impact safety over different time spans.

Modeling Community Goal Dynamics

Every community pursues various goals that contribute to their survival and growth. These goals are critical in the decision making process of the community because they set standards for success and provide direction to the community's leaders. There are a number of goals that a community might pursue, such as the development of transportation infrastructure, the preservation of green space, or the improvement of public health. The CM-2 project is interested in how the goal of seismic safety changes over time with respect to other community goals. The finite number of resources in a community necessitates an investigation of a wide range of community goals when attempting to model the evolution of seismic safety.

In a look at the officially stated goals of a number of communities in the NMFZ between 1990 and 2003, the goal of seismic safety rarely mentioned as a community goal. In order to quantify safety, therefore, it was necessary to include a broad spectrum of safety concerns into our study. Our study revealed that other community goals like economic development usually took priority in small Midwestern communities. This said, without the presence of a disaster, safety is a difficult goal for communities to pursue. For one, investing resources in safety involves a high degree of uncertainty because disaster events are impossible to predict. The goal of safety also differs from competing goals such as economic development because it solicits attention from different stakeholders. While economic development is generally a priority of the private sector, government agencies are usually responsible for pursuing the goal of safety. Furthermore, the goal of safety is difficult to quantify and identify improvement in. There are no absolute markers for determining the level of safety in a community. Finally, the goal of safety requires a great deal of preparation and foresight because it involves planning for an event that has not yet occurred (Cho, 2004).

The purpose of this study is to identify leverage points for increasing the goal of safety without the stimulus of a disaster.

System Dynamics Modeling

In order to effectively pinpoint policy changes that will increase the level of safety in a community, an effective model of community goal dynamics must be produced. For this project we selected a long-term System Dynamics model to characterize the evolution of community goals. Short-term models, which are generally represented as feedback loops, often misinterpret simultaneous events and immediate consequences as unduly correlated to each other. This misinterpretation can lead to policy implementation that ineffective or detrimental to the desired outcome. System dynamics modeling aims to correct some of these common pitfalls by expanding on the standard cause and effect, or feedback loop, model. By incorporating into the model all of the interactions within a closed system, the system dynamic model allows social scientists and policy makers to accurately determine the most effective avenues for producing desired changes over an extended period of time.

System Dynamics Modeling was formally introduced to the scientific community in Jay W. Forrester's 1961 book entitled *Urban Dynamics*. An industrial engineer by training, Forrester experimented with the applicability of the System Dynamics Modeling approach to social and scientific problems, like the puzzling question of urban growth and decay that he highlights in this book. By analyzing a complex and dynamic system of continually interacting feedback loops, Forrester revealed that short term fixes in large systems rarely produce effective long term results (Forrester, 1969).

The challenge of system dynamics modeling is to produce a model that points leaders and policy makers towards the most effective long term solution. Forrester noted that most programs and initiatives undertaken by decision makers are those that address the symptoms rather than the underlying problems. Unlike many simple feedback loops that incorporate only one principle state variable, symptoms in complex systems do not have a simple cause and effect relationship. Thus, the *apparent* cause and effect that jump out are usually just two coincident symptoms arising from the dynamics of the larger system structure. As human observers of this system we are easily fooled by time correlations between these coincident symptoms and are thus prevented from looking at the larger system structure for our solution.

Most of a person's intuitive responses to solving problems are formulated from their daily experience with simple feedback loops. These are usually first-order negative feedback loops that are goal oriented and governed by one primary variable. Forrester uses the example of warming one's hands by a stove to illustrate the simple feedback loop. In this example the principle state variable is the distance from the hot stove. If the child moves his hands too close they will become hot and he will withdraw them. Likewise, if his hands are too cold he will move them closer to the fire. Thus, cause and effect are closely related in time and the relationship between the child's comfort and the distance of his hands from the fire is clear. Simple feedback loops govern many daily activities and reinforce the human tendency to look for cause and effect as closely related in time and location.

Complex systems are not governed by these same simple interactions. Because the complex system is comprised of many variables, multiple rates of flow, intersecting feedback loops, and a variety of system states, cause and effect are rarely correlated in time or space. When a problem arises within the complex system it is difficult to locate its origin. We are often fooled by the large number of system variables and mistake a coincident symptom for a cause of the problem. As we focus our attention on this red herring symptom, we have not only failed to identify the underlying cause, but we have also diverted resources from other areas of the system. The end result is a system that is more unstable and broken than before our intervention.

Even if, by chance, we have isolated the correct cause for the troublesome symptom, it is unlikely that we will choose an efficient strategy for inducing change. Unlike simple loops where causes are directly related to the state variable, in complex systems causes are usually found in the structure or policies of the system. Predicting exactly what these policy changes should be, or what effects a structural change will have

on other system components, further complicates strategies for maintaining a complex system. The extensive lag time between implementing policy changes and the system producing results makes complex systems ideal candidates for system modeling. This strategy for forecasting long range effects of policy changes is referred to here as system dynamics modeling.

In his book Forrester also focuses on the details of building a system dynamics model. The first, and most important, step in this process is selecting an appropriate closed boundary for the system in question. An appropriate closed boundary is one in which “the dynamic behavior and characteristic modes of behavior are generated within the boundary” (Forrester, 1969). A system boundary must be large enough to generate the problem under investigations, but it should not be so large as to obscure this problem amidst other variables. Also, an effective model must have a closed boundary system. While outside factors can and will affect the system, they must not provide the necessary growth or stability characteristics.

Although simple feedback loops are not adequate for modeling the complex interaction between large numbers of system variables, they serve as building blocks for the larger system dynamics model. Feedback loops are comprised of two basic structural elements: the stock or state variable representing accumulations within the feedback loop, and the rate or flow variable representing activity within the feedback loop. Causal loop diagrams, which incorporate multiple feedback loops into systems models, also include converters and connectors. Converters modify the stocks or flows, while connectors help to visualize links between other elements of the model.

This basic structure of the feedback loops provides the dynamic nature of a complex system, but it also makes it difficult to isolate the problem without the aid of a model. Because the rates of each feedback loop will vary, and each of the feedback loops will intersect and contribute to the behavior of other feedback loops, it is easy to see how problematic policies can contribute to effects that take years or decades to reveal themselves. System Dynamics modeling is an effective tool for predicting the long term effects of a policy change.

Another characteristic common to complex systems is that the ultimate equilibrium values are independent of the starting point. This fact helps to demonstrate that complex systems are indeed governed by structure and policy rather than by a set of initial conditions. Furthermore, this observation helps to justify the reasoning behind a system dynamics approach to modeling. Models are never more than educated guesses about the future. Without precise methods for predicting a set of future conditions, it is impossible to produce a model that provides perfectly accurate predictions. A system dynamics model that is less susceptible to these initial conditions and more dependant on a proven structure will be more accurate over time.

After identifying the variables within the complex system and generating a model, it is necessary to test the model on past system behavior. A model should always be able to produce the current state based on the initial starting conditions. Not only does this

serve as a check for basic system structure, but it also helps to establish parameters for the rates within the system.

Recent Seismic Retrofits in St. Louis

As a side study in the larger model of community goal dynamics, I undertook an investigation of recent seismic retrofits in the St. Louis area. This not only developed my understanding of the seismic retrofit process, but it also has the potential to contribute to the system dynamics model by pinpointing the motivations and challenges faced by large retrofit projects.

Introduction

This study was initiated in order to gain a personal understanding of the seismic retrofit process from structural, economic, and logistical standpoints. Although this project was designed primarily for educational purposes, it also has the potential to contribute to the larger system dynamics model by pinpointing the motivations and challenges in the development of a seismic safety goal. This study may also serve as an initial investigation into the applicability of seismic safety models developed for small communities to larger city frameworks. This correlation between safety goals in small communities and large cities will be very important when researchers begin to implement CM-2 into the Memphis test bed project.

Methods

1. Review FEMA 356 and FEMA 276: Example Applications of the NEHRP Guidelines for the Seismic Rehabilitation of Buildings
2. Develop interview questions targeting: (See Appendix 1)
 - structural background of the building
 - seismic retrofit design
 - economic considerations
 - details on final outcome of retrofit project
3. Interview owners, architects, and engineers of three recently retrofitted buildings in St. Louis (See Appendix 2 for photographs of retrofit work)
 - Washington University's Olin Library
 - Clayton High School
 - Anheuser-Busch Brewery
4. Distill relevant information on factors motivating seismic rehabilitation and challenges that hindered the retrofit process

Results

Clayton High School

I interviewed Tim Wonish, Director of the Facilities Services Department of Clayton School District as the respective owner of the retrofitted buildings (Wonish,

2004). Because of his active participation in the seismic retrofit process, and his engineering and construction backgrounds, he was well equipped to answer questions addressed to both the owners and engineers on the project. To supplement some of the data and to verify minor details about the design process, I also conducted brief phone interviews with Paul Sedchak of the Public Relations Department of the Clayton School District (Sedchak, 2004) and Ted Christner of The Christner Partnership, Inc (Christner, 2004). As the principle architect for the project, Mr. Christner was able to quickly verify much of the data that was collected in the initial interview with Mr. Wonish.

Clayton High School is a ten building complex constructed primarily in the 1950's. Typical of structures designed in this period, unreinforced masonry provides the lateral support for these buildings. Unreinforced masonry is classified by FEMA as the least earthquake resistant construction type (Applied Technology Council, 1999). As the school district grew, a number of additions were made in the 1960's and 1980's. Although the building construction type in the additions indicates a trend towards more seismically resistant buildings (rigid steel bents or cross bracing providing some or all of the lateral support), nine of the ten buildings required seismic retrofit to meet the 1990 BOCA Seismic Zone 2 criteria for the life safety objective. (See Appendix 2 for detailed retrofit strategy by building)

The need for seismic rehabilitation was raised in a master planning initiative undertaken by the district in 1990. In addition to planning for and coordinating future construction efforts, a new push was made to evaluate the seismic resistance of existing structures. The Christner Partnership, Inc. was hired to provide a comprehensive analysis of the building stock in the school district. They produced a seismic evaluation for life safety that revealed significant shortcomings in many of the district's school buildings. This report provided startling figures about the likelihood of structural failure in many of the district's buildings. The focal point of the report was the Clayton High School complex, with the threat of 90% of the buildings experiencing significant structural damage over the next 50 years.

Although concerns for life safety precipitated the initial seismic investigation, according to Mr. Wonish, seismic retrofitting work on Clayton High School would have been unlikely if a major renovation and expansion project had not already been planned for the complex. Nevertheless, it is clear that the seismic threat was an important issue to the voting population of Clayton. Funding for the renovation and the seismic retrofit portions of the project were bid out separately in a voter approved bond issue. The expansion and renovation costs were bid at 14 million dollars and the seismic retrofit bid totaled 5.2 million. The seismic portion of the project was approved by more than 2/3 of the voters. No government or other aid was offered for this voluntary retrofit project.

The Clayton School District participates in a pooled insurance program with approximately 400 other school districts across Missouri. Although the retrofit work would have provided a small decrease in premium for the high school complex, this decrease was consumed by the increase in square footage acquired through the simultaneous expansion project.

The three year expansion and retrofit project was a significant monetary investment for the school district, but Mr. Wonish attributes extensive preparation studies for keeping actual project costs very close to the initial cost estimates. Additional mandated improvements like asbestos removal were covered under the bid for the renovation project. Mr. Wonish pointed out that the bids for the seismic retrofit work were fairly high to begin with, due to the cost and difficulty of renovations on a building with high occupancy during the construction work. Occupancy issues were resolved through creative design alternatives that added structural support to the exterior, rather than the interior of the buildings, through heavy construction activity during the summers and break periods, and through a piecemeal retrofit strategy. Largely due to difficulties with occupancy, this project lasted three years, beginning in 1997 and completed in time for the start of school in September 1999.

Overall, Mr. Wonish believes that the seismic retrofit project was a worthwhile investment for the district. In addition to slowing down the collapse of buildings and providing an enhanced level of safety for students in the event of a large earthquake, he feels that the seismic retrofit process was a financially sound investment because of the potential to minimize damage due to a smaller seismic event.

The Olin Library at Washington University in St. Louis

Another recent project in St. Louis was the simultaneous renovation and seismic retrofit of Washington University's Olin Library. Information on this retrofit project was collected in interviews with Frank Freedman of the Washington University Facilities Department (Freedman, 2004) and Victoria Winn of ABS Consulting (Winn, 2004), the structural engineering firm responsible for the final retrofit design.

Olin Library was constructed in 1960 as the main library for Washington University's Hilltop Campus. Although it remained functional through the 1990's, a major renovation project was undertaken in May, 2001 to revamp the library facilities, open up the building to natural light, and add 17,000 square feet to the lower floors. Because this 26.5 million dollar renovation project doubled the building's value, BOCA codes went into effect for the renovated building. These codes required compliance with FEMA's limited safety objective for seismic safety, thus requiring seismic retrofit work in conjunction with the larger renovation project at Olin Library.

The original 200,000 square foot structure was supported by a reinforced concrete frame system with waffle slabs. The lack of true beams in all areas besides the main stairwell, and the weakness of the existing concrete frame, made this structure susceptible to significant damage under lateral loading produced by seismic events. Furthermore, the non-structural components of this building were not properly anchored. The unanchored lighting, piping, and book stacks posed considerable risk to occupant safety in a seismic event.

While there were few difficulties in bringing the non-structural components of the building to code, there was a great deal of debate around how to seismically retrofit the building itself. The original plan proposed by Alper Audi Structural Engineers was to add 4 concrete shear walls to the ground floor of the building. While this design would have brought the building to the “immediate occupancy” safety level, it was an expensive retrofit solution and it conflicted with the original renovation goals of opening up the ground floor and allowing for more natural light. ABS Consulting entered into the design process fairly late to propose an alternative retrofit solution. This structural engineering firm proposed replacing the concrete shear walls with eight diagonal steel braces. Although this design would only bring the building to a limited safety objective for a 10% in 50 year ground motion acceleration, it provided a savings of \$200,000 and replaced the “massive and obtrusive” shear walls with the low profile braces.

During the renovation and retrofit work a number of other improvements were made to the structure. In addition to the removal of asbestos and lead based paint, the building was redesigned so as to exceed the requirements for the Americans with Disabilities Act.

According to Mr. Freedman, one of the greatest challenges in the renovation project was maintaining continual occupancy of the building. This stipulation extended the timeframe of the project to three years and significantly raised the cost of the construction work. Although second and third shifts were used for selective operations such as paint and epoxy, most of the time construction work was done during peak hours of the day. In order to cut down on the noise disturbance, earplugs and construction timelines were provided to library patrons.

Anheuser-Busch Brewery

A third significant retrofit project was undertaken by Anheuser-Busch Brewery (A-B Brewery). I interviewed Jim Taylor of ABS Consulting (Taylor, 2004), the lead structural engineer on this project, but was unable to arrange an interview with A-B Brewery directly. Although I tried multiple times to collect data from the St. Louis plant, the brewery was unresponsive to my inquiry. Nevertheless, Mr. Taylor was able to provide the majority of the information that I was seeking, exclusive of the financial data on this retrofit project.

Not only does the A-B Brewery retrofit provide a model for the retrofit of a historically significant building, but it is also an interesting example of a voluntary retrofit project that was not performed in conjunction with a major renovation, and an illustration of seismic retrofit with the goal of minimizing potential economic losses.

Anheuser-Busch began the retrofit project in St. Louis following a successful and economically beneficial retrofit project on their Van Nuys Brewery in California. In the 1980’s a facilities modernization and seismic retrofit project totaling \$15 million was performed on the Van Nuys Brewery. Only a few years later, the 1994 Northridge Earthquake struck this area of California producing strong ground motion and severe

damage throughout the region. This 6.7 magnitude earthquake became the nation's costliest natural disaster, with direct losses totaling over \$40 billion. While many businesses in the region were closed for an extended period of time during the replacement of damaged infrastructure, A-B Brewery quickly returned to full operation after a minor cleanup of their facilities. None of the retrofitted buildings had sustained significant seismic damage, while the non-essential facilities that had not been retrofitted were largely destroyed by the earthquake. A-B estimated that the retrofit project saved them over \$750 million dollars in direct facilities costs and business interruption losses combined.

After the significant benefits of pre-disaster mitigation were clearly demonstrated at the Van Nuys Brewery, Anheuser-Busch initiated an earthquake risk reduction plan and seismic retrofit of its other major brewery, located in St. Louis, MO. Although a number of the buildings in the A-B brewery complex were seismically strengthened, two buildings integral to the production process were given special attention. The Brewhouse, constructed in 1891 and the Bevo Bottling Plant, constructed in 1916, are both historical structures of unreinforced masonry that were identified as particularly vulnerable to lateral loading produced by seismic activity. A non-structural retrofit was also conducted on the storage tanks in the Stockhouse.

This retrofit project began with a Phase One study to determine the building's vulnerabilities and to provide a maximum probable loss estimate. Although I was not able to access information on this loss estimate, estimated losses were large enough to move to the second phase of seismic retrofit design. Each of the retrofitted buildings was designed to comply with the Enhanced Safety Objective of the 1990 BOCA code, which would ensure full brew capabilities following a moderately sized earthquake. Because of the historical value of each of the buildings slated for retrofit, it was important that the final retrofit design not significantly alter the appearance of the buildings. Of particular concern was the seventh and eighth floor atrium of the Brewhouse, which was supported by a number of decorative cast iron beams. The final retrofit design employed a diverse set of retrofit solutions including cross bracing, the addition of shear walls, and the use of annexes to anchor the building and compensate for eccentric loading on the structure. In addition to structural retrofit, work was done on asbestos and lead based removal and the main buildings were brought into compliance with the ADA.

Although I was unable to obtain detailed financial data on this six year project, Mr. Taylor noted that A-B Brewery did encounter some surprises in the cost of the retrofit work. The foundations of the key facilities were far weaker than anticipated, a factor that added an estimated 10% to the total cost of the retrofit project. Without the extensive field investigation and preparation work that was undertaken before the project began, this cost increase may have been much higher.

Additional costs associated with working in a fully operating food plant also drove up Anheuser-Busch's total expenditure on the retrofit project. Retrofit design and construction work was moved to the outside of the buildings whenever possible, and dust partitions were constructed to seal off the production areas when work was required from

the inside. An alternative epoxy was selected to cut down on odor, and much of the construction work was performed by second and third shift workers to minimize disruptions to the brewery.

Conclusions

As a product of my investigation into Recent Seismic Retrofits in the St. Louis area, I was able to draw a number of conclusions about the motivations behind retrofit projects, the engineering details, and the challenges faced by those initiating the retrofit. Through a detailed investigation of retrofit work on Washington University's Olin Library, the Clayton High School Complex, and the Anheuser-Busch Brewery in St. Louis, it became clear that retrofit work was initiated for a series of diverse and complex reasons that were dependant on the owner, the age and construction type of the building, and the building's function.

These many different motivations behind retrofit make it difficult to categorize or generalize about mitigation projects. Nevertheless, the three examples in my study provide possible target points for encouraging seismic retrofit in a community. At Olin library seismic retrofit was mandatory because building renovation costs totaled more than 50% of the building's original value. Clayton High School, on the other hand, was undergoing far less extensive renovations but decided to undertake an optional retrofit project to upgrade their buildings to a life safety seismic rating. Finally, Anheuser-Busch Brewery undertook an extensive retrofit project to limit potential economic losses from lost productivity due to seismic damage of their facilities.

My research also revealed that while retrofit can be extremely expensive when undertaken as an independent project, when combined with extensive renovation it is fairly efficient. In the case of Olin Library seismic retrofit cost less than one percent of the total cost of renovation.

Finally, because investing resources in retrofit work to prepare for a low frequency, high consequence event like an earthquake is difficult for people to rationalize, it makes sense to target building owners of essential facilities or businesses liable for significant economic loss in order to increase the social and economic impact of the mitigation project.

References

- Alfeld, L.E., & Graham, A.K. *Introduction to Urban Dynamics*. Cambridge, MA: Wright-Allen Press, 1976.
- Applied Technology Council. FEMA-276. *Example Applications of the NEHRP Guidelines for the Seismic Rehabilitation of Buildings*. Washington, D.C. (1999).
- Cho, S. (2004). "Community Goal Dynamics, A Case Study," Dissertation proposal to the George Warren Brown School of Social Work at Washington University in St. Louis, (2004).
- Christner, T. June 24, 2004. Personal interview by M. Mauter with Ted Christner, The Christner Partnership, Inc.
- Forrester, J. W. *Urban Dynamics*. Cambridge, MA: MIT Press, 1969.
- Freedman, F. Personal interview by M. Mauter with Frank Freedman, Facilities Manager, Washington University in St. Louis.
- Gauthier, R. F. "CM-2: Acceptable Consequences-Financial Impact on Seismic Retrofit Policies," Mid-America Earthquake Center.
- Gillespie, D. F., & Robards, K. J. "Facility Management Decision-Making in Mid America: Dynamic Structure of Preparedness and Mitigation," National Science Foundation, USA, (2000).
- Gillespie, D.F., Gould, P., & Cho, S. "Modeling to Assist in the Determination of Acceptable Consequences," National Science Foundation, USA, (2003).
- Gillespie, D.F., Robards, K.J., & Cho, S. "Acceptable Risk and Mitigation Options: Dynamic Structure of Building Safety," National Science Foundation, USA, (2003).
- Gillespie, D.F., Robards, K.J., & Cho, S. "Designing Safe Systems: Using System Dynamics to Understand Complexity," *Natural Hazards Review*, 5:2 (2004), pp. 82-88.
- Godschalk, D. R. "Disaster mitigation and hazard management." *Emergency management: Principles and practice for local government*. In Drabek, T. E. & G. J. Hoetmer (Eds.). Washington D.C., International City Management Association, 1991. pp. 131-160.
- Mid-America Earthquake Center. Grant Application to the National Science Foundations, 2004.
- Mileti, D. S. "Influences on the adoption and implementation of mitigation." *Disasters by design: A reassessment of natural hazards in the United States*. Washington, DC: Joseph Henry Press, 1999. pp. 135-154.
- Sedchak, P. June 22, 2004. Personal interview by M. Mauter with Paul Sedchak, Public Relations Department, Clayton School District.
- Taylor, J. June 16, 2004. Personal interview by M. Mauter with Jim Taylor, ABS Consulting.
- Winn, V. June 16, 2004. Personal interview by M. Mauter with Victoria Winn, ABS Consulting.
- Wonish, T. June 14, 2004. Personal interview by M. Mauter with Tim Wonish, Facilities Manager, Clayton School District.

Appendix 1

INTERVIEW QUESTIONS FOR SEISMICALLY RETROFITTED BUILDINGS

Structural Background of the Building

What is the age and anticipated life span of this structure?

What is the square footage and construction type of the rehabilitated building?

When and how did you first become aware of the need for the seismic rehabilitation of this structure?

What were the perceived consequences of not undertaking this seismic rehabilitation project? (Life threats, business interruption costs, loss or damage of equipment and valuable objects stored in this facility)

Was this retrofit process undertaken as an independent project, or in conjunction with a major renovation project? What was the time span of this rehabilitation project?

Seismic Retrofit Design

What level of seismicity (low, medium, or high) did you design for?

What performance level (limited safety objective, basic safety objective, or enhanced safety objective) did you select for this retrofit project?

Did the decision to seismically rehabilitate this building trigger any additional mandated improvements such as compliance with the American with Disabilities Act or the removal of hazardous materials such as asbestos and lead-based paint? What additional costs did these improvements add to the final project cost?

In addition to the seismic retrofit of the structural components of the building, were any measures taken to improve the seismic resistance of equipment or other non-structural components?

How was this building analyzed for structural deficiencies?

What were the primary structural deficiencies identified in this building?

- General Structural Attributes
- Steel Moment Frames
- Braced Frames
- Diaphragms and Diaphragm Connections
- Foundation and Foundation Connections

What rehabilitation measures were taken to remedy these deficiencies?

Economic Considerations

How was this project funded? Did you receive any government aid or tax abatements for voluntarily retrofitting your building?

What was the total cost of this retrofit project? How close were final costs to early estimates for seismic rehabilitation?

Do you have insurance to cover seismic damage to your building? Did your insurance rate drop after seismic rehabilitation was complete? What is the approximate annual savings?

Project Details

What was the time-span of this project?

Did the retrofit process cause any significant problems or disruptions in the normal utilization of the facilities?

Was occupancy of the building required during the rehabilitation process? How was this addressed and explained to those who would be occupying the building?

Now that this project is complete, do you believe that the seismic retrofit was a worthwhile investment?

Appendix 2

Pictures of Seismic Retrofit Work

Clayton High School Complex



Clayton High School Auditorium during and after retrofit work

Olin Library



Olin Library prior to renovation and retrofit



Olin Library after renovation and retrofit



Steel cross bracing at Olin Library

Anheuser-Busch Brewery



Retrofitted Buildings at Anheuser-Busch Brewery, St. Louis, MO.

Appendix 3

Clayton High School Retrofit Strategy by Building

Building	Construction Date	Lateral Load Resisting System	Seismic Deficiencies	Retrofit Strategy	Cost
Industrial Arts Building	1951	URM	URM does not support lateral load	Add four reinforced concrete shear walls supported by drilled piers	290,000
Home Economics Building	1951	URM	URM does not support lateral load	Add four reinforced concrete shear walls supported by drilled piers	243,000
Boiler Building	1951	URM	URM does not support lateral load	Add six bays of cross bracing	37,000
P.E. Annex	1967, 1978	Cross Bracing	meets code	N/A	N/A
Gymnasium	1951	URM	Small masonry pilasters do not resist lateral load, bulb tee roof does not resist seismic forces	Add two reinforced concrete shear walls and strengthen roof with steel rod cross bracing	873,000
Natorium	1956	URM and rigid steel bents	Steel frames only support half of the building	Add steel bracing to remainder of building	846,000
Auditorium	1951, 1987	URM	URM does not support lateral load, two areas without any lateral force resisting elements, low ductility because roofs and floors at different elevations	Add steel bracing at entrances, steel grid on exterior of all walls to increase ductility	728,000
Cafeteria	1951, 1958	URM	URM does not resist lateral load, bulb tee roof does not resist seismic forces	Add four reinforced concrete shear walls and strengthen roof with steel rod cross bracing	452,000
Library	1963, 1988	semi-rigid type 2 "wind connections" and structural steel frames	Wind connections insufficient to resist seismic forces	Add 11 bays of steel bracing	346,000
Academic Building	1951	URM	URM does not resist lateral load, bulb tee roof does not resist seismic forces	Add reinforced concrete shear walls to exterior, strengthen roof with steel rod cross bracing	1,334,000
Total					5,149,000

3D VISUALIZATION PROGRAM FOR EARTHQUAKE SIMULATION

Christy Nishimoto

Home Institution: University of California, San Diego

REU Institution: University of California, Davis

REU Advisor: Ross Boulanger

Abstract

Looking at hundreds of time histories for sensors in an earthquake simulation experiment can become very cumbersome. The UC Davis Center for Geotechnical Modeling has recently developed a visualization program that gives the user a three-dimensional view of the sensors in an earthquake simulation experiment. The visualization program allows the user to watch the movements of the sensors.

In order to view data from an earthquake simulation in the visualization program, an experiment file is created. The experiment file consists of an instrument file, an event file, and a model container file. The instrument file lists all the sensors used in the experiment, their initial location, type, and whether the sensor is positioned horizontally or vertically. The event file lists all the earthquake simulations performed using the same experiment configuration. Two important sub-files are the channel gain file and the sensor log file. The channel gain file lists the sensors that are used in each event and the sensor log file contains normalized data from the experiment. The main purpose of this study is to document the creation of an experiment file so other people can convert data from their own experiments into the form required by the visualization program.

Introduction to my study

Scientists at the Center for Geotechnical Modeling at the University of California, Davis have created a system that visualizes displacement, acceleration, and strain data collected during an earthquake simulation experiment in a geotechnical centrifuge. “Data and meta-data is currently supplied in form of a PDF experiment report, sketches illustrating an experiment, Microsoft Excel spreadsheets detailing positions of sensors, calibration data and experiment history, and ASCII files containing the transducer recordings” (Weber, 2003). Results of the earthquake simulation experiments were originally visualized “as a set of 2D graphs plotting sensor data as a function of time” (Weber, 2003). This method is very difficult for a scientist because it is hard to get a good idea of what is happening in a model container that contains hundreds of sensors simply by looking at 2D graphs. When a scientist has to look at a 2D graph s/he has to match each time history to the respective sensor, which is very cumbersome. The Center for

Geotechnical Modeling's visualization tool, which is called Shaker, "starts by reading the data describing experiment set-up and displaying this data along with icons for the sensors used during data acquisition, providing spatial context for each sensor. Once a user has selected a particular event, measured data can be displayed as a 2D graph/plot by clicking the corresponding sensor. Sensors can be animated to obtain 3D visualizations of measured data" (Weber, 2003).

This is why I studied it

My part of the Shaker program was to figure out and document the method to convert data from experiments into the form required by the Shaker program. The reason why I researched how to place test data into the Shaker program was because no student had attempted to create a usable Shaker experiment. It was important for someone to figure out how to convert test data into a usable experiment for the Shaker program. My objective for the summer was to become familiar with the Shaker program and to come up with a general procedure for converting test data to a usable experiment for the Shaker program.

Research Approach

Before I could begin working on a procedure for converting test data to a usable experiment for the Shaker program I had to research the visualization program and the types of experiments the program is used for. By researching the visualization program along with the types of experiments the program is used for I was able to gain a better understanding of the program I was working with. Some of the papers that I read in order to gain this understanding were the "Status Report on Study of Modeling of Nonlinear Cyclic Load-Deformation Behavior of Shallow Foundations," "Visualization of Experimental Earthquake Data," "The NEES geotechnical centrifuge at UC Davis," and data reports from experiments performed at the geotechnical centrifuge at UC Davis. Once I felt I had a good understanding of the types of experiments the Shaker program is used for and a good idea of how the Shaker program works, I started to look into how an experiment file is created. I examined an existing experiment, DDC01, to see the types of files that needed to be created for the Shaker program. After examining this experiment and getting pointers from Dan Wilson and Tom Slankard, I took test data and experimented with it to figure out how to transform that test data to the necessary format required by the Shaker program.

My procedure for converting test data

Prior to attempting to convert test data to an experiment file for Shaker, it is a good idea to look at a folder of a created experiment in order to get an idea of the types of files that will need to be created. An example of a good experiment to look at is DDC01. After the files that make up the experiment are examined, a folder needs to be created to hold all the files that will be made. Before any files are created, copy the files named `default_behaviors.xml` and `test.xml`, which can be found in the DDC01 experiment folder, and paste these files into the folder that was created for the new experiment. Also copy the file named `container1.iv` in the DDC01 experiment folder and paste this file into the folder for the new experiment. The file named `container1.iv` is a VRML file that describes the model container and provides a convenient reference frame. If a different model container than the one in the DDC01 experiment is used, a new file will need to be created in order to accurately describe the model container.

There are five different types of files that need to be created when converting test data to an experiment file for Shaker. One of the main files that are created is the `.exp` file. The `.exp` file is the experiment description file. This is the file that is called by Shaker to run the experiment. The `.exp` file contains references to the `.il` file, the `.el` file, the `.iv` file, and the coordinate reference for the x, y, and z coordinate axis. The `.il` file is the instrument list file. The instrument list file contains the instrument location number, the type of instrument, engineering units, location description, the initial x, y, and z coordinates, and whether the instrument is positioned horizontally or vertically. The `.el` file is the event list file. The event list file is a list of all the recorded events during the experiment. The `.el` file contains descriptive information of every event and references two external files for each event. The two external files that are referenced are the `.cgl` files and the `.txt` files. The `.cgl` files are the channel gain lists. A channel gain list is a list of the instrument location numbers that were recorded in a given event. The `.txt` files are the sensor log files. The sensor log files contain the recorded time histories for the channels listed in the `.cgl` file for each event.

In order to easily construct the experiment files, it is useful to use the experiment files from an experiment that has already been created as a template. The DDC01 experiment is an example of an experiment that can be used as a template and is used in the following procedure. The appendix contains an example illustrating how the following procedure is used to convert test data to a usable experiment for Shaker.

The first file that needs to be formed is the `.exp` file. One way to create this file is to open the `.exp` file of an experiment that has already been created, for example DDC01, using Notepad. Rename the `DDC01.il` and the `DDC01.el` files to something appropriate for the experiment that is being created. Use the command "save as" to rename and save

the .exp file. An example of a created .exp file is shown in Fig. 1. Place the saved file in the folder that was created for all the experiment files.

```
HPC01.e1  
HPC01.i1  
container1.iv  
0.0 0.0 0.0  
1.0 0.0 0.0  
0.0 1.0 0.0  
0.0 0.0 1.0
```

Figure 1. An example of a created .exp file.

The next file that is made is the .il file. Before creating this file all the data for the location of all the instruments in the experiment needs to be converted into the coordinate system that Shaker uses. The origin in Shaker is the bottom left corner of the container. The origin, as well as the axis of the Shaker program is shown in Fig. 2.

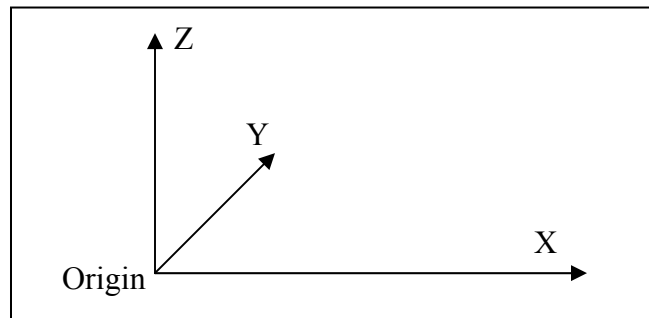


Figure 2. The coordinate system used by Shaker.

After all the coordinates for the sensors are converted to the Shaker coordinate system, open the DDC01.il file from the DDC01 experiment folder using Notepad and rename the file. Replace the data in this file with the data from the experiment being created. The data that is placed in this file is tab delimited. If there are more sensors in the experiment than in the DDC01.il file, then when entering a new row of data, the tab character needs to be inserted between each column of data as well as at the end of each event. An example of how data for an additional sensor is added where the items in parenthesis are keystrokes can be seen in Fig. 3.

```
A1(tab)acc(tab)g's(tab)"Northwest Shaker Table"(tab)0(tab)-46(tab)0(tab)H(tab)(enter)
```

Figure 3. The method for entering data in the instrument list.

The .el file is created next. Form the event list file by opening the DDC01.el file from the DDC01 experiment folder using Notepad and placing the data for the experiment that is being created in this DDC01.el file. To add additional events to this file, follow the same format used to enter data in the instrument list file since the data placed in this file is also tab delimited. Fig. 4 shows how additional events need to be entered where the items in parenthesis are keystrokes. The data shown in Fig. 4 should all be entered on one line. After all the data has been entered save and rename the file.

```
"Wed., 8/18"(tab)2:50 PM(tab)"shake11"(tab)HPC01-2.cgl(tab)shake11.txt(tab)(enter)
```

Figure 4. The method for entering data in the event list.

Once the .el file is made, create the .cgl files for each event. The channel gain list specifies which instrument outputs and in what order the outputs are read for a particular event. To create a channel gain list for a particular event, open the .cgl file from the DDC01 experiment folder using Notepad. Replace the instruments listed in the file with the instruments that were used for the event. The channel gain list is not a tab delimited file. Therefore, when placing the instruments that were used for the event a tab character should not be inserted after the name of each instrument. Fig. 5 illustrates how the channel gain list should be created, where the items in parenthesis are keystrokes.

```
A1(enter)  
A2(enter)  
A3(enter)
```

Figure 5. The method for entering data in the channel gain list.

The final files to be created are the .txt files or the sensor log files. Create the sensor log files using the output data that has been converted to engineering prototype units in MathCAD. These converted output data files have the appendix .prt. The first column in the output data files is the time and the rest of the columns are the sensors in the order that they are listed in the channel gain file. Import the data files into a program like Microsoft Excel. Once the data is in Excel, the data needs to be normalized so that all the values lie between -1 and 1. Normalize the data based upon the type of sensor. For example, all the sensors that measure displacement are normalized with respect to each other, where the sensors that measure acceleration are only normalized with respect to

other sensors that measure acceleration. Time is normalized with respect to itself. To normalize the data for each type of sensor, find the largest data value, either positive or negative, and divide all of that type of data by that value. If the largest value is negative, multiply it by -1 in order to preserve the sign. After the data has been normalized, save the normalized data as a text (tab delimited) document. The easiest way to do this is to first save all the data as a text (tab delimited) document, make a copy of the normalized data in this file, and paste the data in a new document which is also saved as a text (tab delimited) document. Repeat this process for all of the events in the experiment. Place all of the normalized sensor log files in the folder with all of the files for the experiment.

After the experiment is created, load the experiment into the Shaker program to check to see that everything is working properly. Once the Shaker program has been opened, an experiment is loaded into the Shaker program by choosing file and then load experiment. Fig. 6 is an illustration of what the Shaker program should show when the experiment is loaded correctly.

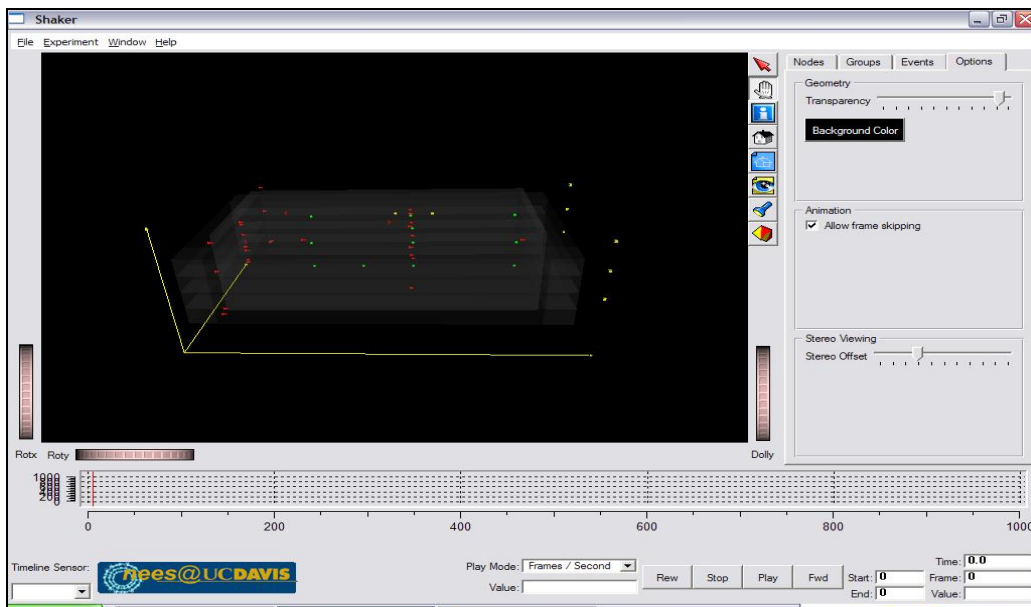


Figure 6. A successfully loaded Shaker experiment.

Once the .exp file is successfully loaded into the Shaker program check the instruments to make sure that they are in the proper location. Also, run each event to make sure that all the data has been properly converted and that all the instruments are functioning correctly. In order to run an event, first click the event tab found towards the top right corner. Next, click the event that you want to run. If the event is selected properly it should appear highlighted. Then click the load button which is located in the lower right corner. After the event loads click the play button in the lower right corner to view the event. A picture of a loaded event running in the Shaker program is shown in Fig. 7.

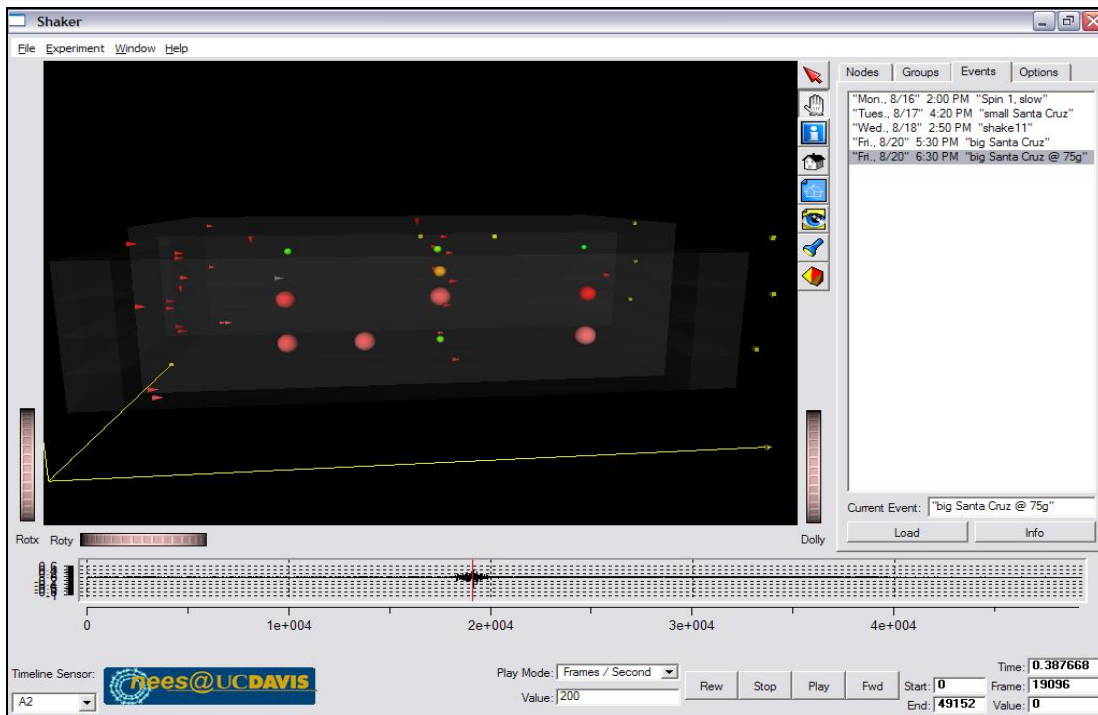


Figure 7. Snapshot of an event running in the Shaker program.

Once an event is loaded, the time history of each instrument can also be viewed. To view the time history of an instrument, click the tab that is titled nodes. The nodes tab is found in the upper right corner. Click on the name of the instrument whose time history is of interest. Then click on the info button found in the lower right corner. To view the time histories for multiple instruments at the same time, control-click each instrument of interest and click the load button. Fig. 8 shows time histories of two of the sensors during the event pictured in Fig. 7.

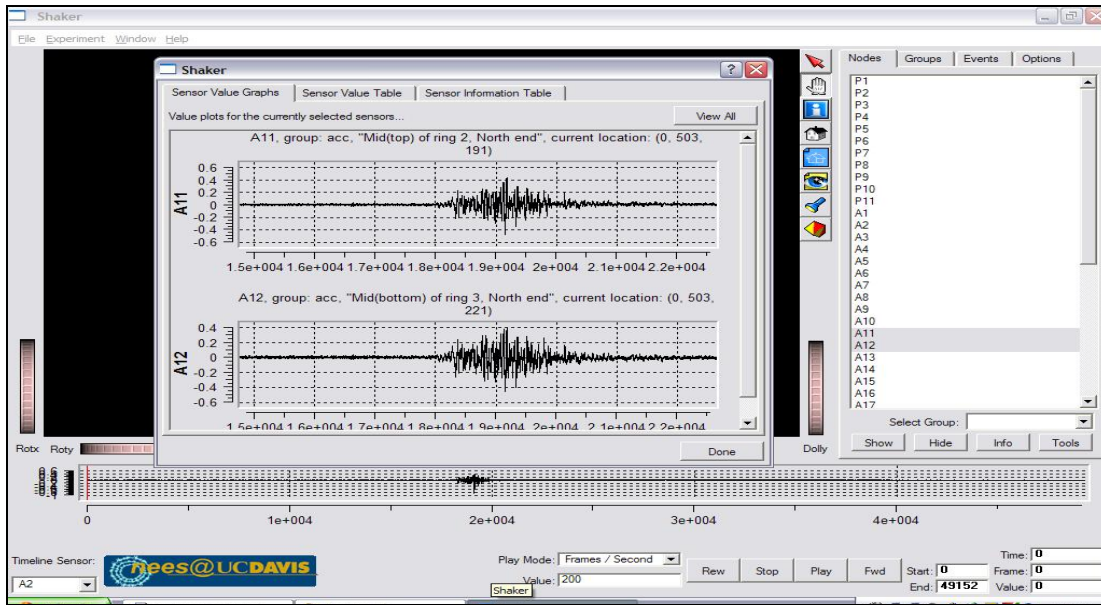


Figure 8. Two sensor time histories for an event in the Shaker program.

The significance of the study

Creating a procedure to take test data and manipulate the data into a usable Shaker experiment was significant because no student had attempted to create a usable Shaker experiment in the past. The main result of coming up with a procedure for converting test data into an experiment file that the Shaker program can use, is that in the future any student that wants to take data and place that data in a Shaker experiment file now has a guide to follow. Having a reference guide will be a tremendous advantage to any student because now s/he does not have to struggle to figure out how experiment files are created in the Shaker program.

Future goals for the Shaker program

One of the main goals in the future for the Shaker program is to connect the Shaker program to the NEESgrid. Once the Shaker program is connected to the NEESgrid, experimental earthquake research groups throughout the U.S. will be able to use the program via the internet. The Shaker program also has a few more immediate goals that will help improve the actual Shaker program. One of these goals is to create the ability to place solid containers in the model as well as sensors. The addition of solid containers in the model will give the user to opportunity to visualize how a structure reacts during an earthquake simulation. The other immediate goal for the Shaker program is to give more degrees of freedom to the sensors. Currently, the sensors can only show horizontal or vertical movement. In the future, the Shaker program will be able to show both horizontal and vertical movement, so in essence the sensors will be able to rotate.

Acknowledgements

This research was conducted as part of the 2004 Research Experience for Undergraduates at the University of California at Davis and was funded by the National Science Foundation. I would like to thank Tom Slankard and Dan Wilson for their guidance and assistance during the entire summer. I would also like to thank my advisor Ross Boulanger for making this summer research experience possible.

References

Weber, Gunther H., et al. "Visualization of Experimental Earthquake Data," *Visualization and Data Analysis 2003*. Santa Clara, CA; January 21-22, 2003.

Appendix

Procedure used to convert the HCP01 test data to a usable experiment for Shaker

Step 1: Preparing to create the experiment

The first thing done in preparation for this experiment was to create a folder to place all the needed files for the experiment. The created folder is titled HCP01. All the files that are created in the following steps are placed into this folder. Before creating any files, the following files were pasted into this folder from the DDC01 experiment folder: container1.iv, default_behaviors.xml, test.xml, and Copy of default_behaviors.xml. The file container1.iv needs to be modified in order to have the same size container that is used in this experiment in the Shaker program.

Step 2: Creating the experiment file

The experiment file was created by opening the DDC01.exp file and renaming the event list and the instrument list. The files were renamed HPC01.el and HPC01.il respectively. The experiment file was saved as HPC01.exp and placed in the HPC01 folder.

Step 3: Creating the instrument list

The coordinates that were used for the location of all the instruments in the experiment were provided. Along with receiving the coordinates, the actual model was looked at in order to visualize the placement of all the instruments. The coordinate system used to place the instruments in the HCP01 experiment took the top northeast corner of the container for the origin. Since the origin for the Shaker program is the bottom northwest corner, the coordinates had to be converted so that the instruments were properly placed in the Shaker program. The coordinates were adjusted in the manner shown in Fig. 9. The coordinates of the model container are illustrated in Figs. 10 and 11 and a drawing illustrating the different origins is shown in Fig. 12.

X-coordinates: remained the same Y-coordinates: 1006 mm - given value Z-coordinates: 570 mm - given value

Figure 9. This figure shows the method for adjusting the coordinates.

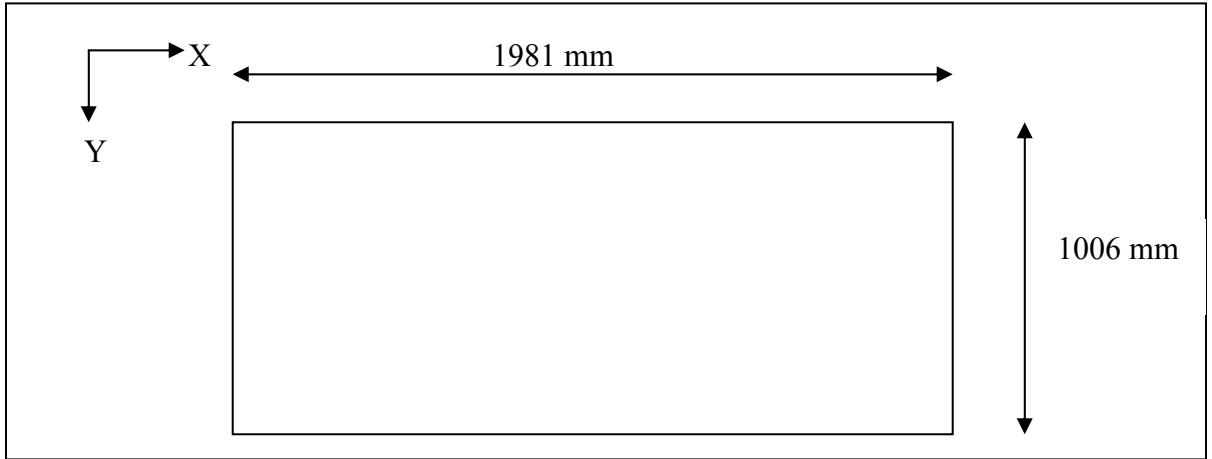


Figure 10. The diagram shows plane view of the container.

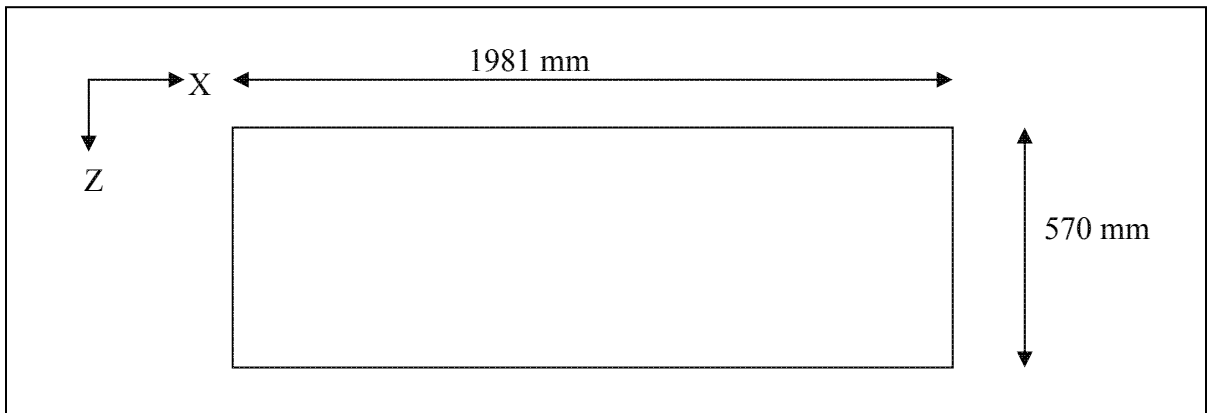


Figure 11. The drawing illustrates elevation view of the container.

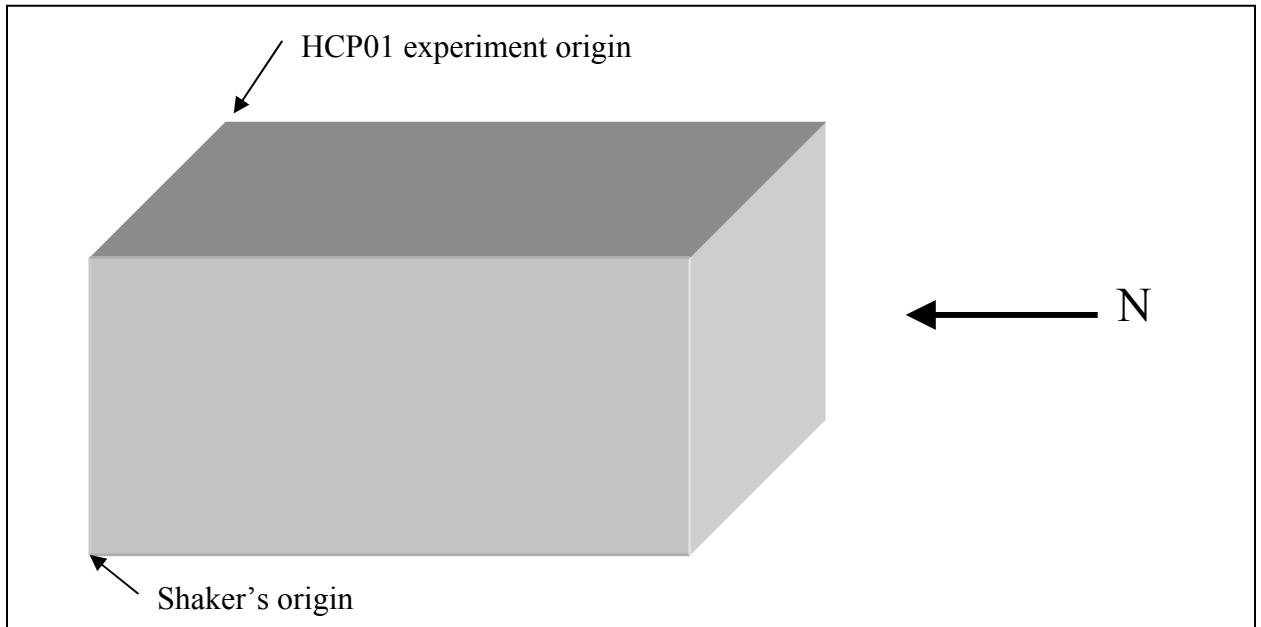


Figure 12. This diagram shows the difference between the two origins

Once the coordinates for the sensors were converted into Shaker's coordinate system, the instrument file was created. The DDC01.il file was used as a template. All the data that was in this file was deleted and the data for this experiment were placed in the file. The file was saved as HCP01.il and placed in the HCP01 folder. An example of how one line of the instrument list was placed in the file is shown in Fig. 13.

```
A1(tab)acc(tab)g's(tab)"Northwest Shaker Table"(tab)0(tab)-46(tab)0(tab)H(tab)(enter)
```

Figure 13. This is a representation of how data is entered in the .il file.

Step 4: Creating the event list

The event list was created by using the file DDC01.el as a template. The data that was in the DDC01.el file was deleted and the data for the HCP01 experiment was placed in the file. The file was then saved as HCP01.el and placed in the HCP01 folder. An example of how a line of data was placed in this file is illustrated in Fig. 14.

```
“Wed., 8/18”(tab)2:50 PM(tab)”shake11”(tab)HPC01-2.cgl(tab)shake11.txt(tab)(enter)
```

Figure 14. This is an illustration of how data was entered in the .el file.

Step 5: Creating the channel gain list

The channel gain lists were created from data that gave the order that the instruments were read for each event. The DDC01.cgl file was used as a template for creating each channel gain list. The instruments listed in the DDC01.cgl file were deleted and the instruments for this experiment were placed in the file in the order in which the data was taken. Each channel gain list file was saved with a unique name that corresponds to the name found in the HPC01.el file for a specific event and placed in the HCP01 folder. An example of how instruments are listed in a channel gain list can be seen in Fig. 15.

```
A2(enter)  
A27(enter)  
A4(enter)
```

Figure 15. This is an example of how data for the .cgl file was entered.

Step 6: Creating the sensor log files

The last step in creating the experiment was to create the sensor log files. The prototype data from the events in the HCP01 experiment was used. The prototype data that was received did not have a space between all positive and negative numbers. Some of the data looked as follows: 4.056-0.0025. In order to quickly correct this problem, the prototype data was copied into Microsoft Word. Once in Microsoft Word, the find and replace command was used to place a space between each number as shown in Fig. 16.

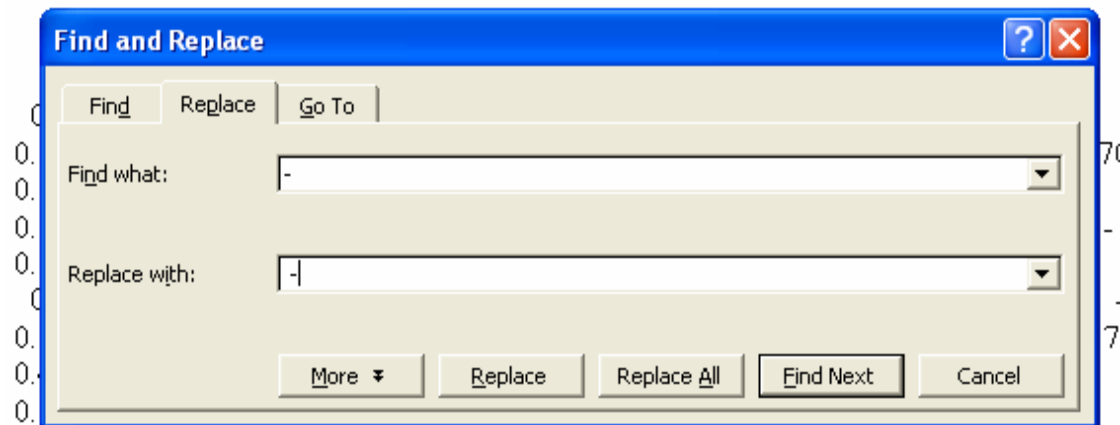


Figure 16. This is a screenshot showing how spaces were placed between the numbers.

The data was then imported into Microsoft Excel. In Excel, the data was normalized so that all the values lied between -1 and 1. The data was normalized based on the type of sensor. For example, for the shake11 event the accelerometers were normalized by dividing all accelerometer data by 6.565 whereas all the linear potentiometer data was divided by 1.042. The normalized data was saved as a text (tab delimited) file and placed in the HCP01 folder.

Step 7: Checking the experiment

After the experiment is created, the experiment is loaded into the Shaker program to check to see that everything is working properly. Once the Shaker program has been opened, an experiment is loaded into the Shaker program by choosing file and then load experiment. Once the HCP01.exp file is successfully loaded into the Shaker program the instruments are checked to make sure that they are in the proper location. Also, each event is run to make sure that all the data has been properly converted and that all the instruments are functioning correctly. In order to run an event, first click the event tab found towards the top right corner. Next, click the event that you want to run. If the event is selected properly it should appear highlighted. Then click the load button which is located in the lower right corner. After the event loads click the play button in the lower right corner to view the event. Once an event is loaded, the time history of each instrument can also be viewed. To view the time history of an instrument, click the tab that is titled nodes. The nodes tab is found in the upper right corner. Click on the name of the instrument whose time history is of interest. Then click on the info button found in the lower right corner. To view the time histories for multiple instruments at the same time, control-click each instrument of interest and click the load button.

HD-2A: INTRA-PLATE SOURCE MODELING

Lindsey Oliver
University of Chicago
University of Memphis
Dr. Roy Van Arsdale

Abstract

This project addresses the need for more accurate fault data in the New Madrid Fault Zone due to the risk of seismic activity. On a regional level, an ARCGIS™ database was created to compile the location of faults, their age, the fault type, and documentation of the fault in the literature.

Additionally the database provides a 30 meter resolution DEM of the Mississippi Embayment, location and magnitude of seismicity, areas of uplift and subsidence, lineaments, fault zones, gravitational and magnetic anomalies, plutons, rivers, cities, counties, states, and highways. On a more local level, the Ellendale Fault and another unnamed fault, which pass under Shelby Farms in Memphis, and the Memphis fault, located near the intersection of James Rd. and Hollywood, were also investigated. An S-wave seismic reflection line was shot at Shelby Farms

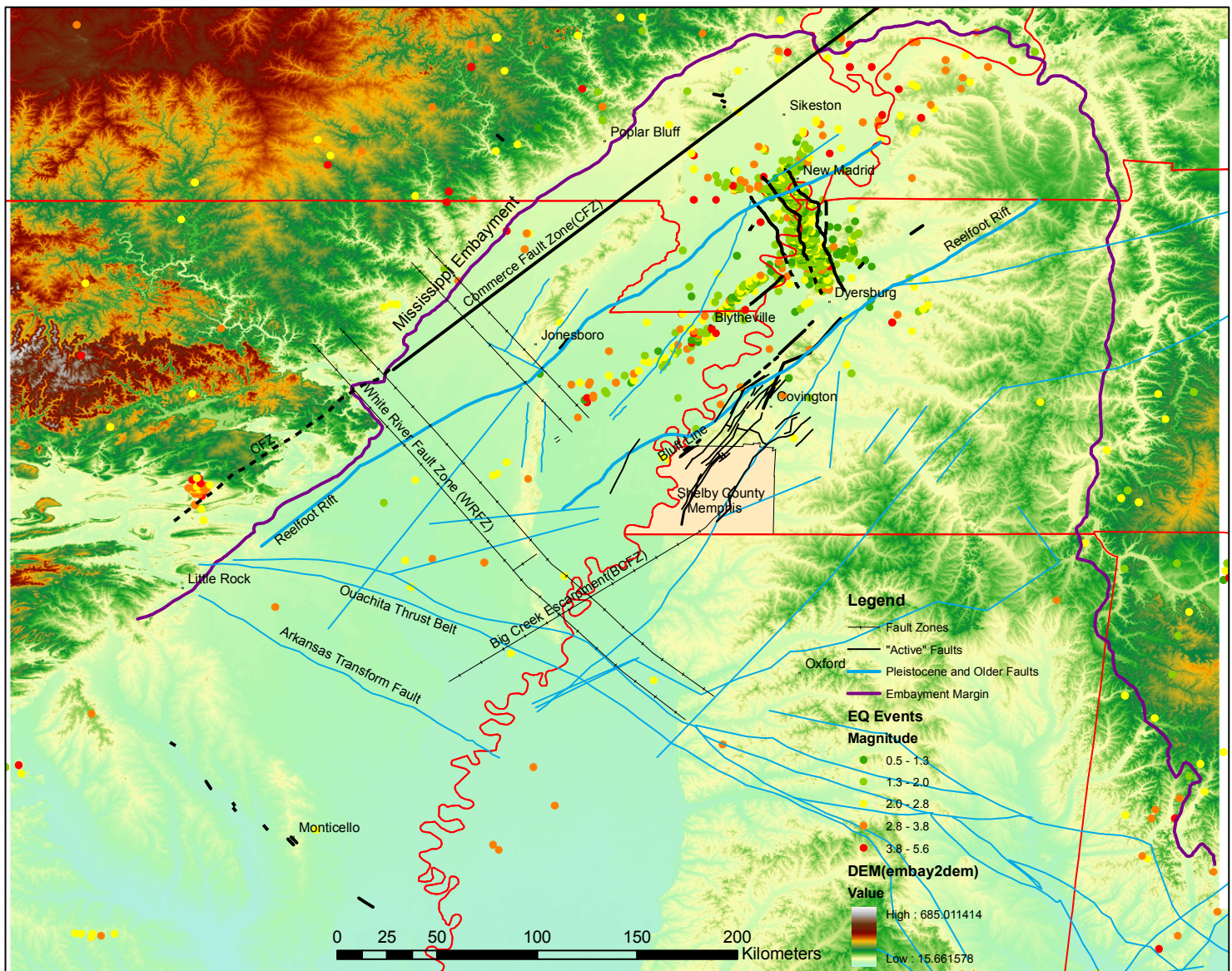


Figure 1. Faults and Seismicity of the Northern Mississippi Embayment

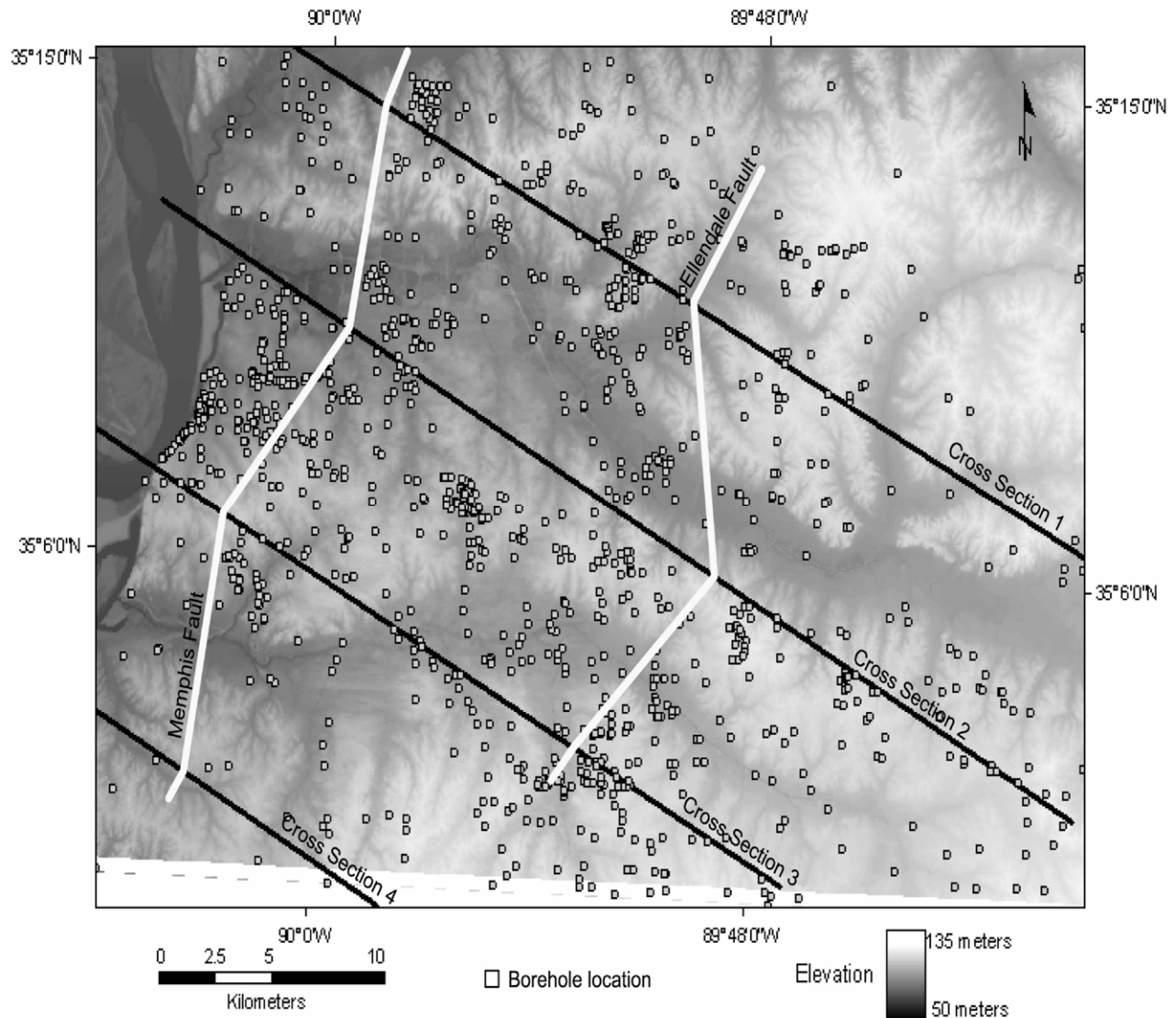


Figure 2.

and conductivity surveys were performed at both sites to find changes in the conductivity in the shallow subsurface which may imply offset strata and evidence of faulting. The areas of greatest transition at Shelby Farms were further investigated by drilling bore holes and collecting core samples, three to five meters in depth. The lateral discontinuity observed in the cores corresponded with the fault locations derived from the conductivity surveys. Based on these tests, the existence of the Memphis Fault, the Ellendale Fault, and an unnamed fault also in Shelby Farms is substantiated. Future work will include trenching across the proposed area of faulting to measure the degree of offset and date the age of the last episode of displacement.

Introduction

The Northern Mississippi Embayment, a shallowly plunging trough filled with Cretaceous and Cenozoic sediments (Cox and Van Arsdale, 2002), lies atop a failed Precambrian rift, resulting in faulting in the generally aseismic interior of the North American Plate (Schweig and Van Arsdale, 1996). The New Madrid seismic zone is the most active of the seismic zones in the region (Fig. 1). Its history of magnitude eight earthquakes (1811-1812) and potential for future large magnitude earthquakes in a region containing soil capable of high seismic amplification and low public awareness is a cause for concern. The potential for a destructive earthquake has led to much study of this seismic zone and preparation for a future seismic event. The hazard posed by many nearby faults, however, is not often taken into consideration. In fact, new faults are still being discovered (Cox and Van Arsdale, 2000) and some previously known faults are poorly understood. Given the number of communities that lie near these faults, including Memphis, it is necessary to address this problem. To do so, a regional database has been created to collect and display information on geologic features, particularly faults, which may better delineate the hazards in the region. On a more local level, two faults in Memphis are currently being investigated and their extents added to the database.

Structure contour maps of the tops of Quaternary and Tertiary layers reveal two steps in the Upland Gravel Lafayette Formation and the Upper and Lower Claiborne Group (Velasco, 2002), located in Shelby County, Tennessee (Fig. 2). Because these units span more than 30 million years it is unlikely that the steps are the result of river terraces, but instead are interpreted to be caused by faulting. Additionally, an anticline and a sand blow (Velasco, 2002) along the Wolf River near of the projection of the eastern step further support the theory that the region is seismically active. Quaternary movement is believed to have occurred on the Memphis Fault, the western step, and the Ellendale Fault to the east. A seismic S-wave survey was run to better locate the Memphis Fault (Fig. 3) and two locations of offset in the near surface were observed. The Memphis Fault is located east of the intersection of Hollywood and James Rd. in north Memphis (Fig. 4) and the Ellendale Fault is located at Shelby Farms in Germantown (Fig. 5). This project contributed to an ongoing search for faults in Memphis, particularly more accurately locating suspected near-surface faults in preparation for trenching. To do so conductivity surveys were taken at the James Road site based on the previously performed seismic survey. At Shelby Farms a more extensive investigation was possible, and a seismic line was run, several conductivity surveys were taken, and bore holes were drilled.

Methods

ARCGIS™ Database

One facet of the project involved constructing a database using a 30 m resolution DEM from USGS as a base map and state boundaries, county boundaries, cities, highways, and rivers obtained from ESRI. These features act as reference points to check the accuracy and improve placement of the digitized features. The geographic data will also help to define which communities are most threatened by active faults and establish the area being studied. Contour maps of the top of the Precambrian (Fig. 6), Paleozoic, Cretaceous, Paleocene, and Tertiary stratigraphic units were delineated utilizing coal well logs, oil exploration wells, and seismic line

data which were imported into the database. Geologic features were digitized and imported using a GTCO acutab digitizer and Arc workstation.

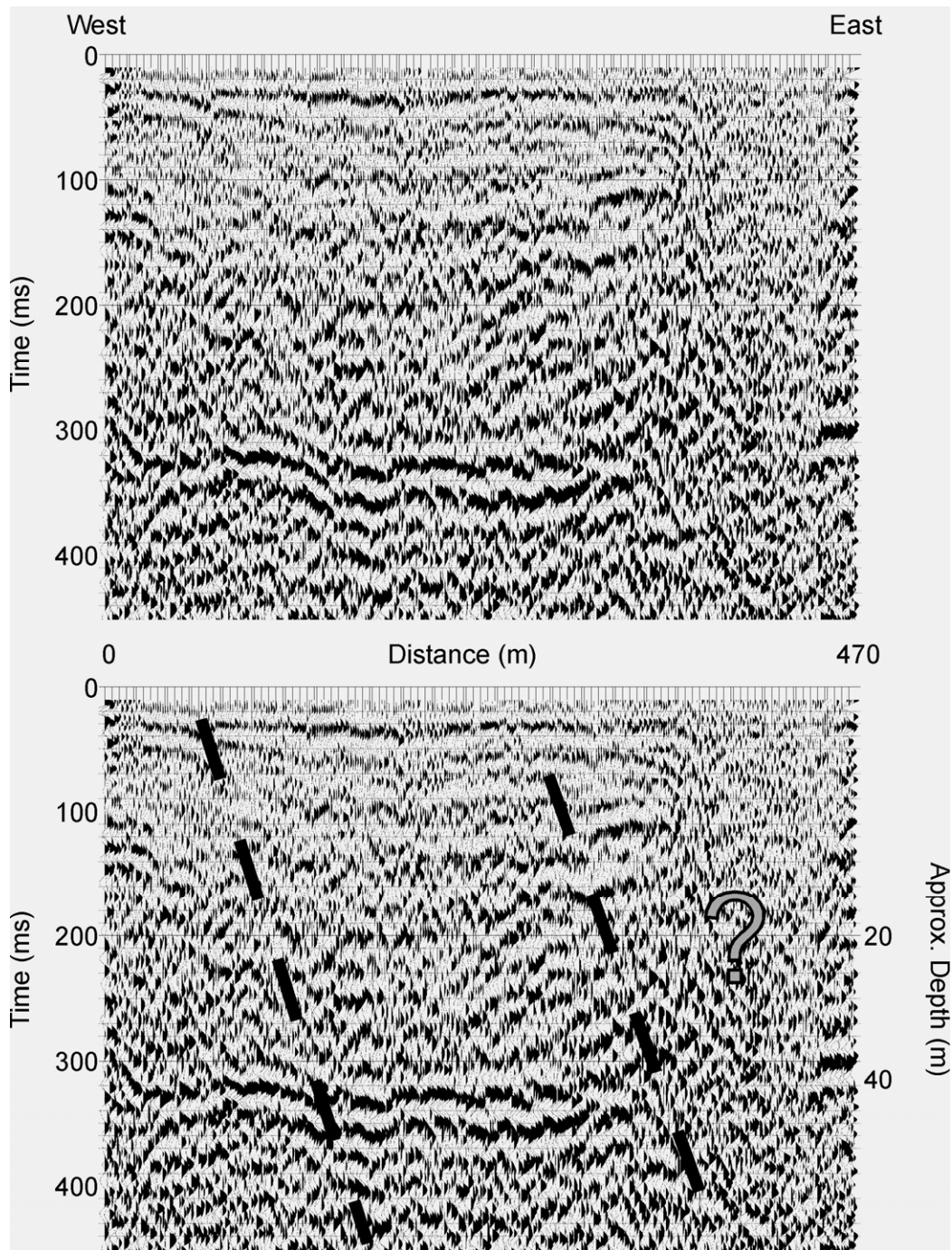


Figure 3. S-wave seismic reflection line at James Road with interpreted figure at the bottom, dashed lines indicate faults.

FAULT EXPLORATION MAP OF HOLLYWOOD AND JAMES RD.
MEMPHIS, TN

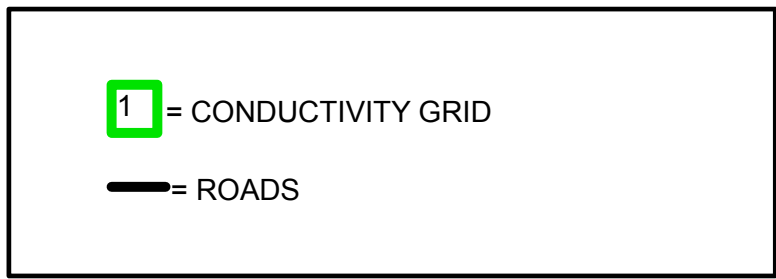
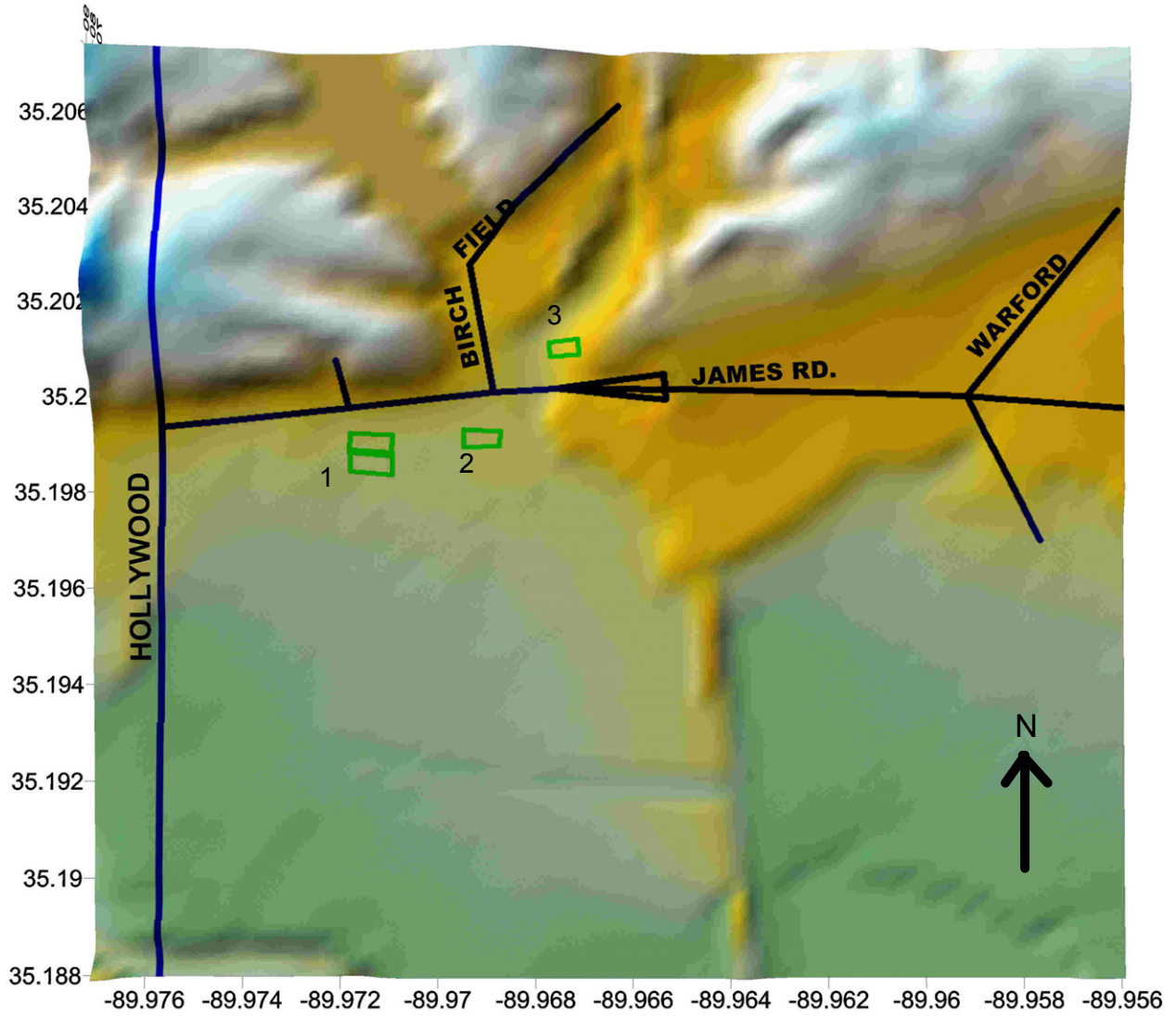


Figure 4. Map of James Road and Hollywood area.

FAULT EXPLORATION MAP OF AGRICENTER (SHELBY FARMS) SHELBY COUNTY, TN

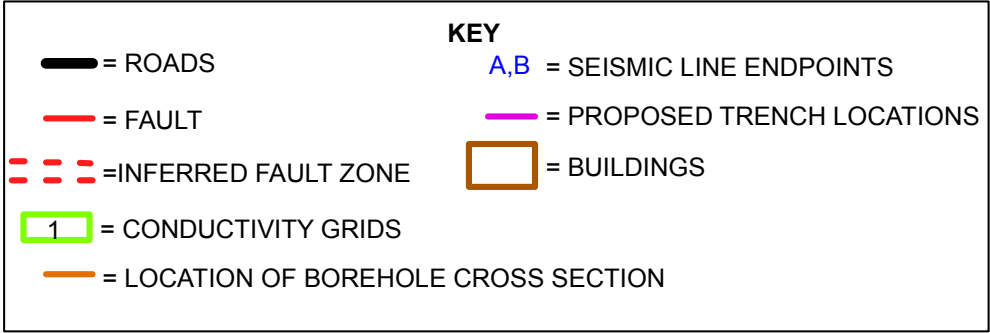
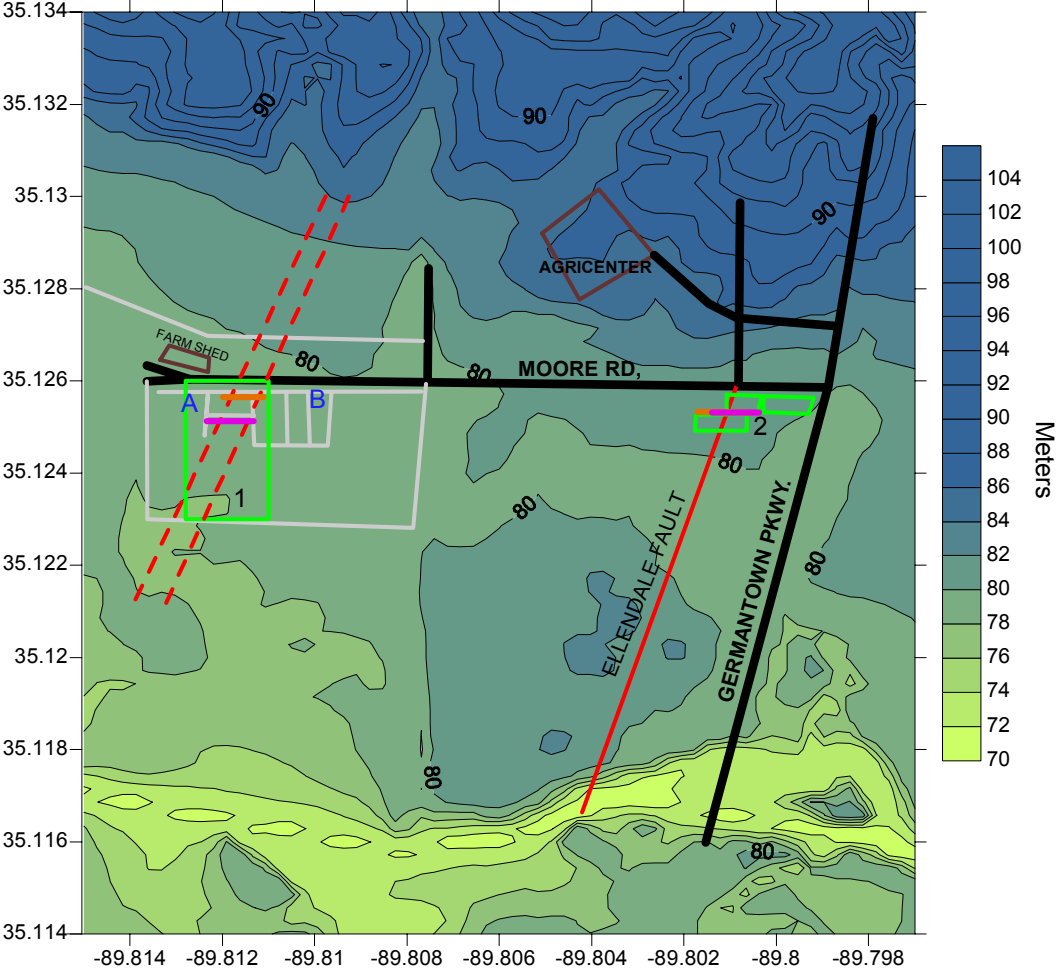


Figure 5. Map of the Shelby Farms investigation site.

They were then imported as coverages and converted into shapefiles for manipulation and interpretation in ArcMap. The source maps were typically accurate to a 1:24,000 scale. These features were obtained from journal articles, graduate student theses, and personal communication. Additional information about the faults was entered into the database, such as the fault type, dip, time of last activity, fault name, and documentation of the fault in the literature. Other geologic features digitized into the database include location, magnitude, and depth of seismic events, areas of subsidence and uplift, lineaments, and plutons. The color, label, and symbology for each feature were then chosen to make the maps easier to read.

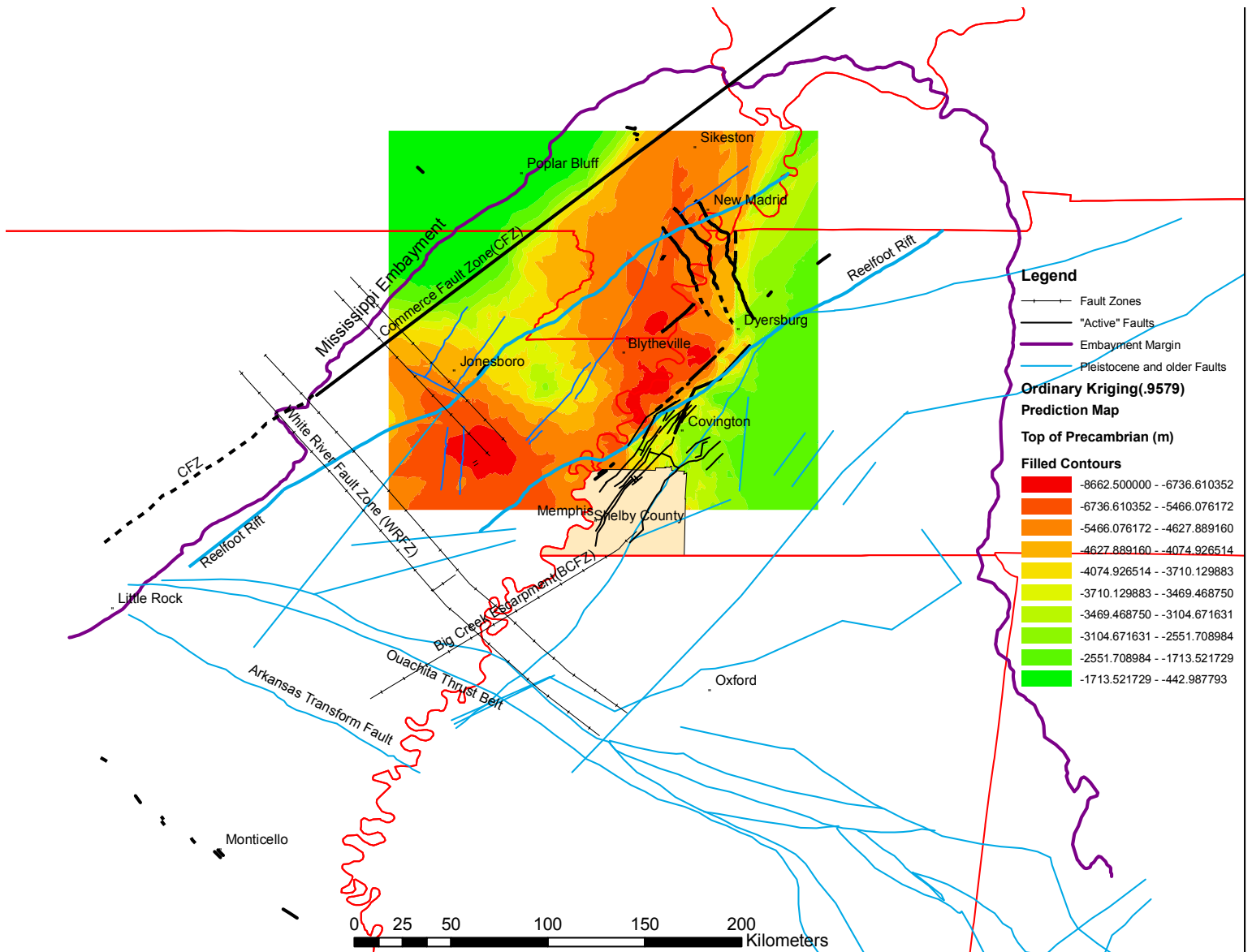


Figure 6. Faults and the top of the Precambrian crystalline basement in the northern Mississippi Embayment.

Reflection Survey

A 195 m S-wave seismic reflection survey was shot along Agricenter Drive at Shelby Farms (Figs. 5 and 7). Thirty-two geophones were placed with two meter spacing and the data were recorded on a 24 channel Seistronix RAS-24 seismograph (Table 1). A sledgehammer hitting an I-beam was used as the source. At the initial shot point geophones 1-24 were recording, at the second shot point, geophones 2-25 were recording. This process continued until data from geophones 13-36 was collected. At this point the back 12 geophones were moved to the front of the line where the process was repeated until the end of the 195 m line.

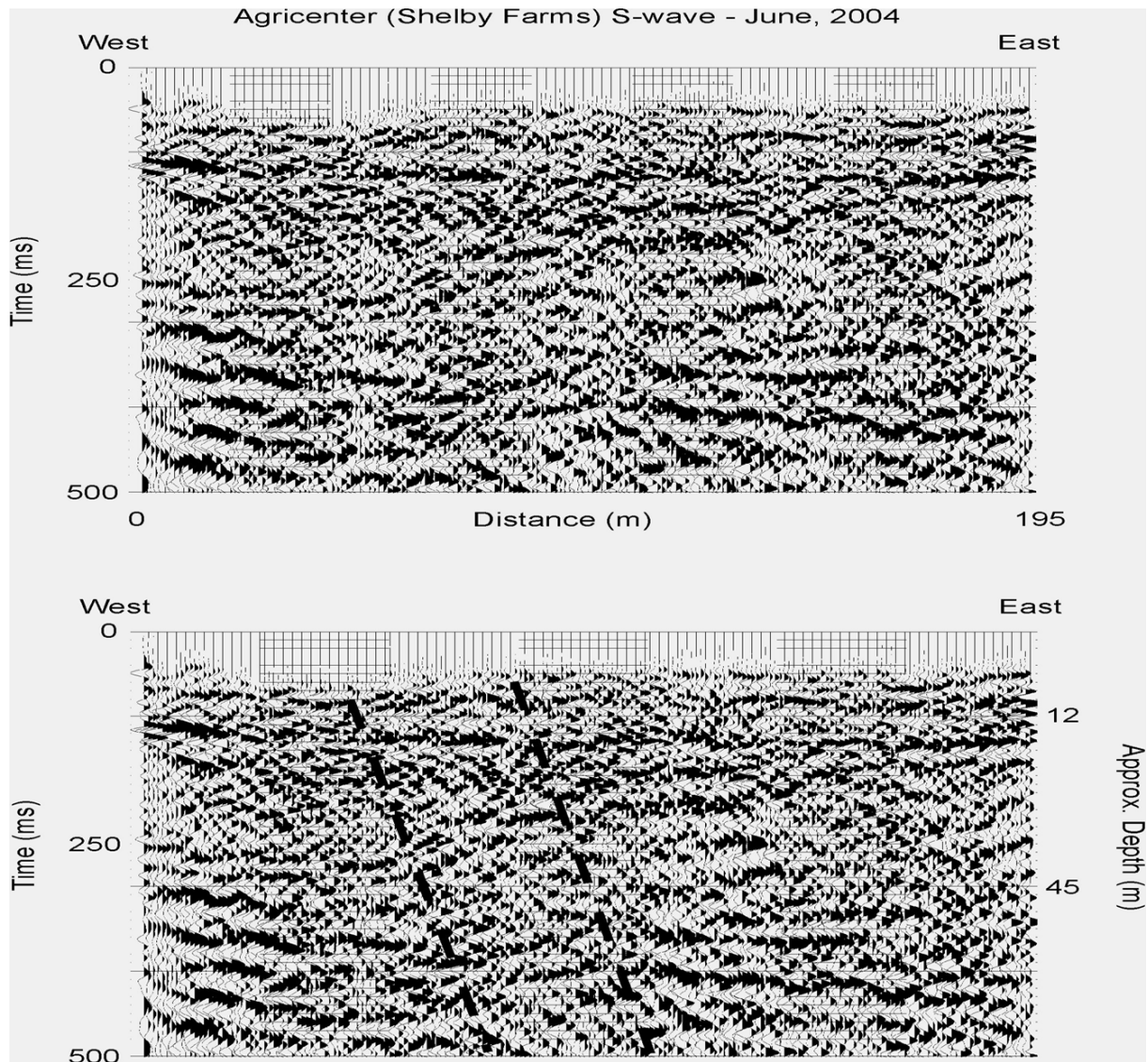


Figure 7. Shelby Farms seismic reflection line with interpreted bottom figure, dashed lines indicate faults.

Parameter	Description
Seismograph	Seistronix RAS-24 (24-channel)
Geophones	14 Hz horizontal (Mark Products)
Geophone Spacing	2 m
Source	1.8 kg sledge hammer/I-beam
Source Offset	1 m
Spread Configuration	split spread (12 geophones on each side of source)

Table 1. Parameters for the Shelby Farms Seismic Reflection Survey.

Conductivity Survey

The conductivity grids were located along the fault projections generated by the seismic reflection surveys. Grids were set up with four meter spacing between grid lines and measurements were taken at each grid point. The area of the survey was determined by the width of the fault zone and limited by the presence of buildings, roads, crops, etc. Some data points were excluded due to inaccessibility (standing water, tree trunks, or crop rows) or metal causing interference with the conductivity meter (irrigation or farming equipment). The conductivity meter determines the conductivity in micromhos/meter of the top four meters of sediment. Clayey or silty sediments will generate relatively higher readings while sandy sediments will produce relatively lower readings. The data were entered into Excel and conductivity contours map were created using Surfer 8, cross sections were created using Grapher 4.

Conductivity surveys were run near the intersection of Hollywood and James Road, where the Memphis fault is projected to be (Figs. 2 and 4). Conductivity surveys were also conducted at two locations in Shelby farms, the proposed location of the Ellendale Fault (Figs. 2 and 5). Several individual surveys done at each site were combined to create a more comprehensive coverage of the areas studied, resulting in a conductivity map of the proposed location for the Ellendale Fault (Figs. 2 and 5), an unnamed fault also in Shelby Farms (Figs. 2 and 5) and the Memphis Fault (Figs. 2 and 4). Because of the sensitivity of the conductivity meter to moisture and solar activity, values from different days can not be immediately combined. One grid must be used as a base value and all values of the other surveys must be changed by the difference at the point of overlap. Grids were named after the nearest road or building for clarity.

Borehole Data

At Shelby Farms conductivity grid one (Fig. 5) six boreholes three to five meters deep were drilled using a Giddings rig. The cores were then laid out next to each other and the lithology and depth of each layer was recorded in detail. The cores were then photographed and samples were taken. Seven boreholes of similar depth were drilled at grid two (Fig. 5) following this same procedure. Knowing the drill depth, extension and the addition of wall scrapings to the

core length could be compensated for. Using this information, geologic cross sections were generated with Canvas and the location of faults was determined by the observed offset.

Results

ARCGIS™ Database

One of the primary objectives of creating a fault database was to generate a comprehensive structure and seismicity map of the Northern Mississippi Embayment (Fig. 1). The different GIS layers containing different geologic and cultural features can be turned on and off. This allows any combination of data to be displayed for the purpose of creating figures or analyzing the spatial relationship between different features. For example, faults can be displayed with different stratigraphic tops (Fig.6) and may show the amount of displacement on the fault, age of faults, or geometric relationships of faults. The database was designed in this way to allow for maximum flexibility in map production and structural comparison. Due to the variety and amount of information included, this is currently the most accurate and complete database of geologic features in the New Madrid seismic zone.

James Road Site

At James Road and Hollywood several surveys were done to better locate the faults suggested by an earlier S-wave seismic line (Fig. 3). The James Road grid one (Figs. 5 and 8) combines two separate surveys and suggests two possible faults. A steep drop in micromhos/meter can be seen from meter 50 to meter 60 of cross section A-A'. The structure contour map also shows a rapid transition from high values to low values in this area and shows a possible fault at least 45 m in length and striking N50E. In cross section B-B' a large decrease occurs from meter 10 to meter 35. A fault in this location, according to the survey, would be at least 55 m in length and strike N8E. While each cross section shows a decrease from about 4 micromhos/meter to 3, cross section A-A' does so under a much shorter distance (about 10 m as opposed to 25 m). Due to the more drastic micromhos gradient in cross section A-A' it is more likely that a fault occurs here. Alternatively, the two faults may actually be part of the same fault. The rise in values in the southeast (bottom right) corner coincides with a ditch filled with standing water. Because moisture causes higher conductivity readings, the change in values in this location can be attributed to the standing water rather than a fault.

James Road conductivity grid two (Fig. 9), located east of grid one, shows evidence of faulting in the northwest corner. A rapid change of high conductivity in the northwest to low conductivity in the southeast is seen in the map. Additionally, cross section C-C' shows a conductivity drop over nearly the entire range of recorded values. The supposed fault is at least 30 m in length and strikes N55E, nearly parallel to the fault seen in cross section A-A' of Figure 8.

James Road Conductivity Survey Grid 1

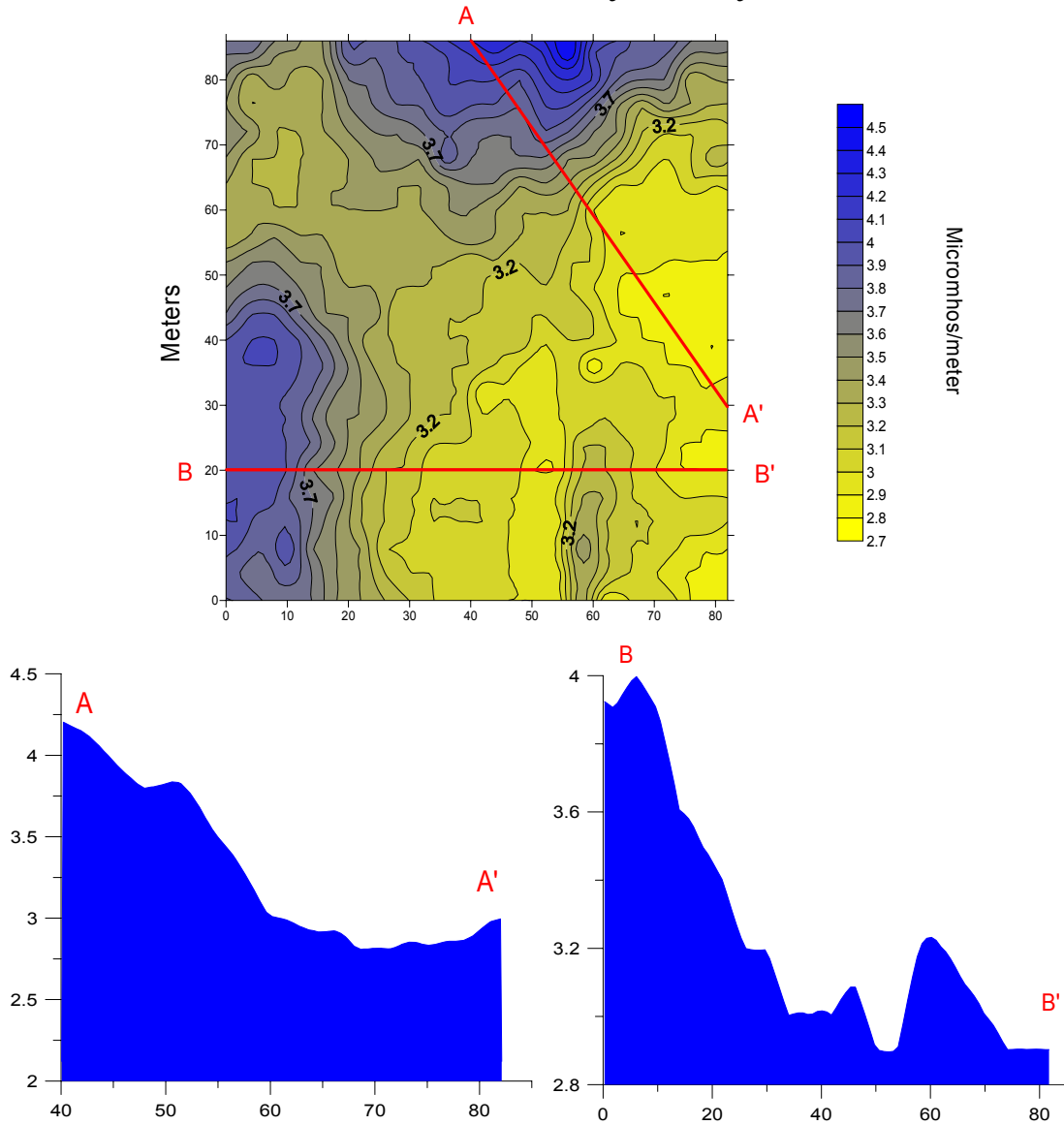


Figure 8. Conductivity contour map and cross sections.

At the James Road conductivity grid three (Fig. 10) a sharp increase and then a gradual decline in values is observed in cross section D-D'. An increase of 1.7 micromhos/meter in about 10 m is observed in the southwestern portion of the grid. The western transition suggests a fault at least 35 m in length and striking N50E. The decrease in values from meter 35 to 56 is too gradual to suggest a fault based on these conductivity readings. This grid is located northeast of James Rd. and Hollywood conductivity grid one and was intended to capture the fault seen in cross section A-A' in grid one. It is likely both areas are the result of the same fault as they have the same strike. The fault in grid one, however, has higher values to the west of the fault while the fault in grid two has higher values to the east. Further study is needed to determine the relationship between these two changes in conductivity.

James Road Conductivity Survey Grid 2

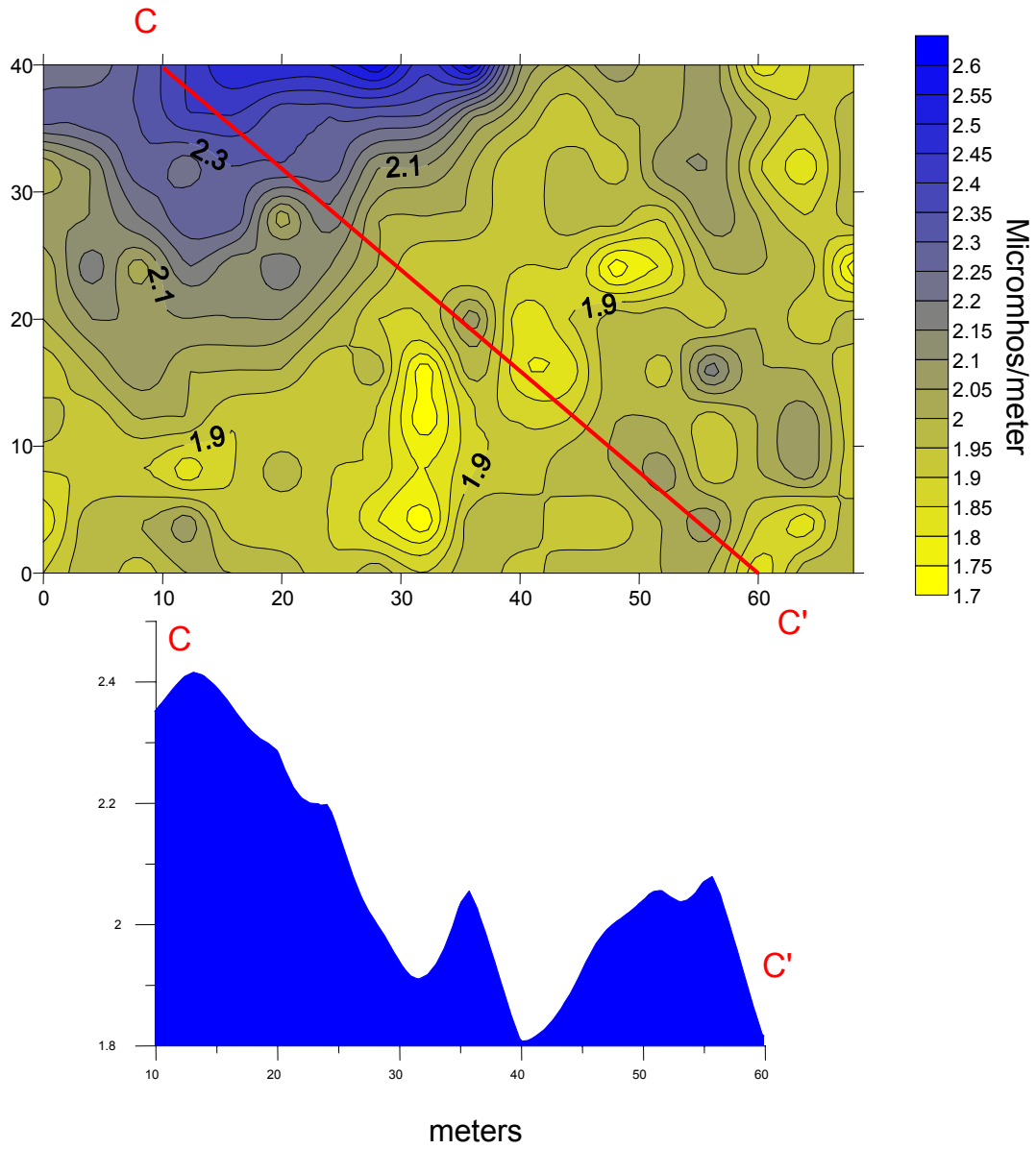


Figure 9. Conductivity contour map and cross section.

James Road Conductivity Survey Grid 3

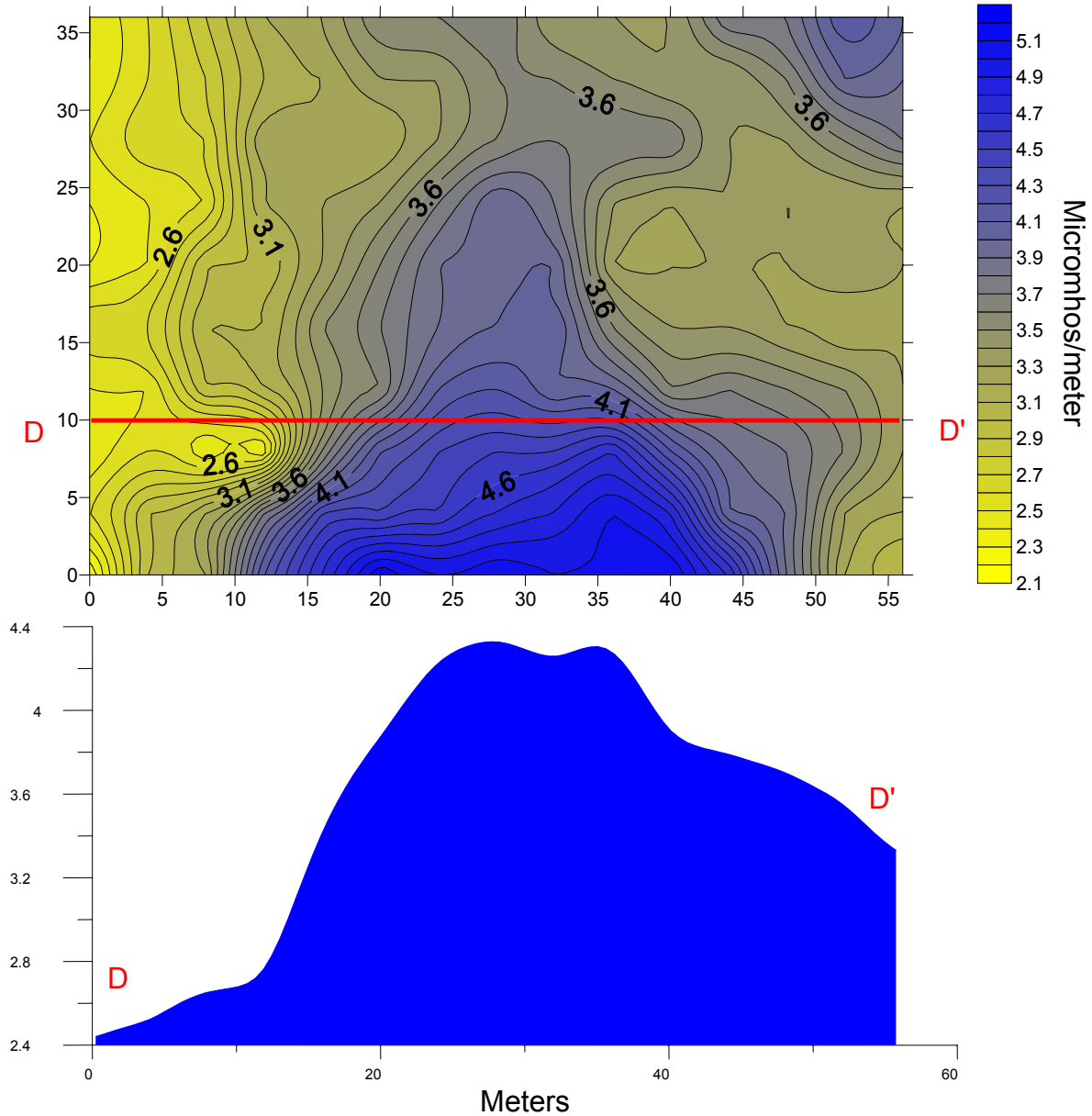


Figure 10. Conductivity Contour map and cross section.

Shelby Farms Site

Reflection Survey

The S-wave survey recorded energy reflected at changes in the medium, in this case rock type, giving a picture of layering in the subsurface. Offset of these layers could be the result of faulting. The S-wave seismic reflection line acquired at Shelby Farms (Figs. 5 and 7) yielded a seismic profile of the near subsurface to a depth of approximately 80 m. Based on the observed

offset two parallel faults were interpreted which approach the surface at 44.7 m and 82.1 m along the line.

Conductivity Surveys

Agrifarm Conductivity Survey Grid 1

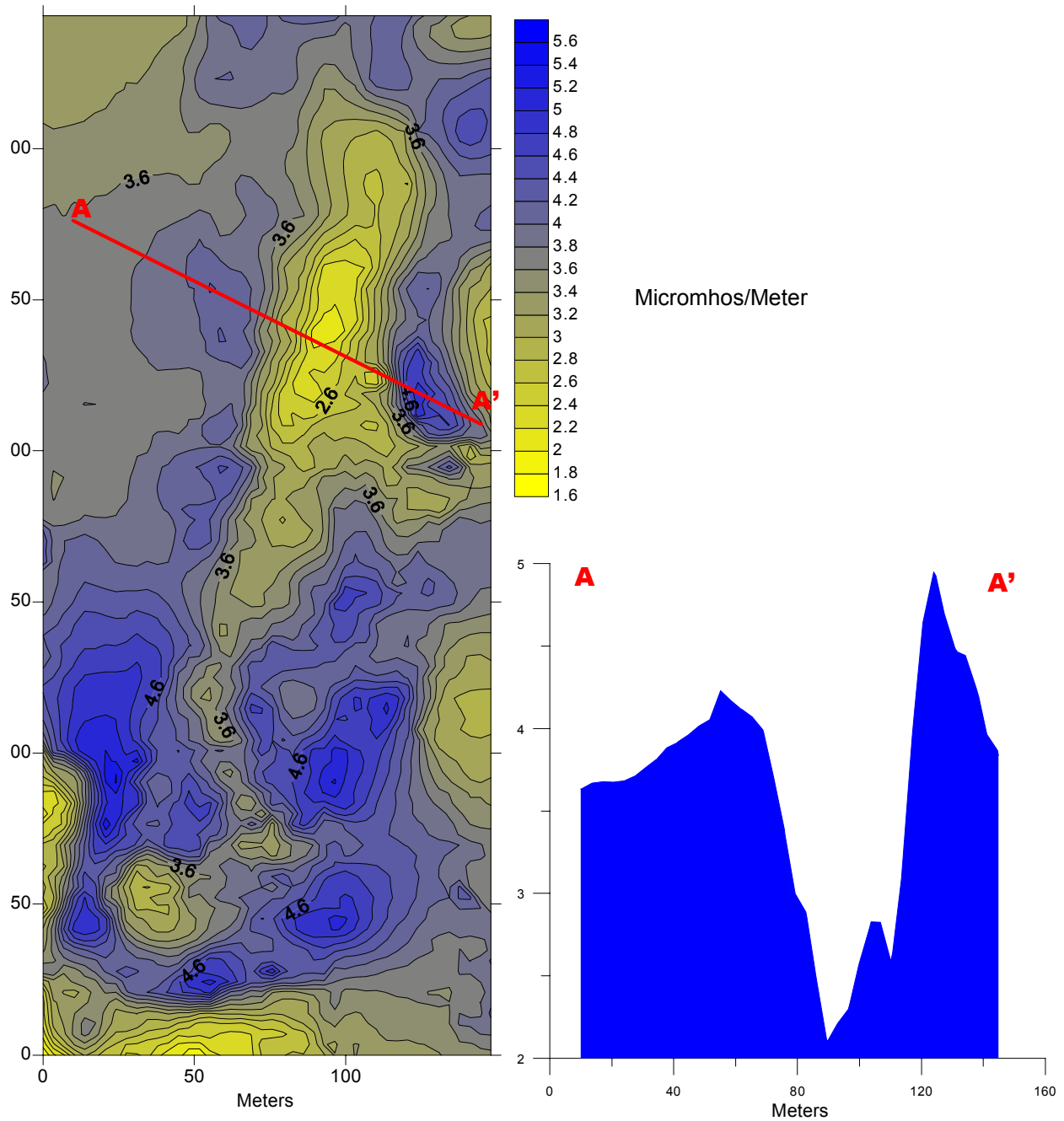


Figure 11. Conductivity contour map and cross section.

Agrifarm conductivity grid one (Fig. 11) is a combined conductivity map of an unnamed fault in Shelby Farms (Fig. 5). It shows a central region of low values, which would be expected if faulting resulted in sand being upthrown next to more conductive clay or silt layers. In cross section A-A' a sharp decrease to lower values and then a sharp increase to the previous higher values was observed, implying two faulting events. The conductivity data indicated that the faults are approximately 200 m long, 20-50 m apart, and strike N20°E. The location of these two faults correlates well with the location suggested by the seismic reflection survey (Fig.7).

Agrifarm conductivity grid two (Fig. 12) is a combined conductivity map of the Ellendale Fault (Fig. 5) which features an area of higher values in the west transitioning into lower values to the east. In cross section B-B' the decrease was sudden, about 2.5 micromhos/meter in 20 m, while in the cross section of C-C' the decrease was less consistent, with a sharp decrease until 20 m, a gradual decrease from 20 to 80 m and then another sharp decrease. Taken together these cross sections suggest one fault at least 88 m long.

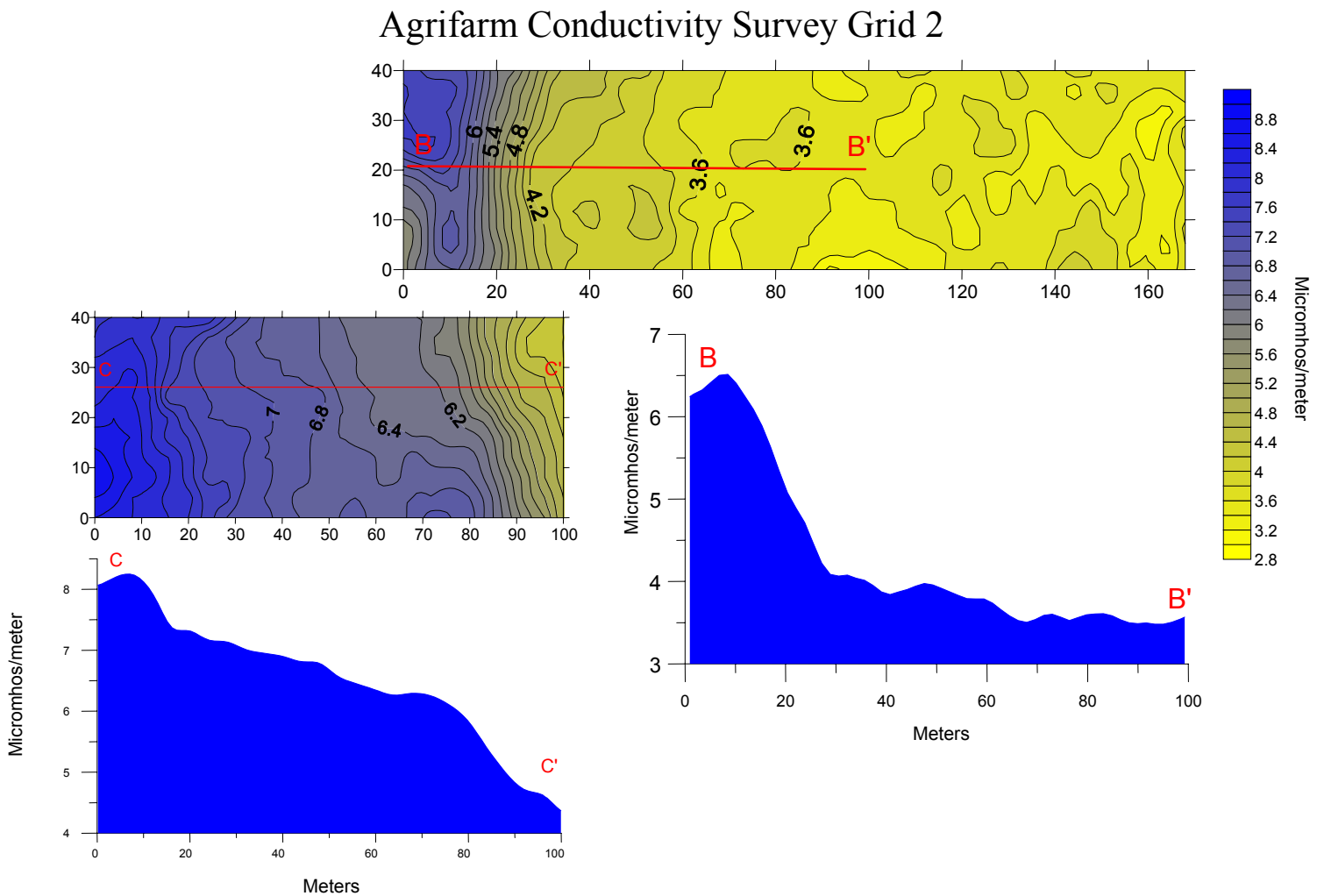


Figure 12. Conductivity contour map and cross sections.

Borehole Data

Based on the fault locations seen in the Agrifarm conductivity surveys (Figs. 11 and 12), boreholes were drilled to get a more detailed look at the subsurface. At grid 1 the cores contained up to six distinct loess layers over a layer of very fine to medium grain sand (Fig. 13). Based on the offset at the contact of the loess and sand, two faults and their relative ages were interpreted. The western fault offsets all but the top two stratigraphic layers between cores I and J, indicating it is the younger of the two faults. The eastern fault offsets the very pale orange silt layer and the two layers below it between cores L and M. These locations of offset have been used to determine the most optimal location for building a trench.

The cores drilled at Shelby Farms conductivity grid 2 (Fig. 12) had three distinct loess layers overlaying a bed of very fine to fine grained sand (Fig 14). Based on the offset at the contact of the loess and sand, three faults were interpreted. The transition from a very pale orange clayey silt in cores F and G to a pale yellowish brown clayey silt in cores A through E in the uppermost stratigraphic layer implies that the eastern most fault is the youngest. A fault intermediate in age is located between cores D and E, given the change in thickness of the second stratigraphic layer across this region. Due to the presence of a sand layer at the base of core A to C which is not located in cores D and E, a fault has been interpreted between cores C and D. This is the youngest fault in the grid because it only produces offset in the lower stratigraphic layers.

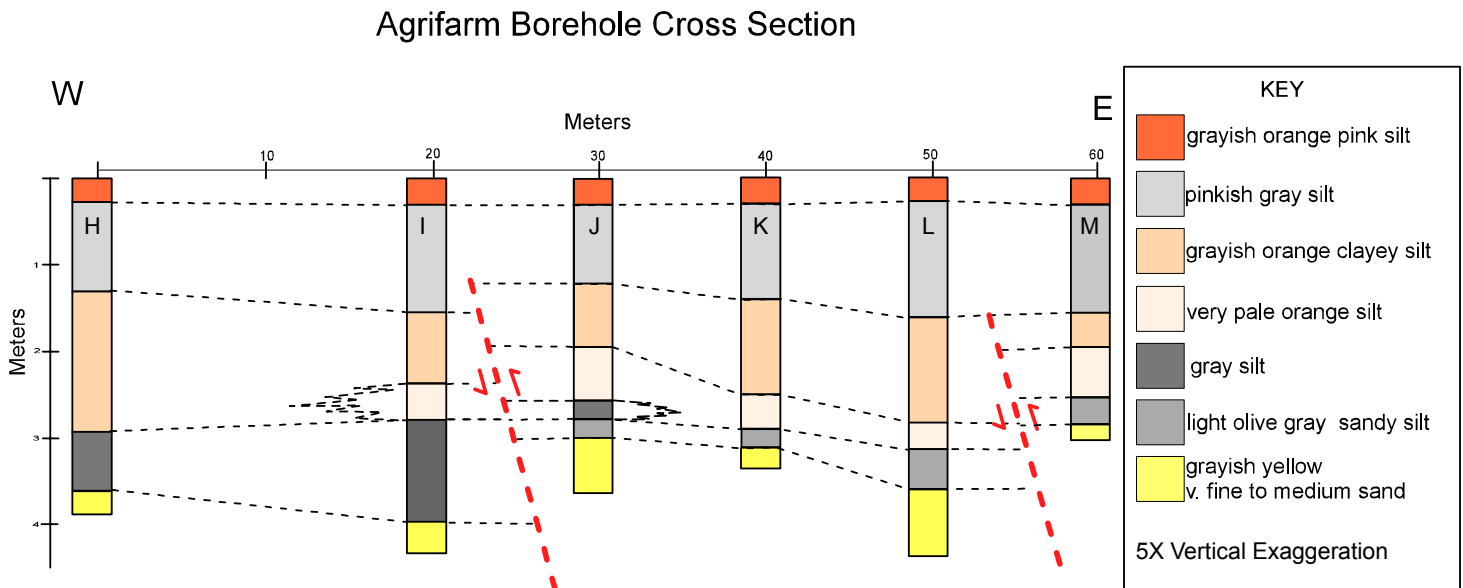


Figure 13. Borehole cross section from Agrifarm conductivity grid 1.

Conclusions

The compilation of two dimensional datasets into a comprehensive and flexible regional database has, in the initial demonstrations, yielded new interpretations and understanding. Individually,

the reflection data, conductivity surveys, and borehole samples taken at Shelby Farms all produce results consistent with those expected from faulting. Taken together, the three tests correlate well, each suggesting faulting and similar locations for those faults. The seismic reflection survey and the conductivity surveys locate those faults within meters of each other while the conductivity surveys and the borehole data project the faults in the exact same location. It is likely that the Ellendale Fault and the unnamed fault pass through the target area and further investigation is warranted. As for the Memphis Fault, the conductivity surveys show evidence consistent with faulting, making this a favorable site for drilling. The two potential faults striking at N50E would be the most promising site for further exploration.

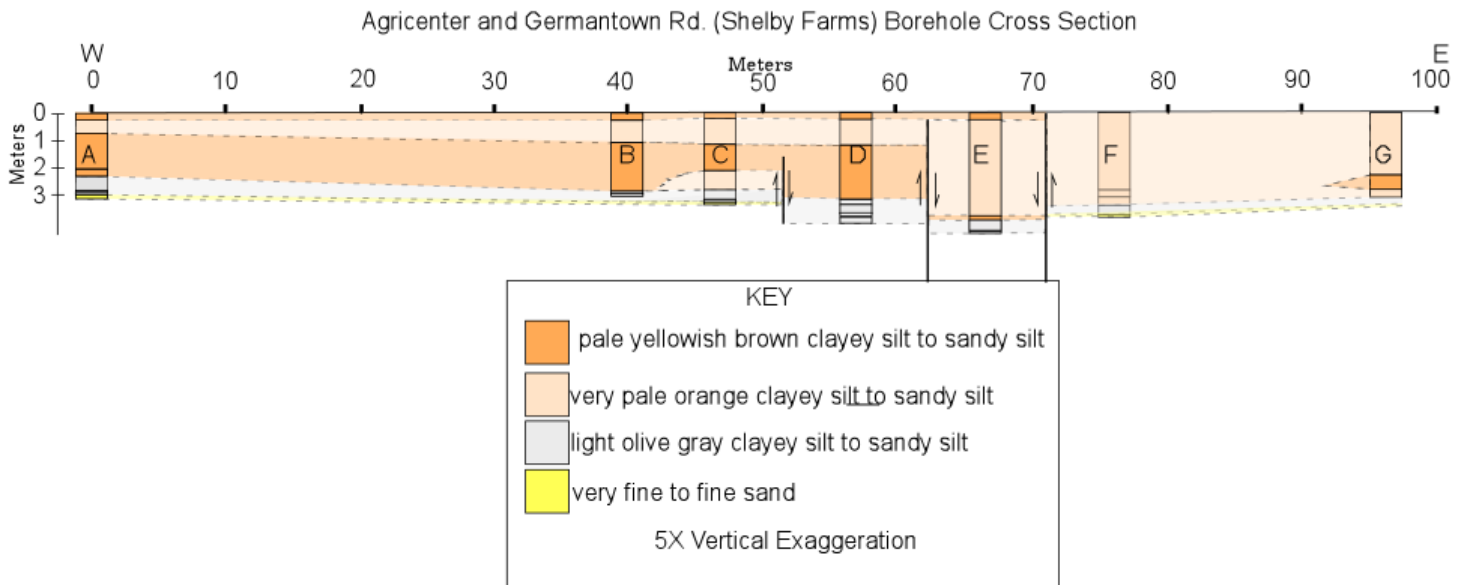


Figure 14. Borehole cross section from Agrifarm conductivity grid 2.

Future Work

The ARCGIS™ database will be imported into Landmark, a three dimensional data processor, along with gravitational, magnetic, P and S wave velocities, and thermal data. This new program will then provide an even more complete database of the Phanerozoic geology of the Northern Mississippi Embayment and provide an opportunity for research through visualization. The three dimensional map of the Northern Mississippi Embayment overlaying the top of the Precambrian (Fig.12) is just one such example of the types of maps and visualizations which will be possible in Landmark.

Digging several trenches at Shelby Farms across the proposed faults is planned. The dimensions of the trenches will be one hundred ft in length, 4ft in width, and 8 ft in depth. Trenching will allow the amount of offset to be determined, dating of offset, and a stratigraphic profile to be constructed. The trench will also allow the type of faulting to be determined, which was not possible with the tests conducted during this portion of the study. A grain size analysis will be

performed with the samples taken from the boreholes A through M. Coring and trenching is planned for the James Road site to collect information about the Memphis Fault.

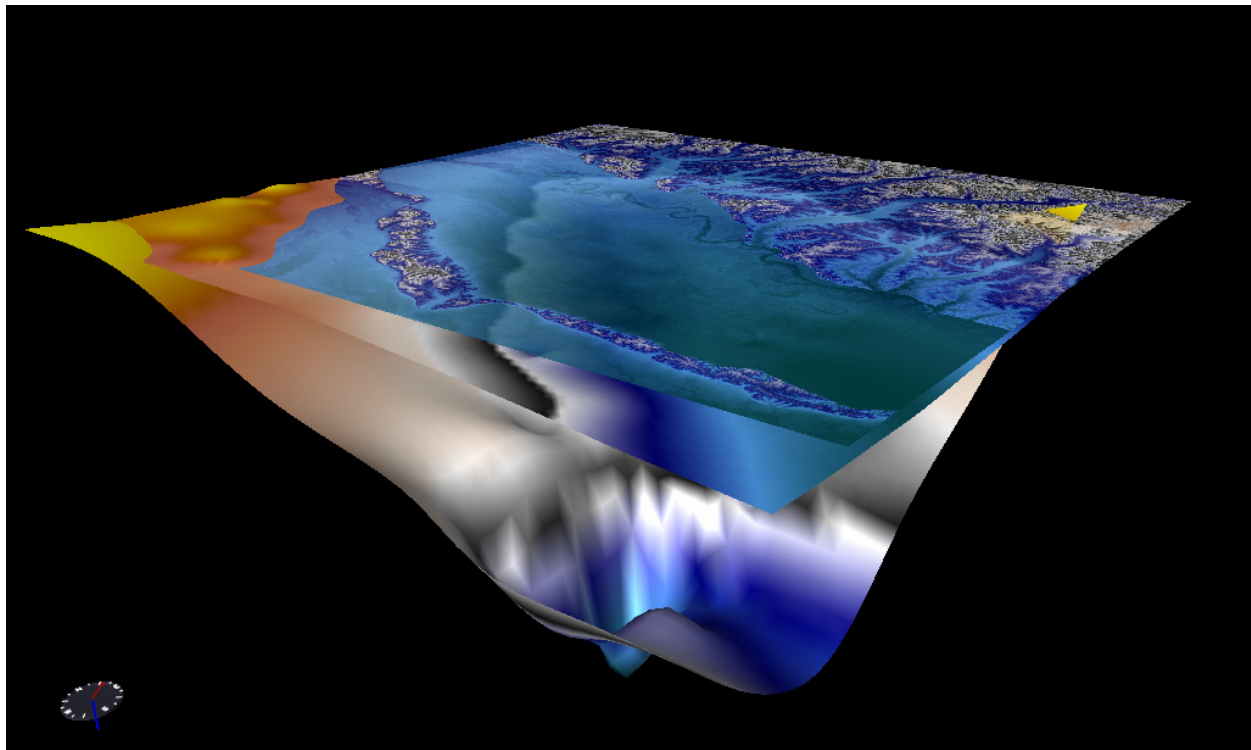


Figure 15. Northern Mississippi Embayment overlying the Precambrian crystalline basement.

Acknowledgements

I'd like to thank the MAE Center and the REU program for their funding, Dr. Roy Van Arsdale of the University of Memphis for allowing me to work with him and all of his guidance in the project, Dr. Jamie Harris of Millsaps College for his interpretation of the Shelby Farms seismic profile and help with running the seismic line, and Tom Deen and Ryan Csontos for working with me and all of their help throughout my research.

References

Cox R. T., Van Arsdale R. B., Quaternary faulting in the southern Mississippi embayment and implications for tectonics and seismicity in an intraplate setting. *Geological Society of America Bulletin*: v. 112, p. 1724–1735.

Cox. R. T., Van Arsdale, R. B., 2002, The Mississippi Embayment, North America: a first order continental structure generated by the Cretaceous superplume mantle event: *Journal of Geodynamics* v. 34 p. 163-176.

Schweig, E. S., and Van Arsdale, R. B., 1996, Neotectonics of the upper Mississippi embayment: *Engineering Geology*, v. 45, p. 185-203.

Velasco, M. S., 2002, Quaternary faulting beneath the cities of Memphis and Germantown, Tennessee [M.S. thesis]: University of Memphis.

LATERAL LOADING OF CAST-IN-DRILLED-HOLE SHAFT

Manuel E. Ponce
University of California, San Diego
University of California, Los Angeles
Jonathan P. Stewart

Abstract

This project aims to better understand the behavior of the commonly used cast-in-drilled-hole (CIDH) shafts under cyclic loading such as that of an earthquake. During past earthquakes shafts experienced great deflections leaving shaft-soil gaps as wide as 2 feet. In a previous project a test was conducted with a shaft 6 feet in diameter. The difference with this test is that it contains a vast amount of instrumentation for a much smaller 2 feet diameter. The test will gauge if the section geometry is proportional to the performance of the shaft. The test results will further aid the California Department of Transportation (CalTrans) in safer shaft design.

My personal involvement in this project has been in assembling the many sensors that will provide the readings from inside the column. My time involved hours at the shop manufacturing parts and pieces that allow the sensors to lie deep in the shaft and detect deflection, stress and strain. The assembly of the testing devices complexly encases them to keep them protected. In order for the sensors to work properly they need to be kept dry and properly anchored when the concrete is curing. The different types of sensors include fiber-optic sensors, inclinometers, strain gauges and linear variable displacement transducers (LVDTs). As of now the rebar cage has been loaded with the instrumentation and cast in place.

Problem Studied

The project looks at the problem with common highway columns that experience a large elasticity just below the ground level, leaving large gaps with the soil after earthquakes. In the Loma Prieta Earthquake in 1989 some shafts had gaps at the ground line as wide as 2 feet. While these gaps don't necessarily pose an imminent threat to the superstructure they do create considerable amount of damage at the hinge point of the column (Janoyan, 2001). A continued lateral loading of the column then creates buckling of the transverse reinforcement bars, which could then cause the column to fail under the weight of the superstructure. As far as I understand the problem concerns CalTrans because these types of shafts are still used for freeway overpasses and bridges.

At the time I began the internship this problem with CIDH shafts had already been studied and researched for the past 3 years by Eric Ahlberg, a doctorate student at the Department of Civil Engineering at the University of California, Los Angeles. Previous to him Kerop Daniel Janoyan wrote his dissertation on a similar project, which involved a column with a 6 feet diameter. The title of Janoyan's dissertation is

Interaction between Soil and Full Scale Drilled Shaft under Cyclic Lateral Load and it is one of the sources for information for Ahlberg's test and this report. This test will also add information that was never obtained from that previous test. Even though this is the second test, there will be a total of 5 drilled hole shaft tests as part of the same CalTrans project.

When I arrived at UCLA the researching was nearly concluded and all that was left to do was the labor and hands on work that would prepare the column for testing. I was not in a position where I needed to study the problem, but I made sure I understood it as well as the proposed solution. Eric took care of having the measurements of parts that would go into the column and it was my duty to have them prepared.

Objectives

The project seeks to obtain data that will provide a better comprehension of the effects of cyclic loading on shafts and their interaction with the soil at the elastic hinge, the most crucial location. The data from the sensors will provide the p - y curves of the column where p represents the soil reaction per unit length and y represents the pile deflection horizontally.

My objective with this internship was to gain a better understanding of the methods of research. A good reason for participating in the program was to gain research experience in preparation for graduate school. The time spent doing my tasks provided a good insight into the level of work that goes into a good dissertation. I also believe that the hours spent working in the lab and shop really made a contribution to earthquake engineering research. With the project my goal was to make myself available in order to be of good use for Ahlberg. I did a good job of learning how to conduct any of tasks that I was assigned in a timely fashion. There were a lot of concepts that I initially didn't understand, so I constantly asked questions. Ahlberg knew that I would always ask how devices worked and why he chose them. The objectives that I put for myself all regarded getting the hands on experience with research.

Research Approach

In order to get the most useful readings within the column the majority of the sensors had to be placed in the plastic hinge length. The plastic hinge length is the section of the column that lies just beneath the ground and where the bending moment is the largest. Figure 1 illustrates that this section is typically 4-5 diameters in depth. The figure also displays the response of the shaft to lateral loading where it can be seen that gaping occurs. The section of the column lying beneath that depth will typically stay anchored unless the soil is too soft, in which case the whole column tilts on an axis at the hinge point. This deeper section contains fewer sensors since it is expected that they will not have as many readings of displacement. As well, the section of the column that lies above the ground has practically no instrumentation since the deflection and moment in this section are known and visible during the test.

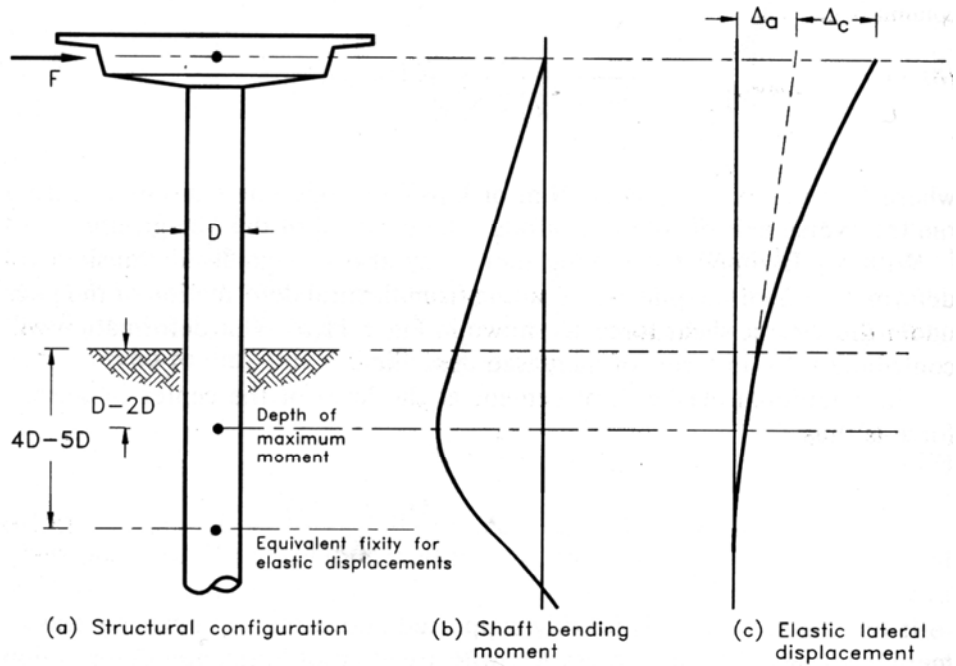


Figure 1

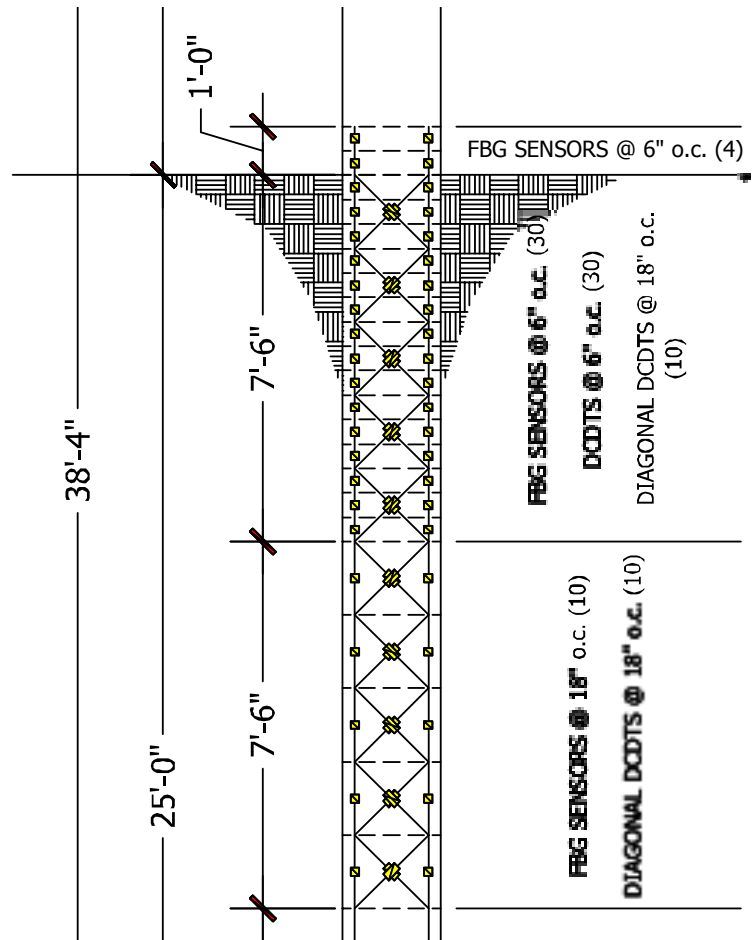
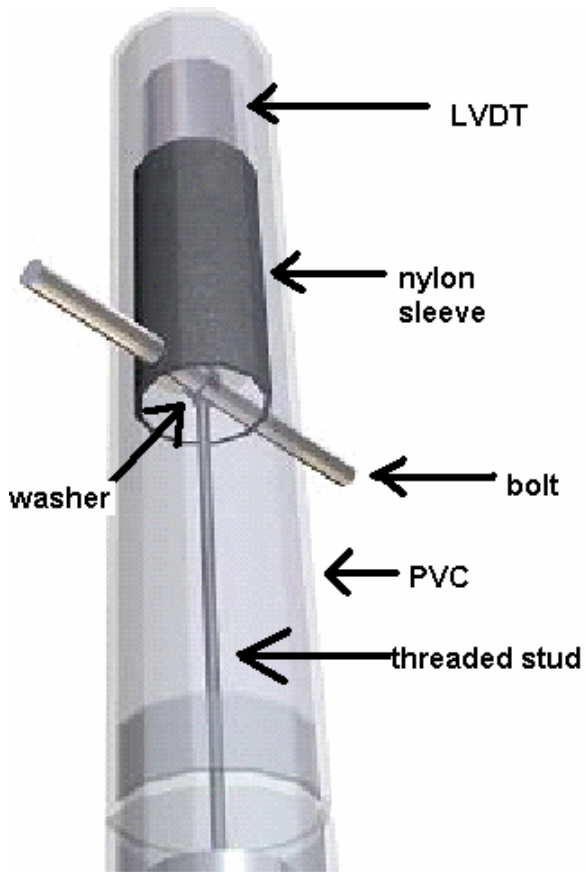


Figure 2. Sensor layout

Ahlberg decided the amounts of sensors that were needed. Figure 2 shows the elastic hinge portion of the column, which is where the bulk of the instrumentation was placed. The figure doesn't show the entire column. The length of the column is 38 feet 4 inches, but with the concrete at the bottom of the drilled shaft and with the concrete block on top, the length should be 40 feet. The yellow boxes represent where a sensor lies. In total there are 30 LVDTs running vertically down the inside walls of the column. There are 20 LVDTs crisscrossing the insides of the column diagonally. 10-15 inclinometers lie down the middle of the shaft. A total of 40 fiber optic sensors are placed where there is an LVDT and even farther down the column. 60 strain gauges are glued to the lateral and transverse reinforcement bars at specified locations. The distances between these sensors were all predetermined; some sensors were manufactured to those specifications. Those sensors were the ones that we placed last in the column since they didn't take more than a few days to install. A vast amount of time at the beginning of the internship was focused on creating the casings for the vertical and diagonal LVDTs.



The linear variable displacement transducers (LVDTs) provide readings when a metal core is pulled in and out of the sensor. The core moves within the sensor and this alters the voltage readings, which is converted to a displacement in inches in a LabVIEW program using a calibration factor. Figure 3 shows how the LVDT is anchored into the concrete. There is a bolt that goes through a PVC tube and a washer. The washer has been drilled and tapped to fit a long threaded stud that is also attached to the metal core. The LVDT lies in a nylon sleeve that is anchored to the next bolt, and so on. The nylon sleeves are all anchored to a bolt and the washer is also attached to that same bolt but it corresponds to the next LVDT. This setup allows for the cores to move independently of their LVDT in order to provide readings.

Figure 3. Assembly for the LVDTs

The LVDTs are damaged if they are wet. During the pouring of the concrete into the shaft there was a danger that water seeping in would damage the sensors. Therefore Ahlberg designed a casing that would keep the LVDTs dry and would also anchor them at the desired location, since they have no easy way of staying attached. Figure 3 shows a rough sketch of what the casing would look like and how it would function. The PVC

tubing is there to keep water from reaching the sensors. The tubing is sealed using cock, which is flexible enough to allow the tube to dislocate from the couplers. The threat of water leaking into the tube would only be there the initial days before the concrete cures. Once the concrete cures the dislocation of the tubes would no longer pose a threat. In order to keep the water from leaking in through the bolts' entrances a rubber washer and silicone was placed around them. The PVC is also flexible enough to sway during the testing without adding a significant strength to the column. The diagonal LVDTs are anchored to the same bolts as the vertical ones, but they are spaced at 18 inches from each other and they are only encased in nylon. Even though the diagonal tubes along with the PVC tubes construct a truss within the column the materials are so weak that the strength they add is negligible compared to that of the steel and concrete.

Creating the casings for the LVDT sensors was lengthy because it involved creating 40 or so couplers with holes drilled at the same location, or tapping a really small thread into 50 washers, or sawing 60 sections of threaded rods on the band saw. Ahlberg took care of coming up with the right lengths and I would deliver the necessary parts. Figure 4 shows an example of the parts that I needed to come up with. I sawed a lot of PVC and nylon tubes, drilled holes into nylon sleeves, metal washers and PVC couplers, tapped tiny thread into the washers, and cut metal bolts to the right lengths. Spending time at the shop was good and it taught me how to use the big machinery.



Figure 4. Pieces for the LVDT casing



Figure 5. LVDT

In order to obtain readings from the LVDTs all its wires have to be connected to a data acquisition board. The way the LVDTs were delivered they only had a few inches of colored wires attached therefore it was my responsibility to attach the exact amount of wiring to go from the depths of the column out the top of the column and to the computer with the data acquisition board. Therefore I cut wires at different lengths for each LVDT and soldered their wire ends together. Figure 5 shows what the LVDT looked like after the wires had been attached and after shrink-wrap was placed over the soldered section. After this extensive process I made sure that the LVDTs all provided a reasonable reading on the LabVIEW program so that I would take care of any mistake in the wiring or the connections to avoid any errors once the column was cast in place. When I worked on the computer with the sensors I better understood how the LVDTs work. I learned

how sensitive they read a displacement. I also gained a better understanding of how LabVIEW can be used for these purposes. These were the only sensors that I got to test since all the other sensors or gauges arrived ready to install.

Once all the LVDTs were encased and well protected we began to assemble the long PVC tube that held them all. The wires of every LVDT were passed all the way to the top end of the tube and coming out the top of the column in order to ensure they would be kept dry. Figure 6 demonstrates how the pieces come together and how they're kept in place until the cock dries. The tube doesn't behave very rigid because the completed tube is made up of so many smaller pieces of PVC and because the cock is flexible. After the vertical LVDTs were in place, the bolts were screwed in with Locktite and the diagonal LVDTs were added. All the preparation for the LVDTs easily took up half of the time from the point that they arrived to the point that they were in the rebar cage.



Figure 6. Axial LVDT assembly

The process was easier to install the Fiber Bragg Grating (FBG also known as fiber optic) sensors. There was one fiber optic sensor for every vertical LVDT, providing readings at 6 inch gauge lengths. Below that there were more sensors at 18 inch and 24 inch gauge lengths. The deeper sensors were placed in order to get overall averages of the displacement, but not very precise readings. Every fiber optic sensor had anchors, which I tied to the PVC tube with zip-ties and they were secured with Krazy Glue. There were a large amount of sensors which made it difficult to place them at the same point along the PVC tube therefore they were scattered along the side of the PVC tube that faced the inside of the column. It was very important to record the exact location of every single anchor of the fiber optic

sensor because the distance of sensors from each other on opposite ends of the column would differ. As well, since the sensors were scattered around the PVC tube some of the sensors would be closer to a rebar and thus experience more stress, or a sensor experience more of the movement of the inside of the column or more of the actual PVC tube itself. Therefore Ahlberg wanted the exact depth and lateral location of every single anchor just in case readings during the test displayed a variation in numbers between sensors at different locations around the PVC tube. Unlike the wiring of the LVDTs the fiber optic sensors connect much easier to the computer though a device that allows the fiber optic wire to just click into a slot. The sensors detect displacement by being stretched at the anchors. Inside the clear section of the sensor lies a smaller tube that contains slits through which wavelengths exit from the wire. When the sensor is stretched the slits get longer and this reflects a different wavelength, which in turn is recorded as a displacement for that specific gauge length. It is important that the sensors maintain the length at which they are shipped in, as well as when the sensors are anchored to the PVC tube. Stretching them could alter the wavelength that is recorded on the package as the unstressed wavelength.

The inclinometers were fabricated to just install in a simple assembly process. A large fiberglass tube was provided to house the inclinometers and to keep the inclinometers aligned. It is important that the inclinometers stay aligned so that they can detect angle of inclination along different parts of the tube. The tube itself is flexible but wont fracture. I got to test one of the inclinometers on the computer to understand how they work and how sensitive they are to slight tilting. Figure 7 shows what an inclinometer looks like. The inclinometers were specifically labeled and directed to give the best readings, so we made sure to align the sensors and keep the tube centered in the shaft in that precise alignment.



Figure 7. Inclinometer



Figure 8. Strain Gauge

In order to attach the strain gauges the rebar had to go through a thorough procedure and the strain gauges were treated with a lot of care. There were about 60 strain gauges with dimensions of about 1 inch by ½ inch. The first step was to reduce spots on the rebar down to a flat surface. I performed this using a metal grinder. In the next step the spot was filed smoothly using a smaller sander. Then there were a number

of chemicals that were used to clean the surface. The strain gauge was glued onto the surface and then finally began the lengthy process of covering them with different coats that each needed a wait time of hours. I was only available for the labor-intensive part and the cleaning, but I know that putting on all the coats took days to complete. The finished work left the strain gauges securely glued to the metal and ended up looking like the big brown glob like the one in Figure 8.

The transformation of the column can be seen from Figures 9 and 10 to Figures 11 and 12, from the day the column arrived to the day it was ready to insert in the drilled hole. The finishing touches on the column were completed once the internship was over but the rebar column was installed on September 24, 2004. I was available to be present to see the column go in. There was a trucking company that delivered the column from UCLA to the site. Malcolm Drilling drilled the hole, another company used a large crane to insert the cage and yet another company mixed and filled the shaft with concrete. The testing site is in a dirt lot under the overpasses that connect Interstate 405 and Interstate 105 in Hawthorne, CA. This lot was also the site of the previous test performed in 2000 by Janoyan. Presently the concrete in the shaft is curing and will not be able to be tested for a few weeks. The time waited will most likely be a total of 28 days, which is when the concrete will reach its desired strength. I will attend the site to see the column get tested, but will not actually know any of the outcomes of the test other than visually.

Since the project is not yet completed I don't have any results to report. What I do know is that this is the 2nd of 5 drilled shaft tests. The first test was the one performed by Janoyan. All 5 tests are expected to be completed by fall of 2006. This test in particular was only of a 2 feet diameter, which is not like real columns, but with the quality and quantify of instrumentation in it, the results will help determine the effect of section geometry on the shaft performance. The project has been funded by CalTrans and the dissertation Ahlberg writes will help them in future shaft design.



Figure 9. Empty rebar cage



Figure 10. Empty rebar column



Figure 11. Column with wiring

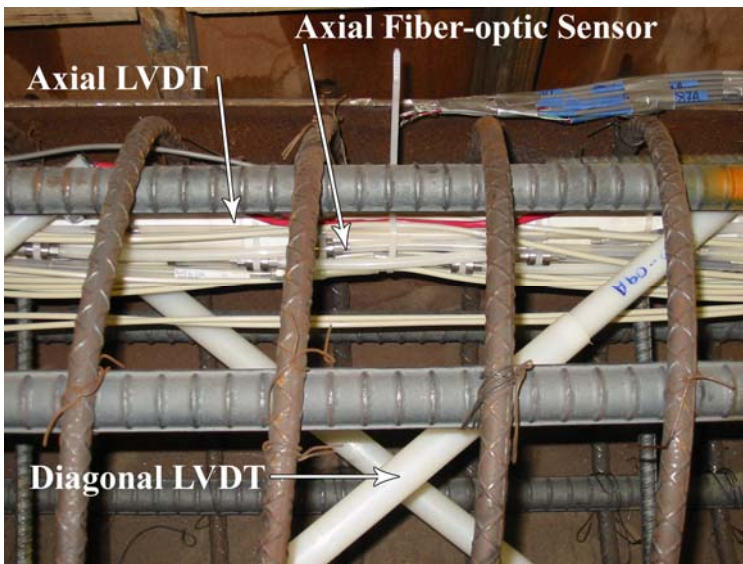


Figure 12. Close up of instrumentation in the cage without the inclinometers

Acknowledgements

I would like to take the time to thank the people that made this internship possible and memorable. First I would like to thank Eric Ahlberg, the doctorate student that had the patience to teach me what he knew and showed me how to work on the column. He was a great partner to work with and a one with a great sense of humor too. Eric always answered my question and took the time to make sure I knew what to do. I would like to thank Professor Jonathan P. Stewart for allowing me to work in his lab and with his students. Professor Stewart was always kept inform of my work and I am glad I was of good use to him. Even though Professor John Wallace was not my advisor, he always took the time to drop a visit and see what was happing with the project. Professors Stewart and Wallace were co-advisors of Eric, therefore I felt as if I also had two advisors. I owe a lot of gratitude to Linda Nelson for being attentive of all of our needs and for being so helpful with everything from emails to providing information, and of course the trip to Charleston, South Carolina. The one reason for which I came up on this internship opportunity was because of my advisor at UCSD, Professor Scott Ashford who told me about the internship and suggested that I apply. I also thank him.

Appendix: The Site Work



Drilling the hole for the column



All the wires exiting at the top of the column.



The crane lifting the column into place.



The column being inserted into the hole.



The concrete once it has been poured to the ground line.



Me and Eric with the column.

References

Janoyan, K.

Interaction between Soil and Full Scale Drilled Shaft under Cyclic Lateral Load
Los Angeles, California, USA, 2001.

IDENTIFYING CONFIGURATION AND CONNECTION DETAILS OF
UNREINFORCED MASONRY STRUCTURES IN MID-AMERICA

Ty A. Stokes
University of South Carolina
REU at the University of Illinois at Urbana-Champaign
Advisor: Professor Y. K. Wen

ABSTRACT

Experience from past earthquakes indicates that some structures perform better than others under similar ground motion conditions. This disparity leads to the conclusion that some structures will be safer, and thus less likely to require repair or cause harm, than others. In order to describe this phenomenon quantitatively, vulnerability functions are developed. Vulnerability functions describe a structure in terms of its likelihood (probability) of exceeding a certain limit state at a specified ground motion condition accounting for the uncertainty in both excitation and structural capacity. Indeed, there are several sources of uncertainty that cannot be eliminated, but in order to create the most accurate relationship possible, any uncertainty that can be reduced, should be reduced. Therefore, the goal of this particular part of this project is to remove some of the uncertainty in the nature of the buildings that are being modeled. By understanding better the connections, typical configurations, size, and shape of a typical unreinforced masonry (URM) building, it is possible to accomplish this goal and create a vulnerability function which may better describe a larger percentage of the population of URM structures in Mid-America.

SECTION 1 VULNERABILITY FUNCTIONS OVERVIEW

Section 1.1 Introduction to Vulnerability Functions

Understanding the response of a structure to an earthquake can be an inexact science. One can never be certain of the nature of ground motion that might exist at a given location, nor can one be sure of the forces that will develop inside the elements of a structure due to ground motion. Therefore, in order to understand the behavior of the structure, one must speak in terms of probability or likelihood of certain events, instead of complete assurance. Vulnerability functions attempt to do just that by relating ground motion parameters to the likelihood that a limit state (in this case, a limit of inter-story drift after which a structure is deemed to lose its functionality) would be reached or exceeded.

In order for these limit state probabilities to be as accurate as possible, it is necessary to understand the uncertainty and if possible reduce the uncertainty and the limit state probability. While quite large uncertainty is inherent in earthquake excitation, still a significant source of uncertainty is in the configuration and connection information of the structure. At the University of Illinois, project DS-4 focuses on URM and other buildings. Finding out information about the structures was the goal of this summer of research.

While ideas abound about the shape and size of most URM buildings, still some evidence is necessary to imply that indeed a structure meets standards that may be considered typical. There are various tools with which to find this evidence (most of

which will be discussed later) and these will be used to make a preliminary suggestion as to the likely nature of URM structure in Mid-America.

Section 1.2 Statement of Purpose

This particular report is based on research done as part of the Mid-America Earthquake Center's Damage Synthesis project DS-4. This report will briefly summarize some of the project goals and will try to describe the processes which were used to achieve these goals. This is tempered with the fact that the author has never actually completed the entire process necessary to generate vulnerability functions therefore, the information about vulnerability functions and the project in general are meant to provide a background as to the ultimate goal of the project for which this research was conducted.

Section 1.3 Describing Vulnerability Functions

The goal of a vulnerability function is to describe in easily understood terms the relationship between ground motion and the likelihood of a limit state being reached or exceeded. This is achieved by plotting spectral acceleration versus probability. The acceleration is that of the ground under the excitation of an earthquake. The probability is that of a specific limit state being reached. Using a simple plot such as this, it is possible to easily relate to stakeholders and others the functionality that can be expected under certain ground motion conditions. Using these plots it is also possible to compare different structures in terms of safety and see which is most likely to experience greater deformations under the same conditions. This can be achieved by plotting several different structures on the same graph and using the same limit state as a governing factor. These principles can be shown on figure 1 below.

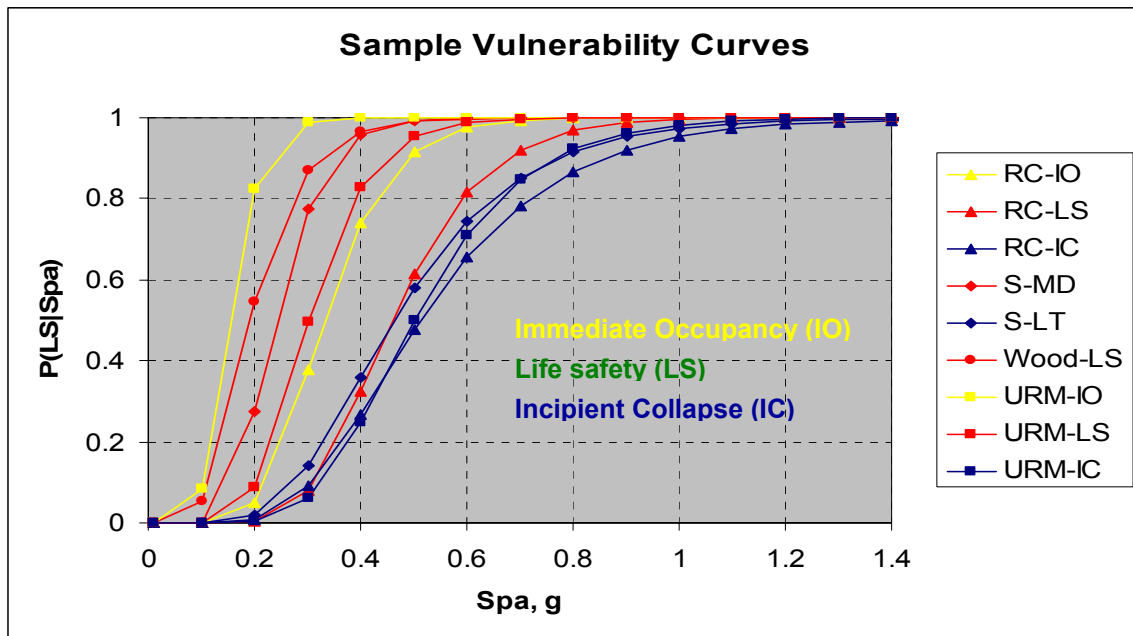


Figure 1: This is a sample of a chart relating vulnerability functions for different conditions. This chart can clearly show which structures are most likely to experience a limit state given a certain ground motion.

This plot shows vulnerability curves for different structures at the same limit states. The immediate occupancy (IO) limit state indicates when a structure may be re-entered without any major repairs immediately following an earthquake. For instance, the reinforced concrete IO limit is not very likely to be reached with a ground motion of 0.2g; however at that same acceleration it is over 80% likely that a URM building would exceed that limit state. Therefore, one can see from this graph that a URM building is *much* more likely to require repair work to re-enter after this ground motion condition than the reinforced concrete building.

Section 1.4 Developing Vulnerability functions

In order to create vulnerability functions to describe a particular structure, quite a bit of information is needed. It is necessary to accurately describe the shape and size of the building, as well as to find out information about the stiffness of the walls and floors, both in and out of plane, for realistic analysis. If stiffness information is missing, that information can be discovered by modeling the structure in SAP2000, and then observing the model's deformation under load. This stiffness is then inputted into ABAQUS, which will run analysis based on a ground motion, and information such as the force in

members and their displacements is calculated. This information is then feed into probability functions developed in order to simplify the process of developing vulnerability curves and those programs will actually feedback the information necessary to graph the vulnerability functions.

Section 1.5 Importance of Vulnerability Functions

Vulnerability functions serve as a communications tool to relate intangible concepts in an easily understood way. Using these relationships, stakeholders can understand more about the sort of response to expect from a structure given a certain ground motion condition. This is useful in accomplishing two of the goals engineers quite often have for themselves: To save money and to save lives.

The ability to save money is found in a possible retrofiting plan. If a building shows a high likelihood (probability) of requiring repair work to re-enter after an earthquake, then it may make sense to retrofit the structure to achieve a lower likelihood. If the structure is not likely to be damaged very severely, or if the cost of retrofiting exceeds the probable benefits achieved, then perhaps it would not make sense to do so. This philosophy is part of project CM-4 on Retrofitting Strategies, which uses vulnerability functions to help make this decision.

Saving lives is hopefully even more of a goal than saving money. This can be accomplished in the development of code that concerns what a city may find to be acceptable consequences in an earthquake. If a city feels that a structure poses too great a threat to human life based on ground conditions that are likely in that area, code can be modified to alleviate that risk. This can be done by forbidding the construction of buildings that pose too great a risk or by requiring the retrofiting of structures that are not otherwise within these limits of tolerance.

Using Vulnerability functions for typical buildings of different materials, it is possible for a city or other organization to make a valid requirement for all buildings of that material. However, this information is only valuable if indeed a structure can be considered “typical.” What may constitute a typical structure is a difficult question to answer. For URM buildings, is the goal of the research described in this report.

SECTION 2 RESEARCH OF URM STRUCTURES

Section 2.1 Introduction

Finding detailed information about ordinary URM structures has turned out to be quite a bit more difficult than originally thought. There has been quite of bit of study done on masonry structures, all which is detailed quite well in library resources. Apparently, however, not so much has been done to describe what a typical masonry structure actually looks like, what its connections are like, or what type of building plan is associated with it. These critical pieces of information would not be easily found in a library resource or online. Instead, searching for this information became more of a piecemeal effort, gathering small bits of usable information from any resource that had viable potential. Finding even the smallest details proved to be a uniquely difficult task,

however there were some resources that proved more useful than others. While there were other sources that provided insight (experienced engineers, websites, other literary sources), the most valuable resources are described below with details of the information that proved most useful.

Section 2.2 Memphis Test Bed Inventory (MTBI)

It can be argued that the MTBI is the most valuable tool in assessing the nature of URM buildings. This test bed inventory is a part of the Mid-America Earthquake Center's DS-2 project which tries to categorize all the structures in the Shelby county/Memphis area. The MTBI gives us the total number of URM structures in Memphis as well as such information as the number of stories, square feet, use, location, and age of the buildings. This tool has proved to be important in advancing the hunt for the various URM structures. With the data that can be found, one can make the most preliminary inferences about the population of structures in Shelby county. For instance, the greatest pool of URM structures lies in industrial, retail trade, and office use. Therefore in constructing a typical model for an unreinforced masonry building, it would make more sense to use these types as a guide. Likewise, the inventory refers to the number of stories in the Memphis area structures. This information tells us that over 70% of the URM structures are one-story, and over 99% are five stories or less. Again, this is useful in helping to make decisions about what type of structure would be best as a model to capture the greatest number of buildings. All of these pieces of information come together to form the fuzziest of pictures of what to expect in a typical URM building.

Based on the information, therefore, the most logical type of building to hunt for/model would be a URM structure with the following criteria:

- 1) Less than five stories (most commonly one); preferably office, industrial, or retail building
- 2) Less than 2,500 square feet (although anywhere less than 50,000 sq. ft. is not unreasonable)
- 3) And if interested in a time period, the URM buildings were most commonly constructed before 1950, although they were still produced quite often even until 1980

The MTBI does have its shortcomings, however. It tries to relay information about the shape of typical buildings— information that is necessary for modeling. Unfortunately, this information is still unavailable. Also, the MTBI does not provide any information about the connections that can be found between the walls and floors of these buildings. Also, it fails to tell what sort of structural elements exist inside the building itself, only the number of square feet and story number. Without these critical pieces of information, it would not be possible to model a structure with reasonable accuracy. To find this information, new sources must be examined.

Section 2.3 Library Discoveries

In the beginning of this report, a brief discussion was given about the nature of information that the library yielded. Most of this information centered around the do-it-yourself construction of masonry walls and the testing of these walls. Rarely did this library information yield anything that would prove useful in determining the typical nature of a masonry structure, or anything about the connections details which are so critical to modeling. But while the library did not provide information on typical structures as a whole, it did contain several books in a series called *Architectural Graphic Standards*. This series assembled the standards that are used by architects and others throughout the nation in construction. While spanning nearly 50 years, still the books showed great consistency in the method by which floor joists were connected to the masonry walls that supported them (detailed later). This information and its consistency, while not necessarily specific to Mid-America URM structures, still provide considerable insight into what might be common in one of these buildings. Some examples are shown in the figures that follow.

This would seem to indicate that the most appropriate type of connection would be one similar to what is seen in these standards: Fire cut joists resting on masonry walls, possibly with a metal strap nailed to the joist that also goes into the wall. Images from field observation will later support this standard.

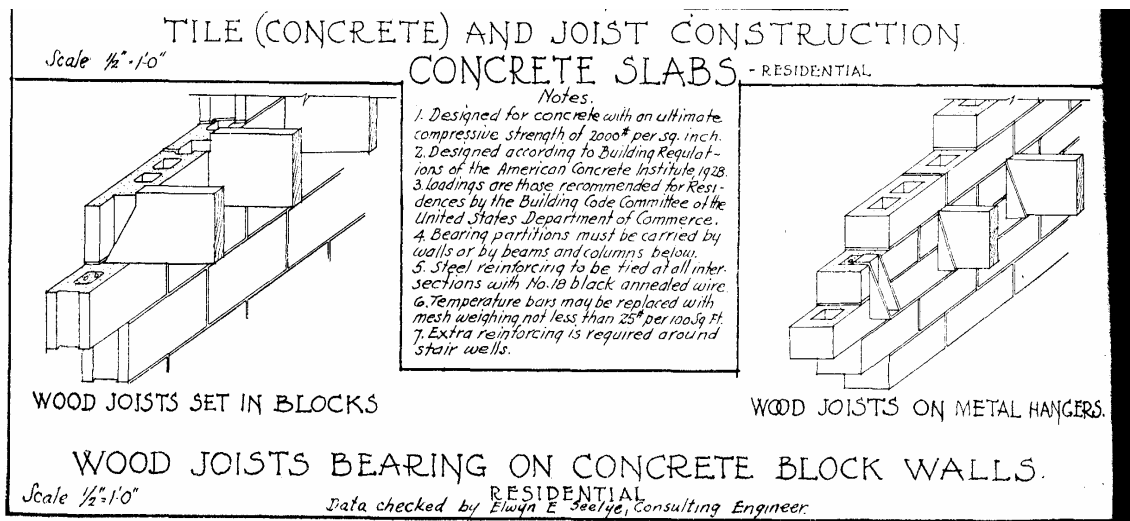


Figure 2: Images of joist-masonry wall connection from the 1932 edition of *Architectural Graphic Standards*.

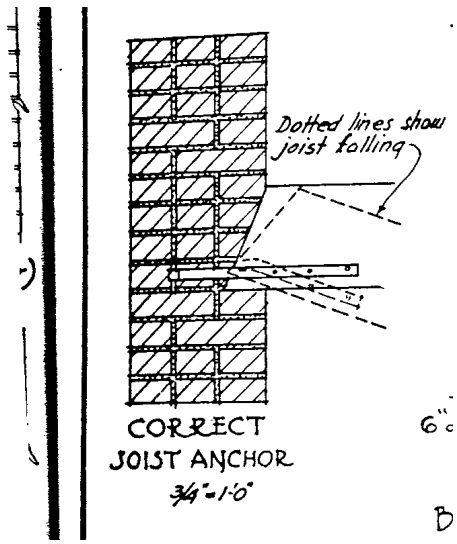
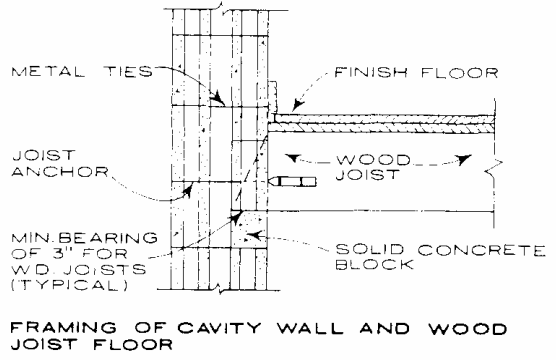
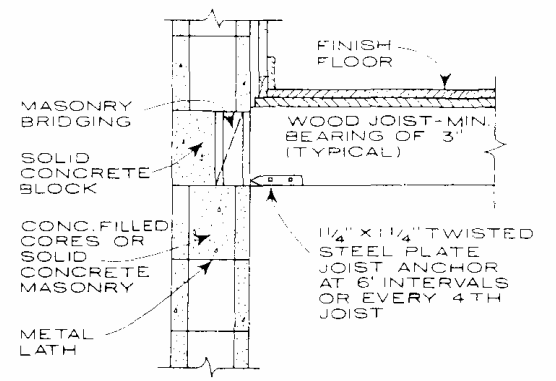


Figure 3: Image from 1952 Architectural Graphic Standards. Note the consistency with earlier edition connection standard and consistency with photographed images.



FRAMING OF CAVITY WALL AND WOOD JOIST FLOOR



FRAMING OF WALL AND WOOD JOIST FLOOR

NOTE:
Joists parallel to and adjacent to walls anchored at 8 foot intervals. Anchors should engage three joists.

Figure 4: Image from 1970 Architectural Graphic Standards. While these images are meant for concrete blocks, still the similarity to the previous standard is shown.

Section 2.4 Thesis

Tianyi Yi had valuable information in his thesis which probably deserves to be commented on as well. In Mr. Yi's Thesis, there was quite a bit of detail about a URM, full-scale firehouse that was constructed at Georgia Tech. Mr. Yi's Thesis also included some information about the connectors that were used for the floor-wall connections. In the firehouse that was constructed at Georgia Tech, there was no fire-cut used, but there were some connectors used which improved the connection between wall and floor diaphragm. Most interesting was a link to www.strongtie.com which contains quite a bit of information on other types of connections that may be used to connect wood floor joists to a masonry wall. Some of these images can be seen below in figures 5-8. While not necessarily intended for URM structures, still these connections should probably be considered as another connection option when modeling a URM building.

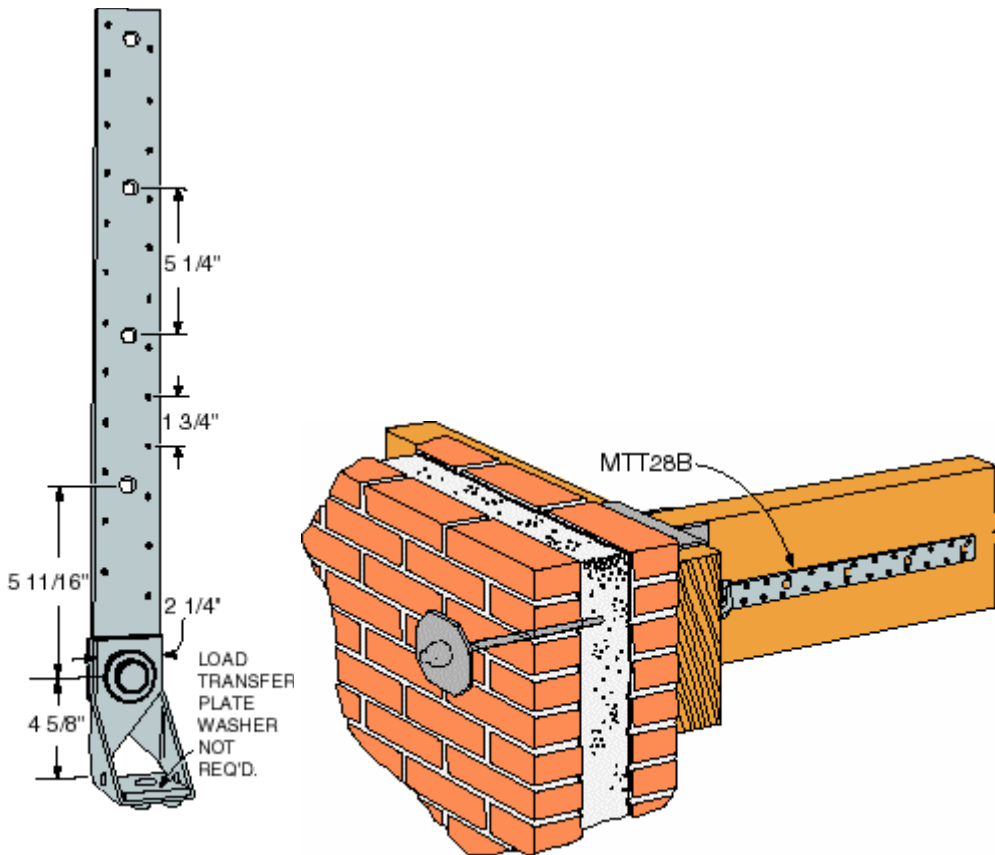
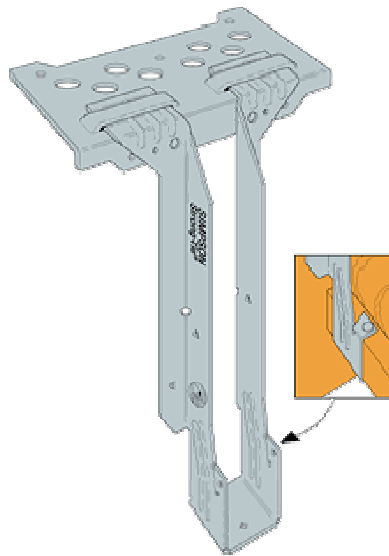
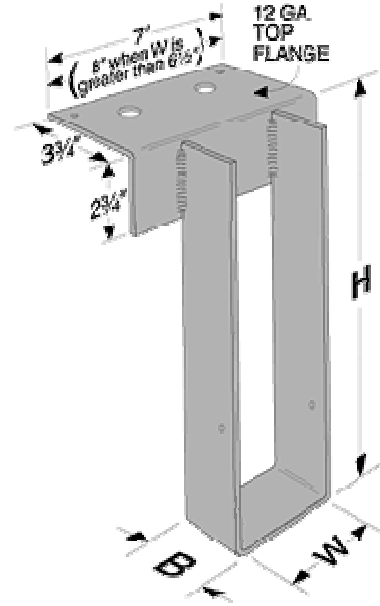
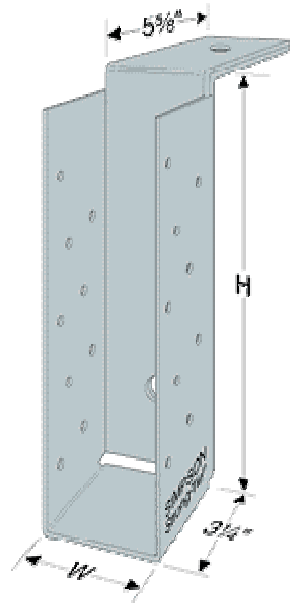


Figure 5: Images of the connections found described and imaged in Mr. Yi's Thesis.



Figures 6,7,8: Examples of masonry hangers for connecting wood joists to masonry walls taken from www.strongtie.com.

Section 2.5 Visual Photographs

Lastly, in an effort to put all the pieces together, as well as to gather information that simply cannot be found inside books, URM buildings in Champaign, Illinois were hunted down and photographed. These structures provided insight into how the interior walls played a role in supporting the structure as well as how a typical structure might be arranged inside. This information also gives the necessary shape and dimensions which the MTBI did not provide. Taking pictures of the buildings was the culmination of the research which provided the last bits of information needed to create realistic models these URM buildings.

Not to underestimate the importance of any of the other facets of this research, but visual photographs are probably the most useful and important when it actually comes time to model a structure. True, the model which will be developed is not going to be identical to the structures that were photographed, but in order to find out information about the nuances of how these structures were built, there is no more effective way than taking pictures.

The structures that were photographed were chosen because of the apparent age of the building, the consistency of the building type with the MTBI, and the availability to go inside the building. The outside photographs of the building give a reasonable estimate of the size, shape, and use of the building. The inside photographs give more details about the connections (refer to section 1.3) as well as the overall design and configuration of the structure. Both outside and inside information is useful for modeling purposes, and given the right conditions, can indeed complete the necessary research in finding typical designs of URM buildings. In reality, the information about things like the built-up-girder, the wall-floor interaction, and the brick column which supports the larger girders makes up the greatest reason to find visual evidence—things that may not have been obvious from other sources.



Figure 9: Floor joists connected to the supporting masonry wall



Figure 10: Supportive beam resting on brick column. This beam supports other floor joists



Figure 11: Details of a connection. This floor joist is supported as most are, except this floor joist has a metal strap nailed into it that is also connected to the masonry wall. Most floor joists had no such strap.

SECTION 3 RECOMMENDATIONS

Section 3.1 Introduction

All of what is listed above would not necessarily convince someone that a structure is typical. The only somewhat guarantee comes from the MTBI, but even still one cannot be sure that information was taken correctly, what the definition of “unreinforced” is, or whether all structures were considered. Therefore, any and all

recommendations contained within this report are only based on what has been observed, and not upon the true population of structures in Memphis, or anywhere for that matter. It would probably be necessary to tear apart most of the brick buildings in Memphis to be sure of their reinforcement characteristics—a completely unfeasible task. Likewise, no structure that is found in this report is guaranteed to be typical. It may indeed be true that the configurations that were examined were the exception and not the rule. However, in the interest of probability and the assumption that indeed most structures in Champaign, Illinois are not too dissimilar from those found in Memphis, Tennessee, a recommendation can be made.

Section 3.2 Recommended principles

A logical recommendation would have to take into account all of the tenants of the MTBI. While, it is likely that a great number of structures adhere to all the general conditions, still a reasonable amount of variation should be considered. In general, the tenants of the MTBI are summarized in the section that focuses on it. The most important part of this summary for modeling purposes is probably the statement concerning the number of stories that are found in typical structures. Using this information, it makes sense to model a structure with less than five stories (as suggested). Likewise, the most valuable information from the library research involves the nature of connections. The fact that the graphical standards suggested a fairly consistent connection type (especially during the time period that the MTBI suggested was the most prolific construction period) would suggest that a model should contain connection information of the nature found in this standard (see section 2.3). Also, the other type of connections which are detailed in section 2.4 should probably also be considered as an option for connections. While, not likely to be as common as the graphic standards model, still the information that is found here should probably not be neglected. Also, information that is detailed in the visual imagery would also be wise to include in a model. Information such as the built up girder made of seven 2x12's, as well as the brick columns upon which it rested, should probably be considered in the modeling of a structure. This should be common in factories or warehouses where a large, open space is required without any stud walls for support. Also, the dimensions of the model itself would probably be best described in terms of the building that was actually photographed. A reasonable amount of tolerance would probably say that these dimensions would be typical (see figure 12 below). This, however, would be only for the rectangular-shaped structures. Please note that URM buildings can be square, L-shaped, T-shaped, H-shaped, or generally irregular shaped. Once information on these configurations are publicized in the MTBI, it would be logical to select the shapes that appear most frequently. However, in Champaign, rectangular seems to be most common and should probably be considered as the most likely model for a structure.

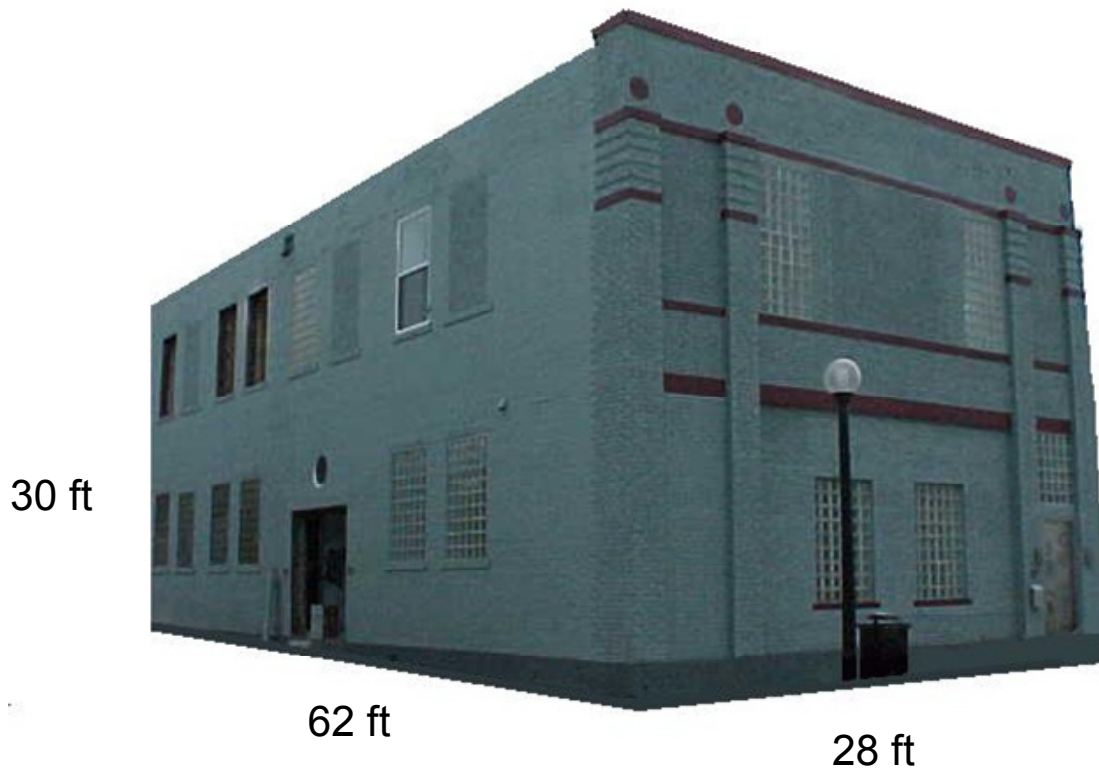


Figure 12: Dimensions of the structure photographed as a typical URM building.

The figure above demonstrates a possibility for the dimensions of a URM structure. These dimensions were used for the modeling of a typical structure. However, the structure depicted above was not specifically modeled, nor do the results of the analysis necessarily indicate the type of response that may be expected for this structure. Rather, the results of the analysis will yield information about a structure similar to the one listed above, with particular emphasis on some of the details which may be similar in most URM structures. These details are found listed above, and images can be found in section 2.5 on visual photographs.

Section 3.3 Conclusion

This report is an effort to briefly describe what has taken weeks of nominal success to compile. The information that has been summarized herein does not even begin to cover the amount of material that has been researched and examined. Instead, this report presents the most useful information from this research, and intends to propose a way to potentially draw a representative model from that search. This model, therefore, should be considered in light of the search that has produced it. Perhaps it would have been possible to conduct research in a different fashion and received more useful results. However, with the available resources, it makes most sense that the configurations presented should be considered an adequate solution in the effort to describe a typical

URM structure. Perhaps some document should be developed that summarizes the construction practices of the nation over its history and includes details of how a typical building of each material and time period were developed. Without access to a great deal of buildings, however, this is probably unfeasible. Nevertheless, this report should serve its purpose and be considered valuable in the effort of describing typical URM buildings.

Useful References

- Boaz, J. N. ed., *Architectural Graphic Standards*. New York, New York, United States of America. 1970.
- Ramsey, C. G., and Sleeper, H. R. *Architectural Graphic Standards*. New York, New York, United States of America. 1952.
- Packard, R. T. ed., *Architectural Graphic Standards*. New York, New York, United States of America. 1981.
- Ramsey, C. G., and Sleeper, H. G., *Architectural Graphic Standards*. New York, New York, United States of America. 1932.
- Yi, T. "Experimental Investigation and Numerical Simulation of an Unreinforced Masonry Structure with Flexible Diaphragms," Georgia Institute of Technology, February 2004.

EFFECTS OF MR DAMPER PLACEMENT ON STRUCTURE VIBRATION PARAMETERS

Karla A. Villarreal

*Home Institution: Dept. of Civil and Env. Engineering FAMU-FSU College of Engineering,
2525 Pottsdamer St., Tallahassee, FL. 32310*

Host Institution: Tokyo University

*Advisors: Claudia M.D. Wilson
Makola M. Abdullah, Ph.D.*

ABSTRACT

Control devices can be used to dissipate energy on a civil structure during an earthquake and therefore reduce structural damage and prevent failure. The MR damper is a control device that consists of a hydraulic cylinder filled with magnetically polarizable particles suspended in a liquid. MR dampers dissipate vibration by absorbing energy. Other researchers found that the damping ratio escalates as the voltage increases and decreases as the amplitude of the forcing function increased. A “sensitive voltage region” (range of voltages for which the amounts of damping added and the shift in natural frequency were very adjustable) has also been found. A relationship between the damper position and equivalent damping ratio has yet to be found. This study’s objective is to find the effect of MR damper placement on the equivalent damping ratio and on the natural frequency of a building. A 3 degree-of-freedom building was selected and free vibration curves were obtained for different placements of the MR damper and different current settings in order to compute the equivalent damping ratio and the frequency shift. To obtain a “sensitive current range,” curves relating the current to added damping and to frequency shift were also obtained.

KEYWORDS

Magneto-rheological (MR) damper, equivalent damping ratio, natural frequency shift, MR damper placement.

PROBLEM STUDIED

An engineer’s ability to reduce a city’s infrastructure’s damage caused by earthquakes is crucial to the economy and human life. Earthquakes can claim the lives of many people, cause millions of dollars in damages and also reduce building longevity. To reduce the effects of earthquakes and high wind loads, engineers have implemented various types of systems to help dissipate vibration. Among more recent developments, the magneto-rheological (MR) damper has emerged as an effective control device.

A control device is a system that helps absorb vibration or movement. There are three types of control: passive, active and semi-active. A passive controller is a system that does not require

power to operate and directly damps vibration or movement. Active control requires significant power to run and applies a force directly into the system to damp vibration. Semi-active control requires minimal power and it applies a force that changes the system's physical properties, therefore damping the vibration. The MR damper is a semi-active control device. It is a cylindrical device with a three stage piston as seen in Fig. 1. Inside the cylinder and surrounding the piston is a type of controllable fluid, that is, a fluid which is able to change its rheological behavior. The controllable fluid is composed of micron-sized, para-magnetic polarizable iron particles suspended in a liquid, which can be water, glycol, synthetic or mineral oil. When a current is introduced into the system, a magnetic field is created along the three stage piston. The para-magnetic particles line up with the magnetic field and form chains, changing the rheological behavior of the controllable fluid, in other words it can change the viscosity of the liquid, depending on the magnetic field intensity. The field, and thus the viscosity, is proportional to the amount of current applied to the damper.

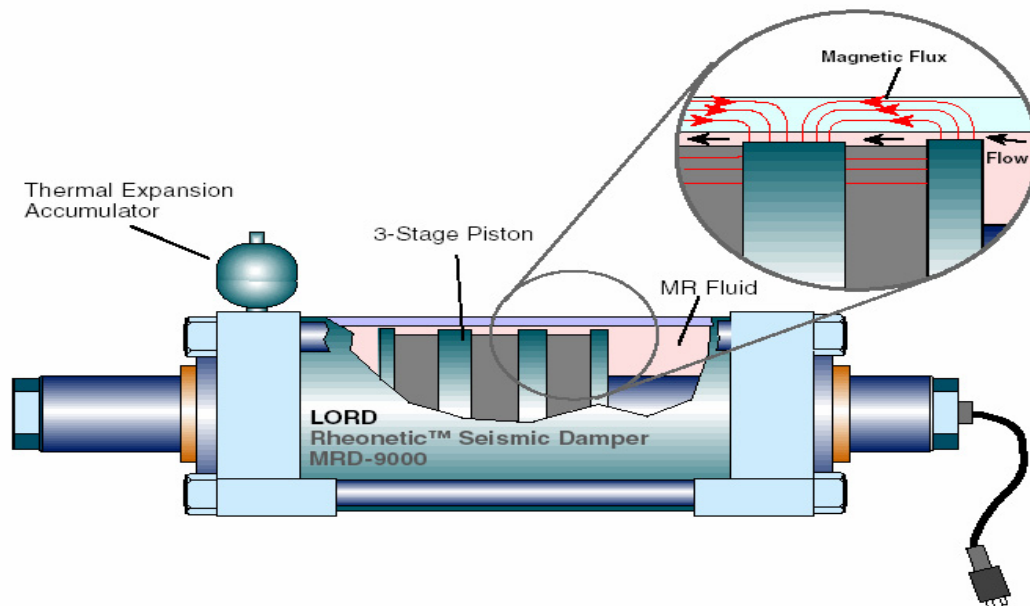


Figure 1. 20-ton large-scale MR fluid damper (Yang 2001)

Lou et al. (2001) researched the modal damping of a cable stay bridge controlled by a 3000 N MR damper. They established that the MR damper caused small shifts in the cable's natural frequencies. The present study will be conducted with two 20-ton MR dampers. On a multi-story building, the placement of the MR damper could have a significant impact on the equivalent damping ratio and also affect the natural frequency of the building.

OBJECTIVES

The objectives of this research are to determine the effects of MR damper placement on the equivalent damping ratio, the natural frequency of a building and to find the sensitive current range of the MR damper.

RESEARCH APPROACH

The Equation of Motion presented below describes the behavior of a controlled building under an earthquake load:

$$\mathbf{M}\ddot{\mathbf{x}} + \mathbf{C}_d\dot{\mathbf{x}} + \mathbf{K}_s\mathbf{x} = -\mathbf{\Gamma}f - \mathbf{M}\boldsymbol{\lambda}\ddot{x}_g \quad (1)$$

Where \mathbf{M} is the mass matrix, \mathbf{C}_d is the damping matrix, \mathbf{K}_s is the stiffness matrix, \mathbf{x} is the vector of floor displacements, $\dot{\mathbf{x}}$ and $\ddot{\mathbf{x}}$ are floor velocity and acceleration vectors, respectively, $\mathbf{\Gamma}$ is a vector of zeros and ones, where 1 will indicate where the MR damper force is being applied, f is the force produced by the damper, $\boldsymbol{\lambda}$ is a matrix of ones and \ddot{x}_g is the acceleration due to an earthquake. For the uncontrolled case, force f produced by the MR damper is zero.

In order to calculate and reproduce the force of the damper, the mechanical model of the MR damper proposed by Spencer et al. (1997) was used. The equations are listed below.

$$f = c_o\dot{y} + k_1(x - x_o) \quad (2a)$$

$$\dot{y} = \frac{1}{c_o + c_1} [\alpha z + c_o\dot{x} + k_o(x - y)] \quad (2b)$$

$$\dot{z} = -\gamma|\dot{x} - \dot{y}|z|z|^{n-1} - \beta(\dot{x} - \dot{y})|z|^n + A(\dot{x} - \dot{y}) \quad (2c)$$

Where:

$$\alpha(i) = 16566i^3 - 87071i^2 + 168326i + 15114 \quad (3a)$$

$$c_o(i) = 437097i^3 - 1545407i^2 + 1641376i + 457741 \quad (3b)$$

$$c_1(i) = -9363108i^3 + 5334183i^2 + 48788640i - 2791630 \quad (3c)$$

Where y is the internal displacement of the MR damper, x is the damper displacement in the x -direction and the additional variables are constants with the following values: $x_o=0.18$ m, $k_1=617.31$ N/m, $k_o=37810$ N/m, $A=2679$ m⁻¹, γ and $\beta=647.46$ m⁻¹, $n=10$ (Yang et al. 2001).

A first order filter was also used in the model to correctly model the dynamics of the MR fluid reaching rheological equilibrium (Yang et al. 2001):

$$H(s) = \frac{31.4}{s + 31.4} \quad (4)$$

These equations were modeled in Simulink as shown in Fig. 2, where the inputs are current and displacement and the output is force.

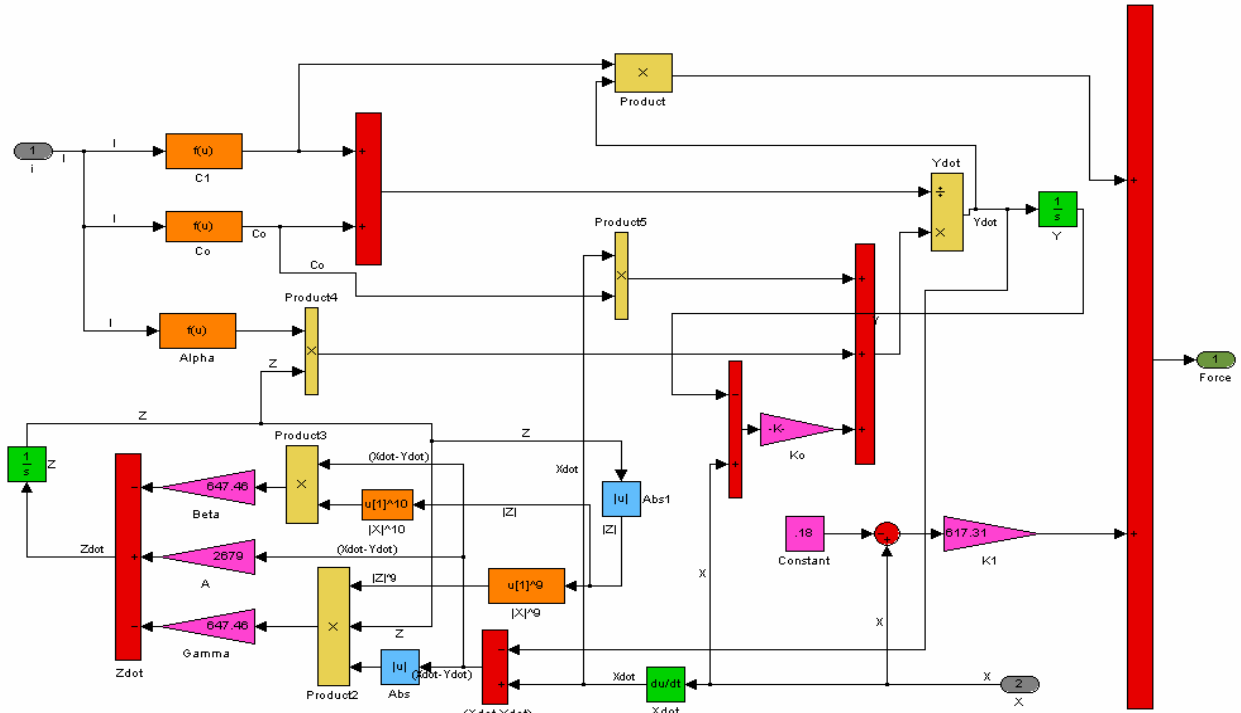


Figure 2. Schematic of the MR damper in Simulink

This model was tested by inputting a constant current of 1 amp and a sine wave with amplitude of 0.0127 m and a frequency of 2π radians. The results were satisfactorily compared to theoretical and experimental results presented in Yang et al. (2001)

A 3 degree of freedom building was chosen and used for the simulations to determine the effects of MR damper placement on equivalent damping ratio and natural frequency. The building's details are listed in Table 1.

Table 1. Building Properties (Park et al. 2002)

Floor Mass	345,600 kg
Floor Stiffness	1.2×10^5 kN/m
Damping Coefficient (ζ)	1%

Mass, stiffness and damping matrices were computed in Matlab. The Matlab code to produce these matrices is presented in the Appendix. The matrices for this building are presented below:

$$\mathbf{M} = \begin{bmatrix} 345600 & 0 & 0 \\ 0 & 345600 & 0 \\ 0 & 0 & 345600 \end{bmatrix} \text{ kg}$$

$$\mathbf{K}_s = \begin{bmatrix} 2.4 & -1.2 & 0 \\ -1.2 & 2.4 & -1.2 \\ 0 & -1.2 & 1.2 \end{bmatrix} \times 10^5 \text{ kN/m}$$

$$\mathbf{C}_d = \begin{bmatrix} 1.7446 & -0.5115 & -0.1111 \\ -0.5115 & 1.6335 & -0.6227 \\ -0.1111 & -0.6227 & 1.1220 \end{bmatrix} \times 10^5 \text{ Ns/m}$$

For application in Simulink, state space equations were derived by solving Eq. 1 for $\ddot{\mathbf{x}}$:

$$\ddot{\mathbf{x}} = -\mathbf{M}^{-1}\mathbf{C}_d\dot{\mathbf{x}} - \mathbf{M}^{-1}\mathbf{K}_s\mathbf{x} - \mathbf{M}^{-1}\mathbf{\Gamma}f - \lambda\ddot{x}_g \quad (5a)$$

and using the following equation:

$$\dot{\mathbf{x}} = \dot{\mathbf{x}} \quad (5b)$$

to produce a system of equations in the form of:

$$\dot{\bar{\mathbf{x}}} = \mathbf{A}\bar{\mathbf{x}} + \mathbf{B}u \quad (6a)$$

$$\mathbf{y} = \mathbf{C}\bar{\mathbf{x}} + \mathbf{D}u \quad (6b)$$

Where, for an uncontrolled building, term $-\mathbf{M}^{-1}\lambda\ddot{x}_g$ in Eq. 1 equals zero, and state space matrices are:

$$\mathbf{A} = \begin{bmatrix} \mathbf{0}_{3 \times 3} & \mathbf{I}_{3 \times 3} \\ -\mathbf{M}^{-1}\mathbf{K}_s & -\mathbf{M}^{-1}\mathbf{C}_d \end{bmatrix} \text{ and } \mathbf{B} = \begin{bmatrix} 0 \\ 0 \\ 0 \\ -1 \\ -1 \\ -1 \end{bmatrix}$$

$$\mathbf{C} = \begin{bmatrix} \mathbf{I}_{3 \times 3} & \mathbf{0}_{3 \times 3} \\ \mathbf{0}_{3 \times 3} & \mathbf{I}_{3 \times 3} \\ -\mathbf{M}^{-1}\mathbf{K}_s & -\mathbf{M}^{-1}\mathbf{C}_d \end{bmatrix} \text{ and } \mathbf{D} = \begin{bmatrix} 0 \\ 0 \\ 0 \\ 0 \\ 0 \\ -1 \\ -1 \\ -1 \end{bmatrix}$$

\bar{x} is the states of the system, defined as a vector of floor displacements and velocities and u is the ground acceleration. For the controlled case, when the MR damper is placed on the first floor of the building, \mathbf{B} , \mathbf{D} and \mathbf{u} become:

$$\mathbf{B} = \begin{bmatrix} \mathbf{0}_{3 \times 1} & \mathbf{0}_{3 \times 1} \\ -\mathbf{1}_{3 \times 1} & -\mathbf{M}^{-1}\mathbf{\Gamma} \end{bmatrix} \quad \mathbf{\Gamma} = \begin{bmatrix} 1 \\ 0 \\ 0 \end{bmatrix} \quad \mathbf{D} = \begin{bmatrix} \mathbf{0}_{3 \times 1} & \mathbf{0}_{3 \times 1} \\ \mathbf{0}_{3 \times 1} & \mathbf{0}_{3 \times 1} \\ -\mathbf{1}_{3 \times 1} & -\mathbf{M}^{-1}\mathbf{\Gamma} \end{bmatrix} \quad \mathbf{u} = \begin{bmatrix} \ddot{x}_g \\ f \end{bmatrix}$$

When the MR damper is placed on the second floor, $\mathbf{\Gamma}$ becomes:

$$\mathbf{\Gamma} = \begin{bmatrix} 0 \\ 1 \\ 0 \end{bmatrix}$$

and correspondingly for the third floor.

The uncontrolled and controlled Simulink simulations ran simultaneously. Fig. 3 shows the complete diagram. The force of the damper is being multiplied by two to represent a damper that can produce a force of 40-tons. To determine the equivalent damping and the natural frequency, the free vibration response was obtained. An initial displacement of 5 cm on each floor was used.

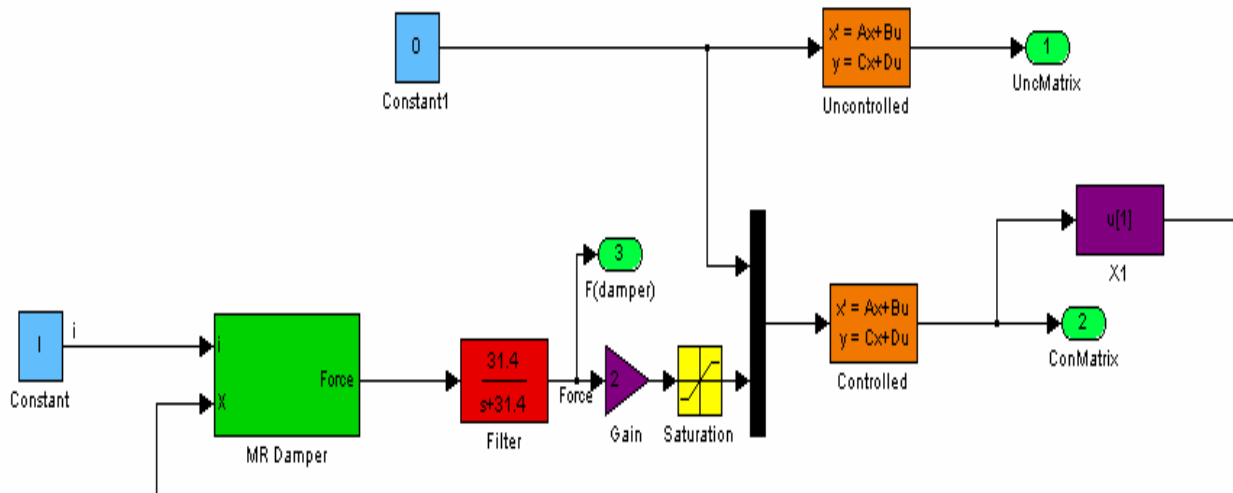


Figure 3. Schematic of the MR damper in Simulink

In each run, the MR damper current was kept constant. Settings of zero to six amperes were analyzed for each MR damper placement. The Matlab program developed is also included in the Appendix. Time response plots were obtained for each case and the equivalent damping was calculated according to Eq. 7 (Chopra, 2001)

$$\zeta = \frac{1}{2\pi * j} \ln \frac{u_i}{u_{i+j}} \quad (7)$$

Where u_i is the highest peak of the free vibration response plot, and u_{i+j} is one of the subsequent peaks, j is the number of peaks between u_i and the u_{i+j} (Fig. 4). The additional damping introduced by the MR damper was determined by calculating the uncontrolled equivalent damping ratio and comparing it to that of the controlled building at each current setting from 0 amps to 6 amps. The average damping ratio for each of the current settings was determined and used for best results.

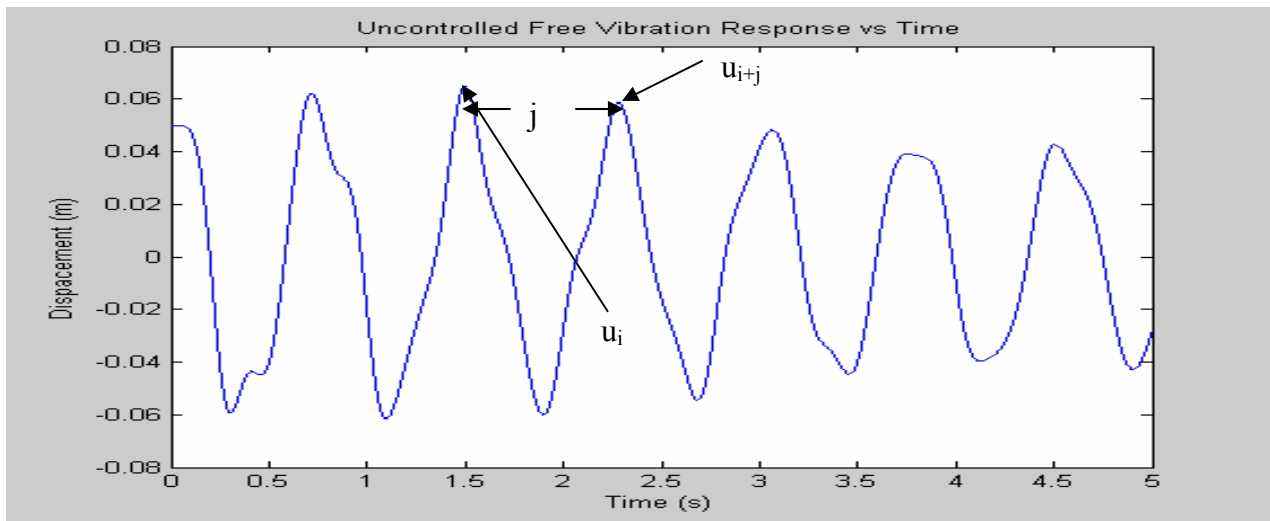


Figure 4. Determining the equivalent damping ratio from free vibration response

The natural frequency shift was obtained from the modal response. Once the modes were separated, the frequency of the first mode was determined by taking the inverse of the period (Δt) as shown in Fig. 5. The program written to separate the modes and find the peaks is included in the Appendix.

The sensitive current range (SCR) was estimated by graphing the additional damping vs. current and also checked by graphing the natural frequency shift vs. current. In the SCR, the graphs would increase at a larger rate during the sensitive current range and increase slightly or with a minimal slope when such range was surpassed.

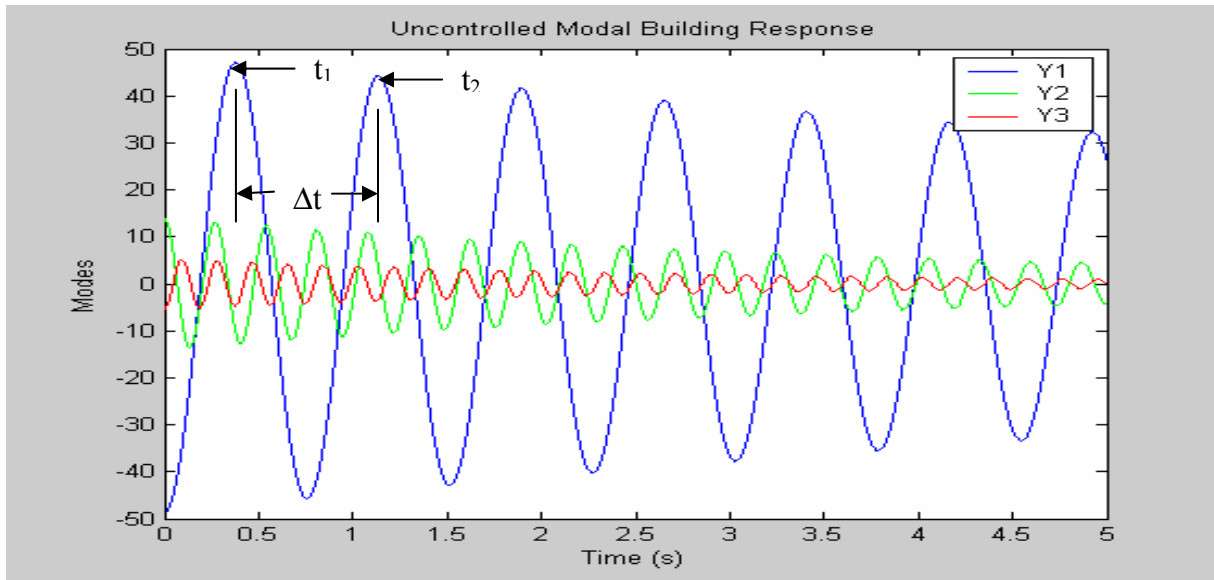


Figure 5. Determining the frequency from the mode shapes

OUTCOMES

Equivalent damping ratios, additional damping ratios, natural frequencies and frequency shifts for the placement of the MR damper on the first floor through the third floor are summarized in Tables 2 to 4.

Table 2. Damping ratio and natural frequency for MR damper on 1st floor

Current (A)	Damping Ratio (%)	Additional Damping Ratio (%)	Natural Freq. (Hz)	Freq. Shift (Hz)
No Damper	2.19365	0.00000	1.31978	0.00000
0	2.80357	0.60992	1.32681	0.00702
1	5.99476	3.80111	1.33374	0.01396
2	6.28860	4.09495	1.33404	0.01426
3	7.14884	4.95519	1.33576	0.01597
4	7.42823	5.23458	1.33620	0.01642
5	7.47207	5.27843	1.33590	0.01611
6	7.47976	5.28612	1.33586	0.01608

Table 3. Damping ratio and natural frequency for MR damper on 2nd floor

Current (A)	Damping Ratio (%)	Additional Damping Ratio (%)	Natural Freq. (Hz)	Freq. Shift (Hz)
No Damper	2.19365	0.00000	1.31977	0.00000
0	3.91337	1.71972	1.32443	0.00467
1	3.60766	1.41401	1.32512	0.00535
2	4.86715	2.67350	1.32499	0.00523
3	3.38542	1.19177	1.33576	0.01599
4	2.19772	0.00408	1.31938	0.00038
5	2.20284	0.00919	1.31916	0.00061
6	2.20450	0.01086	1.31910	0.00066

Table 4. Damping ratio and natural frequency for MR damper on 3rd floor

Current (A)	Damping Ratio (%)	Additional Damping Ratio (%)	Natural Freq. (Hz)	Freq. Shift (Hz)
No Damper	2.19365	0.00000	1.31977	0.00000
0	1.59208	-0.60157	1.31320	0.00657
1	1.27050	-0.92315	1.30979	0.00997
2	2.30744	0.11379	1.30981	0.00996
3	1.13409	-1.05956	1.30933	0.01044
4	1.08789	-1.10576	1.30911	0.01066
5	1.06836	-1.12529	1.30904	0.01073
6	1.05826	-1.13539	1.30899	0.01078

When the system is uncontrolled, the damping ratio is about 2.19%. When the damper is placed on the 1st floor and no current is applied, an increase in damping of 0.61 % was observed. Placing the damper on the second floor also increases the damping by 1.719% (Table 3). However, when the damper is placed on the 3rd floor, a decrease of 0.60% is observed (Table 4). As current to the MR damper is increased from 1 to 6 amps, the additional damping increases up to 5.286 % for the damper on the 1st floor (Table 2). For the damper on the 2nd floor, there is an increase of additional damping as current increases from 0 to 2 amps but a decrease as current is increased further (Table 3). Finally, on the 3rd floor, damping is only added when the damper current is set to 2 amps and it is found to decrease for the other current settings (Table 4). The largest amount of damping added was witnessed on the 1st floor with a current setting of 6 amps.

The shift in frequency was very small for all the settings. When the building is uncontrolled, the frequency is 1.319 Hz. The controlled system with the MR damper functioning with zero input current was slightly different than the uncontrolled case with a shift of 0.0072 Hz for the damper on the 1st floor (Table 2), 0.00467 Hz for the 2nd floor (Table 3) and 0.00657 Hz for the 3rd floor (Table 4). As current for the MR damper is increased from 1 to 6 amps on the 1st floor, frequency shifts increase to a maximum of 0.01642 Hz at 4 amps (Table 2) and then decrease for the next two current settings. When the damper is placed on the 2nd floor, the largest shift occurred at 3 amps with a value of 0.01599 Hz (Table 3), less than the largest shift on the 1st floor. Finally, on the 3rd floor, the largest shift occurred at 6 amps, when a shift of 0.01078 Hz was observed (Table 4).

The graphical analysis of the sensitive current range is plotted in Figs. 6 and 7. Plots from data of the other floors did not present a clear correlation between the current and the additional damping or the frequency shift. Therefore only the data produced when the MR damper was on the first floor was used to determine the sensitive current range.

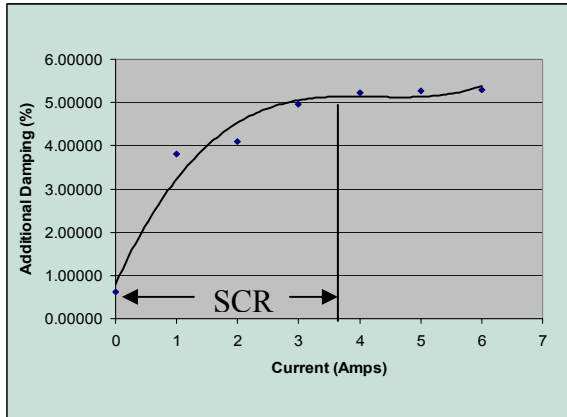


Figure 6. SCR due to Additional Damping

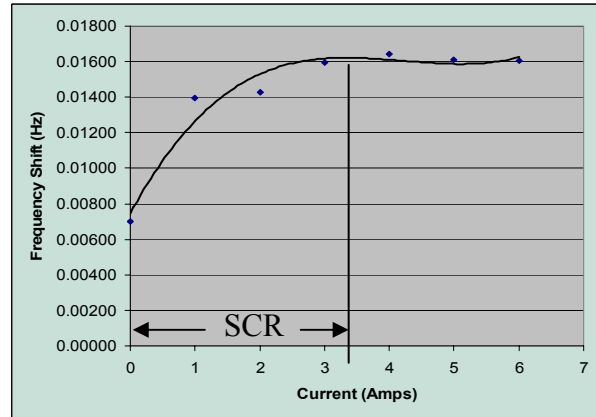


Figure 7. SCR due to Frequency Shift

According to Figs. 6 and 7, it was estimated to be from 0 to 3 amps since this is where the additional damping increased the most and where the largest frequency shifts occurred. The two plots correlated very well and gave similar results.

CONCLUSION

The position of the MR damper was found to affect the equivalent damping ratio. As the position of the damper was moved higher into the building, the additional damping decreased. The MR damper produced the largest additional damping on the 1st floor of the building. The position of the MR damper had very little effect on frequency shifts. These occurred when the damper was placed on every floor of the building but the largest shifts occurred when the MR damper was placed on the 1st floor.

POSSIBLE FUTURE WORK

Possible future work may include determining a correlation between the sensitive current range found in this study and the sensitive voltage range that used to determine similar relations found in previous studies. A larger building could also be modeled and simulations used to determine similar relations. The effects of MR damper placement on bridge vibration parameters could also be studied.

ACKNOWLEDGEMENTS

I would like to acknowledge my advisors Claudia Wilson and Makola M. Abdullah, Ph.D. and the WHEEL family for all their help, support and patience. Also to my REUJAT buddies, Dr. Dyke, the National Science Foundation, Florida A & M University's Undergraduate Program for a great summer research experience. Lastly to my family, friends and especially A.J. who encouraged me and kept my spirits up.

APPENDIX

Matlab code for producing M,K and C matrices

Mass	<pre>%Input Mass of each Floor (kg) F1=345600; F=[F1,F1,F1]; %Mass Matrix M=[diag(F)];</pre>
Stiffness	<pre>%Input Stiffness (N/m) Ks=ones(1,3)*1.2*10^8; K1=Ks(1,2:n); K2=Ks+[K1,0]; %Stiffness Matrix KS=diag(K2)-diag(K1,-1)-diag(K1,1);</pre>
Damping	<pre>%O=modal shapes, NF=natural freq squared [O,NFS]=eig(KS,M); %Input Zeta(n)for nDOF Zeta=ones(1,n)*.01; %Natural Freq. Omega=sqrt(diag(NFS)); %Modal Mass Mm=(O')*M*O; %Calculating damping values for j=1:n c(j)=[2*Omega(j)*Mm(j,j)*Zeta(j)]; end %Modal Damping matrix Cm=diag©; %Damping matrix Cd=inv(O')*Cm*inv(O);</pre>

Matlab code for free vibration of uncontrolled and controlled systems

<pre>clear all clc tic %Input DOF n=3; %Input Current (Amps) I=0; %Input Mass of each Floor (kg) F1=345600; F=[F1,F1,F1]; %Mass Matrix M=[diag(F)];</pre>

```

%Input Stiffness (KN/m)
Ks=ones(1,3)*1.2*10^8;
K1=Ks(1,2:n)
K2=Ks+[K1,0]
%Stiffness Matrix
KS=diag(K2)-diag(K1,-1)-diag(K1,1);
%O=modal shapes, NF=natural freq
squared
[O,NFS]=eig(KS,M);
%Input Zeta(n)for nDOF
Zeta=ones(1,n)*.01;
%Natural Freq.
Omega=sqrt(diag(NFS));
%Modal Mass
Mm=(O')*M*O;
%Calculating damping values
for j=1:n
    c(j)=[2*Omega(j)*Mm(j,j)*Zeta(j)];
end
%Modal Damping matrix
Cm=diag(c);
%Damping matrix
Cd=inv(O')*Cm*inv(O);
%General Use Matrices
Y=eye(n,n);
S=zeros(n,n);
Bs=zeros(n,2);
Gd=-ones(2,1);
Ge=zeros(2,1);
%Enter -ones matrix for nDOF
N=-ones(n,1);
%Enter zeros matrix for nDOF
T=zeros(n,1);
%Input State Space (UNC)
A=[S,Y;-inv(M)*KS,-inv(M)*Cd];
B=[T;N];
C=[Y,S;S,Y;-inv(M)*KS,-inv(M)*Cd];
D=[T;T;N];
%Input State Space (CON)
Bc=[Bs;-1,-1/F1;Gd,Ge];
Dc=[Bs;Bs;-1,-1/F1;Gd,Ge];
IC=[0.05;0.05;0.05;0;0;0]
pack
sim('SimBuildingFVR')
toc

```

Matlab code for obtaining the maximum peaks of plots

```
col=1;
%Enter num. of time steps
m=500001;
%1 of 1: Regulates your limits by taking out the last point
h=1:(m-1);
hh=h';
%2 of 2: Dismisses 1st number and goes directly to second number
j=2:m;
jj=j';
%Simplifies your inputs
TRU=yout(:,col);
%True or False: 2nd number is >= 1st number
TRU(jj)>=TRU(hh);
%T=1, F=0, ans=matrix with all these values
%Multiplies 2nd number matrix by these numbers
BU=ans.*TRU(jj);
%Splits up your data points so you can see matrices
%NOTE: This matrices will start to increase and end in the max number till
%they hit zero...take the LAST NUMBER when you look at these matrices. Make
%sure you have the graph side by side so you can tell if it is a relevant
%max or not.
BUa=BU(1:.125*m,1);
BUb=BU(.125*m:.25*m,1);
BUc=BU(.25*m:.375*m,1);
BUd=BU(.375*m:.5*m,1);
BUe=BU(.5*m:.625*m,1);
BUf=BU(.625*m:.75*m,1);
BUg=BU(.75*m:.825*m,1);
BUh=BU(.825*m:.93*m,1);
BUi=BU(.93*m:m-1,1);
```

Matlab program for obtaining the mode shapes

```
X1=yout(:,1)';
X2=yout(:,2)';
X3=yout(:,3)';
X=[X1;X2;X3];
Ys=inv(O)*X;
Y1=Ys(1,:);
Y2=Ys(2,:);
Y3=Ys(3,:);

Ma=Y1';
Mb=Y2';
Mc=Y3';
```


REFERENCES

- Carlson, J.D. and Spencer Jr., B.F. "Magneto-Rheological Fluid Dampers for Seismic Control," *Proc. 3rd Int. Conf. on Motion and Vibr. Control*, Chiba, Japan, Vol. 3, 35-40, 1996.
- Chopra, A.K. "Free Vibration Tests." *Dynamics of Structures: Theory and Applications to Earthquake Engineering*. 2nd Ed. Prentice Hall, Upper Saddle River, NJ:54-57, 2001.
- Lou, W. J., Ni, Y. Q. and Ko, J. M. "Dynamic Properties of a Stay Cable Incorporated with Magneto-rheological fluid dampers," *Advances in Structural Dynamics*, J. M. Ko and Y. L. Xu (eds.), Elsevier Science Ltd., Oxford, UK, Vol. 2, pp. 1341-1348, 2000.
- Lou, W. J., Ni, Y. Q. and Ko, J. M. "Modal damping and stepping-switch control of stay cables with magnetorheological fluid dampers," *Proc. of SPIE*, Reno, Nevada, Vol. 4330, 44, 2001.
- Park, K. S., Koh, H.M., and Ok, S.Y. "Active Control of Earthquake Excited Structures Using Fuzzy Supervisory Technique," *Advances in Engineering Software* 33, 761-768, 2002.
- Spencer Jr., B.F., Dyke, S.J., Sain, M.K., and Carlson, J.D. "Phenomenological Model of a Magnetorheological Damper," *Journal of Engineering Mechanics, ASCE*, vol 123, No. 3, pp.230-238, 1997.
- G.Yang."Large-Scale Magnetorheological Fluid Damper for Vibration Mitigation: Modeling, Testing and Control," *Ph.D dissertation*, University of Notre Dame, 2001.
- Yang, G., Jung, H.J. and Spencer Jr., B.F. "Dynamic Model of Full-Scale MR Dampers for Civil Engineering Applications," *US-Japan Workshop on Smart Structures for Improved Seismic Performance in Urban Region*, Seattle, WA, Aug. 14-16, 2001.



Research Experience for Undergraduates
**Earthquake Engineering Symposium for
 Young Researchers**

2004 Agenda

Thursday, August 5, 2004	
	Arrive at Charleston Airport, private shuttle to Kiawah Island Resort
7:00 pm	Welcome Reception - World Cup A & B
Friday, August 6, 2004	
8:00 am	Continental Breakfast - World Cup A
8:45 am	Welcome and Symposium Overview - World Cup B
	MCEER - Makola Abdullah
	PEER - Amit Kanvinde
	MAE - Sandra Menke
	Student Presentations - World Cup B
9:15 am	Zaneta Adme, FSU <i>Analysis of NATM Tunnel Responses due to Earthquake Loading in Various Soils</i>
9:30 am	Lisa Anderson, MCEER <i>Development of a One-Story Model for Use on an Educational Shake Table</i>
9:45 am	Nathan Canney, PEER <i>Performance of Concentrically Braced Frames Under Cyclic Loading</i>
10:00 am	Timothy Brownawell, MAE <i>Ground Motion Distance Attenuation Measurement and Tools</i>
10:15 am	Break - World Cup A
	Student Presentations - World Cup B
10:45 am	Karla Villarreal, FAMU <i>Effects of MR Damper Placement on Structure Vibration Parameters</i>
11:00 am	Lindsey Oliver, MAE <i>HD-2 Intra-Plate Source Modeling</i>
11:15 am	Laura Flores, PEER <i>Performance of Existing Reinforced Concrete Columns under Bidirectional Shear & Axial Loading</i>
11:30 am	Lunch - World Cup A



Research Experience for Undergraduates
**Earthquake Engineering Symposium for
 Young Researchers**

2004 Agenda

Friday, August 6, 2004 (continued)	
12:30 pm	Cooper River Bridge Tour
	Leave for Field Trip to Cooper River Bridge Tour
	<i>Tour Leader: Charles T. Dwyer, Project Manager</i>
5:00 pm	Return from Cooper River
	Free Time
7:30 pm	Dinner - Baggar Vance
	<i>After Dinner Speaker: Makola Abdullah, MCEER Diversity Program Director</i>
Saturday, August 7, 2004	
8:45 am	Continental Breakfast - World Cup A
	Student Presentations - World Cup B
9:30 am	Mary Grondin, MAE
	<i>DS-3 Response Analysis Tools</i>
9:45 am	Abiel Carrillo, MCEER
	<i>Seismic Isolation for Small Reinforced Concrete Structures</i>
10:00 am	Vivian Gonzales, PEER
	<i>Building Loss Modeling and Benchmarking: EDP to DV</i>
10:15 am	Meagan Mauter, MAE
	<i>Modeling Community Goal Dynamics</i>
10:30 am	Break - World Cup A
	Student Presentations - World Cup B
11:00 am	Christina Nishimoto, PEER
	<i>3D Visualization Program for Earthquake Simulation</i>
11:15 am	Ashford Kneitel, PEER
	<i>Bridge Abutment Soil Compaction Test</i>
11:30 am	Michael Long, Corey Bergad, MCEER
	<i>Study of Rotational Column with Plastic Hinge</i>
12:00 p.m.	Lunch - World Cup A



Research Experience for Undergraduates
Earthquake Engineering Symposium for
Young Researchers

2004 Agenda

Saturday, August 7, 2004 (continued)	
1:00-3:00 pm	Engineering Ethics - World Cup B
	<i>Dr. Joseph Herkert, North Carolina State University</i>
	<i>Engineering Ethics: What It Is and Why It Matters</i>
3:00 pm	Break - World Cup A
	Student Presentations - World Cup B
3:30 pm	Manuel Ponce, PEER
	<i>Lateral Loading of Cast-in-drilled-hole Shaft</i>
3:45 pm	Kealy Rudersdorf, PEER
	<i>Unbonded Prestressed Structural Steel in Bridge Columns</i>
4:00 pm	Theodore Deligiannidis, MAE
	<i>Damage Functionality Relationships for Bridges</i>
4:15 pm	Raymond Foltz, MAE
	<i>Estimating Damage and Repair Costs</i>
4:30 pm	Ty Stokes, MAE
	<i>DS-4 Vulnerability Functions</i>
6:00 pm	Informal Dinner - Veranda
Sunday, August 8, 2003	
	Breakfast on your own
	Shuttle to Charleston Airport

2004 REU Symposium

Participants List - Guest Speakers, Tour Leader, MCEER-PEER-MAE Staff

Makola Abdullah

MCEER Diversity Program Director
FAMU/FSU College of Engineering
Florida A & M University
2525 Pottsdamer Street
Tallahassee, FL 32310-6046
Phone: 850-410-6386; Fax: 850-410-6502
Email: abdullah@eng.fsu.edu

Joseph Herkert

Guest Speaker
Associate Professor of Multidisciplinary Studies
North Carolina State University
Carter-Williams Building #2 2806 Hillsborough St.
College Station, TX 77843
Phone: 919-515-7993; Fax: 919-515-1828
Email: joe_herkert@ncsu.edu

Karen Buchheit

Meeting Coordinator
Multidisciplinary Center for Earthquake Engineering
Research (MCEER)
State University of New York at Buffalo
Red Jacket Quad
Buffalo, NY 14261
Phone: 716-645-3391 x 126; Fax: 716-645-3399
Email: kmb36@mceermail.buffalo.edu

Amit Kanvinde

PEER Education Committee Member
Dept. of Civil and Environmental Engineering
University of California, Davis
2001 Engineering III, One Shields Ave.
Davis, CA 95616
Phone: 530-752-2605; Fax: 530-752-7872
Email: kanvinde@ucdavis.edu

Charles Dwyer, PE

Project Manager
Engineering, Special Projects
South Carolina Dept. of Transportation
212 Huger Street
Charleston, SC 29403
Phone: 843-534-5001; Fax: 843-534-5080
Email: DwyerCT@dot.state.sc.us

Sandra Menke

MAE Advisor; Education Program Specialist
Mid-America Earthquake Center
University of Illinois at Urbana-Champaign
1239B Newmark Laboratory, 205 Mathews Ave.
Urbana, IL 61801
Phone: 217-244-8297; Fax: 217-333-3821
Email: smenke@uiuc.edu

2004 REU Symposium

Participants List - Students

Zaneta Adme *FSU*
340 Pennell Circle, Apt. 3
Tallahassee, FL 32310
Email: adme@eng.fsu.edu
Host Institution: University of Tokyo
Advisor: Makola Abdullah
Home Institution: Florida State University

Lisa Anderson *MCEER*
6480 Townline Rd.
North Tonawanda, NY 14120
Email: lma9@buffalo.edu
Host Institution: University at Buffalo
Advisor: Michael Constantinou
Home Institution: University at Buffalo

Corey Bergad *MCEER*
2708 East Minnehaha Parkway
Minneapolis, MN 55406
Email: cbergad@bates.edu
Host Institution: University at Buffalo
Advisor: Andrei Reinhorn
Home Institution: Bates College

Timothy Brownawell *MAE*
6965 County Road 477
Fulton, MO 65251
Email: brownawe@uiuc.edu
Host Institution: University of Memphis
Advisor: Charles Langson
Home Institution: University of Illinois

Nathan Canney *PEER*
821 Ford Street
Moscow, ID 83843
Email: canneyn@seattleu.edu
Host Institution: University of Washington
Advisor: Marc Eberhard
Home Institution: Seattle University

Abiel Carrillo *MCEER*
1804 Wyoming Ave., #80
Las Cruces, NM 88001
Email: aabbiieell@hotmail.com
Host Institution: University at Buffalo
Advisor: George C. Lee
Home Institution: New Mexico State University

Theodore Deligiannidis *MAE*
401 West Church St.
Kershaw, SC 29067
Email: gamecocks1@hotmail.com
Host Institution: Georgia Institute of Technology
Advisor: Reginald DesRoches
Home Institution: University of South Carolina

Laura Flores *PEER*
953 S. Esperanza Street
Los Angeles, CA 90023
Email: lmflores@ucsd.edu
Host Institution: University of California, Berkeley
Advisor: Jack Moehle
Home Institution: University of California, San Diego

Raymond Foltz *MAE*
4440 Nassau Court #505D
Little River, SC 29566
Email: foltzr1@citadel.edu
Host Institution: Texas A&M University
Advisor: Mary Beth Hueste
Home Institution: The Citadel

Vivian Gonzales *PEER*
1244 S. Orange St. #C
Glendale, CA 91204
Email: vdgonzal@ucsd.edu
Host Institution: California Institute of Technology
Advisor: Keith Porter
Home Institution: University of California, San Diego

2004 REU Symposium

Participants List - Students

Mary Grondin *MAE*
3853 Peppermill Road
Attica, MI 48412
Email: grondinm@msu.edu
Host Institution: University of Illinois
Advisor: Amr Elnashai
Home Institution: Michigan State University

Lindsey Oliver *MAE*
4861 Gatesbury Dr.
St. Louis, MO 63128
Email: Lindsey@uchicago.edu
Host Institution: University of Memphis
Advisor: Roy Van Arsdale
Home Institution: University of Chicago

Ashford Kneitel *PEER*
9930 Durant Drive, Apt. #1
Los Angeles, CA 90212
Email: mib405@aol.com
Host Institution: University of California, San Diego
Advisor: Scott Ashford
Home Institution: East Los Angeles College

Manuel Ponce *PEER*
1142 Augusta Drive
Los Angeles, CA 90023
Email: mponce@ucsd.edu
Host Institution: University of California, Los Angeles
Advisor: Jonathan Stewart
Home Institution: University of California, San Diego

Michael Long *MCEER*
4606 Cobble Crest
San Antonio, TX 78217
Email: mlong@rice.edu
Host Institution: University at Buffalo
Advisor: Andrei Reinhorn
Home Institution: Rice University

Kealy Rudersdorf *PEER*
315 S. 57th Street
Omaha, NE 68132
Email: 18rudersdorf@cua.edu
Host Institution: Stanford University
Advisor: Sarah Billington
Home Institution: Catholic University of America

Meagan Mauter *MAE*
3044 Corydon Road
Cleveland Heights, OH 44118
Email: mmauter@rice.edu
Host Institution: Washington University
Advisor: Shirley Dyke
Home Institution: Rice University

Ty Stokes *MAE*
8063 Foxchase Drive
Indianapolis, IN 46256
Email: stokes@mailbox.sc.edu
Host Institution: University of Illinois
Advisor: Y.K. Yen
Home Institution: University of South Carolina

Christina Nishimoto *PEER*
1253 Royal Oaks Drive
Stockton, CA 95209
Email: cnishimo@ucsd.edu
Host Institution: University of California, Davis
Advisor: Ross Boulanger
Home Institution: University of California, San Diego

Karla Villarreal *FAMU*
925 E. Magnolia Dr., Apt. E8
Tallahassee, FL 32301
Email: villar@eng.fsu.edu
Host Institution: University of Tokyo
Advisor: Makola Abdullah
Home Institution: Florida State University

Cover Images

Cover Images (top row, from left): The Kiawah Island Golf Course; Group photo; (Middle row, from left): Manuel Ponce and Ph.D. Student Eric Ahlberg with the column containing the instrumentation that will measure “Lateral Loading Cast-in-Drilled-Hole-Shaft”; Group photo taken during the Cooper River Bridge Tour; Corey Bergad with the plastic hinge tested during his research project; (Bottom row, from left): A Student presents research to her peers; Nathan Canney’s research is on “Performance of Concentrically Braced Frames Under Cyclic Loading”; Project Manager Charles T. Dwyer of the South Carolina Department of Transportation gives students a presentation before they toured the Cooper River Bridge.

Acknowledgements

This report was prepared by the Multidisciplinary Center for Earthquake Engineering Research through a grant from the National Science Foundation Earthquake Engineering Research Centers Program, New York State and other sponsors.

The material herein is based upon work supported in whole or in part by the National Science Foundation, New York State and other sponsors. Opinions, findings, conclusions or recommendations expressed in this publication do not necessarily reflect the views of these sponsors or the Research Foundation of the State University of New York.



MULTIDISCIPLINARY CENTER FOR EARTHQUAKE ENGINEERING RESEARCH

A National Center of Excellence in Advanced Technology Applications

University at Buffalo, State University of New York

Red Jacket Quadrangle ■ Buffalo, New York 14261

Phone: (716) 645-3391 ■ Fax: (716) 645-3399

E-mail: mceer@mceermail.buffalo.edu ■ WWW Site <http://mceer.buffalo.edu>



University at Buffalo *The State University of New York*